LPTMS
Laboratoire de Physique Théorique
et Modèles Statistiques

# Portfolio

*Journées du LPTMS à Bordeaux - juin 2022*

*Journées du LPTMS à Deauville - juin 2019*

# Item 1

## *Team Presentation*

Laboratoire de Physique Théorique
et Modèles Statistiques

# Permanent members

# Quantum Systems

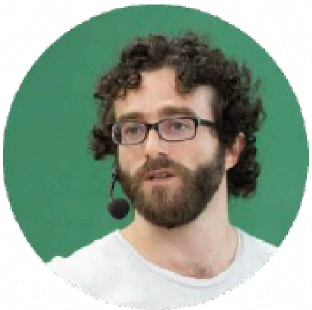
Maurizio Fagotti


Leonardo Mazza


Nicolas Pavloff


Dmitry Petrov


Guillaume Roux


Mikhail Zvonarev

## Emeriti


Eugène Bogomolny


Serguei Brazovskii

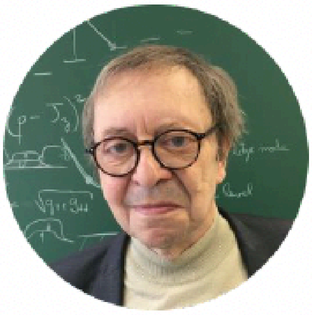
Georgy Shlyapnikov

# Statistical physics, field theory and integrable systems


Françoise Cornu


Satya Majumdar


Sergei Nechaev


Raoul Santachiara


Véronique Terras


Christophe Texier

## Emeritus


Stéphane Ouvry

## Volunteers


Alain Comtet


Hubert Krivine

# Disordered systems, soft matter and interface physics


Thorsten Emig


Silvio Franz


Antoine Fruleux


Martin Lenz


Martial Mazars


Valentina Ros


Alberto Rosso


Denis Ullmo

## Volunteer


Emmanuel Trizac

# Administrative and IT staff

Claudine Le Vaou

Delphine Hannoy

Zhiqiang Qin

Karolina Kolodziej (2017 – 2023)

# Non permanent members

# Post docs

# Quantum Systems

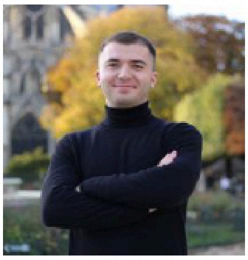

K. Bidzhiev
(2019 – 2022)

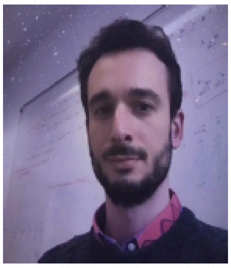

A. Biella
(2021 – 2021)

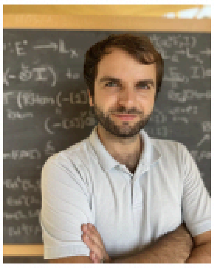

L.Capizzi
(2023)

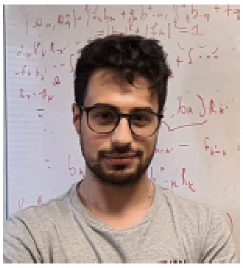

G. Del Vecchio Del Vecchio
(2023)

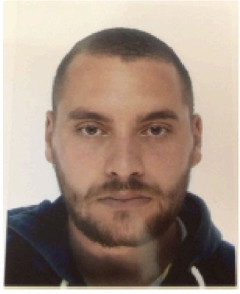

J. Despres
(2022 – 2023)

P. Haldar
(2020 – 2020)

V. Maric
(2021)

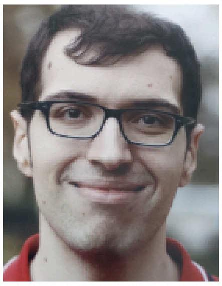

G. Martone
(2016 – 2019)

G. Mousinho Lando
(2021 – 2022)

A. Nardin
(2023)

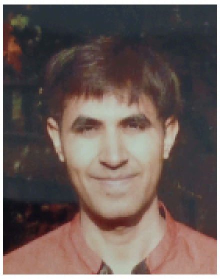

B. Pandey
(2017 – 2019)

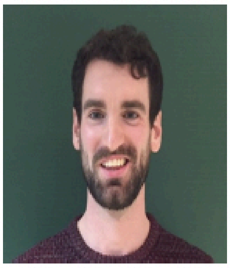

E. Quinn
(2018 – 2020)

A. Tononi
(2021 – 2023)

L. Zadnik
(2019 – 2022)

# Statistical physics, field theory and integrable systems

T. Banerjee
(2018 – 2019)

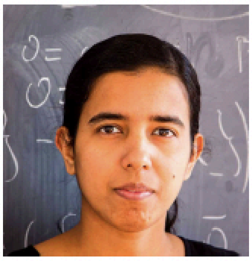

U. Basu
(2017 – 2018)

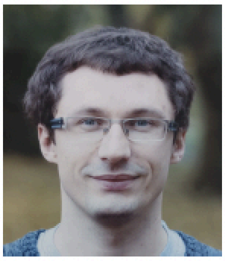

J. Grela
(2016 – 2018)

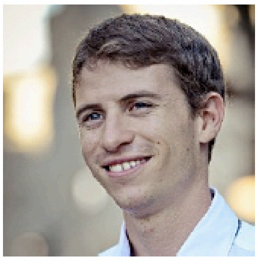

N. Smith
(2019 – 2020)

# Disordered systems, soft matter and interface physics

F. Aguirre Lopez
(2021 – 2023)

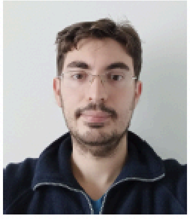

M. Baldovin
(2021 – 2023)

P. Bayati
(2018 – 2021)

M. Bouzid
(2017 – 2020)

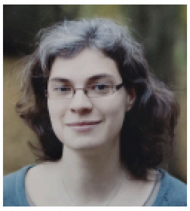

M. Chupeau
(2016 – 2018)

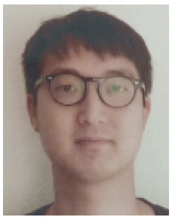

S. Hwang
(2017 – 2019)

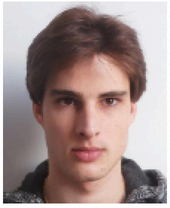

T. Maimbourg
(2019 – 2020)

A. Maitra
(2015 – 2018)

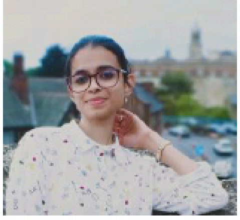

Mayarani M
(2020 – 2022)

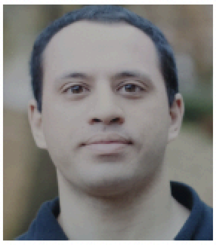

A. Nicolas
(2016 – 2018)

V. Ouazan Reboul
(2023)

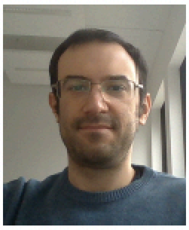

M. Pastore
(2021 – 2023)

C. Plata Ramos
(2020 – 2021)

J. Rocchi
(2017 – 2019)

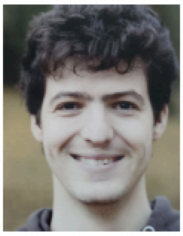

G. Saggiorato
(2016 – 2018)

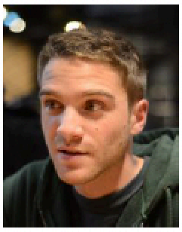

V. Sorichetti
(2022 – 2022)

M. Terzi
(2019 – 2022)

D. Q. Tran
(2021 – 2021)

C. Valencia Gallardo
(2019 – 2019)

A. Zelenskiy
(2023)

# PhD students

# Quantum Systems

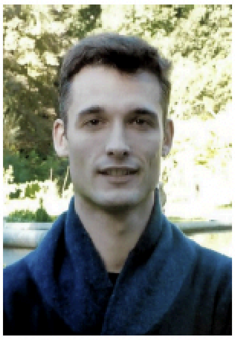
G. Bertoli
(2015-2019)

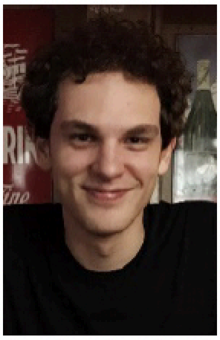
S. Bocini
(2020 – 2023)


G. Ciliberto
(2021)


J. Givois
(2021)


L. Gotta
(2019 – 2022)

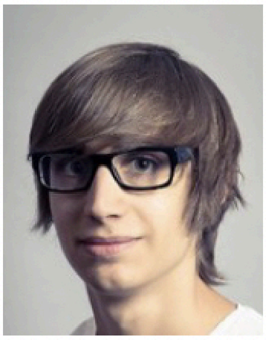
M. Isoard
(2017 – 2020)

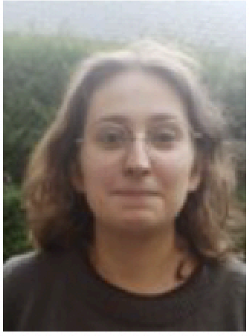
A. Marché
(2023)


N. Milazzo
(2018 – 2021)

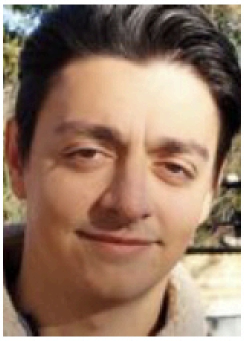
G. Morettini
(2023)

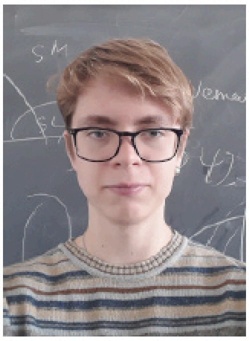
K.Plekhanov
(2015-2018)

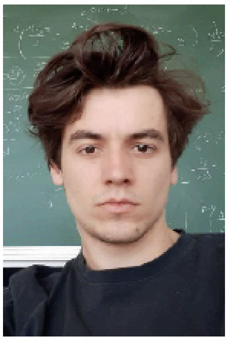
A. Pricoupenko
(2018 – 2021)

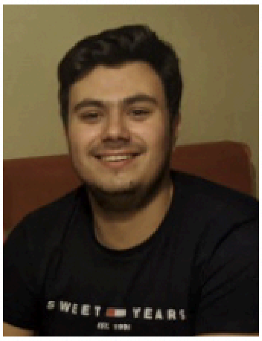
L. Rosso
(2020 – 2023)

# Statistical physics, field theory and integrable systems

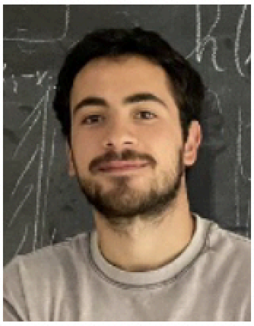
C.Abetian
(2022)


M.Biroli
(2022)


I. Burenev
(2023)


B. De Bruyne
(2020 – 2023)

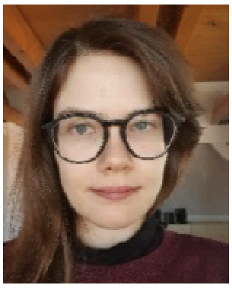
A. Flack
(2020 – 2023)

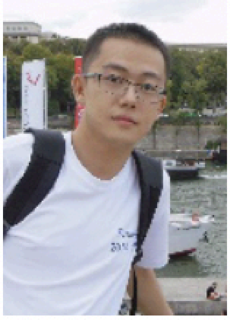
L. Gan
(2020 – 2023)

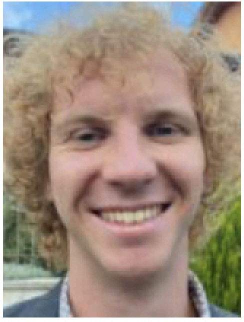
F. Gerbino
(2023)


A. Grabsch
(2015 – 2018)

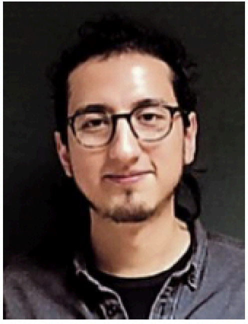
S. Grijalva Gonzalez
(2017 – 2020)

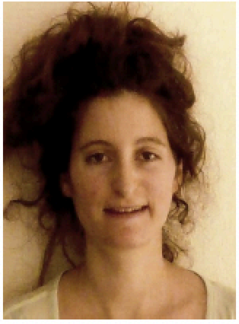
N. Javerzat
(2017 – 2020)


B. Lacroix à chez Toine
(2016 – 2019)


P. Mergny
(2019 – 2022)


F. Mori
(2019 – 2022)

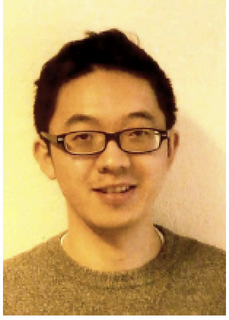
H. Pei
(2017 – 2020)

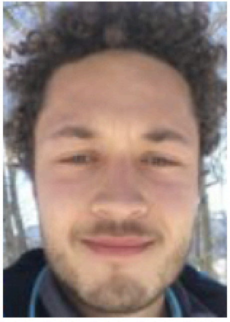
R. Usciati
(2023)

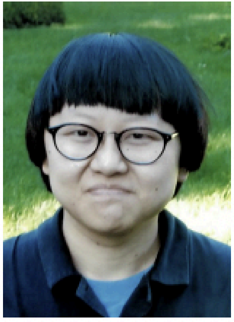
S. Wu
(2015 – 2018)

# Disordered systems, soft matter and interface physics

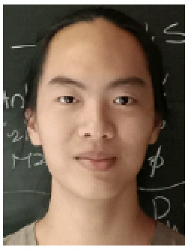
P. Akarapipattana
(2023)

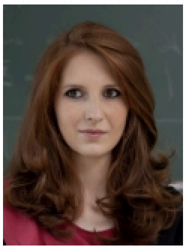
A. Altieri
(2015- 2018)


L. Barberi
(2016 – 2019)


F. Benoist
(2019 – 2022)

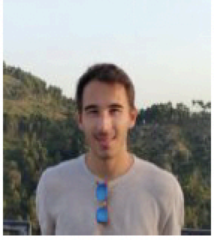
M. Bernard
(2023)

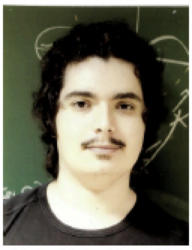
T. Bonnemain
(2016 – 2020)

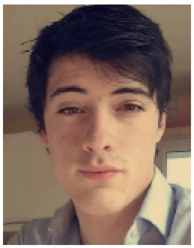
L. Bremaud
(2021)

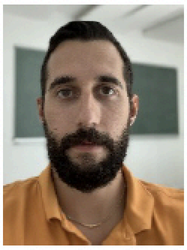
M. Butano
(2021)


S. Cazayus-Claverie
(2016 – 2020)

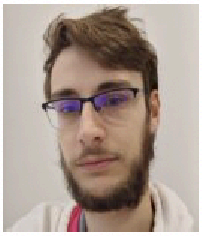
B. Ferté
(2023)

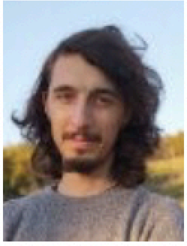
G. Folena
(2017 – 2020)


L. Koehler
(2020 – 2023)

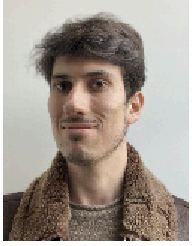
F. Lanza
(2020 – 2023)

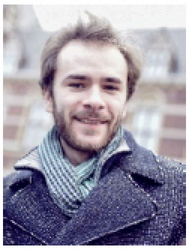
H. Le Roy
(2018 – 2021)


E. Lorenzetti
(2021)


S. Majumdar
(2020 – 2023)

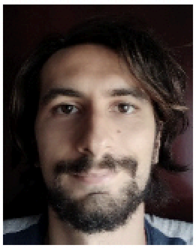
F. Nicoletti
(2019 – 2023)


A. Pacco
(2022)

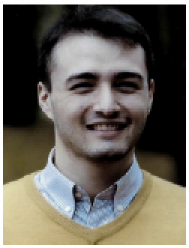
I. Palaia
(2016 – 2019)


I. Rodriguez-Arias
(2015 – 2018)

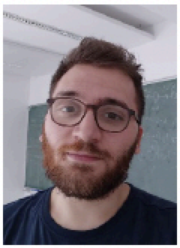
V. Schimmenti
(2020 – 2023)


A. Sclocchi
(2017 – 2020)


D. Tzivrailis
(2023)


L. Varela Alvarez
(2018 – 2021)

# Item 2

## *Visitors, long stays and event organizations*

# Regular visitors

| LAST NAME | FIRST NAME | AFFILIATION |
|---|---|---|
| CAO | Xiangyu | LPENS Paris |
| CHEPELIANSKII | Alexei | LPS Orsay |
| DE LUCA | Andrea | LPTM Cergy |
| KITANINE | Nikolaï | IMB Dijon |
| LE DOUSSAL | Pierre | LPENS Paris |
| SCHEHR | Gregory | LPTHE Paris |
| SYKES | Cécile | LPENS Paris |
| WIESE | Kay | LPENS Paris |

# Visitor programme

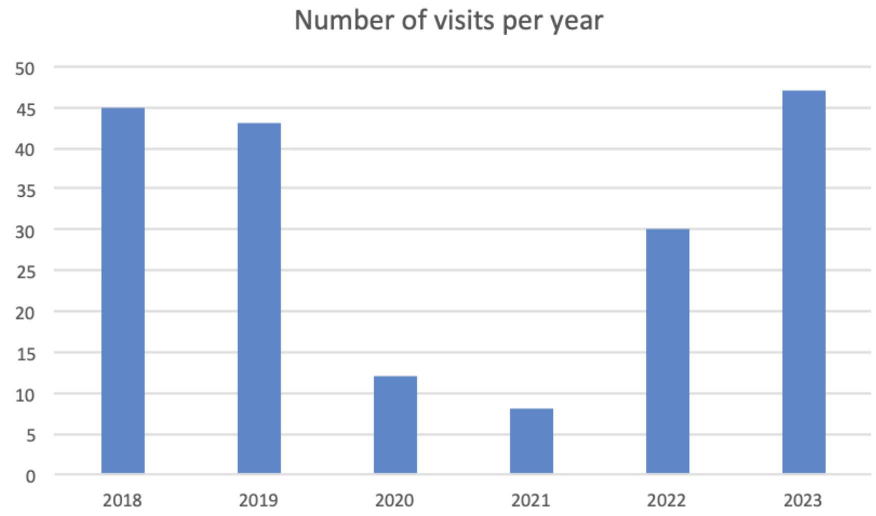

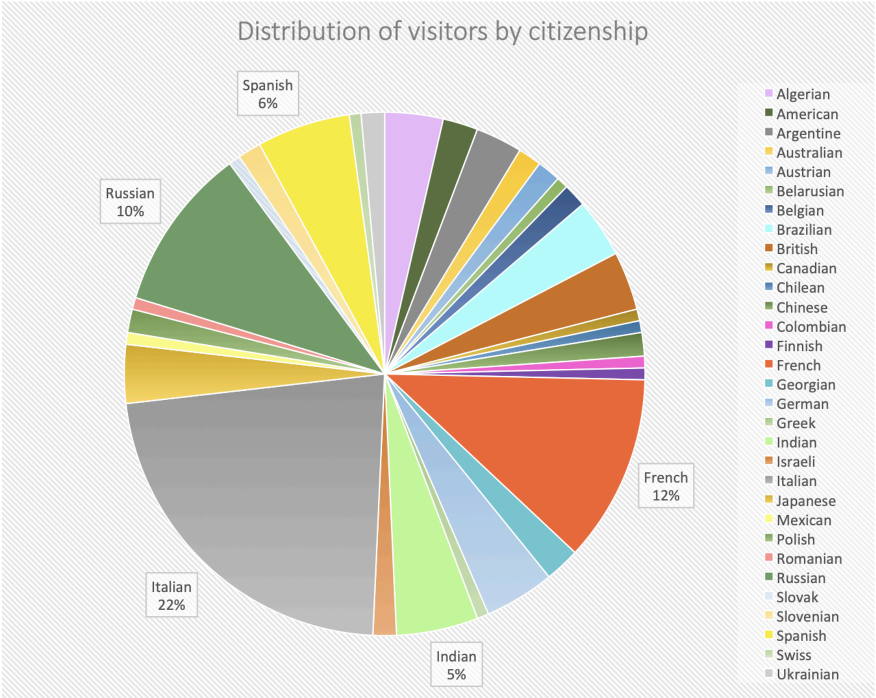

## 2018

| LAST NAME | FIRST NAME | STAY | AFFILIATION |
|---|---|---|---|
| BAIESI | Marco | 4 | Universita di Padova |
| BERNEVIG | Andrei | 37 | Princeton University |
| BILEN | Agustin | 12 | Univ. Nacional de Mar del Plata |
| BRAUN | Daniel | 25 | University of Tubingen |
| CHEIANOV | Vadim | 30 | Leiden University |
| EVANS | Martin | 7 | University of Edinburgh |
| FEDOROV | Aleksey | 8 | Russian Quantum Center Moscou |
| FLEUROV | Victor | 18 | Tel Aviv University |
| FUKUSUMI | Yoshiki | 50 | University of Tokyo |
| GAMAYUN | Oleksandr | 6 | University of Amsterdam |
| GAVRILIOUK | Serguei | 3 | Aix Marseille Université |
| GRADENIGO | Giacomo | 3 | Université de Rome |
| GRITSEV | Vladimir | 8 | University of Amsterdam |
| GUERY-ODELIN | David | 1 | Université Paul Sabatier Toulouse |
| HE | Xiaolong | 16 | Hubei University, Wuhan |
| JOYNER | Christopher | 2 | Queen Mary University of London |
| KAMCHATNOV | Anatoly | 54 | Institute of Spectroscopy, Troitsk |
| KIKTENKO | Evgeniy | 8 | Russian Quantum Center Moscou |
| KOLTON | Alejandro | 30 | Centro Atomico Bariloche |
| KUNDU | Anupam | 20 | Tata Institute Bangalore |

| | | | |
|---|---|---|---|
| KURLOV | Denis | 130 | University of Amsterdam |
| LIENARDY | Jean | 14 | Université Catholique de Louvain |
| LIPPIELLO | Eugenio | 4 | Univ. della Campania L. Vanvitelli Caserta |
| MAGONI | Matteo | 58 | Politecnico di Torino |
| MATVEENKO | Sergey | 153 | Landau Institute Moscou |
| MENDONCA | Jose Ricardo | 1 an | Universidade de Sao Paulo |
| MIZUSAKI | Takahiro | 14 | Senshu University, Tokyo |
| MUKAMEL | David | 4 | Weizmann Institute Rehovot |
| OZORIO DE ALMEIDA | Alfredo | 9 | Centro Brasileiro de Pequisas Fisicas Rio de Janeiro |
| PETRILLO | Giuseppe | 94 | Univ. della Campania L. Vanvitelli Caserta |
| POLOVNIKOV | Kirill | 35 | Lomonosov Moscow State Univ. |
| POLYCHRONAKOS | Alexios | 28 | City College of New York |
| POPLAVSKYI | Mihail | 14 | King's college London |
| RAY | Sayak | 26 | Indian Inst. of science, Mohanpur |
| RONCERAY | Pierre | 19 | Princeton University |
| SAAD | David | 3 | Aston University |
| SAMAJ | Ladislav | 45 | Slovak Acad. of Sciences Bratislava |
| SPOHN | Herbert | 3 | Technische Universitat Munchen |
| TAMM | Mikhail | 15 | State University of Moscow |
| TELLEZ | Gabriel | 14 | Universidad de Los Andes |
| TOURIGNY | Yves | 61 | University of Bristol |
| VALOV | Alexander | 16 | Lomonosov Moscow State Univ. |

|  |  |  |  |
|---|---|---|---|
| WARCHOL | Piotr | 9 | Jagiellonian University Krakow |
| XU | Peng | 16 | Hubei University, Wuhan |
| ZACCANTI | Matteo | 8 | Universita di Firenze |

## 2019

| LAST NAME | FIRST NAME | STAY | AFFILIATION |
|---|---|---|---|
| ALTSHULER | Boris | 31 | Columbia University |
| BALDELLI | Niccolo | 21 | ICFO Barcelone |
| BASU | Urna | 30 | Raman Institute Bangalore |
| BERTINI | Bruno | 14 | University of Ljubljana |
| BILEN | Agustin | 8 | Univ. Nacional de Mar del Plata |
| BOUDJEMAA | Abdelaali | 41 | Hassiba Benbouali Univ. of Chlef |
| BOYER | Denis | 75 | University of Mexico |
| CABRA | Daniel | 8 | La Plata University |
| DEAN | David | 5 | LOMA Talence |
| DUPONT | Maxime | 5 | University of California, Berkeley |
| ENDRES | Manuel | 1 | California Inst. of Technology Pasadena |
| EVANS | Martin | 29 | University of Edinburgh |
| FEDOROV | Aleksey | 5 | Russian Quantum Center Moscou |
| FRANCHINI | Fabio | 5 | Ruder Boskovic Institute Zagreb |
| GARCIA DE SORIA | Maribel | 13 | Universidad de Sevilla |
| GRABSCH | Aurélien | 2 | Leiden University |
| HARTL | Benedikt | 26 | Technical University Vienna |

| | | | |
|---|---|---|---|
| KAHL | Gerhard | 3 | Technical University Vienna |
| KIKTENKO | Evgeniy | 5 | Russian Quantum Center Moscou |
| KRAVTSOV | Vladimir | 5 | ICTP Trieste |
| KURLOV | Denis | 71 | University of Amsterdam |
| LANZA | Federico | 174 | University of Padua |
| MACALUSO | Elia | 1 | Trento University |
| MATVEENKO | Sergei | 63 | Landau Institute Moscou |
| MAYNAR | Pablo | 13 | Universidad de Sevilla |
| MAYS | Anthony | 31 | University of Melbourne |
| MUKAMEL | Davis | 9 | Weizmann Institute Rehovot |
| OPPENHEIMER | Naomi | 178 | Simons Foundation New York |
| PEREIRA DOS SANTOS | Alexandre | 14 | Univ. Federal do Rio Grande do Sul Porto Alegre |
| PLATA | Carlos | 19 | Universidad de Sevilla |
| PODGORNIK | Rudolf | 11 | University of Ljubljana |
| POLYCHRONAKOS | Alexios | 31 | City College of New York |
| POPLAVSKYI | Mihail | 15 | King's college London |
| PRADOS | Antonio | 19 | Universidad de Sevilla |
| RASANEN | Esa | 30 | Tampere University |
| ROSSINI | Davide | 31 | University of Pisa |
| SAMAJ | Ladislav | 29 | Slovak Acad. of Sciences Bratislava |
| TELLEZ | Gabriel | 31 | Universita de Los Andes |
| TOMSOVIC | Steve | 19 | Washington State University |
| TOURIGNY | Yves | 19 | University of Bristol |

| | | | |
|---|---|---|---|
| YUDSON | Vladimir | 6 | National Research Univ. Moscou |
| ZADNIK | Lenart | 5 | University of Ljubljana |

## 2020

| LAST NAME | FIRST NAME | STAY | AFFILIATION |
|---|---|---|---|
| GOIRAND | Florian | 10 | Université Paul Sabatier Toulouse |
| GRABSCH | Aurélien | 4 | Leiden University |
| HENKEL | Malte | 3 | Université de Lorraine Nancy |
| HOCINE | Ahmed | 11 | Hassiba Benbouali Univ. of Chlef |
| IEMINI | Fernando | 12 | Univ. Federal Fluminense Rio de Janeiro |
| KOZLOWSKI | Karol | 2 | ENS Lyon |
| MAYNAR | Pablo | 17 | Universidad de Sevilla |
| POLYCHRONAKOS | Alexios | 26 | City College of New York |
| PUJOL | Pierre | 1 | LPT Toulouse |
| RONCERAY | Pierre | 12 | Princeton University |
| SCHIMMENTI | Vincenzo | 184 | University of Padua |

## 2021

| LAST NAME | FIRST NAME | STAY | AFFILIATION |
|---|---|---|---|
| ARES | Filiberto | 7 | Universidad de Zaragoza |
| EVANS | Martin | 13 | University of Edinburgh |
| GATTOBIGIO | Mario | 2 | INPHYNI Valbonne |
| HAGENDORF | Christian | 31 | Université de Louvain |

|  |  |  |  |
|---|---|---|---|
| POLYCHRONAKOS | Alexios | 14 | City College of New York |
| SANTOS | Luis | 3 | Leibniz University |
| TARRUELL | Leticia | 3 | ICFO Barcelone |
| TOURIGNY | Yves | 27 | University of Bristol |

## 2022

| LAST NAME | FIRST NAME | STAY | AFFILIATION |
|---|---|---|---|
| AGORITSAS | Elisabeth | 33 | EPFL Lausanne |
| ASTRAKHARCHIK | Grigori | 21 | Univ. Politecnica de Catalunya |
| BICEGO | Sara | 6 | Imperial College London |
| BRESOLIN | Sebastiano | 34 | University of Trento |
| CABRA | Daniel | 44 | La Plata University |
| DEL VECCHIO DEL VECCHIO | Giuseppe | 49 | King’s college London |
| EVANS | Martin | 30 | University of Edinburgh |
| GONCHENKO | Marina | 10 | Univ. Politecnica de Catalunya |
| JAGLA | Eduardo | 10 | Centro Atomico Bariloche |
| JAPHARIDZE | Georges | 5 | Ilia State University |
| JAVERZAT | Nina | 16 | SISSA Trieste |
| KALISE | Dante | 2 | Imperial College London |
| MAJEED BHAT | Junaid | 4 | ICTS Bangalore |
| MARTIN | John | 31 | University of Liège |
| MAYNAR | Pablo | 12 | Universidad de Sevilla |
| MERCADO VASQUEZ | Gabriel | 9 | University of Mexico |

|  |  |  |  |
|---|---|---|---|
| MOUDGALYA | Sanjay | 2 | California Inst. of Technology Pasadena |
| NARDIN | Alberto | 7 | University of Trento |
| NIEDDA | Jacopo | 25 | Sapienza Univ. Rome |
| PATRON | Antonio | 93 | Universidad de Sevilla |
| PETRILLO | Giuseppe | 52 | Univ. della Campania Luigi Vanvitelli |
| POLOVNIKOV | Kirill | 51 | Skoltech Moscow |
| POLYCHRONAKOS | Alexios | 25 | City College of New York |
| PRADOS | Antonio | 28 | Universidad de Sevilla |
| SAMAJ | Ladislav | 14 | Slovak Acad. of Sciences Bratislava |
| SASTRY | Srikanth | 4 | Jawaharlal Nehru Centre Bangalore |
| TELLES | Igor | 28 | Univ. Federal do Rio Grande do Sul |
| TELLEZ | Gabriel | 5 | Universita de Los Andes |
| TOURIGNY | Yves | 16 | University of Bristol |
| WALTER | Benjamin | 12 | Imperial College London |

## 2023

| LAST NAME | FIRST NAME | STAY | AFFILIATION |
|---|---|---|---|
| AUPETIT-DIALLO | Gianni | 3 | INPHYNI Valbonne |
| BELLIARD | Samuel | 4 | LMPT Tours |
| BERADZE | Bachana | 59 | Ilia State University |
| BOUDJEMAA | Abdelaali | 19 | Hassiba Benbouali Univ. of Chlef |

| | | | |
|---|---|---|---|
| BOYER | Denis | 28 | University of Mexico |
| CABRA | Daniel | 22 | La Plata University |
| CONGY | Thibault | 4 | Northumbria University |
| DAS | Suchismita | 3 | MPI Dresde |
| DEL VECCHIO DEL VECCHIO | Guiseppe | 3 | King's college London |
| DERIVERY | Emmanuel | 11 | MRC Lab Cambridge |
| DEROSI | Giulia | 2 | Univ. Politecnica de Catalunya |
| DI LIBERTO | Marco | 2 | University of Padova |
| DI SPENA | Sharon | 54 | LPTM Cergy |
| EVANS | Martin | 9 | University of Edinburg |
| FLORIS | Elisa | 3 | Politecnico di Turino |
| GANEVA | Iva | 3 | University of Bern |
| GARUCHAVA | Shota | 59 | Ilia State University |
| GERAGHTY | Patrick | 5 | University of Cologne |
| GIACHETTI | Guido | 365 | LPTM Cergy |
| HOCINE | Ahmed | 5 | Hassiba Benbouali Univ. of Chlef |
| IMURA | Ken Ichiro | 9 | University of Tokyo |
| JAVERZAT | Nina | 5 | SISSA Trieste |
| JOSEPH | Merin | 3 | Leeds University |
| KARDAR | Mehran | 5 | MIT Cambridge |
| KHERUNTSIAN | Karen | 2 | University of Queensland |
| MEHRI | Zohra | 30 | Hassiba Benbouali Univ. of Chlef |
| MUKHERJEE | Soheli | 11 | Ben Gurion University |

| | | | |
|---|---|---|---|
| NARDIN | Alberto | 115 | University of Trento |
| NEJI | Rajendra | 3 | IBB Julich |
| NICOLETTI | Flavio | 8 | Sapienza Univ. Rome |
| NIEDDA | Jacopo | 16 | Sapienza Univ. Rome |
| NUNZI | Carlotta | 117 | LPTM Cergy |
| PELITI | Luca | 32 | SMRI Santa Marinella |
| PETRILLO | Giuseppe | 11 | Univ. della Campania Luigi Vanvitelli |
| POLETTI | Dario | 8 | Singapore University |
| RUSSO | Giovanni | 98 | Universita di Pavia |
| SCARDICCHIO | Antonello | 3 | ICTP Trieste |
| SCHLAGHECK | Peter | 3 | University of Liège |
| SCLOCCHI | Antonio | 3 | EPFL Lausanne |
| TAKAHASHI | Kin'Ya | 3 | University of Tokyo |
| TAMM | Mikhail | 5 | Tallinn University |
| TELLES | Igor | 155 | Univ. Federal do Rio Grande do Sul |
| TOMSOVIC | Steve | 115 | Washington State University |
| TOURIGNY | Yves | 26 | University of Bristol |
| YOSHIDA | Hironobu | 15 | University of Tokyo |
| ZADNIK | Lenart | 7 | SISSA Trieste |
| ZUNDEL | Martina | 8 | LPMMC Grenoble |

## Long stays

| YEAR | NAME | PLACE | DAYS |
|---|---|---|---|
| 2018 | E. Bogomolny | University of Bristol | 98 |
| | E. Bogomolny | Lanzhou (Chine) | 15 |
| | T. Emig | Naples University | 7 |
| | T. Emig | UMI 3466 CNRS MIT | 59 |
| | S. Franz | AIMS Kigali Rwanda | 30 |
| | S. Franz | ICTP Trieste | 10 |
| | S. Franz | La Sapienza University Rome | 138 |
| | O. Giraud | Université de Mar del Plata | 20 |
| | S. Majumdar | Weizmann Institute | 24 |
| | S. Majumdar | Raman Research Institute Bangalore | 14 |
| | S. Majumdar | ICERM Brown University | 21 |
| | S. Ouvry | University Stellenbosch | 27 |
| | S. Ouvry | Uni. Federal Rio Grande do Norte Natal | 12 |
| | S. Ouvry | Uni. British Columbia Vancouver | 8 |
| | S. Ouvry | City College New York | 9 |
| | S. Ouvry | IRD Mbour Sénégal | 22 |
| | R. Santachiara | IFLP Univ. La Plata | 21 |
| | V. Terras | Simons Center Stony Brooks | 14 |
| 2019 | E. Bogomolny | ICTP Trieste | 12 |
| | T. Emig | Polar Electro, Oulu, Finland | 15 |
| | T. Emig | UMI 3466 CNRS MIT | 7 |
| | S. Franz | La Sapienza University Rome | 145 |

| | | | |
|---|---|---|---|
| | O. Giraud | National University of Singapore | 11 |
| | O. Giraud | Université de Mar del Plata | 13 |
| | S. Majumdar | Raman Research Institute Bangalore | 30 |
| | S. Majumdar | TIFR Bombay | 14 |
| | S. Majumdar | Weizmann Institute | 20 |
| | S. Majumdar | Raman Research Institute Bangalore | 27 |
| | S. Ouvry | University Stellenbosch | 20 |
| | S. Ouvry | Institut Physics Natal | 24 |
| | S. Ouvry | CRM Montréal | 8 |
| | S. Ouvry | AIMS Mbour Sénégal | 22 |
| | A. Rosso | RRI Bangalore, TIFR Mumbai | 15 |
| | R. Santachiara | IIP UFRN Natal | 30 |
| 2020 | S. Majumdar | ICTS Bangalore | 21 |
| | S. Ouvry | AIMS Stellenbosch | 19 |
| 2021 | E. Bogomolny | ICTP Trieste | 10 |
| | S. Ouvry | City College New York | 12 |
| 2022 | S. Franz | La Sapienza University Rome | 48 |
| | O. Giraud | National University of Singapore | 20 |
| | O. Giraud | Université de Mar del Plata | 14 |
| | S. Ouvry | AIMS Stellenbosch | 13 |
| | A. Rosso | ICTS TIFR Bangalore, TIFR Mumbai | 9 |
| | V. Terras | Galileo Galilei Inst. Florence | 14 |
| 2022 - 2023 | M. Lenz | Ludwig Maximilian University of Munich | 330 |
| 2022 - 2023 | S. Majumdar | ICTS Bangalore | 28 |
| 2023 | E. Bogomolny | ICTP Trieste | 20 |

| | | | |
|---|---|---|---|
| | T. Emig | Physics Dept. MIT | 15 |
| | S. Franz | La Sapienza University Rome | 62 |
| | S. Majumdar | Raman Research Institute Bangalore | 28 |
| | S. Ouvry | AIMS Stellenbosch | 23 |
| | S. Ouvry | City College New York | 9 |
| | S. Ouvry | University Montreal | 11 |
| | E. Trizac | Institut Physics Bratislava | 11 |

# Organization of events

| | | |
|---|---|---|
| 2018 | Workshop Correlations, fluctuations and anormalous transport in systems far from equilibrium, Weizmann Inst. | S. Majumdar |
| | Journée de physique statistique, Paris | E. Trizac |
| | Workshop Running science meets physics & engineering, MIT, Cambridge | T. Emig |
| | Atelier sur les matrices aléatoires, Paris | G. Schehr |
| | Conference NSPCS, KIAS, Seoul | S. Majumdar |
| | Disordered serendipity: a glassy path to discovery. A workshop in honour of Giorgio Parisi's 70th birthday, La Sapienza Univ. | S. Franz |
| | Conference Probabilistic methods in statistical physics for extreme statistics and rare events, Pise | G. Schehr |
| | 4th international conference on physics and biological systems, Gif sur Yvette | M. Lenz |
| 2019 | 3rd Bangkok workshop on discrete geometry, dynamics and statistics | S. Ouvry |
| | Journée de physique statistique, Paris | E. Trizac |
| | Conference Artificial intelligence and physics, Orsay | A. Rosso |
| | Conference CCEGN 2019, Les Houches | S. Nechaev |
| | Workshop Complex HRV analysis during exercise, Oulu Univ. Finland | T. Emig |
| | Workshop Yielding phenomena in disordered systems, Bariloche | A. Rosso |
| | Workshop New trends in quantum light and nanophysics, Maratea | G. Shlyapnikov |
| | SFT-Paris 2019: Lectures on statistical and condensed matter field theory | R. Santachiara |
| 2020 | Journée de physique statistique, Paris | E. Trizac |
| | Workshop Shortcut to adiabaticity 2020, Toulouse | E. Trizac |
| | Virtual Physiological Human 2020 | M. Lenz |
| 2021 | Workshop on quantum computing, Sotchi | G. Shlyapnikov |
| | 7th Les Houches School in computational physics: dynamics of complex quantum systems, from theory to computation | A. Rosso |
| | Programme Bootstat 2021, Orsay | R. Santachiara |
| | 5th international conference on physics and biological systems, Fully online | M. Lenz |

| | | |
|---|---|---|
| | Summer school FPSP XV, Bruneck | A. Rosso |
| | Programme “Dynamics and local control of impurities in complex quantum environments”, Orsay | M. Zvonarev |
| | Conference on quantum technologies, Moscow | G. Shlyapnikov |
| 2022 | 4th Bangkok workshop on discrete geometry, dynamics and statistics | S. Ouvry |
| | Journée de physique statistique, Paris | E. Trizac |
| | Workshop on quantum computing, Sotchi | G. Shlyapnikov |
| | School Interdisciplinary challenges: from non-equilibrium physics to life sciences, Edinburgh | V. Ros |
| | Workshop Quantum many-body physics in the presence of an environment 2022, Cergy | L. Mazza |
| | 6th international conference on physics and biological systems, Orsay | M. Lenz |
| | Summer school Disorder in complex systems, Orsay | A. Rosso |
| | Workshop New frontiers in liquid matter, Paris | E. Trizac |
| | International school & workshop ECRYS 2022, Cargèse | S. Brazovskii |
| | Workshop Large deviations, extremes and anomalous transport in nonequilibrium systems, ESI, Vienna | S. Majumdar |
| | Conference Statistical mechanics and its applications, Dilijan, Armenia | S. Nechaev |
| | Conference Statistical physics of complex systems, ICTS, Bangalore | S. Majumdar |
| 2023 | 5th Bangkok workshop on discrete geometry, dynamics and statistics | S. Ouvry |
| | From soft matter to biophysics conference, Les Houches | M. Lenz |
| | Journées interdisciplinaires de physique statistique, Orsay | V. Ros |
| | Programme "Dynamical foundations of many-body quantum chaos", Orsay | O. Giraud |
| | Program Quantum many-body physics in the presence of an environment 2023, Orsay | L. Mazza |
| | Congress of the French Physical Society, Paris | M. Lenz |
| | Frustrated self-assembly retreat, Eybens | M. Lenz |

# Item 3

## *lab’s life, seminars*

We describe below the scientific activity of the LPTMS regarding the seminars, meetings, scientific days involving other laboratories in the Paris-Saclay area and beyond, off-site meetings, organization of scientific visits and outreach activities.

## 1- Seminars & regular meetings at the LPTMS

Seminars play a vital role in LPTMS's scientific life. The general LPTMS seminar is held weekly, and it is supplemented by three topical seminar series on complex systems, biophysics and quantum physics, by the PhD and Postdoc seminar and by some group meetings. Further details on each series is provided below.

### LPTMS general seminar (Tuesday, 11 am, every week)

This seminar is contributed by invited visitors, prospective CNRS applicants, as well as lab members (one or two talks per year). The diversity in topics aims at representing all research lines of the LPTMS in a balanced manner. The audience includes also the regular visitors of the lab; when relevant, members of neighboring labs (LPS, LISN and IPhT) are invited. It is a strong tradition of the LPTMS to see this seminar not only as the main occasion for its members to gather and interact, but also as an essential formative experience for PhD students: all students are highly encouraged to attend, and their participation remains consistently high. The seminar series has been conducted online amid the COVID-19 pandemic, and in a hybrid format from 2021 to 2023. It is now transitioning back to in-person sessions. Organizer: Valentina Ros.

### Complex systems seminars (Thursday, 11 am, once or twice per month) and Quantum physics seminars (Friday, 2 pm, once or twice per month)

These two topical seminars take place once or twice per month, with the scope of hosting more technical and detailed talks on the subjects of complex systems and quantum physics, respectively. Their more flexible structure allows also for the inclusion of talks by external visitors who may face travel constraints preventing their participation in general Tuesday seminars, along with students and permanent members of LPTMS. Organizers: Marco Biroli, Valentina Ros (complex systems) and Leonardo Mazza, Alberto Nardin (quantum).

### Physics-Biology interface seminar (Friday, 11 am, twice per month)

Coordinated by both LPTMS and the adjacent lab LPS, this seminar series serves as a primary platform for the research at the interface between physics and biology in the south of Paris. The audience consists of physicists and biologists from the Paris-Saclay area, with a significant presence of experimentalists. Talks within this series occur bi-weekly, alternating between LPTMS and LPS as hosting venues. Organizers: Martin Lenz, Antoine Fruleux.

### PhD and Postdoc seminars (Wednesday, 2 pm, once per month)

This seminar series is independently organized by PhD students and Postdocs from the lab. The format follows a journal-club style, where participants alternate between presenting and discussing scientific papers of broad interest, alongside sharing their own research findings and questions. Organizer: Charbel Abetian.

### Soft Biophysics Group Meeting (Wednesday, 3 pm, each week)

This regular group meeting features journal clubs, informal contributions and technical discussions from students and collaborators of Martin Lenz, Antoine Fruleux, Valentina Ros. Once every two weeks this meeting is held jointly with the group of Erwin Frey at LMU Munich over Zoom. Organizer: Martin Lenz.

## 2- Meetings *“hors les murs”*

### LPTMS days (journées du LPTMS)

Throughout the evaluation period, the LPTMS has organized two off-site meetings involving all the lab members, including the regular visitors and prospective PhD students doing an M2 stage. The scientific program included seminars by a selection of permanents, postdocs and PhD students, with the aim of keeping all lab members informed about the evolving research directions at the LPTMS. These occasions also facilitated discussions on general issues related to the lab life (carbon footprint, seminars organization) through some general assemblies. The LPTMS days 2019 took place in Deauville, organized by Christophe Texier, Leonardo Mazza and Claudine Le Vaou. The LPTMS days 2022 took place in Bordeaux, organized by Silvio Franz, Claudine Le Vaou, Karolina Kolodziej.

### Opération Oxy-Jeunes

The LPTMS has joined the program Oxy-Jeunes aiming at organizing scientific meetings for Phd students and postdocs following the pandemic period. The lab has financed a 3 day meeting at the Ecole de Physique des Houches (31 May-2 June 2021) with a scientific program self-organized by the PhD students and postdocs of the LPTMS and LPS laboratories.

## 3- Seminars & meetings promoting integration with other labs

### FFJ days & colloquia

The LPTMS is a constituent of the Fédération Friedel Jacquinot (FFJ), which encompasses six laboratories (FAST, ISMO, LAC, LPS, LPTMS, LuMIn) that are closely knit both geographically (situated within an 800-meter radius) and scientifically (experimental and theoretical studies of soft and condensed matter). The lab has contributed with talks to the three FFJ Days held yearly from 2021; in addition, the FFJ organizes a series of colloquia of general interest (8 colloquia from autumn 2021 to spring 2024). The LPTMS has proposed and managed the organization of the following colloquia in the period 2021-2023: Michael Berry (December 2021), Michael Kosterlitz (June 2022), Leticia Cugliandolo (December 2023). The LPTMS referent for the FFJ is Raoul Santachiara.

### LPTMS-IPhT Days

Members of the LPTMS have strong scientific connections and collaborations with the IPhT laboratory of CEA Saclay. To highlight and foster these interactions, in 2022 we organized a new edition of the LPTMS-IPhT Days, with two days of seminars featuring presentations by members of both labs on the themes of quantum physics (14 April 2022 at the LPTMS) and statistical physics (20 April 2022 at the IPhT). The LPTMS member responsible for the organization has been Raoul Santachiara.

## Scientific programs of the Institut Pascal

Besides participating as audience to the scientific programs of the Institut Pascal (IPa) which shares the building with the LPTMS, several members of the lab have contributed actively to the organization of the following scientific programs since the beginning of the activity of the IPa until 2023:

☐ Artificial intelligence and physics (2 days, 2019). LPTMS organizer: Alberto Rosso

☐ Dynamics and local control of impurities in complex quantum environments (4 weeks, 2021). LPTMS organizer: Mikhail Zvonarev

☐ Bootstat 2021: Conformal bootstrap and statistical models (4 weeks, 2021). LPTMS organizer: Raoul Santachiara

☐ Disorder in complex Systems (2 weeks, 2022). LPTMS organizer: Alberto Rosso

☐ OpenQMBP (3 weeks, 2023). LPTMS organizer: Leonardo Mazza

☐ Dynamical Foundations of Many-Body Quantum Chaos (5 weeks, 2023). LPTMS organizer: Olivier Giraud

# Item 4

## *Carbon footprint*

The unit has planned over the recent period various actions regarding its carbon footprint. We summarize below what has been done and the future challenges regarding the environmental impact of the lab.

## 1- Context and timeline of the activities

We first recall some key dates and facts setting the context in which the unit is embedded. We focus on the French research community. We first recall that the implementation of a national low-carbon strategy for France gives an objective of 2 tCO2e / person in 2050 (and carbon neutrality assuming carbon compensation) with an intermediate target of 6 tCO2e / person around 2030.

Some key dates for the French research community are

- ~2019-today : creation of the collective Labo1Point5, which became a GDR in June 2021, many laboratories carry out their greenhouse gas assessments (BGES), mainly with the GES1point5 tool.
- ~2018 : Hcéres takes into account initiatives to reduce the environmental footprint of laboratories during its evaluations.
- October 21, 2020 : Letter from CNRS DG and CPU President “contribute to the regulation of the carbon impact of academic activities.”
- January - March 2021 : meetings in Paris-Saclay and at the CNRS on the implementation of BGES. (again in 2022 and 2023)
- November 2022 : the ministry MESR publishes its Climate-biodiversity and ecological transition plan for higher education and research with an objective of -2% reduction per year.
- November 2022 : the CNRS announces its Low Carbon Transition Plan
- December 5, 2022 : COMETS (ethics committee) publishes a key report
- January 2023 : publication of the sufficiency plan of the University Paris-Saclay
- during 2023 : Working group at the CoNRS regarding the evaluation of researchers in the light of the carbon issue. Workshop "Impact of ecological, energy and digital transitions on research in laboratories” within the framework of the INP prospective.

At the LPTMS level, a strategy fully supported by the two successive directors over the period:

- June 2019 : presentation of the climate issue and its implications in the academic world at the laboratory days.
- November 2020 : Appointment of Guillaume Roux as sustainable development referent with the CNRS and the University of Paris-Saclay.
- April 2021 : extended laboratory council acting on the preparation of the laboratory's carbon accounting (BGES). Guillaume Roux is assisted by Claudine Le Vaou, Karolina Kolodziej and Olivier Giraud.
- May 2022 : presentation of the results of the BGES at the lab’s days. Creation of a committee to make propositions for a reduction plan. Composition of the committee: L. Brémaud (PhD student), O. Giraud (DR), K. Kolodziej (ITA), S. Ouvry (DR), G. Roux (MCF)
- March 29, 2023 : general assembly of the laboratory that took several actions.
- 2024 : Implementation of the first actions.

## 2- Results of the carbon accounting

There exists a non-public 30 pages report that explains the results. The methodology is similar to the one of GES1point5 but at that time, this tool was incomplete on several items that were relevant to us so we developed our own analysis. The summarized result is

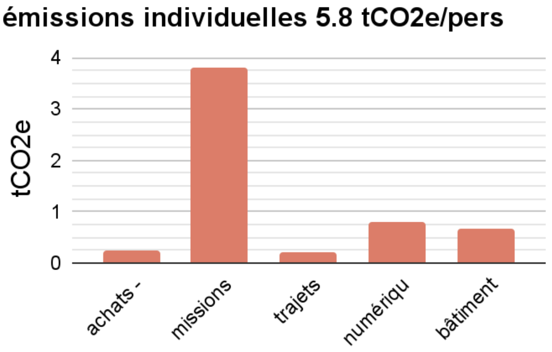
émissions individuelles 5.8 tCO2e/pers

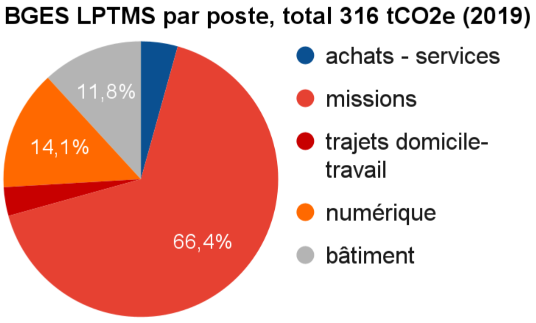
BGES LPTMS par poste, total 316 tCO2e (2019)

with the following comments (in particular specifying differences with the GES1point5 methodology)

- people : we count permanent and non-permanent, with LPTMS affiliation, with a weight 1 (GES1point5 counts only 0.5 for university members) but not visitors nor trainees (about 55 people in all).
- missions (traveling) : the main scope. Aviation footprint includes trails condensation effects. We counted everything for members and visitors from all financial sources. GES1point5 counts only missions paid by CNRS with an expense.
- building : both energy and construction (typically half and half in contributions).
- numerics : both material and services
- purchases : most of the things the lab pays for for everyday work.

An arbitrary though realistic ambitious reduction plan with order of magnitude to try to reach almost 2tCO2e is given below, separating actions resorting to individual and collective decisions

| | **Simulateur de réductions** | | |
|---|---|---|---|
| | **actuel [kgCO2e/pers]** | **simulé 2030 [kgCO2e/pers]** | **hypothèses** |
| ***individuels*** | ***4 009*** | ***1 060*** | |
| missions | 3 816 | 954 | -75% |
| trajets domicile-travail | 194 | 106 | électrification des véhicules |
| ***communs*** | ***1 741*** | ***1 255*** | |
| numérique | 811 | 649 | -20% (sobriété + baisse sociétale des FE) |
| bâtiment | 681 | 407 | chaufferie géothermie + baisse température |
| achats - services | 249 | 199 | -20% (sobriété + baisse sociétale des FE) |
| ***total*** | ***5 750*** | ***2 315*** | ***-59,74%*** |

Essentially, for our unit, the main lever on which the lab policy can act are missions, but all scopes are being and need to be addressed.

## 3- Reduction plan voted in general assembly and the future

End of March 2023, a general assembly voted the following actions

- awareness actions : display of 2 posters in common rooms about order of magnitudes for missions
- communication actions : web page dedicated to the lab footprint and actions
- footprint monitoring : missionary calculates its footprint and sends it to the secretary and the director. Implementation of anonymous monitoring by all members on the total and distribution of the mission footprint.
- mission regulation :
    - No plane if there is a train journey of less than 5 hours
    - Reduction targets. The members of the laboratory agree on an objective overall (all missions monitored) of approximately -50% in 2030 compared to 2019. Every two years, the objectives are re-discussed based on follow-up and collective assessment.
    - distribution policy and decision support for the DU for the policy of choosing assignments.

## 4- Other climate related activities

Guillaume Roux has participated in several institutional activities on the question of integrating the environmental challenge in Physics research. This includes

◊ Plenary keynote with André Estevez-Torres in the congrès général des 150 ans de la Société Française de Physique 2023

◊ participation in the committee writing the report *Intégrer les enjeux environnementaux à la recherche en Physique* (hal-04255371) for CNRS Physics prospective. 2023

◊ working group for CoNRS on *Evaluation in research in times of environmental challenges,* 2023.

◊ participation to workshops helping colleagues, PhD advisor and directors setting up their carbon strategy both at University and CNRS, 2022 & 2023

◊ co-organization of the doctoral school ECOCLIM 2022 to which LPTMS provided financial support.

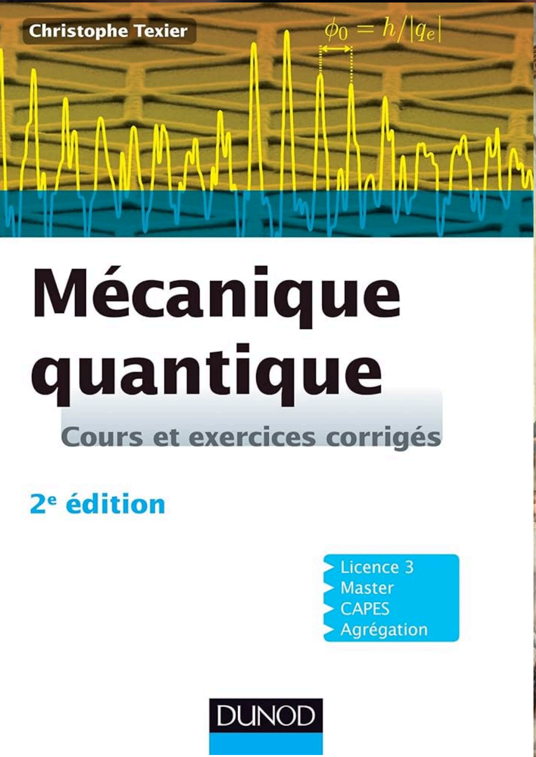

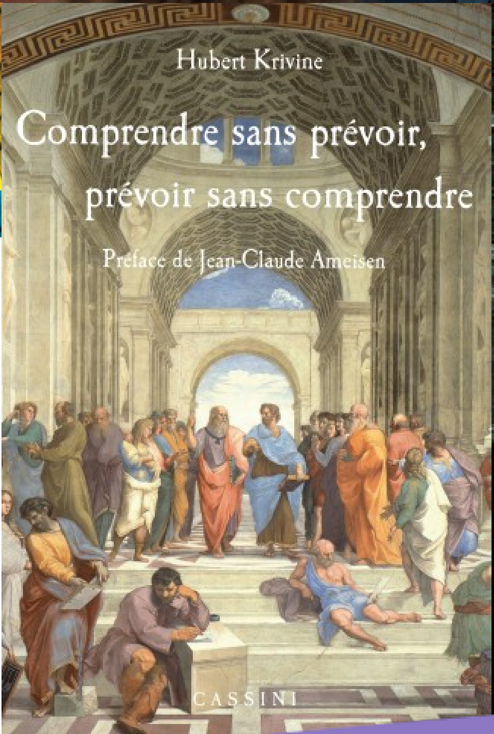

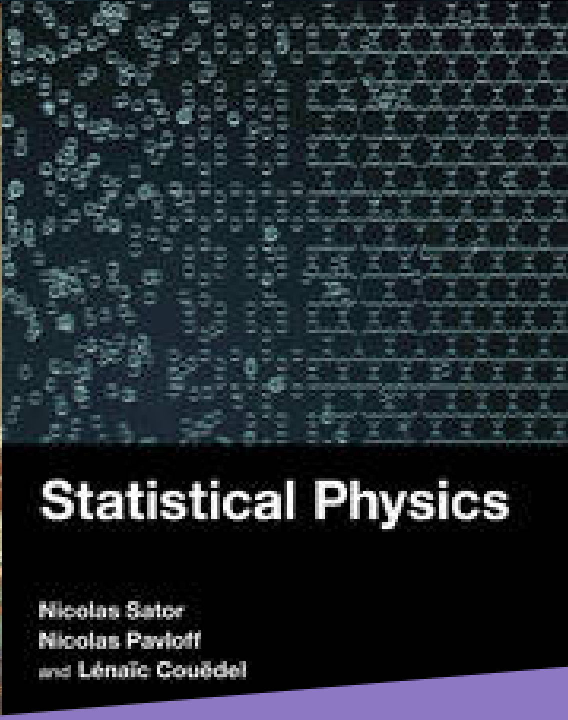

# Item 5

## *Teaching and Outreach*

# 1. Teaching

Many members of the unit are involved in teaching. We list below salient actions and contributions in this essential activity.

## Involvement in the teaching landscape

Over the last 6 years, 7 members of the lab were professors, assistant professors or "professeur agrégé" affiliated to the Paris-Saclay University (Franz, Mazars, Mazza, Pavloff, Roux, Texier, Trizac), less than 30% of the permanent staff. All are involved in courses for the Physics department of the University and contribute significantly to both bachelor and master programs. At bachelor levels, they are involved in all tracks and, at master levels, they take or took part in M2 ICFP (Roux, Texier, Trizac), M2 PCS (Pavloff, Roux, Texier, Trizac) and M2 QLMN (Roux, Pavloff). At the bachelor level, one specificity of the Paris-Saclay curriculum is the existence of a Magistère de Physique that gathers students meant to research training, originating university & ENS Paris Saclay. The department also offers Physics lectures for students from engineering schools and international ones (General Physics). At the M2 level, there is a big shuffle of students and they usually gather students from all the Paris area and well beyond.

The LPTMS members specialize in teaching statistical physics and quantum mechanics but contribute to all sorts of general physics education. They hold several responsibilities as head / representative of educational tracks : ICFP (Texier), PCS (Trizac, Texier), L3 Physique (Roux). Martial Mazars has a teaching load of 384h each year and he is a key teacher in experimental works and education tracks for future teachers (Agrégation de Physique).

Several members are currently or previously IUF members (Trizac, Franz, Pavloff). Despite the small number of university members of the unit, most of them have participated actively in local and national collective instances over the last 6 years : CNU (Mazza), CoNRS (Roux), CCUPS (Mazza, Pavloff, Roux, Texier), Conseil du département de physique (Pavloff, Roux, Texier).

CNRS members have always been involved in teaching. They usually participate in master programs : M2 ICFP (Lenz, Ros, Rosso), M2 PCS (Lenz, Giraud, Ullmo), but also teach in other institutions such as CentraleSupélec (Santachiara), Mines ParisTech (Lens), ENS Lyon (Majumdar) and ESPCI (Rosso, Terras).

Members have also participated to the AIMS program (Franz, Ouvry).

Many PhD students contribute to teaching, essentially through the "doctoral mission" program of the Physics department.

## Original contributions, books

University members have written books, both for students and for outreach or essays on Science. The whole list can be found on the webpage of the lab

https://www.lptms.universite-paris-saclay.fr/activites/publication/librairie/

Over the 2018-2023 period, books have been released

- "Prévoir sans comprendre, comprendre sans prévoir", H. Krivine, éd. Cassini, 2018.
- L'IA peut-elle penser ? Miracle ou mirage de l'intelligence artificielle (2021)
- Enjeux de la transition écologique, G. Roux, EDP Sciences Open EBook, 428 pages (2021). https://cnrs.hal.science/LPTMS/hal-03461012v1
- "On nous aurait menti, de la rumeur aux fake news", H. Krivine, éd. De Boeck, 2022.
- Statistical Physics (2023), Nicolas Sator, Nicolas Pavloff, Lenaic Couedel

Many of the teachers (University or CNRS) share freely useful materials either from their webpage or from the dedicated page for the lab

https://www.lptms.universite-paris-saclay.fr/wiki-cours/index.php/Main_Page

Hubert Krivine has been appointed as expert for the national GEPP in charge of elaborating the new Physics and Chemistry programs for highschools.

Guillaume Roux has participated in the setting of the interdisciplinary object AllCan since 2020, which offers a university track in coordination with CentraleSupélec and other components of the Paris-Saclay university. In 2019-21, he participated to the creation and development of the SPOC "Challenges of the ecological transition"

## 2. Outreach

### Fêtes de la science Paris-Saclay

Since its inception, the LPTMS has actively participated in the "Fête de la Science" organized annually by the University Paris-Saclay. Specifically, the laboratory offers six workshops meticulously crafted by its members to present fundamental and intricate concepts, spanning from quantum mechanics to fractals, to both high school students and families without specific backgrounds in science. The LPTMS has consistently stood out by involving a considerable number of PhD students, postdocs, and permanent members during these "Fête de la Science" events, thereby fostering an enthusiastic and constructive atmosphere around science for students and families alike.
See more at https://www.lptms.universite-paris-saclay.fr/wiki/index.php/Fete_de_la_science

### Stages des troisième

In collaboration with the FFJ, we annually host students for their "*stage de découverte professionnelle du 3eme*". For one week, the students interact with senior and young researchers of our laboratory with the aim of providing them a glimpse into the life of a researcher and of the educational path to pursue this career.

### Outside the walls

Here, we list public seminars for broad audience, media broadcasting and outreach actions taking place outside the University wall in which LPTMS members have been involved in. Notice that several non-permanent members have been also active in this field but we have less traces of their contributions.

**Thorsten Emig**
◊ Conférence/débat public, Salon Sport Unlimitech, Lille, 24/09/2021
◊ Presse écrite, British Milers Club News, Vol.15 Issue 2 (2018).
**Hubert Krivine**
◊ Invité à quatre émissions scientifiques sur France Inter et France culture, divers articles de vulgarisation et présentations de livres dans des librairies et des lycées en France et à l'étranger (Tunisie, Égypte et Madagascar dans le cadre de AEFE)
◊ Animations de plusieurs "forum des mathématiques"; plusieurs vidéos dont :

- "Cinq à sept" de l'académie des sciences, Est-on sûr de l'âge de la terre ? 2018
- "les mardis de l'espace des sciences de Rennes" : Peut-on être sûr de l'âge de la Terre ? 2019
- émission "médiapart", L'Intelligence artificielle: que peut-elle vraiment ? 2019,
-"Timeworld 2021", le hasard est-il une limitation de l'intelligence artificielle ? 2021.

**Martin Lenz**

◊ Pint of Science; Spoke about protein aggregation at a festival in a bar (Kremlin-Bicêtre 2019)

◊ EPSAA student projects; Designed outreach materials with graphic arts students (Paris 2019-present)

◊ Viens voir mon taf; Hosted disadvantaged middle school students for 1 week/year (Orsay 2019-present)

◊ Telescience; discussed research during lockdown with Indian high schoolers (Kerala 2020)

◊ U. Paris-Saclay; organized exhibition of graphic artwork based on our and others' research (Orsay 2022)

◊ L'origine de la vie de l'univers à la terre; Outreach round table (Orsay 2023)

◊ Le dessin scientifique et la chambre claire; Outreach conference and hands-on activity (Orsay 2023)

**Nicolas Pavloff**

◊ Participation à un film de vulgarisation de 6mn30s réalisé par M. Relid du service de communication de l'Université Paris-Saclay (COMPAS) au sujet des trous noirs acoustiques.
http://www.canal-u.tv/video/scavo/les_trous_noirs_acoustiques.49705

**Valentina Ros**

◊ Outreach lecture within the course "Comunicare la fisica e la matematica" at the Master in Scientific journalism Franco Prattico, SISSA, Trieste, Italy, 2022. Title of intervention: Complex systems: metastability, slow dynamics, and what do a glass and a bacterial ecosystem have in common

**Guillaume Roux**

◊ Table ronde *Quelle est la place de l'écologie en Recherche ?* au Festival double science, parrainé par la SFP, 2023.

◊ Écopolien seminar *Face à l'anthropocène : quels regards adopter pour accompagner l'orientation et l'action ?* 2023

◊ Outreach conference on Anthropocene in highschool Colbert and at *Prof En Fac*, Sorbonne Université, 2022.

◊ Intervention D'Alembert colloquium *Promesses des sciences et sciences des promesses*, 2022.

◊ Interview dans l'édition 2021 du Big bang au big band.

**Emmanuel Trizac**

◊ Round table on Time and irreversibility in La Nuit des Temps, 2021
https://www.sfpnet.fr/la-nuit-des-temps-2021

# Item 6

## *Research Training*

We summarize here the involvement of the LPTMS in training through research. This training plays a central role in the life of the unit, through the supervision of young researchers (doctoral students, post-doctoral researchers, or internship students) or through the management of the doctoral school itself.

## 1- LPTMS PhD students during the period 2018-2023

The unit is very involved in doctoral training : 52 doctoral students have been officially trained in LPTMS during the period 2018-2023 (113 since the creation of the laboratory), among which 35 defended during the period. On average, there have been 5 new doctoral students each year at LPTMS.

Concerning the origin of the funding, LPTMS usually obtains 1 to 2 contracts from the doctoral school competition each year (1,5 in average per year during the period), the others students being funded from various other programs : among the 35 PhD students which have been hired during the period 2018-2023, one counts 4 fundings from CDSN (2 from ENS Ulm, 1 from ENS Lyon and 1 from ENS Paris-Saclay), 2 from ERC, 3 from foreign fellowships, 1 from the Labex, 6 from CNRS, the other ones being from very various origins (Labex, Idex, DIM, QuantEdu, CFM or Bettencourt-Schueller foundation…).

Concerning the academic and/or geographical origin of doctoral students, the natural recruitment pool is that of the various master's degrees in the Paris region, in particular the ICFP and Physics of Complex Systems master's degrees. Despite its relative distance from the center of Paris, the LPTMS remains attractive for good students from these masters. Thus, a large majority of doctoral students recruited over the period came from there. But there are also a certain number of doctoral students coming directly from foreign master's degrees (many Italians, but also a few doctoral students from other European or even non-European master's degrees). On the other hand, we have relatively few doctoral students from provincial master's degrees, but this is a general phenomenon for all laboratories affiliated to the doctoral school.

Among the 35 PhD students who defended during the period, 22 (more than 60%) continued an academic career : the majority in a post-doctoral position, 2 of them having already obtained a permanent position. Many of the others found quite easily interestings jobs as scientists or consultants in private companies. 2 became high school teachers.

We can mention that, in total since the creation of the laboratory, 27 former PhD students have obtained an academic permanent position in France (17 in CNRS, 7 at university, 1 ESPCI, 1 ENS, 1 CIRAD).

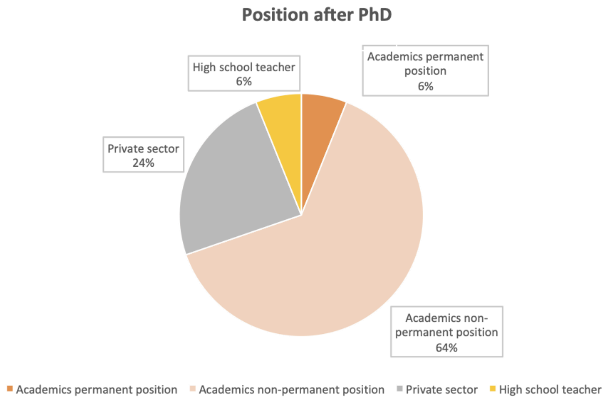

## 2- Involvement in the management of the doctoral school

The unit is affiliated with the Doctoral School « Physique en Ile-de-France » (EDPIF, ED564), which is one of the 4 doctoral schools in the scope the Graduate School of Physics of Université Paris-Saclay. This doctoral school is formally hosted by Université PSL, and driven jointly with Sorbonne Université, Université Paris Cité, and Université Paris-Saclay. The doctoral school is governed by a board, made up of a director (professor at ENS) and 3 deputy directors, each representing one of the partner institutions. The deputy director of Paris-Saclay is one of the LPTMS CNRS researchers, Véronique Terras. She is therefore directly in charge of the organization of the Paris-Saclay's part of the doctoral school, which represents around 200 PhD students spread in 18 research units across Université Paris-Saclay.

## 3- Post-doctoral researchers

Over the evaluation period 2018-2023, the LPTMS hosted 38 post-docs. 11 of them were hired thanks to ANR grants, 13 of them thanks to ERC grants, the funding of the other ones coming from different other sources (Simon Foundation, Cefipra, Bettencourt-Schueller Foundation, Labex…).

Most of them (23) are still doing research, among which 3 of them are now CNRS permanent researchers, 7 hold an academic position abroad, and 13 are still in post-doc. The other 8 work in the private sector, either in France or abroad.

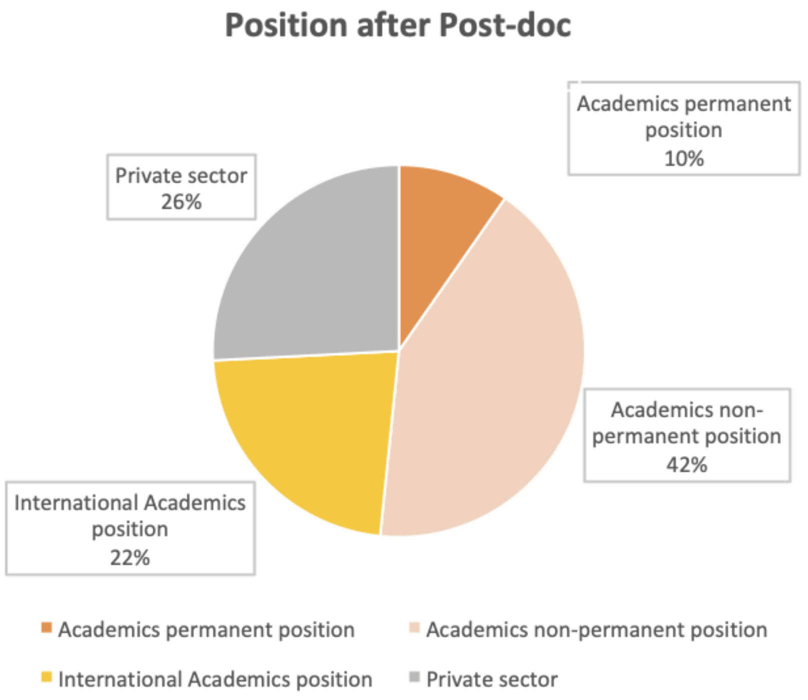

## 4- Internship students

LPTMS' members supervised 89 interns (from L3 to M2) during the evaluation period 2018-2023.

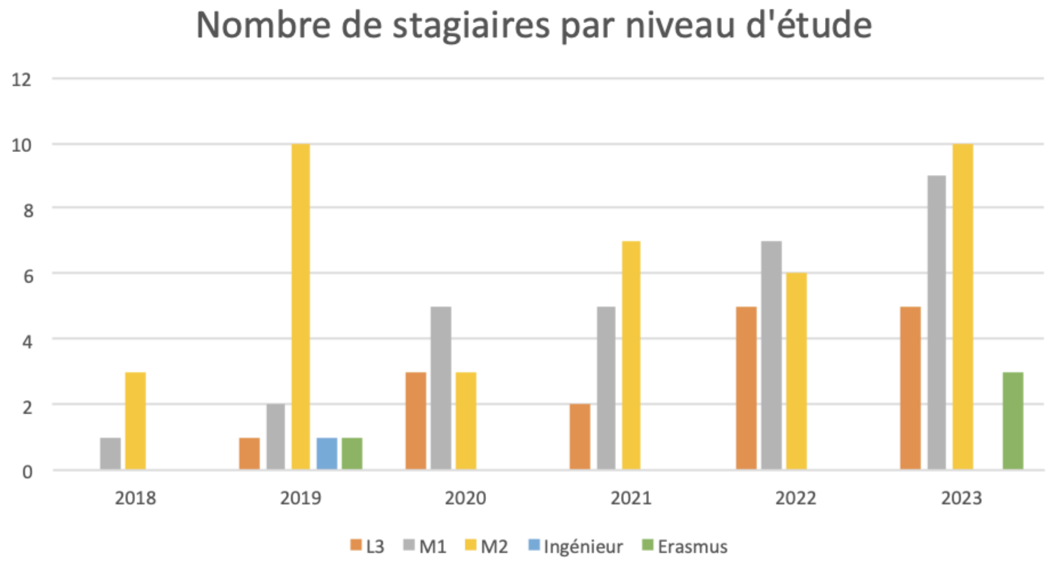

This represents a strong involvement, both in terms of the time devoted to the students and of the financial resources that are allocated. In the table below, we give the number of interns per year and their repartition according to the source of the funding.

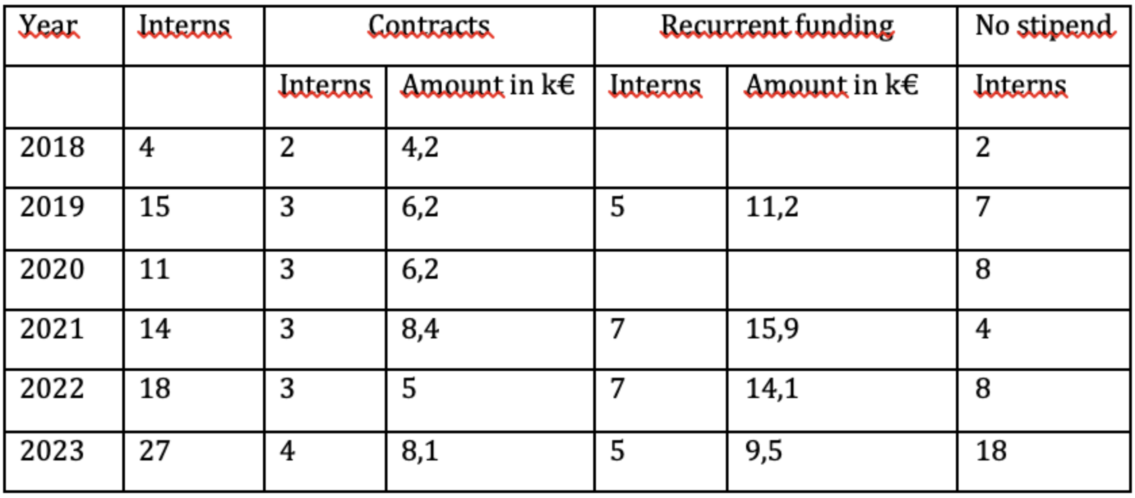

| Year | Interns | Contracts | | Recurrent funding | | No stipend |
|---|---|---|---|---|---|---|
| | | Interns | Amount in k€ | Interns | Amount in k€ | Interns |
| 2018 | 4 | 2 | 4,2 | | | 2 |
| 2019 | 15 | 3 | 6,2 | 5 | 11,2 | 7 |
| 2020 | 11 | 3 | 6,2 | | | 8 |
| 2021 | 14 | 3 | 8,4 | 7 | 15,9 | 4 |
| 2022 | 18 | 3 | 5 | 7 | 14,1 | 8 |
| 2023 | 27 | 4 | 8,1 | 5 | 9,5 | 18 |

## Satya Narayan Majumdar

Chercheur en physique théorique

©Laurent Ardhuin

### Médaille d’argent du CNRS 2019

Chercheur en physique théorique et responsable du groupe Physique statistique, théorie des champs et systèmes intégrables au Laboratoire de physique théorique et modèles statistiques[1] , spécialiste de la physique statistique et ses applications.

"Les évènements extrêmes tels que les tremblements de terre, tsunamis et typhons sont rares mais ont souvent des effets dévastateurs. À partir de 2006, je me suis graduellement intéressé à leurs propriétés statistiques, qui sont la clé pour comprendre tout un ensemble de problèmes relevant de l’informatique, de la finance et de la climatologie. L’approche, qui utilise les outils de la physique statistique et qui s’appuie sur la théorie des matrices aléatoires, a mis en évidence le caractère universel des transitions de phase du troisième ordre. Avec mes collègues, l’objectif à long terme est de développer une théorie unifiée des extrêmes dans les systèmes fortement corrélés."

- Laboratoire de physique théorique et modèles statistiques
- Institut de physique
- Délégation Île-de-France Gif-sur-Yvette

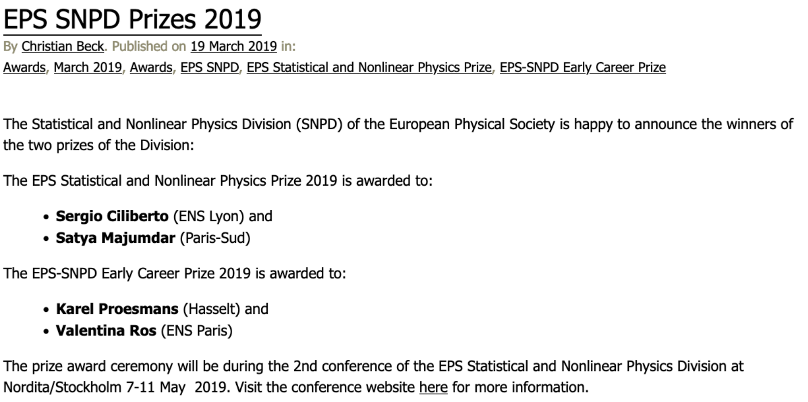

## EPS SNPD Prizes 2019

By Christian Beck. Published on 19 March 2019 in: Awards, March 2019, Awards, EPS SNPD, EPS Statistical and Nonlinear Physics Prize, EPS-SNPD Early Career Prize

The Statistical and Nonlinear Physics Division (SNPD) of the European Physical Society is happy to announce the winners of the two prizes of the Division:

The EPS Statistical and Nonlinear Physics Prize 2019 is awarded to:

- **Sergio Ciliberto** (ENS Lyon) and
- **Satya Majumdar** (Paris-Sud)

The EPS-SNPD Early Career Prize 2019 is awarded to:

- **Karel Proesmans** (Hasselt) and
- **Valentina Ros** (ENS Paris)

The prize award ceremony will be during the 2nd conference of the EPS Statistical and Nonlinear Physics Division at Nordita/Stockholm 7-11 May  2019. Visit the conference website here for more information.

# Item 7

## Scientific productions

arXiv:2303.05407v2 [cond-mat.str-el] 9 Nov 2023

# Asymptotic Quantum Many-Body Scars

Lorenzo Gotta,[1, 2, *] Sanjay Moudgalya,[3, 4, †] and Leonardo Mazza[2, ‡]
[1] *Department of Quantum Matter Physics, University of Geneva,*
*24 Quai Ernest-Ansermet, 1211 Geneva, Switzerland*
[2] *Université Paris-Saclay, CNRS, LPTMS, 91405, Orsay, France*
[3] *Department of Physics and Institute for Quantum Information and Matter,*
*California Institute of Technology, Pasadena, California 91125, USA*
[4] *Walter Burke Institute for Theoretical Physics, California Institute of Technology, Pasadena, California 91125, USA*

(Dated: November 13, 2023)

We consider a quantum lattice spin model featuring exact quasiparticle towers of eigenstates with low entanglement at finite size, known as quantum many-body scars (QMBS). We show that the states in the neighboring part of the energy spectrum can be superposed to construct entire families of low-entanglement states whose energy variance decreases asymptotically to zero as the lattice size is increased. As a consequence, they have a relaxation time that diverges in the thermodynamic limit, and therefore exhibit the typical behavior of exact QMBS although they are not exact eigenstates of the Hamiltonian for any finite size. We refer to such states as *asymptotic* QMBS. These states are orthogonal to any exact QMBS at any finite size, and their existence shows that the presence of an exact QMBS leaves important signatures of non-thermalness in the rest of the spectrum; therefore, QMBS-like phenomena can hide in what is typically considered the thermal part of the spectrum. We support our study using numerical simulations in the spin-1 XY model, a paradigmatic model for QMBS, and we conclude by presenting a weak perturbation of the model that destroys the exact QMBS while keeping the asymptotic QMBS.

***Introduction*** — Quantum Many-Body Scars (QMBS) [1–4] in non-integrable quantum lattice models of any dimension are one of the paradigms for the weak violation of the Eigenstate Thermalization Hypothesis (ETH) [5, 6], according to which all local properties of energy eigenstates in the middle of the spectra of non-integrable models coincide with those of a thermal Gibbs density matrix at a suitable temperature [7–10]. QMBS are isolated energy eigenstates that are outliers in many respects, e.g., in the expectation value of a local observable or in the entanglement entropy. Numerous instances of lattice models featuring exact towers of QMBS at finite size have been discovered [2, 7, 8, 11–13, 16, 17, 19–23]. Most of these results have also been understood via unified frameworks or systematic construction recipes [3, 13, 17, 20, 24–30].

A question that has been less explored is whether the presence of a finite-size QMBS affects the properties of the rest of the spectrum. Ref. [3] pointed out the existence of low-entanglement states in the PXP model which exhibit slow relaxation even though they are orthogonal to the known exact QMBS: the energy variance of such states is independent of system size and thus their fidelity relaxation time does not decrease [32]. This is a remarkable phenomenology to be contrasted with that of short-range correlated states, whose energy variance grows with system size, whereas the fidelity relaxation time decreases.

Are there even more drastic examples of slowly relaxing states [33], for instance with an energy variance decreasing with system size, which would lead to a relaxation time that *diverges polynomially* in the thermodynamic limit (TL)? Slow relaxation of hydrodynamic origin is ubiquitous in systems with continuous symmetries, where it occurs at a diverging timescale known as the *Thouless time* [34–37], and is related to diffusion or subdiffusion [38–43]. The interpretation of QMBS as an unconventional non-local symmetry [29, 44] motivates the search for such slow relaxation. Long-lived quasiparticles, e.g. the phonons of a superfluid with Beliaev decay [45], also induce slow relaxation. QMBS are associated to quasiparticles with specific momenta and infinite lifetime [4], hence it is natural to look for long-lived quasiparticles at neighboring momenta.

In this letter we address these questions by considering the spin-1 XY model featuring exact QMBS at any finite size [2] and show that it is possible to construct slowly-relaxing low-entanglement initial states that exhibit QMBS-like features, but nevertheless are orthogonal to the exact QMBS. They have an energy variance that goes to zero in the TL and asymptotically display the typical dynamical phenomenology of a QMBS, i.e. the lack of thermalization; hence we refer to such initial states as *asymptotic* QMBS. Our work widens the range of initial states that qualitatively exhibit a non-thermalizing phenomenology and motivates the search for non-thermal features in regions of the spectrum where entanglement signatures do not make them evident.

***The model and the exact QMBS*** — We consider a one-dimensional spin-1 chain of length $L$ even, and consider a spin-1 XY model with external magnetic field and axial anisotropy:

$$\begin{aligned} H =& J \sum_j \left( S_j^x S_{j+1}^x + S_j^y S_{j+1}^y \right) + h \sum_j S_j^z \\ &+ D \sum_j \left( S_j^z \right)^2 + J_3 \sum_j \left( S_j^x S_{j+3}^x + S_j^y S_{j+3}^y \right), \end{aligned} \quad (1)$$

where $S_j^\alpha$, with $\alpha = x, y, z$, are the spin-1 operators on site $j$. We use open boundary conditions (OBC) for the numerical simulations and periodic boundary conditions (PBC) for some of the analytical results. This model with OBC has been numerically shown to be non-integrable; the last term breaks a hidden non-local symmetry [2, 4, 46].

The Hamiltonian in Eq. (1) exhibits QMBS for any finite value of $L$ [2]. In order to see that, we define the fully-polarised state $|\Downarrow\rangle = |- - \cdots - -\rangle$ with all spins in the eigenstate of $S_j^z$ with eigenvalue $-1$, and the operator

$$J_k^+ = \frac{1}{2} \sum_{j=1}^{L} e^{ikj} \left( S_j^+ \right)^2. \quad (2)$$

The scar states read:

$$|n, \pi\rangle = \frac{1}{\sqrt{N_{n,\pi}}} \left( J_\pi^+ \right)^n |\Downarrow\rangle, \quad (3)$$

where $N_{n,\pi}$ is a normalisation constant. The state satisfies the energy eigenvalue equation $H |n, \pi\rangle = (-Lh + 2nh + LD) |n, \pi\rangle$ and for generic values of $h$ and $D$ it lies in the middle of the Hamiltonian spectrum. Its existence is related to quantum interference effects, similar to those that are responsible for the existence of $\eta$-pairing states in the Hubbard model [16].

Moreover, it is possible to consider the reduced density matrix $\rho_{A,n,\pi}$ of $|n, \pi\rangle$ defined on half the system (conventionally, the region $A$ is $1 \le j < L/2$), and to compute its entanglement entropy, $S_{n,\pi} = -\mathrm{tr}[\rho_{A,n,\pi} \log \rho_{A,n,\pi}]$. The explicit calculation has been done in Ref. [2], and it shows that it scales as $\log L$, displaying a mild logarithmic violation of an entanglement area law, see Supplementary Materials (SM) [47] and Ref. [1] for details. QMBS are easily found numerically by plotting the entanglement entropy $S_{E_i}$ of $\rho_{A,E_i}$, the reduced density matrix of the eigenstate $|E_i\rangle$, as a function of energy. Indeed, almost all the eigenstates appear to satisfy the ETH and are characterised by an $S_{E_i}$ that is only a function of the energy $E_i$; they have a higher amount of entanglement than the QMBS states, which indeed violate ETH.

***A family of states obtained by deforming the exact QMBS*** — We now consider other initial states for the dynamics of the model in Eq. (1); they read as follows:

$$|n, k\rangle = \frac{1}{\sqrt{N_{n,k}}} J_k^+ \left( J_\pi^+ \right)^{n-1} |\Downarrow\rangle, \quad (4)$$

where $N_{n,k}$ is a normalisation constant, which coincide with the exact QMBS in Eq. (3). When $k \neq \pi$ and is an integer multiple of $\frac{2\pi}{L}$, they are *orthogonal* to the exact QMBS: the relation $\langle n, k | n', \pi\rangle = \delta_{n,n'} \delta_{k,\pi}$ for any $1 \le n, n' \le L - 1$ is proved in the SM [47]. Models where such classes of multimagnon states are exact eigenstates have been studied in [49], however for $k \neq \pi$ these are *not* eigenstates of the spin-1 XY model. It is easy to show that the average energy of these states does not depend on $k$ and reads $\langle n, k| H |n, k\rangle = -Lh + 2nh + LD$ [47].

Furthermore, the entanglement of the states in Eq. (4) scales with system size as a sub-volume law. For a quick proof, since $|n, k\rangle \propto J_k^+ |n - 1, \pi\rangle$, we note that $J_k^+$ can be straightforwardly expressed as a Matrix Product Operator (MPO) of bond dimension $\chi = 2$ [3, 50, 51], hence the half-subsystem entanglement entropies of $|n - 1, \pi\rangle$ and $|n, k\rangle$ can differ at most of an additive term $\log 2$. In other words, since the operator $J_k^+$ can be split in two terms, one acting on $j < L/2$ and one on $j \ge L/2$, it is possible to show [47] that the total number of Schmidt states in $|n, k\rangle$ is at most twice than that in $|n - 1, \pi\rangle$.

To further characterise the states in Eq. (4), we compute the variance of the energy $\Delta H^2$ under the Hamiltonian $H$ in PBC, and as we show in the SM [47], we obtain:

$$\Delta H^2 = 4 \left[ J^2 \cos^2\left(\frac{k}{2}\right) + J_3^2 \cos^2\left(\frac{3k}{2}\right) \right]. \quad (5)$$

Among the states defined in Eq. (4), the $|n, \pi\rangle$ are the only eigenstates of the Hamiltonian, because $\Delta H^2 = 0$ only for $k = \pi$. When $k \neq \pi$, $|n, k\rangle$ must be a linear superposition of the energy eigenstates of $H$, which are mostly in a window centered around the same energy of $|n, \pi\rangle$ and in a width of about $\Delta H$. When $k \neq \pi$ is chosen to be an integer multiple of $\frac{2\pi}{L}$, $|n, \pi\rangle$ is not part of this set of states due to orthogonality. Since $|n, \pi\rangle$ numerically appear to be the only exact QMBS of $H$ [2], we conclude that such states $|n, k\rangle$ must be a linear superposition of "thermal" eigenstates, i.e., those that are typically said to satisfy ETH, having an entanglement entropy and expectation values of local observables that are smooth functions of energy.

We have numerically verified this statement using the python-based package QuSpin [52]: we diagonalize the Hamiltonian (1) and compute the bipartition entanglement entropy $S_{E_i}$ and the average square magnetisation $S_{E_i}^{z2} = \frac{1}{L} \sum_j \langle (S_j^z)^2 \rangle$ of all eigenstates. Subsequently, we compute the scalar product of the state $|n, k\rangle$ with all eigenstates for $n = L/2$ and $k = \pi - \frac{2\pi}{L}$ and look at the properties of the eigenstates with whom the overlap is not zero. The results are reported in Fig. 1, and support our thesis.

***Dynamics and asymptotic QMBS*** — The dynamical properties of the states $|n, k\rangle$ for large system sizes depend on how we approach $L \to \infty$. If the limit is taken while the momentum $k$ is held fixed, then the

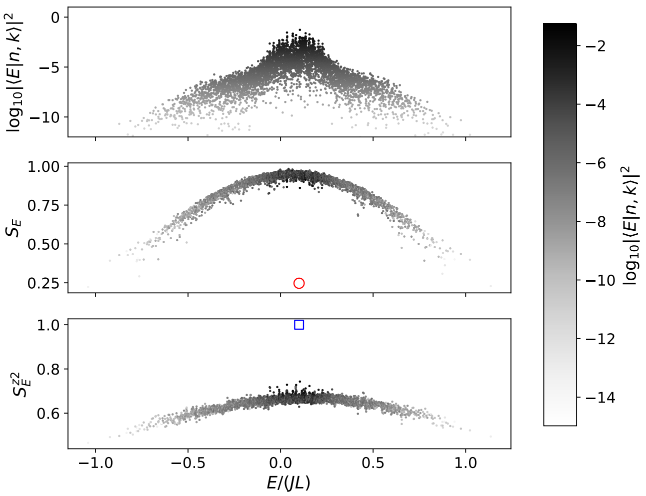

FIG. 1. Top: Squared overlap of $|n,k\rangle$ for $n = L/2$ and $k = \pi - \frac{2\pi}{L}$ with the eigenstates $|E_i\rangle$ of Hamiltonian (1) with zero magnetisation, $S_z = 0$; the parameters of the simulation are $\{J, h, D, J_3\} = \{1, 0, 0.1, 0.1\}$ and $L = 10$. The information on $|\langle E_i|n,k\rangle|^2$ is also encoded in the color code of the marker of all panels using a logarithmic scale, see colorbar. Middle and bottom: We plot the data of the top panel in a diagram with the energy $E$ on the abscissa and the bipartition entanglement entropy $S_E$ or the average square magnetisation $S^{z2}(E)$ of the eigenstate on the ordinate, respectively. For the entanglement entropy, we use the natural logarithm and we divide the result by $L/2$ to obtain an intensive quantity. The state $|n,k\rangle$ has overlap only with states whose $S_{E_i}$ or $S^{z2}_{E_i}$ lies on the continuous "thermal" curve. The red circle and the blue square highlight the regions of the plots where the QMBS $|n = L/2, \pi\rangle$ appear: the absence of any grey mark means that the scalar product is compatible with the numerical zero.

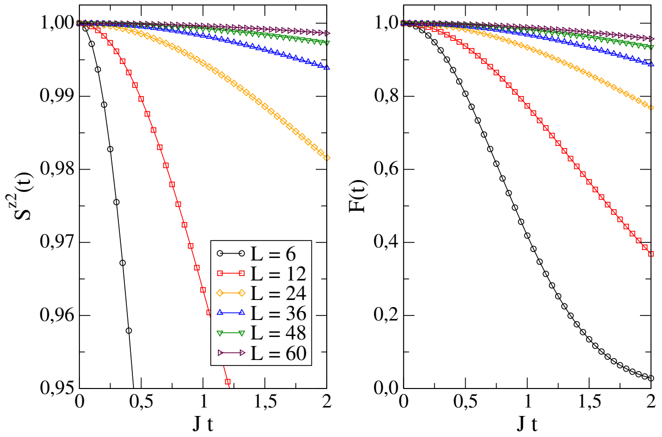

FIG. 2. The properties of the state $e^{-iHt}|n,k\rangle$ for $n = L/2$ and $k = \pi - 2\pi/L$ as a function of time for various system sizes $L$. Left: time evolution of the squared magnetisation $S^{z2}(t)$. Right: time evolution of the fidelity with the initial state $F(t)$.

variance is finite in the TL (see Ref. [3] for examples in the PXP model). Loosely speaking, we can invoke the well-known energy-time uncertainty relation, linking the typical timescale of the dynamics $\tau$ of a quantum state to the fluctuations of the energy:

$$\tau \geq \frac{\hbar}{2\Delta H}, \tag{6}$$

to claim that for these states the dynamics is frozen up to a given time-scale $\tau$ that is independent of $L$ and that afterwards an evolution towards thermal equilibration takes place [47]. To be more precise, the energy variance $\Delta H^2$ of the initial state determines the fidelity relaxation time $\tau \sim 1/\Delta H$ [6], since the fidelity $F(t) = |\langle\Psi|e^{-iHt}|\Psi\rangle|^2$ of an initial state $|\Psi\rangle$ decays at short times as $\sim \exp(-\Delta H^2 t^2)$; $\tau$ is a lower bound for the relaxation time of local observables [4, 10].

Another class of states can be obtained by approaching the TL while letting $k$ flow to $\pi$. This can be done by setting $k = \pi + \frac{2\pi}{L}m$, with the coefficient $m \in \mathbb{Z}$ kept constant while $L \to \infty$. In this case the energy variance scales as $\Delta H^2 \sim (J^2 + 9J_3^2)(k-\pi)^2$ and tends to zero as $1/L^2$. We refer to this second class of states as *asymptotic QMBS* of the model, since according to (6), the typical relaxation timescale of their dynamics scales as $\tau \sim L$, i.e., the system is frozen for timescales that *increase* polynomially with the system size. On the contrary, low entanglement states, by virtue of their diverging variance [33], are typically expected to lose fidelity on timescales that decrease with system size, and the expectation values of typical observables relax in timescales that do not change drastically with system size [5, 10, 55–59, 61]. Hence the dynamics of this class of states asymptotically approaches QMBS-like behavior even though they are *not* exact QMBS of the system at finite size, and moreover they are *orthogonal* to all the exact QMBS $|n,\pi\rangle$. To the best of our knowledge, this phenomenology has never been discussed before.

We support the previous statements with a numerical simulation of the dynamics of the states $|n,k\rangle$ under the action of $H$ using a time-evolving block decimation (TEBD) code based on a Matrix-Product-State (MPS) representation of the state obtained via the ITensor library [62, 63]. We consider in particular the state $|n = L/2, k = \pi - 2\pi/L\rangle$ for several system sizes up to $L = 60$ and truncation error $10^{-12}$. We then compute the observable $S^{z2}(t) = \frac{1}{L}\sum_j \langle (S^z_j)^2 \rangle_t$ and the fidelity of the time-evolved state with the initial state $F(t) = |\langle n,k|e^{-iHt}|n,k\rangle|^2$. The results, reported in Fig. 2, show in both cases an important slow-down of the dynamics as the size increases. In the SM we show that the data concerning the fidelity can be collapsed via a rescaling of time by a factor of $L$ [47], which suggests the divergence of the relaxation time in the TL. The result on the fidelity $F(t)$ shows undoubtedly that the time-evolved state maintains an overlap with the initial state that increases with $L$ and it implies the freezing of the state. In the SM we complement this analysis by contrasting it with the typical dynamics of other states [47]; we also analyze states obtained by acting on the exact QMBS with $(J_k^+)^m$, i.e., creating multiple quasiparticles of momenta close to $\pi$, and we argue that they should also be asymptotic QMBS as long as $m$ does not scale with $L$ [47].

***Slow relaxation and non-thermalness in the middle of the energy spectrum*** — Two properties make the asymptotic QMBS particularly interesting: (a) they have a limited amount of entanglement, i.e., a subvolume law, but an extensive amount of energy; (b) they have an energy variance $\Delta H^2$ that drops fast enough to zero in the TL. Any state that satisfies these conditions is guaranteed to have a long relaxation time, both in the fidelity and in the observables, while having an average energy that lies in the middle of the Hamiltonian spectrum. Note that both (a) and (b) are necessary features that make the behavior of asymptotic QMBS atypical. While any linear superposition of thermal eigenstates with small energy variance relaxes slowly, it typically has a large entanglement [33]. On the other hand, a typical low-entanglement state has an energy variance that increases with system size [33].

It is tempting to think that the existence of asymptotic QMBS should imply some kind of "non-thermalness" [3] or ETH-violation in the "thermal" states orthogonal to the exact QMBS, even at finite system size. Note that ETH consists of two parts [6, 9, 64], pertaining to diagonal and off-diagonal matrix elements of a local operator in the energy eigenbasis. The diagonal matrix elements control the late-time expectation values of observables, and the existence of asymptotic QMBS does not imply any violation of diagonal ETH since we expect them to eventually thermalize for any finite system size. On the other hand, the timescale of relaxation is controlled by both the energy variance of the initial state and the off-diagonal matrix elements [5]. It is plausible that our result entails a violation of off-diagonal ETH at least in a part of the Hamiltonian spectrum.

***Asymptotic QMBS without exact QMBS*** — Our definition of asymptotic QMBS is based on a deformation of the tower of exact QMBS supported at finite size; it is not clear whether asymptotic QMBS can exist in models without any exact QMBS or at energies distant from those of the exact QMBS.

We now show that it is possible to weakly perturb the Hamiltonian $H$ in a way that destroys all exact QMBS, but such that the perturbed model maintains the asymptotic QMBS. As an example, we consider $H' = H + V$ with $V = (J_z/L)\sum_j S_j^z S_{j+1}^z$, which is still a non-trivial local perturbation since its spectral norm $\|V\|_\infty$ corresponding to its largest singular value is subextensive and scales as $O(1)$. Using the python-based QuSpin package [52], we numerically diagonalize $H'$ and compute the the entanglement entropy $S_{E_i}$ and the average square magnetisation $S^{z2}(E_i)$ for all eigenstates. The plots, in Fig. 3, do not indicate the presence of any exact QMBS.

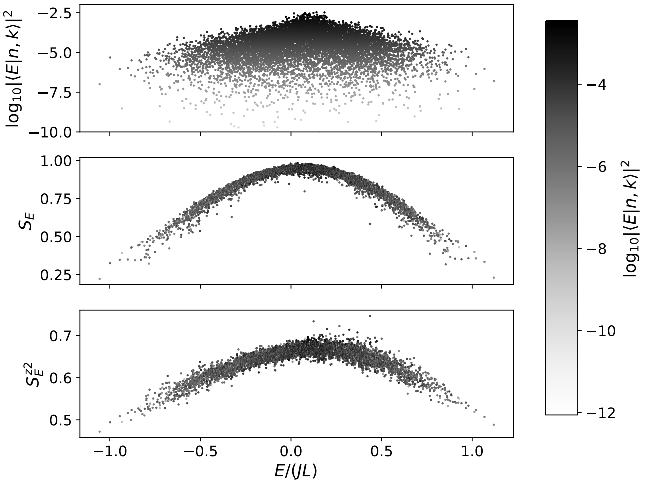

FIG. 3. Properties of the eigenstates of Hamiltonian $H'$ in the zero magnetization sector $S_z = 0$; the parameters of the simulation are $\{J, h, D, J_3, J_z\} = \{1, 0, 0.1, 0.1, 1\}$ and $L = 10$. Top: Squared overlap of $|n,\pi\rangle$ for $n = L/2$ with the eigenstates $|E_i\rangle$ of Hamiltonian $H'$ with zero magnetisation, $S_z = 0$. The information on $|\langle E_i|n,\pi\rangle|^2$ is also encoded in the color code of the marker of all panels using a logarithmic scale, see colorbar. Middle and bottom: We plot the data of the top panel in a diagram with the energy $E$ on the abscissa and the bipartition entanglement entropy $S_E$ or the average square magnetisation $S^{z2}(E)$ of the eigenstate on the ordinate, respectively. The state $|n,\pi\rangle$ has overlap only with states whose $S_{E_i}$ or $S^{z2}(E_i)$ lies on a continuous curve. In the SM [47] we show the entire spectrum and show that the model does not have any QMBS (here the spectrum is incomplete because we plot only state that have a non-negligible overlap with $|n,\pi\rangle$).

We now consider the state $|n,\pi\rangle$ of Eq. (3), which is an exact QMBS of $H$ but *not* an eigenstate of $H'$. Using the ITensor library [62, 63], we compute $S^{z2}(t)$ and the fidelity $F(t)$ for the time-evolved state $|\Psi(t)\rangle = e^{-iH't}|n,\pi\rangle$; the results are in Fig. 4. The plots display the phenomenology of an asymptotic QMBS in a Hamiltonian that does not show any exact QMBS at finite size, and the $F(t)$ curves exhibit a collapse when time is rescaled by a factor $\sqrt{L}$ [47], indicating a diverging relaxation time. This behavior can be directly attributed to the fact that the variance of the state $|n,\pi\rangle$ under the Hamiltonian $H'$ scales as $\sim 1/L$ when $n$ is a finite fraction of $L$, as it is proven in the SM [47].

***Conclusions*** — In this letter we revisited the paradigmatic one-dimensional spin-1 XY model that supports exact QMBS at finite size, and we explored the properties of the rest of the spectrum. We showed that it is possible to construct other states, dubbed asymptotic QMBS, with little entanglement and whose relaxation time diverges polynomially in the thermodynamic limit. These asymptotic QMBS indicate the existence of

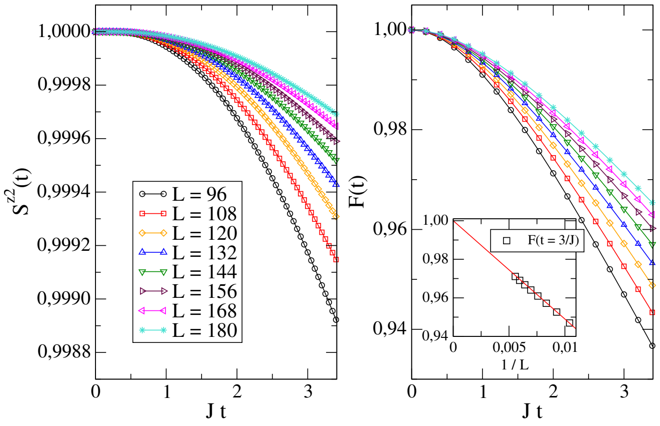

FIG. 4. The properties of the state $e^{-iH't}\,|n,\pi\rangle$ for $n = L/2$ as a function of time; the parameters of the Hamiltonian employed in the simulation are the same of Fig. 3. Left: time evolution of the squared magnetisation $S^{z2}(t)$; right: time evolution of the fidelity with the initial state $F(t)$. The inset shows the scaling as a function of size of the values of $F(t = 3/J)$; we find a scaling to 1 as $1/L \to 0$.

slowly relaxing modes and novel long-lived quasiparticles in systems with exact QMBS; it would be interesting to understand their relations to analogous slowly relaxing modes of hydrodynamic origin.

Remarkably, asymptotic QMBS are linear combinations of "thermal" eigenstates whose entanglement entropy and average squared magnetization are "smooth" functions of energy; we leave for future work the investigation of a possible violation of off-diagonal ETH [65–71].

Asymptotic QMBS with similar properties can also be constructed in higher dimensional spin-1 XY models [47], but other extensions would also be interesting, considering first the exhaustive algebra of local Hamiltonians that have the same exact QMBS $|n,\pi\rangle$ [29]. Second, they likely can always be constructed in Hamiltonians with simple quasiparticle towers of exact QMBS [7, 11–13, 17, 19, 25, 72]. Third, there are many different types of exact QMBS [3], e.g., with non-local "quasiparticles" [13, 27, 73], or with non-isolated states [24, 32]; they could appear in gauge theories [74, 75] or Floquet systems [28, 76–78]. Are there asymptotic QMBS in these models?

Finally, one could also consider deformations of Hamiltonians with exact QMBS (a problem that we partially addressed in the final part of this letter), and ask what are the conditions for a Hamiltonian to display an asymptotic QMBS without any exact QMBS.

***Acknowledgements*** — We warmly acknowledge enlightening discussions with Saverio Bocini, Xiangyu Cao, Maurizio Fagotti, David Huse, Michael Knap, Lesik Motrunich and Nicolas Regnault. We also thank Lesik Motrunich for useful comments on a draft. L.G. and L.M. also thank Guillaume Roux and Pascal Simon for discussions on previous shared projects. This work is supported by the Walter Burke Institute for Theoretical Physics at Caltech and the Institute for Quantum Information and Matter, by LabEx PALM (ANR-10-LABX-0039-PALM) in Orsay, by Region Ile-de-France in the framework of the DIM Sirteq and by the Swiss National Science Foundation under Division II. S.M. also acknowledges the hospitality of the Laboratoire de Physique Théorique et Modèles Statistiques (LPTMS) in Orsay, where this collaboration was initiated, and the Physik-Insitut of the University of Zurich, where some of this work was performed.

---

[*] lorenzo.gotta@unige.ch
[†] sanjaym@caltech.edu
[‡] leonardo.mazza@universite-paris-saclay.fr

[1] Maksym Serbyn, Dmitry A. Abanin, and Zlatko Papić, "Quantum many-body scars and weak breaking of ergodicity," Nature Physics **17**, 675–685 (2021).

[2] Zlatko Papić, "Weak Ergodicity Breaking Through the Lens of Quantum Entanglement," in *Entanglement in Spin Chains: From Theory to Quantum Technology Applications*, edited by Abolfazl Bayat, Sougato Bose, and Henrik Johannesson (Springer International Publishing, Cham, 2022) pp. 341–395.

[3] Sanjay Moudgalya, B Andrei Bernevig, and Nicolas Regnault, "Quantum many-body scars and hilbert space fragmentation: a review of exact results," Reports on Progress in Physics **85**, 086501 (2022).

[4] Anushya Chandran, Thomas Iadecola, Vedika Khemani, and Roderich Moessner, "Quantum Many-Body Scars: A Quasiparticle Perspective," Annual Review of Condensed Matter Physics **14**, 443–469 (2023).

[5] J. M. Deutsch, "Quantum statistical mechanics in a closed system," Physical Review A **43**, 2046–2049 (1991).

[6] Mark Srednicki, "Chaos and quantum thermalization," Physical Review E **50**, 888–901 (1994).

[7] Marcos Rigol, Vanja Dunjko, and Maxim Olshanii, "Thermalization and its mechanism for generic isolated quantum systems," Nature **452**, 854–858 (2008).

[8] Anatoli Polkovnikov, Krishnendu Sengupta, Alessandro Silva, and Mukund Vengalattore, "Colloquium: Nonequilibrium dynamics of closed interacting quantum systems," Reviews of Modern Physics **83**, 863–883 (2011).

[9] Luca D'Alessio, Yariv Kafri, Anatoli Polkovnikov, and Marcos Rigol, "From quantum chaos and eigenstate thermalization to statistical mechanics and thermodynamics," Advances in Physics **65**, 239–362 (2016).

[10] Takashi Mori, Tatsuhiko N Ikeda, Eriko Kaminishi, and Masahito Ueda, "Thermalization and prethermalization in isolated quantum systems: a theoretical overview," Journal of Physics B: Atomic, Molecular and Optical Physics **51**, 112001 (2018).

[11] Sanjay Moudgalya, Stephan Rachel, B. Andrei Bernevig, and Nicolas Regnault, "Exact excited states of nonintegrable models," Physical Review B **98**, 235155 (2018).

[12] Sanjay Moudgalya, Nicolas Regnault, and B. Andrei Bernevig, "Entanglement of exact excited states of affleck-kennedy-lieb-tasaki models: Exact results, many-body scars, and violation of the strong eigenstate thermaliza-

tion hypothesis," Phys. Rev. B **98**, 235156 (2018).

[13] Daniel K. Mark, Cheng-Ju Lin, and Olexei I. Motrunich, "Unified structure for exact towers of scar states in the affleck-kennedy-lieb-tasaki and other models," Phys. Rev. B **101**, 195131 (2020).

[2] Michael Schecter and Thomas Iadecola, "Weak ergodicity breaking and quantum many-body scars in spin-1 $xy$ magnets," Phys. Rev. Lett. **123**, 147201 (2019).

[8] Julia Wildeboer, Christopher M. Langlett, Zhi-Cheng Yang, Alexey V. Gorshkov, Thomas Iadecola, and Shenglong Xu, "Quantum many-body scars from einstein-podolsky-rosen states in bilayer systems," Phys. Rev. B **106**, 205142 (2022).

[16] Chen Ning Yang, "$\eta$ pairing and off-diagonal long-range order in a hubbard model," Physical Review letters **63**, 2144 (1989).

[17] Sanjay Moudgalya, Nicolas Regnault, and B. Andrei Bernevig, "$\eta$-pairing in hubbard models: From spectrum generating algebras to quantum many-body scars," Phys. Rev. B **102**, 085140 (2020).

[7] Daniel K. Mark and Olexei I. Motrunich, "$\eta$-pairing states as true scars in an extended hubbard model," Phys. Rev. B **102**, 075132 (2020).

[19] K. Pakrouski, P. N. Pallegar, F. K. Popov, and I. R. Klebanov, "Many-body scars as a group invariant sector of hilbert space," Phys. Rev. Lett. **125**, 230602 (2020).

[20] K. Pakrouski, P. N. Pallegar, F. K. Popov, and I. R. Klebanov, "Group theoretic approach to many-body scar states in fermionic lattice models," Phys. Rev. Research **3**, 043156 (2021).

[21] Hironobu Yoshida and Hosho Katsura, "Exact eigenstates of extended SU$(n)$ hubbard models: Generalization of $\eta$-pairing states with $n$-particle off-diagonal long-range order," Phys. Rev. B **105**, 024520 (2022).

[22] Lorenzo Gotta, Leonardo Mazza, Pascal Simon, and Guillaume Roux, "Exact many-body scars based on pairs or multimers in a chain of spinless fermions," Phys. Rev. B **106**, 235147 (2022).

[23] Masaya Nakagawa, Hosho Katsura, and Masahito Ueda, "Exact eigenstates of multicomponent Hubbard models: SU$(N)$ magnetic $\eta$ pairing, weak ergodicity breaking, and partial integrability," arXiv e-prints (2022), arXiv:2205.07235 [cond-mat.str-el].

[24] Naoto Shiraishi and Takashi Mori, "Systematic construction of counterexamples to the eigenstate thermalization hypothesis," Phys. Rev. Lett. **119**, 030601 (2017).

[25] Sanjay Moudgalya, Edward O'Brien, B. Andrei Bernevig, Paul Fendley, and Nicolas Regnault, "Large classes of quantum scarred hamiltonians from matrix product states," Phys. Rev. B **102**, 085120 (2020).

[26] Jie Ren, Chenguang Liang, and Chen Fang, "Quasisymmetry groups and many-body scar dynamics," Phys. Rev. Lett. **126**, 120604 (2021).

[27] Nicholas O'Dea, Fiona Burnell, Anushya Chandran, and Vedika Khemani, "From tunnels to towers: Quantum scars from lie algebras and $q$-deformed lie algebras," Phys. Rev. Research **2**, 043305 (2020).

[28] Pierre-Gabriel Rozon, Michael J. Gullans, and Kartiek Agarwal, "Constructing quantum many-body scar hamiltonians from floquet automata," Phys. Rev. B **106**, 184304 (2022).

[29] Sanjay Moudgalya and Olexei I. Motrunich, "Exhaustive Characterization of Quantum Many-Body Scars using Commutant Algebras," arXiv e-prints (2022), arXiv:2209.03377 [cond-mat.str-el].

[30] Pierre-Gabriel Rozon and Kartiek Agarwal, "Broken unitary picture of dynamics in quantum many-body scars," arXiv e-prints , arXiv:2302.04885 (2023).

[3] Cheng-Ju Lin, Anushya Chandran, and Olexei I. Motrunich, "Slow thermalization of exact quantum many-body scar states under perturbations," Phys. Rev. Res. **2**, 033044 (2020).

[32] Cheng-Ju Lin and Olexei I. Motrunich, "Exact quantum many-body scar states in the Rydberg-blockaded atom chain," Phys. Rev. Lett. **122**, 173401 (2019).

[33] Mari Carmen Bañuls, David A. Huse, and J. Ignacio Cirac, "Entanglement and its relation to energy variance for local one-dimensional hamiltonians," Phys. Rev. B **101**, 144305 (2020).

[34] D. J. Thouless, "Maximum metallic resistance in thin wires," Phys. Rev. Lett. **39**, 1167–1169 (1977).

[35] Amos Chan, Andrea De Luca, and J. T. Chalker, "Spectral statistics in spatially extended chaotic quantum many-body systems," Phys. Rev. Lett. **121**, 060601 (2018).

[36] Mauro Schiulaz, E. Jonathan Torres-Herrera, and Lea F. Santos, "Thouless and relaxation time scales in many-body quantum systems," Phys. Rev. B **99**, 174313 (2019).

[37] Anatoly Dymarsky, "Bound on eigenstate thermalization from transport," Phys. Rev. Lett. **128**, 190601 (2022).

[38] Paul M Chaikin, Tom C Lubensky, and Thomas A Witten, *Principles of condensed matter physics*, Vol. 10 (Cambridge university press Cambridge, 1995).

[39] Subroto Mukerjee, Vadim Oganesyan, and David Huse, "Statistical theory of transport by strongly interacting lattice fermions," Phys. Rev. B **73**, 035113 (2006).

[40] Jonathan Lux, Jan Müller, Aditi Mitra, and Achim Rosch, "Hydrodynamic long-time tails after a quantum quench," Phys. Rev. A **89**, 053608 (2014).

[41] Andrey Gromov, Andrew Lucas, and Rahul M. Nandkishore, "Fracton hydrodynamics," Phys. Rev. Res. **2**, 033124 (2020).

[42] Johannes Feldmeier, Pablo Sala, Giuseppe De Tomasi, Frank Pollmann, and Michael Knap, "Anomalous diffusion in dipole- and higher-moment-conserving systems," Phys. Rev. Lett. **125**, 245303 (2020).

[43] Sanjay Moudgalya, Abhinav Prem, David A. Huse, and Amos Chan, "Spectral statistics in constrained many-body quantum chaotic systems," Phys. Rev. Res. **3**, 023176 (2021).

[44] Berislav Buča, "Unified theory of local quantum many-body dynamics: Eigenoperator thermalization theorems," arXiv e-prints (2023), arXiv:2301.07091 [cond-mat.stat-mech].

[45] L. Pitaevskii and S. Stringari, *Bose-Einstein Condensation* (Oxford University Press, 2016).

[46] Atsuhiro Kitazawa, Keigo Hijii, and Kiyohide Nomura, "An su(2) symmetry of the one-dimensional spin-1 xy model," Journal of Physics A: Mathematical and General **36**, L351 (2003).

[47] "See the supplemental material,".

[1] Oskar Vafek, Nicolas Regnault, and B. Andrei Bernevig, "Entanglement of exact excited eigenstates of the Hubbard model in arbitrary dimension," SciPost Phys. **3**, 043 (2017).

[49] Long-Hin Tang, Nicholas O'Dea, and Anushya Chandran, "Multimagnon quantum many-body scars from tensor operators," Phys. Rev. Res. **4**, 043006 (2022).

[50] Gregory M. Crosswhite and Dave Bacon, "Finite automata for caching in matrix product algorithms," Phys. Rev. A **78**, 012356 (2008).

[51] Johannes Motruk, Michael P. Zaletel, Roger S. K. Mong, and Frank Pollmann, "Density matrix renormalization group on a cylinder in mixed real and momentum space," Phys. Rev. B **93**, 155139 (2016).

[52] Phillip Weinberg and Marin Bukov, "QuSpin: a Python package for dynamics and exact diagonalisation of quantum many body systems part I: spin chains," SciPost Phys. **2**, 003 (2017).

[6] Lorenzo Campos Venuti and Paolo Zanardi, "Unitary equilibrations: Probability distribution of the loschmidt echo," Phys. Rev. A **81**, 022113 (2010).

[4] Takashi Mori and Naoto Shiraishi, "Thermalization without eigenstate thermalization hypothesis after a quantum quench," Phys. Rev. E **96**, 022153 (2017).

[55] Sheldon Goldstein, Takashi Hara, and Hal Tasaki, "Time scales in the approach to equilibrium of macroscopic quantum systems," Phys. Rev. Lett. **111**, 140401 (2013).

[56] Artur S. L. Malabarba, Luis Pedro García-Pintos, Noah Linden, Terence C. Farrelly, and Anthony J. Short, "Quantum systems equilibrate rapidly for most observables," Phys. Rev. E **90**, 012121 (2014).

[57] Sheldon Goldstein, Takashi Hara, and Hal Tasaki, "Extremely quick thermalization in a macroscopic quantum system for a typical nonequilibrium subspace," New Journal of Physics **17**, 045002 (2015).

[58] Peter Reimann, "Typical fast thermalization processes in closed many-body systems," Nature Communications **7**, 10821 (2016).

[59] Luis Pedro García-Pintos, Noah Linden, Artur S. L. Malabarba, Anthony J. Short, and Andreas Winter, "Equilibration time scales of physically relevant observables," Phys. Rev. X **7**, 031027 (2017).

[5] Henrik Wilming, Thiago R. de Oliveira, Anthony J. Short, and Jens Eisert, "Equilibration times in closed quantum many-body systems," in *Thermodynamics in the Quantum Regime: Fundamental Aspects and New Directions*, edited by Felix Binder, Luis A. Correa, Christian Gogolin, Janet Anders, and Gerardo Adesso (Springer International Publishing, Cham, 2018) pp. 435–455.

[61] Jonathon Riddell, Luis Pedro García-Pintos, and Álvaro M. Alhambra, "Relaxation of non-integrable systems and correlation functions," arXiv e-prints , arXiv:2112.09475 (2021).

[62] Matthew Fishman, Steven R. White, and E. Miles Stoudenmire, "The ITensor Software Library for Tensor Network Calculations," SciPost Phys. Codebases , 4 (2022).

[63] Matthew Fishman, Steven R. White, and E. Miles Stoudenmire, "Codebase release 0.3 for ITensor," SciPost Phys. Codebases , 4–r0.3 (2022).

[64] Naoto Shiraishi and Takashi Mori, "Shiraishi and mori reply," Phys. Rev. Lett. **121**, 038902 (2018).

[65] Ehsan Khatami, Guido Pupillo, Mark Srednicki, and Marcos Rigol, "Fluctuation-dissipation theorem in an isolated system of quantum dipolar bosons after a quench," Phys. Rev. Lett. **111**, 050403 (2013).

[66] R. Steinigeweg, J. Herbrych, and P. Prelovšek, "Eigenstate thermalization within isolated spin-chain systems," Phys. Rev. E **87**, 012118 (2013).

[67] Wouter Beugeling, Roderich Moessner, and Masudul Haque, "Off-diagonal matrix elements of local operators in many-body quantum systems," Phys. Rev. E **91**, 012144 (2015).

[68] Jonas Richter, Anatoly Dymarsky, Robin Steinigeweg, and Jochen Gemmer, "Eigenstate thermalization hypothesis beyond standard indicators: Emergence of random-matrix behavior at small frequencies," Phys. Rev. E **102**, 042127 (2020).

[69] Jonathan Wurtz and Anatoli Polkovnikov, "Emergent conservation laws and nonthermal states in the mixed-field ising model," Phys. Rev. B **101**, 195138 (2020).

[70] Sho Sugiura, Pieter W. Claeys, Anatoly Dymarsky, and Anatoli Polkovnikov, "Adiabatic landscape and optimal paths in ergodic systems," Phys. Rev. Res. **3**, 013102 (2021).

[71] Federica Maria Surace, Matteo Votto, Eduardo Gonzalez Lazo, Alessandro Silva, Marcello Dalmonte, and Giuliano Giudici, "Exact many-body scars and their stability in constrained quantum chains," Phys. Rev. B **103**, 104302 (2021).

[72] Thomas Iadecola and Michael Schecter, "Quantum many-body scar states with emergent kinetic constraints and finite-entanglement revivals," Phys. Rev. B **101**, 024306 (2020).

[73] Christopher M. Langlett, Zhi-Cheng Yang, Julia Wildeboer, Alexey V. Gorshkov, Thomas Iadecola, and Shenglong Xu, "Rainbow scars: From area to volume law," Phys. Rev. B **105**, L060301 (2022).

[74] Saptarshi Biswas, Debasish Banerjee, and Arnab Sen, "Scars from protected zero modes and beyond in $U(1)$ quantum link and quantum dimer models," SciPost Phys. **12**, 148 (2022).

[75] Debasish Banerjee and Arnab Sen, "Quantum scars from zero modes in an abelian lattice gauge theory on ladders," Phys. Rev. Lett. **126**, 220601 (2021).

[76] Kaoru Mizuta, Kazuaki Takasan, and Norio Kawakami, "Exact floquet quantum many-body scars under rydberg blockade," Phys. Rev. Research **2**, 033284 (2020).

[77] Sho Sugiura, Tomotaka Kuwahara, and Keiji Saito, "Many-body scar state intrinsic to periodically driven system," Phys. Rev. Research **3**, L012010 (2021).

[78] Thomas Iadecola and Sagar Vijay, "Nonergodic quantum dynamics from deformations of classical cellular automata," Phys. Rev. B **102**, 180302 (2020).

# Online supplementary material for: Asymptotic Quantum Many-Body Scars

Lorenzo Gotta[1,2], Sanjay Moudgalya[3,4], Leonardo Mazza[2]
[1] *Department of Quantum Matter Physics, University of Geneva, 24 Quai Ernest-Ansermet, 1211 Geneva, Switzerland*
[2] *Université Paris-Saclay, CNRS, LPTMS, 91405, Orsay, France*
[3] *Department of Physics and Institute for Quantum Information and Matter, California Institute of Technology, Pasadena, California 91125, USA*
[4] *Walter Burke Institute for Theoretical Physics, California Institute of Technology, Pasadena, California 91125, USA*

November 13, 2023

In this Supplementary Material we present the explicit calculations of the main relevant properties of the asymptotic QMBS presented in the main text:

## S1. ORTHOGONALITY OF THE ASYMPTOTIC QMBS WITH THE EXACT QMBS

In this section, we demonstrate the orthogonality of the states $\{|n,k\rangle\}$, defined in Eq. (4) of the main text. First, we note that $|n,k\rangle$ is orthogonal to $|n',k'\rangle$ when $n \neq n'$ because they have a different magnetisation $S^z = \sum_j S^z_j$, which is a simple function of $n$: $S^z = -L + 2n$. We now consider states with the same $n$ and take the system size $L$ to be even and $k$ to be an integer multiple of $\frac{2\pi}{L}$ for simplicity. We then observe that $\langle n,k\,|n,k'\rangle \propto \langle n-1,\pi|\, J^-_k J^+_{k'}\,|n-1,\pi\rangle$ for $n \geq 1$. By definition of the operators $J^+_k$ in Eq. (2) of the main text we have:

$$\begin{aligned}
\langle n-1,\pi|\, J^-_k J^+_{k'}\,|n-1,\pi\rangle &= \frac{1}{4}\sum_{j,j'=1}^{L} e^{-i(kj-k'j')}\,\langle n-1,\pi|\,(S^-_j)^2(S^+_{j'})^2\,|n-1,\pi\rangle \\
&= \frac{1}{4}\sum_{j=1}^{L} e^{-i(k-k')j}\,\langle n-1,\pi|\,(S^-_j)^2(S^+_j)^2\,|n-1,\pi\rangle + \frac{1}{4}\sum_{j\neq j'} e^{-i(kj-k'j')}\,\langle n-1,\pi|\,(S^-_j)^2(S^+_{j'})^2\,|n-1,\pi\rangle \\
&= \frac{1}{4}\alpha\sum_{j=1}^{L} e^{-i(k-k')j} + \frac{1}{4}\beta\sum_{j=1}^{L} e^{i(\pi-k)j}\sum_{j'\neq j} e^{i(k'-\pi)j'} = \frac{1}{4}L(\alpha-\beta)\delta_{k,k'} + \frac{1}{4}\beta L^2\delta_{k,\pi}\delta_{k',\pi},
\end{aligned} \tag{S7}$$

where $\alpha = 4\frac{\binom{L-1}{n-1}}{\binom{L}{n-1}} = 4\frac{L+1-n}{L}$ and $\beta = 4\frac{\binom{L-2}{n-2}}{\binom{L}{n-1}} = 4\frac{(n-1)(L-n+1)}{L(L-1)}$, and we have used the fact that $k$ and $k'$ are integer multiples of $\frac{2\pi}{L}$. This calculation is done directly by using the expression of $|n,\pi\rangle$ as an equal amplitude superposition of "fully-magnetised" product states

$$|n,\pi\rangle = \sqrt{\frac{1}{2^{2n}\binom{L}{n}}}\sum_{1\leq j_1<j_2<\ldots<j_n\leq L} e^{i\pi\sum_{i=1}^{n} j_i}\left(S^+_{j_1}\right)^2\left(S^+_{j_2}\right)^2\ldots\left(S^+_{j_n}\right)^2|\Downarrow\rangle\,, \tag{S8}$$

and studying the action of the sandwiched operator on the basis states separately when $j = j'$ and when $j \neq j'$, and carefully accounting for the phase factors and normalization factors. It is important to visualise the combinatorial nature of this state, expanded on a basis of states where the bimagnons created by $\left(S_j^+\right)^2$ are equally distributed everywhere. When $j = j'$, we obtain that $\alpha$ in Eq. (S7) is simply related to the number of fully-magnetised product states that do not have a bimagnon at site $j$, or else the action of $(S_j^-)^2(S_j^+)^2$ vanishes on such a basis state. This number is $\binom{L-1}{n-1}$; if we consider the normalisation factor and the specific matrix elements of $\left(S_j^-\right)^2(S_j^+)^2$, we obtain its expression, given after Eq. (S7). Similarly, when $j \neq j'$ and $n > 1$, we obtain that $\beta$ in Eq. (S7) is related to the number of fully-magnetised product states that have one bimagnon at site $j$, and no bimagnon at $j'$, which is $\binom{L-2}{n-2}$. Its expression, given after Eq. (S7), then follows directly after taking into account the normalization factors and matrix elements. Hence using Eq. (S7) for any $k \neq k'$ it is clear that we obtain $\langle n, k' | n, k\rangle = 0$. Given that we work with normalised states, we can combine the arguments above to conclude that $\langle n, k \,| n', \pi\rangle = \delta_{n,n'}\delta_{k,\pi}$ whenever $k$ is an integer multiple of $\frac{2\pi}{L}$ and $L$ is even.

## S2. AVERAGE ENERGY AND ENERGY VARIANCE FOR THE ASYMPTOTIC QMBS

In this section, we compute the average energy and variance of the asymptotic QMBS states $\{|n, k\rangle\}$ defined in Eq. (4) of the main text.

### A. Rewriting the asymptotic QMBS

For the convenience of explicit calculations, we propose the following rewriting of the asymptotic QMBS:

$$|n, k\rangle = \frac{1}{\sqrt{\mathcal{M}_{n,k}}} J_k^+ \,|n-1, \pi\rangle \,. \tag{S9}$$

where the states $|n-1, \pi\rangle$ and $|n, k\rangle$ are normalised. As a first step, we compute the normalization factor coefficient $\mathcal{M}_{n,k}$, which can be directly deduced from Eq. (S7). That is, its expression reads

$$\mathcal{M}_{n,k} = \langle n-1, \pi|\, J_k^- J_k^+ \,|n-1, \pi\rangle = \frac{(L-n+1)(L-n)}{L-1} + \frac{L(L-n+1)(n-1)}{L-1}\delta_{k,\pi} \tag{S10}$$

### B. Average energy

To compute the average energy of the state $|n, k\rangle$, we first rewrite the OBC spin-1 XY Hamiltonian, along with the symmetry breaking perturbation [see discussion below Eq. (1) in the main text], as:

$$H = \frac{J}{2}\sum_{j=1}^{L-1}\left(S_j^+ S_{j+1}^- + S_j^- S_{j+1}^+\right) + h\sum_{j=1}^{L} S_j^z + D\sum_j \left(S_z^z\right)^2 + \frac{J_3}{2}\sum_{j=1}^{L-3}\left(S_j^+ S_{j+3}^- + S_j^+ S_{j+3}^-\right). \tag{S11}$$

In order to compute the average energy, we need to study the action of $[S_j^+ S_{j+1}^- + h.c.]$ onto the state $|n, k\rangle$, and for this it is convenient to consider the decomposition of $|n, k\rangle$ over sites $j$ and $j+1$. For example, we can rewrite $|n, \pi\rangle$ as

$$|n, \pi\rangle = \alpha_{n,\pi} \,|+\rangle_j \,|+\rangle_{j+1} |\psi_{n,\pi,1}\rangle + \beta_{n,\pi} \,|-\rangle_j \,|-\rangle_{j+1} |\psi_{n,\pi,2}\rangle + \gamma_{n,\pi}\left(\frac{|+\rangle_j \,|-\rangle_{j+1} - |-\rangle_j \,|+\rangle_{j+1}}{\sqrt{2}}\right)|\psi_{n,\pi,3}\rangle\,; \tag{S12}$$

where $\alpha_{n,\pi}$, $\beta_{n,\pi}$, and $\gamma_{n,\pi}$ are numbers with $|\alpha_{n,\pi}|^2 + |\beta_{n,\pi}|^2 + |\gamma_{n,\pi}|^2 = 1$, and $\{|\psi_{n,\pi,\ell}\rangle\}$ for $1 \leq \ell \leq 3$ are some states with support on sites other than $j$ and $j+1$, and we have denoted the three spin-1 states on a site $j$ by $|+\rangle_j$, $|-\rangle_j$, and $|0\rangle_j$. One can similarly rewrite the $|n, k\rangle$ as:

$$\begin{aligned}|n, k\rangle =& \alpha_{n,k} \,|+\rangle_j \,|+\rangle_{j+1} |\psi_{n,k,1}\rangle + \beta_{n,k} \,|-\rangle_j \,|-\rangle_{j+1} |\psi_{n,k,2}\rangle + \\ &+ \gamma_{n,k}\left(\frac{|+\rangle_j \,|-\rangle_{j+1} - |-\rangle_j \,|+\rangle_{j+1}}{\sqrt{2}}\right)|\psi_{n,k,3}\rangle + \upsilon_{n,k}\left(\frac{|+\rangle_j \,|-\rangle_{j+1} + e^{ik}\,|-\rangle_j \,|+\rangle_{j+1}}{\sqrt{2}}\right)|\psi_{n,k,4}\rangle\,,\end{aligned} \tag{S13}$$

where $\alpha_{n,k}$, $\beta_{n,k}$, $\gamma_{n,k}$, and $\upsilon_{n,k}$ are numbers such that $|n,k\rangle$ is normalized and $\{|\psi_{n,\pi,\ell}\rangle\}$ for $1 \leq \ell \leq 4$ are some states without support on $j$ and $j+1$. The action of the term $[S_j^+ S_{j+1}^- + h.c.]$ can then be directly computed to be:

$$\left(S_j^+ S_{j+1}^- + h.c.\right)|n,k\rangle = \sqrt{2}\upsilon_{n,k}\left(1+e^{ik}\right)|0\rangle_j\,|0\rangle_{j+1}\,|\psi_{n,k,4}\rangle\,. \tag{S14}$$

Using Eq. (S13), it then directly follows that $\langle n,k|\left(S_j^+ S_{j+1}^- + h.c.\right)|n,k\rangle = 0$. A similar reasoning can be carried out for the interaction term proportional to $J_3$ to show that $\langle n,k|\left(S_j^+ S_{j+3}^- + h.c.\right)|n,k\rangle = 0$, hence in all we obtain $\langle n,k|\,H\,|n,k\rangle = h(-L+2n) + DL$ for all $k$. We conclude by noticing that the same result holds in PBC as well.

### C. Energy variance

To compute the energy variance in any state, it is easy to see that the contribution of the terms in the Hamiltonian for which the state is an eigenstate simply vanishes. Hence, in the computation of the variance of $|n,k\rangle$, we can simply ignore the magnetic field and anistropy terms in $H$ of Eq. (S11), i.e., those that are proportional to $h$ and $D$, since $|n,k\rangle$ are their eigenstates. For simplicity, we refer to the terms in $H$ proportional to $J$ and $J_3$ as $H_1$ and $H_3$, respectively, and work with PBC. As we showed in the previous section, $\langle n,k|\,H_1\,|n,k\rangle = \langle n,k|\,H_3\,|n,k\rangle = 0$, and using similar ideas one can also show that $\langle n,k|\,H_1\,H_3\,|n,k\rangle = \langle n,k|\,H_3\,H_1\,|n,k\rangle = 0$. Hence the expression of the variance of $|n,k\rangle$ in $H$ reduces to $\Delta H^2 = \langle n,k|\,(H_1+H_3)^2\,|n,k\rangle = \langle n,k|\,(H_1^2+H_3^2)\,|n,k\rangle$. We now propose a rewriting of each term:

$$\begin{aligned}\langle n,k|\,H_\ell^2\,|n,k\rangle =& \frac{1}{\mathcal{M}_{n,k}}\langle n-1,\pi|\,J_k^- H_\ell^2 J_k^+\,|n-1,\pi\rangle = \frac{1}{\mathcal{M}_{n,k}}\langle n-1,\pi|\,[J_k^-,H_\ell]\,[H_\ell,J_k^+]\,|n-1,\pi\rangle = \\ =& \frac{1}{\mathcal{M}_{n,k}}\langle n-1,\pi|\,[H_\ell,J_k^+]^\dagger\,[H_\ell,J_k^+]\,|n-1,\pi\rangle\,,\end{aligned} \tag{S15}$$

where $\ell = 1,3$, and we have exploited the fact that $H_\ell\,|n-1,\pi\rangle = 0$. We a few straightforward algebraic passages, it is possible to show that:

$$\begin{aligned}[H_1,J_k^+] &= \frac{J}{2}\sum_{j=1}^{L} e^{ikj}[S_j^+ S_{j+1}^- + S_j^- S_{j+1}^+, \frac{1}{2}(S_j^+)^2 + \frac{e^{ik}}{2}(S_{j+1}^+)^2] \\ &= -\frac{J}{2}\sum_{j=1}^{L} e^{ikj}\left[\{S_j^z,S_j^+\}S_{j+1}^+ + e^{ik}S_j^+\{S_{j+1}^z,S_{j+1}^+\}\right],\end{aligned} \tag{S16}$$

where $\{\cdot,\cdot\}$ denotes the anti-commutator and we have used the identity $[S_m^+ S_n^-, (S_n^+)^2] = -2S_m^+\{S_n^z,S_n^+\}$. The calculation proceeds by substituting Eq. (S16) into Eq. (S15) and it is greatly simplified by the fact that $S_j^z S_j^+\,|n-1,\pi\rangle = S_j^z S_j^-\,|n-1,\pi\rangle = 0$. First, using this identity simplifies the action of $[H_1,J_k^+]$ on $|n-1,\pi\rangle$ to

$$[H_1,J_k^+]\,|n-1,\pi\rangle = -\frac{J}{2}\sum_{j=1}^{L} e^{ikj}\left[S_j^+ S_j^z S_{j+1}^+ + e^{ik}S_j^+ S_{j+1}^+ S_{j+1}^z\right]|n-1,\pi\rangle\,, \tag{S17}$$

and Eq. (S15) then reads

$$\langle n,k|\,H_1^2\,|n,k\rangle = \frac{J^2}{4\mathcal{M}_{n,k}}\sum_{j,j'=1}^{L} e^{ik(j-j')}\langle n-1,\pi|\,[S_{j'}^z S_{j'}^- S_{j'+1}^- + e^{-ik}S_{j'}^- S_{j'+1}^z S_{j'+1}^-][S_j^+ S_j^z S_{j+1}^+ + e^{ik}S_j^+ S_{j+1}^+ S_{j+1}^z]\,|n-1,\pi\rangle\,. \tag{S18}$$

We then notice that in Eq. (S18), all the terms with $j \neq j'$ in the sum vanish since the action of the sandwiched operator on $|n-1,\pi\rangle$ in such cases leads to inevitable appearance of spins with states $|0\rangle_m$ on certain sites $m$, which in turn have a vanishing overlap with $\langle n-1,\pi|$. Hence, we can simplify Eq. (S18) to

$$\begin{aligned}\langle n,k|\,H_1^2\,|n,k\rangle &= \frac{J^2}{4\mathcal{M}_{n,k}}\sum_{j=1}^{L}\langle n-1,\pi|\,[S_j^z S_j^- S_{j+1}^- + e^{-ik}S_j^- S_{j+1}^z S_{j+1}^-][S_j^+ S_j^z S_{j+1}^+ + e^{ik}S_j^+ S_{j+1}^+ S_{j+1}^z]\,|n-1,\pi\rangle \\ &= \frac{J^2}{4\mathcal{M}_{n,k}}\langle n-1,\pi|\sum_{j=1}^{L}\Bigg[e^{-ik}S_j^- S_j^+ S_j^z S_{j+1}^z S_{j+1}^- S_{j+1}^+ + S_j^- S_j^+ S_{j+1}^z S_{j+1}^- S_{j+1}^+ S_{j+1}^z \\ &\quad + S_j^z S_j^- S_j^+ S_j^z S_{j+1}^- S_{j+1}^+ + e^{ik}S_j^z S_j^- S_j^+ S_{j+1}^- S_{j+1}^+ S_{j+1}^z\Bigg]\,|n-1,\pi\rangle\,,\end{aligned} \tag{S19}$$

Now we consider the expansion of $|n-1,\pi\rangle$ in the product state basis, as shown in Eq. (S8) and note that each of the terms in Eq. (S19) vanish on the basis states unless there is no bimagnon on both sites $j$ and $j+1$. Hence we can simply count the number of such states and incorporate the normalization factor to obtain:

$$\langle n,k|\,H_1^2\,|n,k\rangle = \frac{J^2}{\mathcal{M}_{n,k}}\sum_{j=1}^{L}\frac{\binom{L-2}{n-1}}{\binom{L}{n-1}}\left[e^{-ik}+1+1+e^{ik}\right] = \frac{4J^2\cos^2\left(\frac{k}{2}\right)}{1+\delta_{k,\pi}\frac{L(n-1)}{L-n}} = 4J^2\cos^2\left(\frac{k}{2}\right)\,, \tag{S20}$$

where in the last step we have used the fact that the numerator anyway vanishes for $k=\pi$. The same calculation can be carried out in OBC and amounts to a multiplication of the result in Eq. (S20) by a factor $1-\frac{1}{L}$, which does not change the PBC result in the thermodynamic limit. With similar arguments one can prove that:

$$\langle n,k|\,H_3^2\,|n,k\rangle = 4J_3^2\cos^2\left(\frac{3k}{2}\right)\,, \tag{S21}$$

thus recovering the result in Eq. (5) of the main text. Once again, the choice of OBC amounts to a correction factor $1-\frac{3}{L}$, which is irrelevant in the thermodynamic limit.

### D. Considerations on multiparticle asymptotic QMBS

The set of asymptotic QMBS is not limited to the single-particle asymptotic QMBS explicitly discussed above. For instance, the action of an operator $(J_k^+)^m$ for $k=\pi-\epsilon$ (for $\epsilon\sim 1/L$ small) and $m\ll L$, on any exact QMBS eigenstate results in a state with variance scaling approximately as $\sim m\epsilon^2$; a set of numerical results supporting this claim is given in Fig. S1. Based on these results, we can identify also the multiparticle QMBS as asymptotic QMBS. In the rest of this section, we present an analytical calculation of the energy variance of the aforementioned state:

$$\frac{\langle n-1,\pi|\,(J_k^-)^m H^2 (J_k^+)^m\,|n-1,\pi\rangle}{\langle n-1,\pi|\,(J_k^-)^m (J_k^+)^m\,|n-1,\pi\rangle} = \frac{\|H(J_k^+)^m\,|n-1,\pi\rangle\|^2}{\|(J_k^+)^m\,|n-1,\pi\rangle\|^2}, \tag{S22}$$

where $\|\bullet\|$ denotes the $L^2$ norm. Although we are not able to compute the variance exactly, we will show that via some approximations we can reproduce the scalings obtained in Fig. S1.

Let us first remark that the formula in Eq. (S22) follows from the following facts: (i) the state $(J_k^+)^m\,|n-1,\pi\rangle$ is an exact eigenstate of the Hamiltonian parts proportional to $h$ and $D$, with eigenvalue $-Lh+2(n-1+m)h+LD$; (ii) it has zero expectation value of $H_1+H_3$. Both results follow from the fact that $(J_k^+)^m\,|n-1,\pi\rangle$ is only a linear superposition of $|+\rangle$ and $|-\rangle$ spin states, with $z$ the spin-quantisation axis: the action of $H_1$ and $H_3$ necessarily creates two $|0\rangle$ spin states, and thus make the state orthogonal to the initial one. A similar reasoning has been presented in Sec. S2 B for $m=1$.

As long as the energy variance is considered, we can thus simply focus on $H=H_1+H_3$. Yet, for the sake of simplicity, in this Section we will only consider $H_1$. The results can be easily generalized to $H_3$.

We first focus on the denominator of the expression in Eq. (S22):

$$\begin{aligned}&\|(J_k^+)^m\,|n-1,\pi\rangle\|^2 = \langle n-1,\pi|\,(J_k^-)^m(J_k^+)^m\,|n-1,\pi\rangle = \\ &\quad= \frac{(m!)^2}{2^{2m}}\sum_{j_1<\ldots<j_m}\sum_{l_1<\ldots<l_m} e^{ik(l_1+\ldots+l_m-j_1-\ldots-j_m)}\,\langle n-1,\pi|\,(S_{j_1}^-)^2\ldots(S_{j_m}^-)^2(S_{l_1}^+)^2\ldots(S_{l_m}^+)^2\,|n-1,\pi\rangle\,.\end{aligned} \tag{S23}$$

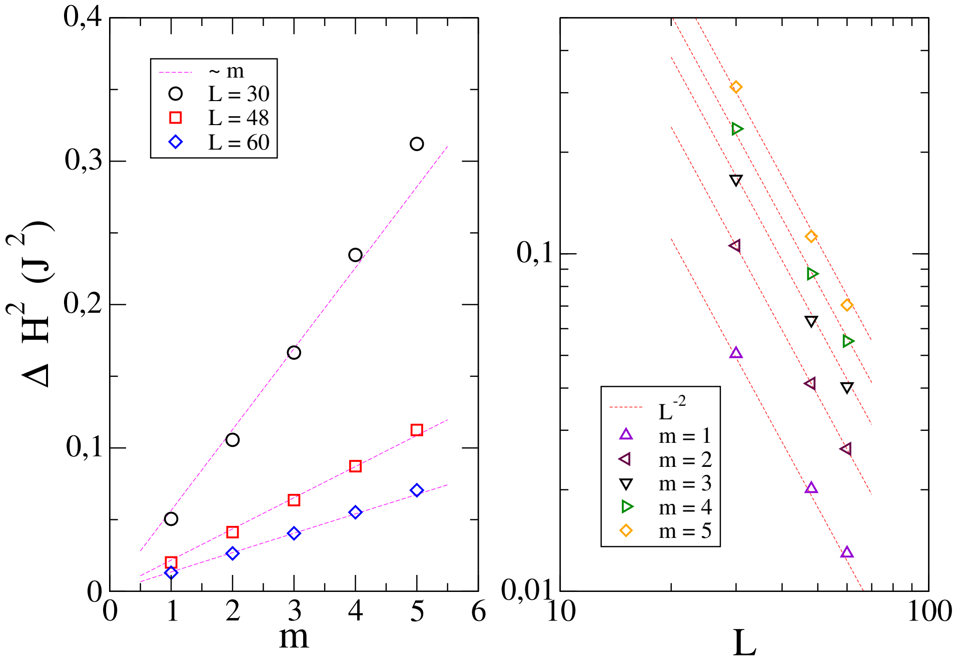

FIG. S1. Energy variance $\Delta H^2$ of the multiparticle QMBS obtained by acting $m$ times a bimagnon operator $J_k^+$ with $k = \pi - 2\pi/L$ on an exact scar $|n,\pi\rangle$. The state we are considering is thus proportional to $(J_k^+)^m |n,\pi\rangle$. We study three different system sizes, $L = 30$, 48 and 60, and five different values of $m$, from 1 to 5. The numerical data, obtained with a MPS representation of the states, yield a scaling of $\Delta H^2$ that is approximately linear in $m$ and proportional to $L^{-2}$. In the left panel the data are plotted versus $m$; in the right panel the same data are plotted versus $L$. The dashed lines are a guide to the eye to highlight the approximate behaviours as $\tilde{m}$ and as $\tilde{L}^{-2}$; note that the scalings are not precise at large $m$.

The evaluation of this sum is a formidable task, and we approximate it by considering only the leading terms $j_i = l_i$, which are characterised by the fact that the phase is stationary. The factor $(m!)^2$ takes into account the possible orderings of the indexes. Other terms will be characterised by an oscillating phase and thus are expected to be inessential in the thermodynamic limit. The denominator is then approximated by the following expression:

$$\begin{aligned}\|(J_k^+)^m\,|n-1,\pi\rangle\|^2) &\approx \frac{(m!)^2}{2^{2m}} \sum_{j_1<\ldots<j_m}\ \sum_{l_1<\ldots<l_m} \delta_{j_1,l_1}\ldots\delta_{j_m,l_m}\, 2^{2m}\, \frac{\binom{L-m}{n-1}}{\binom{L}{n-1}} = \\ &= (m!)^2 \binom{L}{m} \frac{\binom{L-m}{n-1}}{\binom{L}{n-1}} = m!\,\frac{(L-n+1)!}{(L-n-m+1)!}.\end{aligned} \tag{S24}$$

We now move to the numerator of Eq. (S22); for its evaluation, the following relation is useful:

$$[[H_1 + H_3, J_k^+], J_k^+] = 0. \tag{S25}$$

Let us prove Eq. (S25) using the explicit expression of the commutator in Eq. (S16); we will only focus on the term $H_1$ of the Hamiltonian since the extension to $H_3$ is straightforward:

$$[[H_1, J_k^+], J_k^+] = -\frac{J}{2} \sum_j e^{ikj} \left[ \{S_j^+, S_j^z\} S_{j+1}^+ + e^{ik} S_j^+ \{S_{j+1}^+, S_{j+1}^z\}, \frac{1}{2} e^{ikj} (S_j^+)^2 + \frac{1}{2} e^{ik(j+1)} (S_{j+1}^+)^2 \right] \tag{S26}$$

The commutator can be easily split into the sum of four commutators; let us begin by analysing the first:

$$\left[\{S_j^+, S_j^z\} S_{j+1}^+, (S_j^+)^2\right] = \left[(S_j^+ S_j^z + S_j^z S_j^+), (S_j^+)^2\right] S_{j+1}^+ = \left(S_j^+ \left[S_j^z, (S_j^+)^2\right] + \left[S_j^z, (S_j^+)^2\right] S_j^+\right) S_{j+1}^+. \tag{S27}$$

The commutator that appears in the last expression can be explicitly computed: $\left[S_j^z, (S_j^+)^2\right] = 2(S_j^+)^2$. We thus obtain an expression proportional to $(S_j^+)^3$, that for a spin-1 system is equal to zero. The thesis follows by applying similar calculations to the other three commutators.

With the help of Eq. (S25), it is possible to show by induction that:

$$H(J_k^+)^m \left|n-1,\pi\right\rangle = m(J_k^+)^{m-1}[H,J_k^+]\left|n-1,\pi\right\rangle, \quad 1 \le m \le L-n+1. \tag{S28}$$

Hence we obtain that:

$$\|H(J_k^+)^m \left|n-1,\pi\right\rangle\|^2 = \|m(J_k^+)^{m-1}[H,J_k^+]\left|n-1,\pi\right\rangle\|^2 = m^2 \left\langle n-1,\pi\right| [H,J_k^+]^\dagger (J_k^-)^{m-1}(J_k^+)^{m-1}[H,J_k^+]\left|n-1,\pi\right\rangle \tag{S29}$$

Using Eq. (S16) we obtain:

$$\begin{aligned}\|H(J_k^+)^m \left|n-1,\pi\right\rangle\|^2 = & \frac{m^2[(m-1)!]^2}{2^{2m-2}}\left(\frac{J}{2}\right)^2 \sum_{j_1<\ldots<j_{m-1}}\sum_{l_1<\ldots<l_{m-1}}\sum_{r,s} e^{-ikr}(1+e^{-ik})e^{iks}(1+e^{ik})\times \\ & \times e^{ik(l_1+\ldots+l_{m-1}-j_1-\ldots-j_{m-1})}\times \\ & \times \left\langle n-1,\pi\right| S_r^- S_{r+1}^- (S_{j_1}^-)^2\ldots(S_{j_{m-1}}^-)^2 (S_{l_1}^+)^2\ldots(S_{l_{m-1}}^+)^2 S_s^+ S_{s+1}^+ \left|n-1,\pi\right\rangle.\end{aligned} \tag{S30}$$

The evaluation of this expression can be performed using an approximation similar to that employed for the denominator: only the terms whose phase does not oscillate are retained, and namely those for which $j_i = l_i$ and $r = s$. The term inside the sum can then be evaluated analytically thanks to the special nature of exact quantum many-body scars: it reads

$$2(1+\cos k)\delta_{r,s}\left[\prod_{t=1}^{m-1}\delta_{j_t,l_t}(1-\delta_{j_t,r})\right]2^{2m}\frac{\binom{L-m-1}{n-1}}{\binom{L}{n-1}}. \tag{S31}$$

We can use the identities:

$$\sum_r \sum_{j_1<\ldots<j_{m-1}}\prod_{t=1}^{m-1}(1-\delta_{j_t,r}) = L\binom{L-1}{m-1}, \qquad L(m-1)!\frac{\binom{L-m-1}{n-1}\binom{L-1}{m-1}}{\binom{L}{n-1}} = \frac{(L-n+1)!}{(L-m-n)!(L-m)} \tag{S32}$$

and finally express:

$$\|H(J_k^+)^m \left|n-1,\pi\right\rangle\|^2 = 2J^2m^2(m-1)!(1+\cos k)\frac{(L-n+1)!}{(L-m-n)!(L-m)}. \tag{S33}$$

At this stage, we can compute the ratio of the numerator and of the denominator:

$$\begin{aligned}\Delta H_1^2 \approx & \frac{2J^2m^2(1+\cos k)}{L-m}\,\frac{(m-1)!(L-n+1)!}{(L-m-n)!}\,\frac{(L-m-n+1)!}{m!(L-n+1)!} = \\ = & m4J^2\frac{L-m-n+1}{L-m}\cos^2\left(\frac{k}{2}\right) \xrightarrow[m+n\ll L]{L\to+\infty} m\times 4J^2\cos^2\left(\frac{k}{2}\right)\end{aligned} \tag{S34}$$

We thus obtain that a state obtained by applying $m$ times the $J_k^+$ operator on an exact quantum many-body scars has an energy variance scaling linearly in $m$. Thus, as long as $m$ does not scale with the system size $L$, the state remains and asymptotic quantum many-body scar.

### E. Norm and variance of the localized bimagnon state

In order to highlight the properties of the asymptotic QMBS states, we study here the properties of the localised bimagnon state:

$$\left|\psi_j\right\rangle = \frac{1}{\sqrt{4\frac{L-n+1}{L}}}(S_j^+)^2\left|n-1,\pi\right\rangle = \frac{1}{\sqrt{L(L-n+1)}}\sum_k e^{-ikj}J_k^+\left|n-1,\pi\right\rangle = \sum_k e^{-ikj}\left|\psi_k\right\rangle \qquad \text{for } 1\le n\le L. \tag{S35}$$

The localised bimagnon state is thus a linear superposition of the states $\left|n,k\right\rangle$, since expression in Eq. (S9) allows us to write:

$$\left|\psi_k\right\rangle = \frac{1}{\sqrt{L(L-n+1)}}J_k^+\left|n-1,\pi\right\rangle = \sqrt{\frac{\mathcal{M}_{n,k}}{L(L-n+1)}}\left|n,k\right\rangle. \tag{S36}$$

Note that the scaling of the prefactor is $L^{-1/2}$. This localised bimagnon state has average energy 0 and thus its energy variance reads:

$$\begin{aligned} \langle\psi_j|\left(H_1^2+H_3^2\right)|\psi_j\rangle &= \sum_k \langle\psi_k|\left(H_1^2+H_3^2\right)|\psi_k\rangle = \sum_k \frac{\mathcal{M}_{n,k}}{L(L-n+1)} \langle n,k|\left(H_1^2+H_3^2\right)|n,k\rangle\,, \\ &= \frac{4(J^2+J_3^2)(L-n)}{L(L-1)} \sum_k \cos^2\left(\frac{k}{2}\right) = \frac{2(J^2+J_3^2)(L-n)}{(L-1)}, \end{aligned} \tag{S37}$$

where we have used PBC and hence $\langle n,k'|\,H_1\,|n,k\rangle = 0$ for $k \neq k'$; and also that $\langle n,k|\,H_1 H_3\,|n,k\rangle = 0$, and that $|\psi_j\rangle$ is an eigenstate of all the other terms of the Hamiltonian. It is clear that this energy variance is finite in the thermodynamic limit for any $\frac{n}{L} < 1$. As a consequence, the fidelity relaxation time of this state is finite in the thermodynamic limit and the state cannot be considered as an asymptotic QMBS.

## S3. ENTANGLEMENT ENTROPY OF THE EXACT AND ASYMPTOTIC QMBS

In this section we review the calculation of the entanglement entropy for the states $|n,k\rangle$, which proceeds along the lines of calculations performed in [1, 2].

We first divide the lattice into two parts, $A$ and $B$. Typically, one considers $A$ as the set of lattice sites with $j \leq L/2$ and $B$ the rest, but this is not necessary. The key observation is that it is always possible to split the $J_k^+$ operators as a sum of an operator acting on $A$ and of an operator acting on $B$:

$$J_k^+ = J_{k,A}^+ + J_{k,B}^+ = \frac{1}{2}\sum_{j\in A} e^{ikj}\left(S_j^+\right)^2 + \frac{1}{2}\sum_{j\in B} e^{ikj}\left(S_j^+\right)^2. \tag{S38}$$

The state $|\Downarrow\rangle$ is a product state: $|\Downarrow\rangle_A \otimes |\Downarrow\rangle_B$. Hence, for $|n,\pi\rangle$, we obtain [1, 2]

$$|n,\pi\rangle = \frac{1}{\sqrt{N_{n,\pi}}}\left(J_{\pi,A}^+ + J_{\pi,B}^+\right)^n |\Downarrow\rangle_A \otimes |\Downarrow\rangle_B = \frac{1}{\sqrt{N_{n,\pi}}}\sum_{m=0}^{n}\binom{n}{m}\left(J_{\pi,A}^+\right)^m |\Downarrow\rangle_A \otimes \left(J_{\pi,B}^+\right)^{n-m}|\Downarrow\rangle_B\,, \tag{S39}$$

where $N_{n,\pi}$ is the normalization factor for the state $|n,\pi\rangle$, given by $\binom{L}{n}$. Additional care must be used in truncating the sum in the proper way: if $A$ is composed of $L_A$ lattice sites, it is not possible to apply the $J_{k,A}^+$ operator more than $L_A$ times; similarly for $L_B$. Hence for simplicity, here we assume that $n < L_A, L_B$. Therefore, the expansion in Eq. (S39) gives the Schmidt decomposition of the state, which is composed of the $n+1$ orthogonal states $\{J_{k,\ell}^m |\Downarrow\rangle\}_{m=0}^n$ for the $\ell \in \{A,B\}$ part. In the presence of $n+1$ orthogonal states, the highest entropy state is the maximally mixed one, where they all have the same Schmidt coefficients; in that case $S_A = \log(n+1)$. If we consider a lattice of length $L$ and the bipartition with $L_A = L_B = L/2$, the states with an extensive number of bimagnons are those such that $n = \alpha L$, with $0 < \alpha < 1$, and thus these states satisfy the following $S_A \sim \log L + \log\alpha$. As it is well-known, the quantum many-body scars have an entropy scaling with the logarithm of the volume.

Let us now consider the asymptotic QMBS states, $|n,k\rangle$. In this case, we use Eq. (S9) to obtain

$$\begin{aligned} |n,k\rangle = \frac{1}{\sqrt{\mathcal{M}_{n,k}}} J_k^+ |n-1,\pi\rangle =& \frac{1}{\sqrt{\mathcal{M}_{n,k}N_{n-1,\pi}}}\sum_{m=0}^{n-1}\binom{n-1}{m} J_{k,A}^+ (J_{\pi,A}^+)^m |\Downarrow\rangle_A \otimes (J_{\pi,B}^+)^{n-1-m}|\Downarrow\rangle_B \\ &+ \frac{1}{\sqrt{\mathcal{M}_{n,k}N_{n-1,\pi}}}\sum_{m=0}^{n-1}\binom{n-1}{m}(J_{\pi,A}^+)^m|\Downarrow\rangle_A \otimes J_{k,B}^+(J_{\pi,B}^+)^{n-1-m}|\Downarrow\rangle_B\,. \end{aligned} \tag{S40}$$

Note that unlike for the $|n,\pi\rangle$, Eq. (S40) is in general is not the Schmidt decomposition of the state. Yet, if we consider one subsystem, say A, the Schmidt states of a fixed magnetisation $-L_A + 2m$ are in the two-dimensional subspace spanned by the following linearly independent states:

$$\left(J_{\pi,A}^+\right)^m |\Downarrow\rangle_A\,, \qquad J_{k,A}^+\left(J_{\pi,A}^+\right)^{m-1}|\Downarrow\rangle_A\,. \tag{S41}$$

Hence we can conclude that the total number of Schmidt states is at most $2n$, and for an extensive number of bimagnons $n = \alpha L$, we obtain that in the highest entropy situation $S_A \sim \log 2 + \log\alpha + \log L$. Thus, with respect to the exact QMBS $|n-1,\pi\rangle$, the asymptotic QMBS $|n,k\rangle$ has at most an additive correction of $\log 2$.

## S4. VARIANCE OF THE EXACT QMBS FOR THE PERTURBED HAMILTONIAN

We consider the perturbed Hamiltonian $H' = H + V$, where $H$ is the Hamiltonian (S11) with exact scars at finite size with PBC and $V = \frac{J_z}{L}\sum_j S^z_j S^z_{j+1}$. Since $|n,\pi\rangle$ is an eigenstate of $H$, the variance can be computed focusing only on $V$:

$$\begin{aligned} \Delta H'^2 &= \Delta V^2 = \langle n,\pi|\, V^2 \,|n,\pi\rangle - \langle n,\pi|\, V\,|n,\pi\rangle^2 \\ &= \frac{J_z^2}{L^2}\sum_{j,j'=1}^{L} \left(\langle n,\pi|\, S^z_j S^z_{j+1} S^z_{j'} S^z_{j'+1}\,|n,\pi\rangle - \langle n,\pi|\, S^z_j S^z_{j+1}\,|n,\pi\rangle \langle n,\pi|\, S^z_{j'} S^z_{j'+1}\,|n,\pi\rangle\right). \end{aligned} \tag{S42}$$

We can then use the structure of $|n,\pi\rangle$ to compute various correlation functions that appear in Eq. (S42). We first compute the two point correlation function to be

$$\langle n,\pi|\, S^z_j S^z_{j+1}\,|n,\pi\rangle = \frac{\binom{L-2}{n-2} + \binom{L-2}{n} - 2\binom{L-2}{n-1}}{\binom{L}{n}} \equiv F_2, \tag{S43}$$

where we have used the action of $S^z_j S^z_{j+1}$ on the product basis states that compose $|n,\pi\rangle$, i.e., Eq. (S8), and noting that it takes the value of $+1$ if there are zero or two bimagnons on sites $j$ and $j+1$, and $-1$ if there is one bimagnon. Using similar ideas, we obtain that when $j' \neq j-1, j, j+1$, the four point correlation function reads

$$\langle n,\pi|\, S^z_j S^z_{j+1} S^z_{j'} S^z_{j'+1}\,|n,\pi\rangle = \frac{\binom{L-4}{n} - 4\binom{L-4}{n-1} + 6\binom{L-4}{n-2} - 4\binom{L-4}{n-3} + \binom{L-4}{n-4}}{\binom{L}{n}} \equiv F_4 \tag{S44}$$

Note that $F_2$ and $F_4$ in Eqs. (S43) and (S44) are numbers that only depend on $L$ and $n$, and are independent of $j$; and we have assumed that $n \geq 4$ and PBC. When $j' = j-1, j, j+1$, we obtain the following expressions for the "four point" correlation functions

$$\langle n,\pi|\, S^z_{j-1}\left(S^z_j\right)^2 S^z_{j+1}\,|n,\pi\rangle = \langle n,\pi|\, S^z_j \left(S^z_{j+1}\right)^2 S^z_{j+2}\,|n,\pi\rangle = \langle n,\pi|\, S^z_j S^z_{j+1}\,|n,\pi\rangle = F_2, \quad \langle n,\pi|\left(S^z_j\right)^2\left(S^z_{j+1}\right)^2|n,\pi\rangle = 1. \tag{S45}$$

Combining Eqs. (S42)-(S45), and using translation invariance, we obtain that

$$\Delta H'^2 = \frac{J_z^2}{L^2}\left[\sum_j \sum_{j'\neq j-1,j,j+1} (F_4 - F_2^2) + \sum_j (1 - F_2^2) + 2\sum_j (F_2 - F_2^2)\right] = J_z^2\left[F_4\left(1 - \frac{3}{L}\right) - F_2^2 + \frac{2}{L}F_2 + \frac{1}{L}\right] \tag{S46}$$

Using Eq. (S46), we find that when $n/L = \nu$, where $\nu$ is a constant, $\Delta H'^2$ asymptotically scales as $\sim \frac{16\nu^2(1-\nu)^2}{L}$. On the other hand, when $n$ is kept finite, $\Delta H'^2$ asymptotically scales as $\sim \frac{16n(n-1)}{L^3}$.

## S5. DYNAMICS OF INITIAL STATES THAT ARE NOT ASYMPTOTIC QMBS

In this section, we study the dynamics of certain initial states, that are not asymptotic QMBS, under the Hamiltonian $H$ in Eq. (1) of the main text. We present this study in order to further support our claim that the dynamics of $|n, k = \pi - 2\pi/L\rangle$ is special.

### A. Initial state with finite energy variance

First, we consider the states $|n, k = 0\rangle$, which are in the family of states in Eq. (4) of the main text, but are not asymptotic QMBS since they have a finite energy variance in the thermodynamic limit, as evident from Eq. (5) of the main text. Note that a state with finite energy variance was already discussed in Ref. [3], reaching similar conclusions. In Fig. S2 we study the dynamics of $|n, k = 0\rangle$ by presenting similar numerical results for the time-evolution of the latter state. The dynamics of the observable $S^{z2}(t)$ is "activated" on a short time-scale of order $J^{-1}$ that does not depend on $L$ (see the first panel of Fig. S2). The dynamics reaches a "pre-thermal" plateau [4] that increases to the initial value for $L \to \infty$. Note that this result does not contradict the fact that at finite size and in the long-time

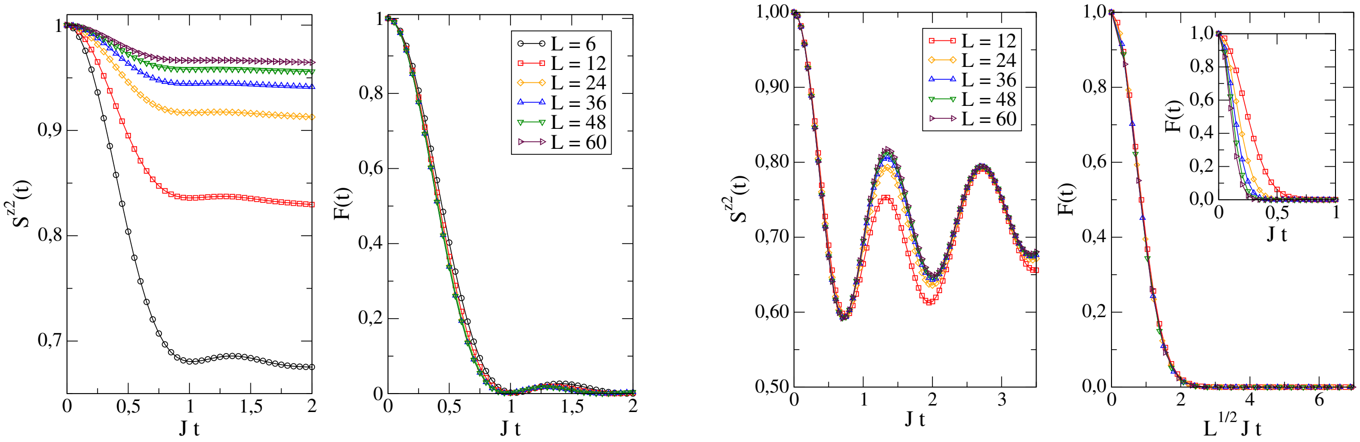

FIG. S2. First and second panel: The properties of the state $e^{-iHt}|n,k\rangle$ for $n = L/2$ and $k = 0$ as a function of time. First panel: time evolution of the squared magnetization $S^{z2}(t)$. Second panel: time evolution of the fidelity with the initial state $F(t)$. Third and fourth panel: The properties of the state $e^{-iHt}|+-+-+-\dots\rangle$ as a function of time. Third panel: time evolution of the squared magnetization. Fourth panel: time evolution of the fidelity with the initial state $F(t)$; in the inset we show the bare data, whereas in the main plot we rescale time by a factor $\sqrt{L}$ to display a clear collapse.

limit, observables should relax to their thermal value predicted by the diagonal ensemble. However, the thermalization timescale is much longer than the typical times that we can probe numerically using MPS-based methods. We have performed long-time simulations using exact diagonalization on small system sizes, and verified that this is indeed the case. Although the apparently long thermalization time may lead one to consider these states as asymptotic QMBS, the study of the fidelity with the initial state $F(t)$ is qualitatively very different. This is shown in the second panel of Fig. S2: on the same time-scale $J^{-1}$ the state becomes essentially orthogonal to the initial one, and the data for different sizes are basically indistinguishable. The data on the fidelity relaxation time can be understood as a consequence of the finite energy-variance of the state $|n = L/2, k = 0\rangle$.

### B. Initial Product State

It is also interesting to contrast the dynamics of the asymptotic QMBS with that of an uncorrelated product state; we consider here the staggered state $|\dots+-+-+-\dots\rangle$ which has the same zero magnetisation as the states considered in the main text and the same average squared magnetisation as the asymptotic QMBS, equal to one. The data on the dynamics of $S^{z2}(t)$ collapse on the same curve for all $L$ considered (third panel of Fig. S2); the fidelity relaxation time instead becomes shorter with increasing $L$ (fourth panel of Fig. S2). The behaviour is consistent with expectations for the time evolution of generic product states [5, 6], and is radically different from that of the asymptotic QMBS.

## S6. SPECTRAL PROPERTIES OF THE HAMILTONIAN $H'$

In this section, we analyze the spectrum of the Hamiltonian $H' = H + V$ discussed in the main text where $H$ is the spin-1 XY Hamiltonian exhibiting exact QMBS and the perturbation reads:

$$V = \frac{J_z}{L}\sum_j S^z_j S^z_{j+1}. \tag{S47}$$

Our goal is to better clarify the disappearance of the exact QMBS that is present for $J_z = 0$ and that is absent for $J_z = 1$. In Fig. S3 we discuss the spectral properties of the model for several values of $J_z$ ranging from 0 to 1 for a spin chain of length $L = 10$. The plots show the bipartite entanglement entropy of all eigenstates and the expectation value of $S^{z2} = \sum_j (S^z)^2$. At these system sizes, we observe the presence of a clear outlying state for $J_z \lesssim 0.2$ in both the entanglement entropy and the observable. For $J_z \lesssim 0.6$ we can observe a state that is an outlier in what concerns the expectation value of $S^{z2}$, but that has an elevated entanglement entropy, comparable to that of other eigenstates

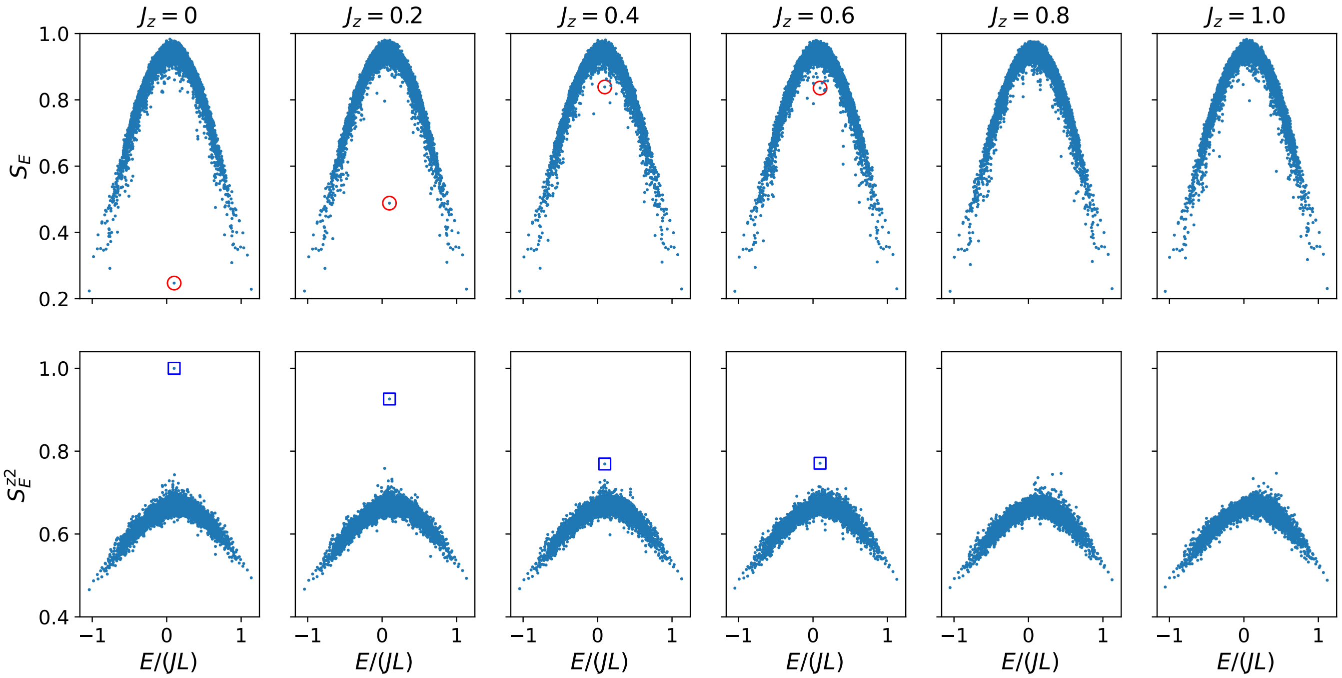

FIG. S3. Spectral properties of the Hamiltonian $H' = H + V$ in the zero magnetization sector $S_z = 0$ for several values of $J_z$, ranging for $J_z = 0$ to $J_z = 1$; results are obtained by performing exact diagonalization on a spin chain of length $L = 10$. The parameters of the simulation are $\{J, h, D, J_3\} = \{1, 0, 0.1, 0.1\}$ and $J_z$ is varied. In the first line we plot the bipartite entanglement entropy $S_E$ of the eigenstates as a function of their energy $E$; in the second line we focus instead on the expectation value $S_E^{z2}$ of the observable $S^{z2} = \sum_j (S_j^z)^2$ on the eigenstate with energy $E$. The plots highlight the behaviour of the exact scar of the model at $J_z = 0$ and that disappears as $J_z$ increases.

with the same energy. For larger values of $J_z$ it is difficult to identify a unique outlier QMBS, although the spectrum maintains a few states that are not collapsed on the main curve. It is important to stress that these simulations have been performed at finite size and that a proper scaling towards the thermodynamic limit could make disappear the outliers that we have shown for $J_z \neq 0$. We also considered the case of negative values of $J_z$ and obtained results very similar to those in Fig. S3, which are not reported here for brevity.

## S7. UNIVERSAL RESCALING OF FIDELITIES

In this section, we present the data collapse of the fidelities for the asymptotic QMBS for various system sizes presented in the main text. Such a data collapse occurs at short times, once the time is rescaled by a factor that depends on the size of the system, as shown in Fig. S4. In the left panel, we present data for the asymptotic QMBS $|n, k = \pi - 2\pi/L\rangle$ time-evolved with the spin-1 XY Hamiltonian $H$ of Eq. (1) of the main text, which includes the term proportional to $J_3$, and the collapse is obtained by rescaling the time as $\tau = t/L$. In the right panel, we present data for the state $|n, \pi\rangle$ time-evolved with the Hamiltonian $H' = H + V$; the collapse is obtained by rescaling the time as $\tau = t/L^{1/2}$.

It is interesting to link these results to the energy-time uncertainty relation in Eq. (6) of the main text, whose proof is presented in many quantum mechanics textbooks and will not be reviewed here. The overlap of the time-evolved state with the initial one is related to the expectation value of the Hamiltonian and of its powers as [6]

$$\langle\Psi| e^{-iHt} |\Psi\rangle \approx 1 - it \langle\Psi| H |\Psi\rangle - \frac{1}{2}t^2 \langle\Psi| H^2 |\Psi\rangle + \frac{i}{6}t^3 \langle\Psi| H^3 |\Psi\rangle + \dots \tag{S48}$$

and thus we can express the fidelity as

$$F(t) = |\langle\Psi| e^{-iHt} |\Psi\rangle|^2 \approx 1 - t^2 \left(\langle\Psi| H^2 |\Psi\rangle - \langle\Psi| H |\Psi\rangle^2\right) + \dots \tag{S49}$$

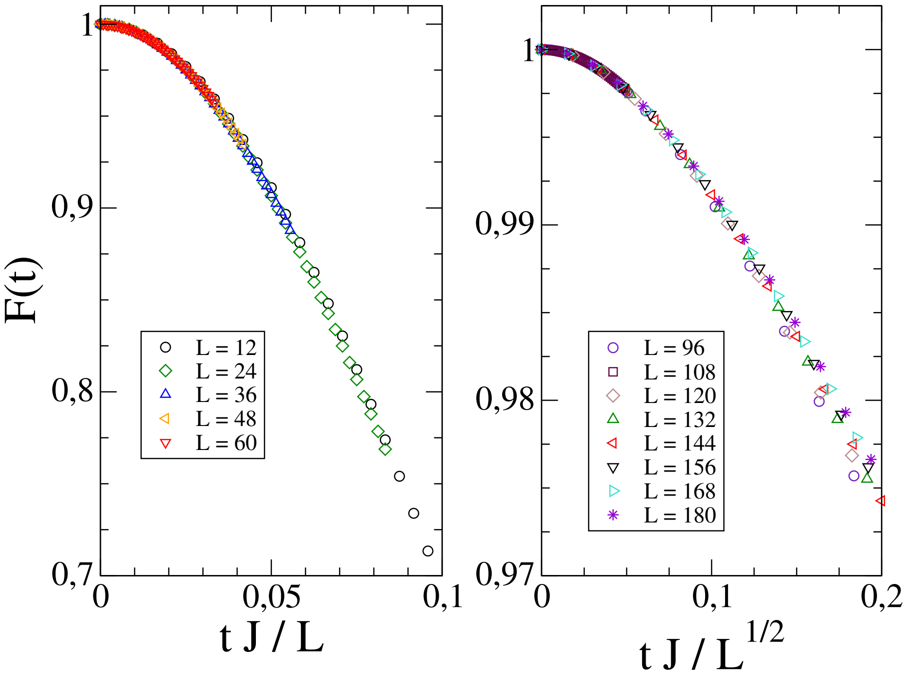

FIG. S4. Rescaling of the fidelities $F(t)$ plotted in Fig. 2 and Fig. 4 of the main text.

The short-time fidelity dynamics is thus completely dictated by the energy-variance of the initial state with respect to the Hamiltonian of the dynamics.

Note that the precise scaling of the relaxation time depends on the definition. The fidelity of an initial state at short times decays as $F(t) \sim \exp\left(-\Delta H^2 t^2\right)$ [6], where $\Delta H^2$ is the variance, this gives a timescale $\tau \sim 1/\Delta H$. On the other hand, one can define the fidelity relaxation time as the timescale at which fidelity decays to the the typical fidelity between two many body states, which scales as $\exp(-L)$ [6], this adds an extra factor of $\sqrt{L}$. In this work, we use the former definition, and are mostly interesting in the relative decay timescales between initial states of different variances.

It is interesting to study a state with a Gaussian energy spread, for which the calculation of the time-dynamics of the fidelity is exactly possible. In fact here it is possible to show that it minimizes the inequality and has a fidelity $F(t)$ whose dynamics happens on the shortest possible timescale. Consider indeed an initial state that is a Gaussian linear superposition of energy eigenstates with average energy $E_0$ and energy variance $\sigma^2$ (we introduce also a normalisation prefactor $\alpha \in \mathbb{C}$): Assuming that the density of states in the energy window $[E_0 - \sigma, E_0 + \sigma]$ is approximately constant and takes the value $\rho(E_0)$, the scalar product between the time-evolved state and the initial one is given by:

$$\langle \Psi_0 | \, e^{-iHt} \, |\Psi_0\rangle \approx \int |\alpha|^2 e^{-\frac{(E-E_0)^2}{2\sigma^2}} e^{-iEt} \rho(E) dE = |\alpha|^2 \sqrt{2\pi\sigma^2} e^{-iE_0 t} e^{-\frac{\sigma^2 t^2}{2}} \rho(E_0). \tag{S50}$$

The normalisation of the state, computed for $t = 0$, requires that $|\alpha|^2 \sqrt{2\pi\sigma^2} \rho(E_0) = 1$. The fidelity $F(t)$ is the squared modulus of this scalar product and hence $F(t) = \exp\left[-\sigma^2 t^2\right]$; we can define the typical time scale of the fidelity dynamics as $\tau = 1/(2\sigma)$, and the energy-time inequality is satisfied and minimised.

In general terms, we thus expect that the dynamics of the fidelity at short times takes place on time-scales that are the shortest possible and minimize the energy-time inequality. This short-time behaviour is indeed verified by the numerics plotted in Fig. S4. In the left panel we have $\tau \sim L$ and $\sigma \sim 1/L$; in the right panel we have $\tau \sim \sqrt{L}$ and $\sigma \sim 1/\sqrt{L}$. Note that this timescale also matches the rigorous lower bounds on relaxation times for weak perturbations of models with exact QMBS [3] by setting the perturbation strength $\lambda = 1/L$, although we note the latter is the observable relaxation time, which we generically expect to be different from the fidelity relaxation time we discuss. However, it is important to keep in mind that the numerics has been performed only at short times and that long-time behaviours would need further investigation.

## S8. HIGHER DIMENSIONAL GENERALISATIONS OF ASYMPTOTIC QMBS

Finally, we show that the existence of the asymptotic QMBS is not limited to one-dimensional systems, but can be easily generalised to higher-dimensional lattices. As an example, we consider a simple cubic Bravais lattice in $d > 1$ dimensions with primitive vectors $\mathbf{t}_i$ and $i = 1, \dots d$; the vectors are adimensional and orthonormal: $\mathbf{t}_i \cdot \mathbf{t}_j = \delta_{ij}$. The lattice has linear dimension $L$ and is composed of $L^d$ sites; periodic boundary conditions (PBC) are applied. On each site of the lattice there is a spin-1 degree of freedom and we define the spin-1 operators $S^{\alpha}_{\mathbf{r}}$, with $\alpha = x, y, z$. We then consider a nearest-neighbor XY model with external magnetic field:

$$H = J \sum_{\mathbf{r}} \sum_{i=1}^{d} \left( S^x_{\mathbf{r}} S^x_{\mathbf{r}+\mathbf{t}_i} + S^y_{\mathbf{r}} S^y_{\mathbf{r}+\mathbf{t}_i} \right) + h \sum_{\mathbf{r}} S^z_{\mathbf{r}}. \tag{S51}$$

As discussed in [2, 7], this model in Eq. (S51) exhibits exact QMBS for any finite value of $L$ and for any dimension $d$. Note that when $d > 1$, the model of Eq. (S51) is non-integrable, and unlike in the one-dimensional case in Eq. (1) of the main text, we need not add the anisotropy term proportional to $D$ or the longer range term proportional to $J_3$ to break integrability or unusual symmetries. Starting from the fully-polarised state $|\Downarrow\rangle$, we define the quasiparticle creation operator $J^+_{\mathbf{k}} = \frac{1}{2} \sum_{\mathbf{r}} e^{i\mathbf{k}\cdot\mathbf{r}} \left(S^+_{\mathbf{r}}\right)^2$.

The exact QMBS states then read $|n, \boldsymbol{\pi}\rangle = \frac{1}{\sqrt{N_{n,\boldsymbol{\pi}}}} \left(J^+_{\boldsymbol{\pi}}\right)^n |\Downarrow\rangle$ where $\boldsymbol{\pi}$ is the vector with all $d$ components equal to $\pi$. It is easy to show that $H\,|n, \boldsymbol{\pi}\rangle = h(-L^d + 2n)\,|n, \boldsymbol{\pi}\rangle$, hence the state is an exact QMBS in the middle of the spectrum of the Hamiltonian [2, 7, 8]. The states that we are interested in are:

$$|n, \mathbf{k}\rangle = \frac{1}{\sqrt{N_{n,\mathbf{k}}}} J^+_{\mathbf{k}} (J^+_{\boldsymbol{\pi}})^{n-1} |\Downarrow\rangle\,, \tag{S52}$$

where $\mathbf{k}$ is any vector of the reciprocal space confined to the first Brillouin zone (1BZ). Similar to the one-dimensional case, it is possible to show that as long as the momentum $\mathbf{k}$ is chosen compatible with PBC in all directions, we can show that $\langle n, \mathbf{k} | n', \mathbf{k}'\rangle = \delta_{n,n'}\delta_{\mathbf{k},\mathbf{k}'}$. With these states, we can directly repeat the proof in Sec. S2 *mutatis mutandis.* We find that the average energy is given by $\langle n, \mathbf{k}|\, H\, |n, \mathbf{k}\rangle = h(-L^d + 2n)$, and the energy variance is given by

$$\Delta H^2 = \frac{4J^2 \sum_{i=1}^{d} \cos^2\left(\frac{k_i}{2}\right)}{1 + \frac{(n-1)L^d}{L^d - n}\delta_{\vec{k},\vec{\pi}}} = 4J^2 \sum_{i=1}^{d} \cos^2\left(\frac{k_i}{2}\right). \tag{S53}$$

Thus, if we consider $\mathbf{k}$ with components $k_i = \pi + \frac{2\pi}{L} m_i$ and keep the $m_i \in \mathbb{Z}$ fixed while $L \to \infty$, the variance reduces to zero while being orthogonal to the exact QMBS. For such states, we expect the same phenomenology of asymptotic QMBS discussed for the one-dimensional case.

---

[*] lorenzo.gotta@unige.ch

[†] sanjaym@caltech.edu

[‡] leonardo.mazza@universite-paris-saclay.fr

[1] O. Vafek, N. Regnault, and B. A. Bernevig, SciPost Phys. **3**, 043 (2017).

[2] M. Schecter and T. Iadecola, Phys. Rev. Lett. **123**, 147201 (2019).

[3] C.-J. Lin, A. Chandran, and O. I. Motrunich, Phys. Rev. Res. **2**, 033044 (2020).

[4] T. Mori and N. Shiraishi, Phys. Rev. E **96**, 022153 (2017).

[5] H. Wilming, T. R. de Oliveira, A. J. Short, and J. Eisert, "Equilibration times in closed quantum many-body systems," in *Thermodynamics in the Quantum Regime: Fundamental Aspects and New Directions*, edited by F. Binder, L. A. Correa, C. Gogolin, J. Anders, and G. Adesso (Springer International Publishing, Cham, 2018) pp. 435–455.

[6] L. Campos Venuti and P. Zanardi, Phys. Rev. A **81**, 022113 (2010).

[7] D. K. Mark and O. I. Motrunich, Phys. Rev. B **102**, 075132 (2020).

[8] J. Wildeboer, C. M. Langlett, Z.-C. Yang, A. V. Gorshkov, T. Iadecola, and S. Xu, Phys. Rev. B **106**, 205142 (2022).

arXiv:2001.01492v1 [cond-mat.stat-mech] 6 Jan 2020

# Universal survival probability for a $d$-dimensional run-and-tumble particle

Francesco Mori,[1] Pierre Le Doussal,[2] Satya N. Majumdar,[1] and Grégory Schehr[1]
[1] *LPTMS, CNRS, Univ. Paris-Sud, Université Paris-Saclay, 91405 Orsay, France*
[2] *Laboratoire de Physique de l'Ecole Normale Supérieure, PSL University, CNRS, Sorbonne Universités, 24 rue Lhomond, 75231 Paris, France*

(Dated: January 7, 2020)

We consider an active run-and-tumble particle (RTP) in $d$ dimensions and compute exactly the probability $S(t)$ that the $x$-component of the position of the RTP does not change sign up to time $t$. When the tumblings occur at a constant rate, we show that $S(t)$ is independent of $d$ for any finite time $t$ (and not just for large $t$), as a consequence of the celebrated Sparre Andersen theorem for discrete-time random walks in one dimension. Moreover, we show that this universal result holds for a much wider class of RTP models in which the speed $v$ of the particle after each tumbling is random, drawn from an arbitrary probability distribution. We further demonstrate, as a consequence, the universality of the record statistics in the RTP problem.

The first time $t_{\rm f}$ at which a stochastic process reaches a fixed target level is a fundamental observable with many applications. Statistics of $t_{\rm f}$ plays a crucial role in various situations, including e.g., the encounter of two molecules in a chemical reaction [1], the capture of a prey in a hunting scenario [2], or the escape of a comet from the solar system [3, 4]. In the context of finance, agents often use limit orders to buy/sell a stock only when its price is below/above a target value. Thus, it is important to estimate if and when that target value will be reached and this question has been intensively studied during decades (for recent reviews see [2, 5–9]). Due to the ubiquity of these problems, novel applications are constantly being identified, raising in turn new challenging questions.

In recent years, tremendous efforts have been devoted to the study of statistical fluctuations in active matter systems [10–13]. In contrast to a passive matter such as a Brownian motion (BM), whose dynamics is driven by thermal fluctuations of the environment, this class of active non-equilibrium systems is characterized by self-propelled motility based on continuous consumption of energy from the environment. For example, models of active matter have been used to describe vibrating granular matter [14], active gels [15, 16], bacteria [17, 18] or collective motion of "animals" [15, 19–21]. In this context, one of the most studied model is the run-and-tumble particle (RTP) [22, 23], also known as "persistent random walk" [24, 25]. In the simplest version of the model, an RTP performs a ballistic motion along a certain direction at a constant speed $v_0 \geq 0$ ("run") during a certain "time of flight" $\tau$. Following this run, it "tumbles", i.e., chooses a new direction uniformly at random and then performs a new run along this direction again with speed $v_0$ during a random time $\tau$ and so on (see Fig. 1). Typically these tumblings occur with constant rate $\gamma$, i.e. the $\tau$'s of different runs are independently distributed via exponential distribution $p(\tau) = \gamma e^{-\gamma\tau}$, though other distributions will also be considered later. Despite its simplicity, this RTP model exhibits complex interesting features such as clustering at boundaries [11], non-Boltzmann distribution in the steady state in the presence of a confining potential [22, 26–29], motility-induced phase separation [23], jamming [30] etc. Variants of the RTP model where the speed $v \geq 0$ of the particle is renewed after each tumbling by drawing it from a probability density function (PDF) $W(v)$ [31, 32] or where the RTP undergoes random resetting to its initial position at a constant rate [34, 35] have also been studied.

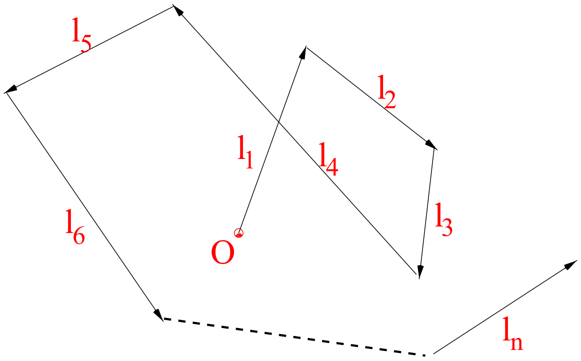

FIG. 1: Typical trajectory of a RTP in two dimensions. The particle starts at the origin $O$, chooses a random direction and moves ballistically in that direction for a distance $l_1 = v_0\,\tau_1$ , where $v_0$ is constant and $\tau_1$ is a random time drawn from the exponential distribution $p(\tau) = \gamma\, e^{-\gamma\tau}$. At the end of this first flight, the particle tumbles instantaneously and chooses a new random direction and again moves ballistically a distance $l_2 = v_0\tau_2$ with $\tau_2$ drawn independently from the same $p(\tau)$. Then the particle tumbles again and so on.

In the $d = 1$ case, the first-passage properties of the RTP model and of its variants have been widely studied [24, 36–39]. Several recent studies investigated the survival probability of an RTP in $d = 1$, both in the absence and in the presence of a confining potential/wall [27, 37–40]. The $d = 1$ case is analytically tractable because the velocity has only two possible directions $\pm v_0$, which simplifies the problem in $d = 1$. However, in $d > 1$, the first-passage problems become much more difficult

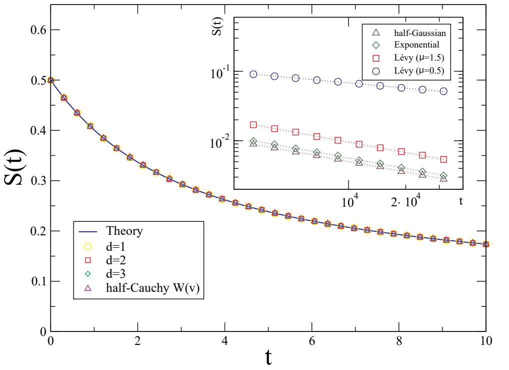

FIG. 2: Survival probability $S(t)$ as a function of time $t$, for $\gamma = 1$. The continuous blue line corresponds to the exact result in Eq. (1). The symbols correspond to simulations with the choices $d = 1, 2, 3$, $W(v) = \delta(v - 1)$ and $p(\tau) = e^{-\tau}$ and one case where $d = 2$, $W(v) = 2/(\pi(1 + v^2))$ with $v > 0$ (half-Cauchy) and $p(\tau) = e^{-\tau}$. They all fall on the analytical blue line for all $t$. **Inset:** Numerical computation of $S(t)$ in $d = 2$ for different distributions $p(\tau)$: (i) half-Gaussian, (ii) exponential, (iii) asymmetric Lévy distribution with Lévy index $\mu = 3/2$ and (iv) asymmetric Lévy with $\mu = 1/2$. In all these cases, $S(t) \sim t^{-\theta}$ for large $t$ with $\theta = \frac{1}{2}$ in cases (i)-(iii) and $\theta = \mu/2 = 1/4$ for case (iv) corresponding to $\mu = 1/2$.

because the orientation of the velocity is a continuous variable. Consequently, exact results are difficult to obtain in $d \geq 2$, though approximation schemes have been developed recently for the mean first-passage time in a confined geometry [41].

In this Letter we consider an RTP in $d$-dimensions, starting from the origin with a random velocity, and compute exactly the probability $S(t)$ that the $x$-component of the RTP does not change sign up to time $t$. It is useful to view $S(t)$ as the "survival probability" of the RTP in the presence of an absorbing hyperplane passing through the origin and perpendicular to the $x$-axis. For a passive particle executing Brownian motion (BM), it is clear that $S(t)$ is independent of $d$, since each component of the displacement performs an independent one-dimensional BM [42]. In contrast, for an RTP in $d$ dimensions, the different spatial components are coupled (see Fig. 1) and, consequently one may expect that $S(t)$ would depend on the dimension $d$ and the speed $v_0$. Performing first simulations in $d = 1, 2, 3$ (see Fig. 2) we found, rather amazingly, that $S(t)$ is completely independent of both $d$ and $v_0$, at *any finite time* $t$ (and not just at large times only) !

The principal goal of this Letter is to understand and prove this remarkably universal result valid even at finite $t$. We compute $S(t)$ exactly for all $t$ in arbitrary dimension $d$, and demonstrate that it is indeed independent of the dimension $d$ and speed $v_0$ for any time $t$ and is given by a simple formula

$$S(t) = \frac{1}{2} e^{-\gamma t/2} \left( I_0\left(\gamma t/2\right) + I_1\left(\gamma t/2\right) \right) \ , \tag{1}$$

where $I_0(z)$ and $I_1(z)$ are modified Bessel functions. When $t \to 0$, $S(t)$ goes to the limiting value $1/2$, which is just the probability that the $x$-component of the initial direction is positive. On the other hand, at late times it decays as $S(t) \sim 1/\sqrt{\pi \gamma t}$. By mapping our $d$-dimensional process to an effective $1d$-process we show below that the universality of this result (1) is inherited from the universality of the Sparre Andersen (SA) theorem [43] for the survival probability of a one-dimensional discrete-time random walk. In the special case $d = 1$, as a bonus, we recover here using a completely different method, the result in Eq. (1) obtained in previous works [24, 37, 38] via Fokker-Planck approaches. In Fig. 2, we compare our formula for $S(t)$ in (1) with numerical simulations for $d = 1, 2$ and 3, finding an excellent agreement at all $t$. Furthermore, this universal result (1) also holds for a broader class of RTP models where the speed $v$, and not just the direction, is also renewed afresh after each tumbling, chosen each time independently from the PDF $W(v)$, with $v \in [0, \infty)$. The standard RTP model corresponds to the choice $W(v) = \delta(v - v_0)$ but this also includes fat tailed PDF $W(v)$ such as the half-Cauchy distribution: $W(v) = 2/[\pi\,(1 + v^2)]$ $(v \geq 0)$, as shown in Fig. 2 . Our main result thus states that for the most common RTP model with exponentially distributed time of flights $p(\tau) = \gamma e^{-\gamma \tau}$, the survival probability $S(t)$ at all $t$ is not only independent of the dimension $d$, but also on the velocity distribution $W(v)$ and is given by Eq. (1). We further show that this universal behavior ceases to hold if the distribution of the $\tau$'s is not an exponential. In fact, if $p(\tau)$ has a well defined first moment then one still has $S(t) \propto t^{-1/2}$ at large times but $S(t)$ is not universal for finite time $t$. Finally, for very fat tailed distribution such that the first moment is not defined, e.g. for $p(\tau) \propto \tau^{-1-\mu}$ for large $\tau$ with $\mu < 1$ (in the $1d$ case this corresponds to Lévy walks, see e.g. [44]), then $S(t) \propto t^{-\mu/2}$ as $t \to \infty$ but again the finite $t$ behavior of $S(t)$ is not universal.

Interestingly, the SA theorem was also used recently [36] to compute first-passage statistics in a variant of the one dimensional RTP model. In this "wait-then-jump model" the particle waits a random time during tumbling and then jumps instantaneously to a new position. Combining the SA theorem with additional combinatorial arguments, the authors of Ref. [36] derived nice results for general jump distributions in their 'wait-then-jump' model. Unfortunately, their clever method can not be adapted to compute the survival probability in the standard RTP model considered here, where the trajectory of the particle is continuous in time. In fact our method turns out to be more general: it not only provides an exact solution for the standard RTP problem in $d$-dimensions and its generalization to RTP's with an arbitrary speed distribution $W(v)$, but also recovers the results of Ref. [36] by a simpler non-combinatorial method (see [45] for details).

To sketch the derivation of our main result in Eq. (1), we consider a typical trajectory of an RTP in $d$-dimensions, starting at the origin $O$ at $t = 0$ (see Fig. 1). For simplicity, we start with the case $W(v) = \delta(v - v_0)$. Note that in a fixed time window $t$, the number of tumblings $n$ undergone by the particle is a random variable and varies from trajectory to trajectory. We will count the starting point $O$ as a tumbling, which implies $n \geq 1$. The time $\tau$ between two tumblings is drawn from $p(\tau) = \gamma e^{-\gamma\tau}$ independently after each tumbling and we denote the time interval after the $i^{\mathrm{th}}$ tumbling as $\tau_i$. Note that the duration $\tau_n$ of the last interval travelled by the particle before the final time $t$ is yet to be completed. Hence, the probability of no tumbling during that time interval is $\int_{\tau_n}^{\infty} p(\tau)d\tau = e^{-\gamma\tau_n}$. Thus, the joint distribution of the time intervals $\{\tau_i\} = \{\tau_1, \tau_2, ..., \tau_n\}$ and the number of tumblings $n$, for a fixed duration $t$, is given by

$$P\left(\{\tau_i\}, n|t\right) = \left[\prod_{i=1}^{n-1} \gamma\, e^{-\gamma\,\tau_i}\right] e^{-\gamma\,\tau_n}\,\delta\left(\sum_{i=1}^{n}\tau_i - t\right)\,, \quad (2)$$

where the $\delta$ function enforces the constraint that the total time is $t$. Let $\{l_i\} = \{l_1, l_2, ..., l_n\}$ denote the straight distances travelled by the particle up to time $t$ (see Fig. 1). Clearly $l_i = v_0\tau_i$ and $l_i \geq 0$ for all $i$. Consequently, using Eq. (2), the joint distribution of $\{l_i\}$ and the number of tumblings $n$ is given by

$$P\left(\{l_i\}, n|t\right) = \frac{1}{\gamma}\left[\prod_{i=1}^{n}\frac{\gamma}{v_0}\, e^{-\gamma\, l_i/v_0}\right]\delta\left(t - \sum_{i=1}^{n}\frac{l_i}{v_0}\right). \quad (3)$$

We now want to write the joint distribution of the $x$-components of these random vectors $\{\vec{l_i}\}$ with given norms $\{l_i\}$. To proceed, we consider a random vector $\vec{l}$ in $d$ dimensions whose norm $l = |\vec{l}|$ is fixed and whose direction is uniformly distributed. Let $x$ denote the $x$-component of this random vector $\vec{l}$. The distribution of this $x$-component *given* the fixed norm $l$ is $P_d(x|l) = (1/l)f_d(x/l)$, with (for derivation see [45])

$$f_d(z) = \frac{\Gamma(d/2)}{\sqrt{\pi}\,\Gamma((d-1)/2)}\,(1-z^2)^{(d-3)/2}\,\theta(1-|z|)\,, \quad (4)$$

where $\Gamma(y)$ is the Gamma function and $\theta(y)$ is the Heaviside step function: $\theta(y) = 1$ if $y \geq 0$ and $\theta(y) = 0$ if $y < 0$. We denote as $x_i$ the $x$-component of the vector $\vec{l_i}$. Since at each tumbling the new direction is drawn independently, the joint probability distribution of the $x$-components, given the distances $\{l_i\}$ factorises as $P(\{x_i\}|\{l_i\}) = \prod_{i=1}^{n}(1/l_i)f_d(x_i/l_i)$. Using this result and Eq. (3), we can now write the joint probability distribution of $\{x_i\}$, $\{l_i\}$ and $n$ as

$$\begin{aligned} P(\{x_i\}, \{l_i\}, n|t) &= P(\{x_i\}|\{l_i\})P(\{l_i\}, n|t) \\ &= \frac{1}{\gamma}\left[\prod_{i=1}^{n}\frac{1}{l_i}f_d\left(\frac{x_i}{l_i}\right)\frac{\gamma}{v_0}\,e^{-\gamma\,l_i/v_0}\right]\delta\left(t - \sum_{i=1}^{n}\frac{l_i}{v_0}\right). \end{aligned} \quad (5)$$

By integrating over the $\{l_i\}$ variables, we obtain the joint distribution of the $x_i$'s and $n$, $P(\{x_i\}, n|t)$. Due to the presence of the delta-function in (5), it is convenient to compute its Laplace transform with respect to (w.r.t) $t$. After integrating over the $l_i$'s, we obtain (see [45])

$$\int_0^{\infty} dt\, e^{-s\,t}\, P\left(\{x_i\}, n|t\right) = \frac{1}{\gamma}\left(\frac{\gamma}{\gamma+s}\right)^n \prod_{i=1}^{n}\tilde{p}_s(x_i), \quad (6)$$

where we have defined

$$\tilde{p}_s(x) = \int_0^{\infty}\frac{dl}{l}f_d\left(\frac{x}{l}\right)\frac{(\gamma+s)}{v_0}\,e^{-(\gamma+s)\,l/v_0}\,. \quad (7)$$

One can easily check that $\tilde{p}_s(x)$ is non-negative and normalised to unity (see [45]): it can thus be interpreted as a PDF, parametrized by $s$, $d$, $\gamma$ and $v_0$. Moreover, due to the symmetry of $f_d(z) = f_d(-z)$, $\tilde{p}_s(x)$ is also symmetric, i.e., $\tilde{p}_s(x) = \tilde{p}_s(-x)$. While the PDF $\tilde{p}_s(x)$ in Eq. (7) can be computed explicitly for arbitrary $d$, we will show that its precise expression is not relevant for our purpose. All that matters for our purpose is that it is continuous and symmetric in $x$. By performing a formal inversion of the Laplace transform in Eq. (6), we derive the joint distribution of the $x_i$'s and $n$, given $t$,

$$P\left(\{x_i\}, n|t\right) = \int\frac{ds}{2\pi\, i}e^{s\,t}\,\frac{1}{\gamma}\left(\frac{\gamma}{\gamma+s}\right)^n\prod_{i=1}^{n}\tilde{p}_s(x_i)\,, \quad (8)$$

where the integral is over the Bromwich contour (imaginary axis in this case) in the complex $s$ plane. We see from Eq. (8) that the $d$-dimensional RTP (see Fig. 1), when projected in the $x$-direction, constitutes an effective one-dimensional random walk (RW) where the increments $x_i$'s are now correlated in a nontrivial way. Our goal is now to compute the survival probability $S(t)$ for this RW, starting from $x_0 = 0$.

To proceed, we notice that the survival probability $S(t)$ of this $x$-component process up to time $t$ is, by definition, the probability of the event that the successive sums $x_1$, $x_1{+}x_2$, …, $x_1{+}x_2{+}\ldots x_n$ are all positive. Here, the number of steps $n$ of the RW, i.e. the number of tumblings in the initial RTP problem, in the fixed time interval $[0, t]$ is itself a random number. Hence, to compute $S(t)$ we need to sum over all possible values of $n \geq 1$. This yields

$$S(t) = \sum_{n=1}^{\infty}\int_{-\infty}^{\infty}dx_1\ldots\int_{-\infty}^{\infty}dx_n\,\Theta_n(\{x_i\})\,P\left(\{x_i\}, n|t\right)\,, \quad (9)$$

where we used the notation $\Theta_n(\{x_i\}) = \theta(x_1)\theta(x_1 + x_2)\ldots\theta(x_1{+}x_2{+}\ldots{+}x_n)$ to constrain the partial sums to be positive. By inserting the expression of $P\left(\{x_i\}, n|t\right)$ given in (8) into Eq. (9) we obtain

$$S(t) = \int\frac{ds}{2\pi\, i}e^{s\,t}\,\frac{1}{\gamma}\sum_{n=1}^{\infty}\left(\frac{\gamma}{\gamma+s}\right)^n q_n\,, \quad (10)$$

where we have defined the multiple integral

$$q_n = \int_{-\infty}^{\infty} dx_1 \ldots \int_{-\infty}^{\infty} dx_n \, \Theta_n(\{x_i\}) \prod_{i=1}^{n} \tilde{p}_s(x_i) \, . \quad (11)$$

In fact, $q_n$ in Eq. (11) has a very simple and nice interpretation. Consider a discrete-time continuous-space random walk starting at the origin 0 in one dimension. At each step $k \geq 1$, the position of the random walker $X_k$ jumps by a random distance $x_k$ drawn, independently at each step, from the continuous and symmetric PDF $\tilde{p}_s(x)$, i.e. $X_k = X_{k-1} + x_k$, starting from $X_0 = 0$. Then, $q_n$ in (11) just denotes the probability that the walker stays on the positive side up to step $n$. Since the jump distribution $\tilde{p}_s(x)$ is continuous and symmetric, we can use the Sparre Andersen theorem [43] which states that $q_n$ is universal, i.e. independent of $\tilde{p}_s(x)$, and simply given by $q_n = \binom{2n}{n} 2^{-2n}$ for $n \geq 0$. Note that this formula is independent of the jump distribution for all $n$, and not just asymptotically for large $n$. The generating function of $q_n$ is thus also universal and given by

$$\sum_{n=0}^{\infty} q_n \, z^n = \frac{1}{\sqrt{1-z}} \, . \quad (12)$$

This formula has been used recently in several statistical physics problems [7, 46], in particular in the context of record statistics [47–51] (see also below and in [45] for the record statistics in the RTP problem). Here we use this result (12) choosing $z = \gamma/(\gamma + s)$ in Eq. (10), taking care of the fact that the sum in Eq. (10) does not include the $n = 0$ term. This leads to our amazingly universal result

$$S(t) = \int \frac{ds}{2\pi \, i} e^{s\,t} \, \frac{1}{\gamma} \, \left[ \sqrt{\frac{\gamma + s}{s}} - 1 \right] . \quad (13)$$

This result is evidently independent of the dimension $d$ and the speed $v_0$. The dimensional dependence appears in Eq. (10) through the PDF $\tilde{p}_s(x)$ which however disappears as a consequence of the SA theorem. The Laplace inversion in Eq. (13) can be exactly done and we obtain the explicit expression for $S(t)$ presented in Eq. (1). Let us emphasize, once more, that the result (1) is valid at all times $t$ and in any dimension $d$.

In fact, the result (1) turns out to be valid for a much broader class of $d$-dimensional RTP models where the speed during a flight is itself a random variable, drawn from a generic speed distribution $W(v)$ – while the time of flights are still exponentially distributed, i.e. $p(\tau) = \gamma \, e^{-\gamma \tau}$. For a general $W(v)$, all the steps of our calculation leading to $S(t)$ in (10) and (11) go through, except that $\tilde{p}_s(x)$ in Eq. (7) gets modified to [45]

$$\tilde{p}_s(x) = \int_0^{\infty} \frac{dl}{l} f_d\left(\frac{x}{l}\right) \int_0^{\infty} dv \, W(v) \, \frac{(\gamma + s)}{v} \, e^{-(\gamma+s)\,l/v} \, , \quad (14)$$

which is normalized to unity and is both continuous and symmetric. Using the SA theorem, we then conclude that $S(t)$ is again independent of the precise form of $\tilde{p}_s(x)$ and is given by the same universal formula (1). Hence, $S(t)$ in (1) is independent, at all time $t$, of the dimension $d$ as well as the speed distribution $W(v)$ – which we have also checked numerically (see [45]).

The universal result (1) is derived assuming $p(\tau)$ is exponential. Does this result hold for other flight time PDF's $p(\tau)$? For non-exponential $p(\tau)$ it is difficult to compute $S(t)$ exactly for all $t$. With our method, this amounts to compute the survival probability of an effective $1d$ RW of $n$ steps where the last jump (corresponding to the last incomplete run in the original RTP) differs from the $(n-1)$ first ones (the complete runs of the RTP). For the exponential jump distribution with rate $\gamma$, the weight of the last jump differs from the $(n-1)$ first ones by a constant pre-factor $\gamma$ [see Eq. (2)] and we can still use the SA theorem, which requires an identical jump distribution for each step. Unfortunately, for other $p(\tau)$, this trick can not be used and the SA theorem can no longer be applied. Our numerical simulations in the inset of Fig. 2 indeed indicate that $S(t)$ is no longer given by (1) for non-exponential $p(\tau)$. For such distributions, even if computing the exact expression of $S(t)$ for any finite $t$ seems challenging, it is reasonable to expect that the RTP and the aforementioned "wait-then-jump" model [36] behave, at late times, in a qualitatively similar way. In particular, the survival probability should decay, at large time $t$, as $S(t) \propto t^{-\theta}$ with the same exponent $\theta$ for both models. From the "wait-then-jump" model, one can then show [36] (see also [45]) that $\theta = 1/2$ if $p(\tau)$ admits a well defined first-moment while, if the first moment is not defined, e.g. for $p(\tau) \propto \tau^{-1-\mu}$ for large $\tau$ with $\mu < 1$, then $\theta = \mu/2$. In the inset of Fig. 2 we numerically verify these predictions for $\theta$ for the RTP with different $p(\tau)$, finding a good agreement.

As an interesting application, our universal result for $S(t)$ with an exponential $p(\tau)$ in Eq. (1) can further be used to derive the universal properties of other interesting observables for the $x$-component process of the $d$-dimensional RTP. For instance, we show in [45] that the statistics of the number of lower records $S_N(t)$ in time $t$ for this effective 1-d process is also universal for all $t$ and can be computed exactly. The statistics of the number of records is an important problem with a variety of applications ranging from climate science to finance [51], but with very few exact analytical results. Here we show that the record statistics in the RTP problem is not only exactly solvable but is also universal. For example, we show that the mean number of lower records $\langle N(t) \rangle$ at all times $t$ is given by the universal formula [45]

$$\langle N(t) \rangle = \frac{e^{-\frac{\gamma t}{2}}}{2} \left( (2\gamma t + 3) I_0\left(\frac{t}{2}\right) + (2\gamma t + 1) I_1\left(\frac{\gamma t}{2}\right) \right) .$$

To conclude, we computed exactly the probability $S(t)$

that the $x$-component of an RTP in $d$-dimensions does not cross the origin up to time $t$. For an RTP with a constant tumbling rate, we demonstrated that $S(t)$ is remarkably universal at all $t$, i.e., independent of $d$ as well as the speed distribution $W(v)$. These results are used to further compute the universal record statistics for an RTP in $d$-dimensions. It would be interesting to see if such universality extends to other other observables in RTP as well as to other models of active self-propelled particles.

We would like to thank A. Dhar and A. Kundu for stimulating discussions at the earliest stage of this work.

---

[1] P. Hänggi, P. Talkner, M. Borkovec, Rev. Mod. Phys. **62**, 251 (1990).

[2] P. Bénichou, C. Loverdo, M. Moreau, R. Voituriez, Rev. Mod. Phys. **83**, 81 (2011).

[3] J. M. Hammersley, Proceedings of the Fourth Berkeley Symposium on Math. Stat. and Proba. **3**, 17 (1961).

[4] S. N. Majumdar, Curr. Sci. **89**, 2076 (2005); also available at http://xxx.arXiv.org/cond-mat/0510064.

[5] S. Redner, *A Guide to First-Passage Processes* (Cambridge University Press, 2001).

[6] S. N. Majumdar, Curr. Sci. **77**, 370 (1999).

[7] A. J. Bray, S. N. Majumdar, and G. Schehr, Adv. in Phys. **62**, 225 (2013).

[8] R. Metzler, G. Oshanin, S. Redner, *First-Passage Phenomena and Their Applications*, (World Scientific, 2014).

[9] J. Masoliver, *Random Processes: First-passage and Escape* (World Scientific, 2018).

[10] M. C. Marchetti, J. F. Joanny, S. Ramaswamy, T. B. Liverpool, J. Prost, M. Rao, and R. Aditi Simha, Rev. Mod. Phys. **85**, 1143 (2013).

[11] C. Bechinger, R. Di Leonardo, H. Löwen, C. Reichhardt, G. Volpe, and G. Volpe, Rev. Mod. Phys. **88**, 045006 (2016).

[12] S. Ramaswamy, J. Stat. Mech. 054002 (2017).

[13] F. Schweitzer, *Brownian Agents and Active Particles: Collective Dynamics in the Natural and Social Sciences*, Springer: Complexity, Berlin, (2003).

[14] L. Walsh, C. G. Wagner, S. Schlossberg, C. Olson, A. Baskaran and N. Menon, Soft matter, **13**, 8964-8968 (2017).

[15] S. Ramaswamy, Annu. Rev. Condens. Matter Phys. **1.1** (2010): 323-345.

[16] R. Nitzan, R. Voituriez, and N. S. Gov, Phys. Rev. E **99**, 022419 (2019)

[17] H. C. Berg, *E. coli in Motion* (Springer, 2014).

[18] M. E. Cates, Rep. Prog. Phys. **75**, 042601 (2012).

[19] T. Vicsek, A. Czirók, E. Ben-Jacob, I. Cohen and O. Shochet, Phys. Rev. Lett. **75**, 1226 (1995).

[20] S. Hubbard, P. Babak, S. T. Sigurdsson and K. G. Magnússon, Ecological Modelling, **174**, 359-374 (2004).

[21] T. Vicsek, A. Zafeiris, Phys. Rep. **517**, 71 (2012).

[22] J. Tailleur and M. E. Cates, Phys. Rev. Lett. **100**, 218103 (2008).

[23] M. E. Cates, J. Tailleur, Annu. Rev. Condens. Matter Phys. **6**, 219 (2015).

[24] G. H. Weiss, Physica A **311**, 381 (2002).

[25] J. Masoliver and K. Lindenberg, Eur. Phys. J B **90**, 107 (2017).

[26] F. J. Sevilla, A. V. Arzola, E. P. Cital, Phys. Rev. E **99**, 012145 (2019).

[27] A. Dhar, A. Kundu, S. N. Majumdar, S. Sabhapandit, G. Schehr, Phys. Rev. E **99**, 032132 (2019).

[28] E. Mallmin, R. A. Blythe, M. R. Evans, J. Stat. Mech. P013204 (2019).

[29] U. Basu, S. N. Majumdar, A. Rosso, S. Sabhapandit, G. Schehr, preprint arXiv:1910.10083.

[30] A. B. Slowman, M. R. Evans, and R. A. Blythe, Phys. Rev. Lett. **116**, 218101 (2016).

[31] G. Gradenigo and S. N. Majumdar, J. Stat. Mech. **5**, 053206 (2019).

[32] It is interesting to point out that the joint probability distribution of the position and velocity $P(\vec{x}, \vec{v}, t)$ at time $t$ of this generalized RTP can be interpreted as a Wigner function for the problem of a quantum particle under continuous monitoring [33].

[33] X. Cao, A. Tilloy, A. De Luca, SciPost Phys. **7**, 024 (2019)

[34] M. R. Evans, S. N. Majumdar, J. Phys. A: Math. Theor. **51**, 475003 (2018).

[35] J. Masoliver, Phys. Rev. E **99**, 012121 (2019).

[36] R. Artuso, G. Cristadoro, M. Degli Esposti and G. Knight, Phys. Rev. E **89**, 052111 (2014).

[37] K. Malakar, V. Jemseena, A. Kundu, K. Vijay Kumar, S. Sabhapandit, S. N. Majumdar, S. Redner, A. Dhar, J. Stat. Mech. **4**, 043215 (2018).

[38] P. Le Doussal, S. N. Majumdar, and G. Schehr, Phys. Rev. E **100**, 012113 (2019).

[39] T. Demaerel and C. Maes, Phys. Rev. E **97**, 032604 (2018).

[40] L. Angelani, R. Di Lionardo, and M. Paoluzzi, Euro. J. Phys. E **37**, 59 (2014).

[41] J.-F. Rupprecht, O. Bénichou, R. Voituriez, Phys. Rev. E **94**, 012117 (2016).

[42] Note that for BM, $S(t)$ is non-zero only if the particle starts initially away from the origin.

[43] E. Sparre Andersen, Math. Scand. **2**, 195 (1954).

[44] V. V. Palyulin, G. Blackburn, M. A. Lomholt, N. W. Watkins, R. Metzler, R. Klages, A. V. Chechkin, New J. Phys. **21**, 103028 (2019).

[45] F. Mori, P. Le Doussal, S. N. Majumdar, and G. Schehr, see Supplemental Material.

[46] S. N. Majumdar, Physica A, 389, 4299 (2010).

[47] S. N. Majumdar, R. Ziff, Phys. Rev. Lett. **101**, 050601 (2008).

[48] P. Le Doussal, K. J. Wiese, Phys. Rev. E **79**, 051105 (2009).

[49] S. N. Majumdar, G. Schehr, and G. Wergen, J. Phys. A: Math. Theor. **45**, 355002 (2012).

[50] C. Godrèche, S.N. Majumdar, and G. Schehr, Phys. Rev. Lett. **117**, 010601 (2016)

[51] C. Godrèche, S. N. Majumdar, and G. Schehr, J. Phys. A: Math. Theor. **50**, 333001 (2017).

# Universal survival probability for a $d$-dimensional run-and-tumble particle: supplemental material

Francesco Mori,[1] Pierre Le Doussal,[2] Satya N. Majumdar,[1] and Grégory Schehr[1]
[1] *LPTMS, CNRS, Univ. Paris-Sud, Université Paris-Saclay, 91405 Orsay, France*
[2] *Laboratoire de Physique de l'Ecole Normale Supérieure, PSL University, CNRS, Sorbonne Universités, 24 rue Lhomond, 75231 Paris, France*

(Dated: January 7, 2020)

We give the principal details of the calculations described in the main text of the Letter.

## I. DERIVATION OF THE SURVIVAL PROBABILITY $S(t)$

In this section we give the details of the derivation of Eq. (1) in the main text, i.e. of the probability $S(t)$ that the $x$-component of the run-and-tumble particle (RTP) does not take negative values up to time $t$. We perform the computation in the most general setup, where the velocity $v$ is drawn after each tumbling from a distribution $W(v)$ with positive support and normalized to unity. It is possible to recover the usual RTP model by setting $W(v) = \delta(v - v_0)$. We consider a single RTP moving in $d$-dimensions, starting at the origin $O$ and evolving for a total time $t$. The particle initially chooses a random direction and a random velocity $v_1$ and moves ballistically in that direction during a random time interval $\tau_1$ that is drawn from an exponential distribution $p(\tau) = \gamma\, e^{-\gamma\tau}$. The distance travelled during this flight $l_1 = v_1\tau_1$ is thus also a random variable. After that, the particle tumbles instantaneously, i.e., it chooses randomly a new direction and a new velocity. Then, it moves ballistically in that direction for an exponentially distributed time $\tau_2$ drawn independently from the same distribution $p(\tau) = \gamma\, e^{-\gamma\tau}$ and so on. More precisely, in a small time interval $dt$:

- With probability $\gamma\, dt$, the particle changes its direction of motion and velocity randomly.
- With the complementary probability $(1 - \gamma dt)$, the particle retains its direction and moves forward in that direction by a distance $v\, dt$, where $v$ is the constant velocity of the current flight.

Note that the number $n$ of tumblings is also random. We consider the starting point $O$ as a tumbling. Thus, we always have $n \geq 1$. As explained in the letter, the last time interval $\tau_n$ will not be completed yet. Consequently, its distribution is given by the probability $e^{-\gamma\,\tau_n}$ that no tumbling happens during the interval $\tau_n$. At variance with the previous intervals, each of which is distributed independently according to the normalized distribution $p(\tau) = \gamma\, e^{-\gamma\,\tau}$, the distribution of $\tau_n$ is not normalized to unity. Hence, the joint distribution of the time intervals $\{\tau_i\} = \{\tau_1, \tau_2, \ldots, \tau_n\}$ *and* the number of tumblings $n$, for a fixed duration $t$ of the particle, is given by

$$P\left(\{\tau_i\},\, n|t\right) = \left[\prod_{i=1}^{n-1} \gamma\, e^{-\gamma\,\tau_i}\right] e^{-\gamma\,\tau_n}\, \delta\left(\sum_{i=1}^{n} \tau_i - t\right) . \tag{1}$$

Let $\{l_i\} = \{l_1, l_2, \ldots, l_n\}$ denote the straight distances travelled by the particle up to time $t$ and $\{v_i\} = \{v_1, v_2, \ldots, v_n\}$ the magnitude of the velocities in each flight. Clearly $l_i = v_i\,\tau_i$ and $l_i \geq 0$ for all $i$. Thus, using Eq. (1), the joint distribution of $\{l_i\}$, $\{v_i\}$ and the number of tumblings $n$ is given by

$$P\left(\{l_i\},\, \{v_i\},\, n|t\right) = \frac{1}{\gamma}\left[\prod_{i=1}^{n} W\left(v_i\right) \frac{\gamma}{v_i}\, e^{-\gamma\, l_i/v_i}\right] \delta\left(t - \sum_{i=1}^{n} \frac{l_i}{v_i}\right) . \tag{2}$$

By integrating over the speed variables $\{v_i\}$ we obtain the joint distribution of $\{l_i\}$ and $n$:

$$P\left(\{l_i\},\, n|t\right) = \frac{1}{\gamma}\int_0^\infty dv_1 \ldots \int_0^\infty dv_n \left[\prod_{i=1}^{n} W\left(v_i\right) \frac{\gamma}{v_i}\, e^{-\gamma\, l_i/v_i}\right] \delta\left(t - \sum_{i=1}^{n} \frac{l_i}{v_i}\right) . \tag{3}$$

As explained in the main text, the joint distribution of the $x$-components of the random vectors $\{\vec{l_i}\}$ with given norms $\{l_i\}$ can be written as (see Sec. II for the derivation of this result):

$$P\left(\{x_i\}|\{l_i\}\right) = \prod_{i=1}^{n} P_d(x_i|l_i) = \prod_{i=1}^{n} \frac{1}{l_i} f_d\left(\frac{x_i}{l_i}\right) \tag{4}$$

where

$$f_d(z) = \frac{\Gamma(d/2)}{\sqrt{\pi}\,\Gamma((d-1)/2)}\,(1 - z^2)^{(d-3)/2}\,\theta(1 - |z|)\,. \tag{5}$$

Here $\Gamma(y)$ is the Gamma function and $\theta(y)$ is the Heaviside step function: $\theta(y) = 1$ if $y \geq 0$ and $\theta(y) = 0$ if $y < 0$. We can then write down explicitly the joint distribution of the $x$-components $\{x_i\}$, the norms $\{l_i\}$ and the number of tumblings $n$ at fixed total time $t$ as

$$\begin{aligned} P\left(\{x_i\}, \{l_i\}, n|t\right) &= P\left(\{x_i\}|\{l_i\}\right)\, P\left(\{l_i\},\, n|t\right) \\ &= \frac{1}{\gamma}\int_0^\infty dv_1 \ldots \int_0^\infty dv_n \left[\prod_{i=1}^{n} \frac{1}{l_i} f_d\left(\frac{x_i}{l_i}\right) W(v_i) \frac{\gamma}{v_i}\, e^{-\gamma\, l_i/v_i}\right] \delta\left(t - \sum_{i=1}^{n} \frac{l_i}{v_i}\right) , \end{aligned} \tag{6}$$

where we used the results in Eqs. (3) and (4). Having obtained this joint distribution we can now integrate over the $\{l_i\}$ variables to obtain the marginal joint distributions of $\{x_i\}$ and $n$, given $t$

$$P\left(\{x_i\},\, n|t\right) = \frac{1}{\gamma}\int_0^\infty dl_1 \ldots \int_0^\infty dl_n \int_0^\infty dv_1 \ldots \int_0^\infty dv_n \left[\prod_{i=1}^n \frac{1}{l_i} f_d\left(\frac{x_i}{l_i}\right) W\left(v_i\right) \frac{\gamma}{v_i}\, e^{-\gamma\, l_i/v_i}\right] \delta\left(t - \sum_{i=1}^n \frac{l_i}{v_i}\right) . \tag{7}$$

The result in Eq. (7) then provides us an effective $x$-component process $\{x_i\}$ projected from the $d$-dimensional RTP of fixed duration $t$. To further simplify this $x$-component process, we take a Laplace transform with respect to $t$ that decouples the integrals over the $\{l_i\}$ variables

$$\begin{aligned}\int_0^\infty dt\, e^{-s\,t}\, P\left(\{x_i\},\, n|t\right) &= \frac{1}{\gamma}\int_0^\infty dl_1 \ldots \int_0^\infty dl_n \int_0^\infty dv_1 \ldots \int_0^\infty dv_n \left[\prod_{i=1}^n \frac{1}{l_i} f_d\left(\frac{x_i}{l_i}\right) W\left(v_i\right) \frac{\gamma}{v_i}\, e^{-(\gamma+s)\, l_i/v_i}\right] \\ &= \frac{1}{\gamma}\left(\frac{\gamma}{\gamma+s}\right)^n \prod_{i=1}^n \int_0^\infty \frac{dl_i}{l_i} f_d\left(\frac{x_i}{l_i}\right) \int_0^\infty dv_i\, W\left(v_i\right) \frac{(\gamma+s)}{v_i}\, e^{-(\gamma+s)\, l_i/v_i} \\ &= \frac{1}{\gamma}\left(\frac{\gamma}{\gamma+s}\right)^n \prod_{i=1}^n \tilde{p}_s(x_i) \end{aligned} \tag{8}$$

where we have defined

$$\tilde{p}_s(x) = \int_0^\infty \frac{dl}{l} f_d\left(\frac{x}{l}\right) \int_0^\infty dv\, W\left(v\right) \frac{(\gamma+s)}{v}\, e^{-(\gamma+s)\, l/v} . \tag{9}$$

Note that in getting from the first to the second line above, we have multiplied and divided by a factor $(\gamma+s)^n$ so that the function $\tilde{p}_s(x)$, which depends on the parameters $s$, $d$, $\gamma$ and on the speed distribution $W(v)$, can be interpreted as a probability density function (PDF) of a random variable $x$. Manifestly $\tilde{p}_s(x)$ is non-negative and normalized to unity. Indeed, integrating over $x$ one gets

$$\begin{aligned}\int_{-\infty}^\infty \tilde{p}_s(x)\, dx &= (\gamma+s)\int_0^\infty dl \int_{-\infty}^\infty \frac{dx}{l} f_d\left(\frac{x}{l}\right) \int_0^\infty \frac{dv}{v} W\left(v\right) e^{-(\gamma+s)\, l/v} \\ &= (\gamma+s)\int_0^\infty \frac{dv}{v} W\left(v\right) \int_0^\infty dl\, e^{-(\gamma+s)\, l/v} \int_{-1}^1 dz\, f_d(z) \\ &= \int_0^\infty dv\, W\left(v\right) = 1, \end{aligned} \tag{10}$$

where we used the fact that $f_d(z)$ given in Eq. (5) is supported over the finite interval $z \in [-1, 1]$ and is normalized to unity and that $W(v)$ is normalized to unity. As we will see below, the precise expression for $\tilde{p}_s(x)$ is not relevant, as long as it is continuous and symmetric in $x$. Note that this property for $\tilde{p}_s(x)$ will hold for general factorized jump distributions $P\left(\{x_i\}|\{l_i\}\right) = \prod_{i=1}^n P_d(x_i|l_i)$ as in Eq. (4), provided the conditional distribution $P_d(x|l)$ is symmetric in $x$, i.e. $P_d(x|l) = P_d(-x|l)$. Finally, inverting the Laplace transform in Eq. (8) formally, we have the joint distribution of $\{x_i\}$ and $n$ for a fixed $t$

$$P\left(\{x_i\}, n|t\right) = \int \frac{ds}{2\pi\, i} e^{s\,t}\, \frac{1}{\gamma}\left(\frac{\gamma}{\gamma+s}\right)^n \prod_{i=1}^n \tilde{p}_s(x_i)\, , \tag{11}$$

where the integral is over the Bromwich contour (imaginary axis in this case) in the complex $s$ plane.

The survival probability $S(t)$ of this $x$-component process up to time $t$ is the probability of the event that the successive sums $x_1$, $x_1 + x_2$, …, $x_1 + x_2 + \ldots x_n$ are all positive. We recall that the number of tumblings $n$ is also a random variable. Thus, summing over $n$ one obtains

$$S(t) = \sum_{n=1}^\infty \int_{-\infty}^\infty dx_1 \ldots \int_{-\infty}^\infty dx_n\, \left[\theta(x_1)\,\theta(x_1+x_2)\ldots\theta(x_1+x_2+\ldots+x_n)\right]\, P\left(\{x_i\}, n|t\right)\, , \tag{12}$$

where $P\left(\{x_i\}, n|t\right)$ is the joint distribution of $\{x_i\}$ and $n$ for fixed $t$. Plugging the expression for $P\left(\{x_i\}, n|t\right)$ given in Eq. (11) gives

$$\begin{aligned} S(t) &= \int \frac{ds}{2\pi\, i} e^{s\,t}\, \frac{1}{\gamma} \sum_{n=1}^\infty \left(\frac{\gamma}{\gamma+s}\right)^n \int_{-\infty}^\infty dx_1 \ldots \int_{-\infty}^\infty dx_n\, \left[\theta(x_1)\,\theta(x_1+x_2)\ldots\theta(x_1+x_2+\ldots+x_n)\right] \prod_{i=1}^n \tilde{p}_s(x_i) \\ &= \int \frac{ds}{2\pi\, i} e^{s\,t}\, \frac{1}{\gamma} \sum_{n=1}^\infty \left(\frac{\gamma}{\gamma+s}\right)^n q_n\, , \end{aligned} \tag{13}$$

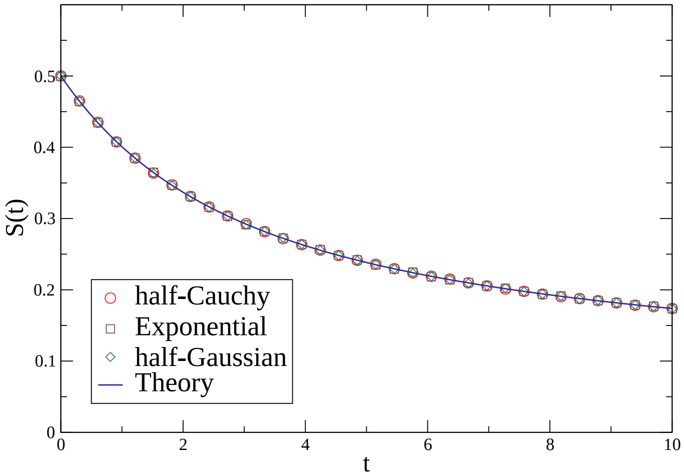

FIG. 1. Plot of $S(t)$ evaluated numerically for different velocity distributions $W(v)$ and an exponential distribution $p(\tau)$ in dimension $d = 2$. The solid line corresponds to the exact analytical result in Eq. (18).

where we have defined the multiple integral

$$q_n = \int_{-\infty}^{\infty} dx_1 \ldots \int_{-\infty}^{\infty} dx_n \, [\theta(x_1)\, \theta(x_1 + x_2) \ldots \theta(x_1 + x_2 + \ldots + x_n)] \prod_{i=1}^{n} \tilde{p}_s(x_i)\,. \tag{14}$$

However, as mentioned in the text, this quantity $q_n$ in Eq. (14) has the following interpretation. Consider a one-dimensional discrete-time random walk, starting at the origin $x = 0$ and making independent jumps at each step with jump length drawn from the PDF $\tilde{p}_s(x)$. Then $q_n$ is just the probability that the walker does not visit the negative axis up to step $n$. Notably, since $\tilde{p}_s(x)$ is continuous and symmetric, the Sparre Andersen theorem [1] states that $q_n$ is universal, i.e., independent of $\tilde{p}_s(x)$ and is given by:

$$q_n = \binom{2n}{n} 2^{-2n} \qquad\qquad n = 0, 1, 2, \ldots \tag{15}$$

Note that this formula is valid for any $n$, and hence the universality holds for all $n$, and not just asymptotically for large $n$. The generating function of $q_n$ is thus also universal

$$\sum_{n=0}^{\infty} q_n\, z^n = \sum_{n=0}^{\infty} \binom{2n}{n} \left(\frac{z}{4}\right)^n = \frac{1}{\sqrt{1-z}}\,. \tag{16}$$

Using this result (16) in Eq. (13) and noticing that the sum in Eq. (13) does not include the $n = 0$ term leads to the result

$$S(t) = \int \frac{ds}{2\pi\, i} e^{s\,t}\, \frac{1}{\gamma} \,\left[\sqrt{\frac{\gamma + s}{s}} - 1\right]\,, \tag{17}$$

which is Eq. (13) in the main text. Note that this result is universal in the sense that it does not depend on the dimension $d$ or on the speed distribution $W(v)$. Indeed, $W(v)$ and $d$ appear only in Eq. (13) through the PDF $\tilde{p}_s(x)$. However, we have seen that as a consequence of the Sparre Andersen theorem the result is completely independent of the specific form of $\tilde{p}_s(x)$, as long as it is symmetric and continuous. As explained in the main text, the Laplace inversion in Eq. (17) can be explicitly performed leading to

$$S(t) = \frac{1}{2}\, e^{-\gamma t/2}\, \left[I_0(\gamma t/2) + I_1(\gamma t/2)\right] \tag{18}$$

where $I_0(z)$ and $I_1(z)$ are modified Bessel functions, as given in Eq. (1) in the main text. In Fig. 1 we show a plot of $S(t)$ evaluated numerically for different velocity distributions $W(v)$ and an exponential distribution $p(\tau)$ in dimension $d = 2$, which shows a very good agreement with our exact result (18).

## II. DERIVATION OF THE FORMULA IN EQ. (5) FOR THE MARGINAL DISTRIBUTION $P_d(x|l)$

We consider a random vector $\vec{l}$ of fixed magnitude $l$ in $d$-dimensions and compute the marginal distribution $P_d(x|L)$ of its $x$-component, given fixed $l$. The PDF of a random vector $\vec{l}$ of fixed magnitude $l$ is simply

$$P(\vec{l}) = \frac{1}{S_d\, l^{d-1}}\, \delta\left(|\vec{l}| - l\right) , \tag{19}$$

where

$$S_d = \frac{2\pi^{d/2}}{\Gamma(d/2)} \tag{20}$$

is just the surface area of a $d$-dimensional sphere of unit radius. It is convenient to rewrite Eq. (19) as

$$P(\vec{l}) = \frac{2}{S_d\, l^{d-2}}\, \delta\left(|\vec{l}|^2 - l^2\right) . \tag{21}$$

Let $|\vec{l}|^2 = z_1^2 + z_2^2 + \ldots z_d^2$ where $z_k$ denotes the component of the vector $\vec{l}$ along the $k$-th direction. Therefore, the marginal distribution $P_d(x|l)$, for instance along the $x$ direction, is obtained by keeping $z_1 = x$ fixed while integrating over the other components

$$\begin{aligned} P_d(x|l) &= \int P(\vec{l})\, \delta(z_1 - x)\, dz_1\, dz_2\, \ldots dz_d \\ &= \frac{2}{S_d\, l^{d-2}} \int \delta\left(z_2^2 + z_3^2 + \ldots + z_d^2 - (l^2 - x^2)\right)\, dz_2\, dz_3\, \ldots dz_d\,, \end{aligned} \tag{22}$$

where we used Eq. (21) in going from the first to the second line above. Let $R^2 = z_2^2 + z_3^2 + \ldots + z_d^2$. Then the $(d-1)$-dimensional integral in Eq. (22) can be performed in the radial coordinate

$$P_d(x|L) = \frac{2\, S_{d-1}}{S_d\, l^{d-2}} \int_0^\infty \delta\left(R^2 - (l^2 - x^2)\right)\, R^{d-2}\, dR \tag{23}$$

where we recall $S_{d-1}$ is the surface area of a $(d-1)$-dimensional unit sphere. The single radial integral in Eq. (23) can be trivially done by making a change of variable $R^2 = u$

$$\begin{aligned} P_d(x|l) &= \frac{S_{d-1}}{S_d\, l^{d-2}} \int_0^\infty \delta\left(u - (l^2 - x^2)\right)\, u^{(d-3)/2}\, du \\ &= \frac{S_{d-1}}{S_d\, l^{d-2}}\, (l^2 - x^2)^{(d-3)/2}\, \theta(l - |x|)\,. \end{aligned} \tag{24}$$

Using the formula for $S_d$ in Eq. (19) and rearranging the terms, we get

$$P_d(x|l) = \frac{1}{l}\, f_d\left(\frac{x}{l}\right) , \tag{25}$$

where

$$f_d(z) = \frac{\Gamma(d/2)}{\sqrt{\pi}\, \Gamma((d-1)/2)}\, (1 - z^2)^{(d-3)/2}\, \theta(1 - |z|)\,, \tag{26}$$

as given in Eq. (4) in the main text. One can check easily that $f_d(z)$ is normalized to unity over the support $z \in [-1, 1]$.

## III. SURVIVAL PROBABILITY FOR RANDOM WALKS WITH SPATIO-TEMPORAL CORRELATIONS

As mentioned in the main text, the RTP model is a particular case of a random walk (RW) with spatio-temporal correlation. Let us consider a RW on the real line. Let

$$(x_1, \tau_1),\ (x_2, \tau_2), \ldots, (x_j, \tau_j), \ldots \tag{27}$$

be a sequence of independent identically distributed pairs of random variables corresponding to the step length $x_i$ and the associated time $\tau_i$. We assume that each pair $(x_i, \tau_i)$ is distributed according to the some joint PDF $p(x, \tau)$, which is assumed to be continuous in $x$ and spatially symmetric: $p(x, \tau) = p(-x, \tau)$. After $n$ steps the RW will be in position $X_n$ at time $T_n$, where

$$X_n = \sum_{k=0}^{n} x_k, \qquad T_n = \sum_{k=0}^{n} \tau_k \, . \tag{28}$$

To study the probability $S(t)$ that the negative side of the $x$-axis is not reached up to time $t$ we also need to specify how the walker moves when taking a step. One possibility is that in order to take a step $x_i$ in a time $\tau_i$ the walker moves with constant velocity $v_i = x_i/\tau_i$, as in the case of the RTP. Another possibility is that the walker remains in its position for a time $\tau_i$ and then takes an instantaneous jump $x_i$. It turns out that for this latter "wait-then-jump model" the survival probability $S(t)$ can be computed exactly for any distribution $p(x, \tau)$. This result was recently obtained by Artuso et al. using a combinatorial lemma [2] combined with the Sparre Andersen theorem. Here we propose an alternative non-combinatorial derivation based on our technique presented in Sec. I. It is convenient to derive the probability $\pi(t)$ that the first entrance to the negative axis happens at time $t$. One can then obtain the survival probability $S(t)$ using the relation

$$S'(t) = -\pi(t) \, . \tag{29}$$

In fact, Artuso et. al. [2] computed exactly the Laplace transform of $\pi(t)$, rather than of $S(t)$, but these two are simply related due to the relation (29). In order to compare to the result of the RTP in Eq. (18), we will compute $S(t)$ for the "wait-then-jump model".

Consider a trajectory of the "wait-then-jump model" up to time $t$. By definition, in the "wait-then-jump model" there are $n$ complete jumps such that $\sum_{i=1}^{n} \tau_i = t$, where each pair $(x_i, \tau_i)$ is drawn independently from the PDF $p(x, \tau)$. This corresponds to imposing that there is a jump at time $t$. Note that the number of jumps $n$ in time $t$ is a random variable, as in the RTP. The joint PDF of $\{(x_i, \tau_i)\}_{1 \le i \le n}$ and of $n$, at fixed total time $t$ is then given by

$$P(\{(x_i, \tau_i)\}, n|t) = \prod_{i=1}^{n} p(x_i, \tau_i) \, \delta\left(\sum_{i=1}^{n} \tau_i - t\right) , \tag{30}$$

where the delta function enforces the constraint on the total time. We integrate over the $\tau$ variables to obtain the marginal of $\{x_i\}$ and $n$

$$P(\{x_i\}, n|t) = \int_0^\infty d\tau_1 \ldots \int_0^\infty d\tau_n \prod_{i=1}^{n} p(x_i, \tau_i) \, \delta\left(\sum_{i=1}^{n} \tau_i - t\right) . \tag{31}$$

Taking a Laplace transform with respect to $t$ we decouple the integrals over the $\tau$ variables

$$\int_0^\infty dt \, P(\{x_i\}, n|t) \, e^{-st} = \prod_{i=1}^{n} \int_0^\infty d\tau_i p(x_i, \tau_i) \, e^{-s\,\tau_i} \, . \tag{32}$$

It is useful to rewrite the right-hand side of Eq. (32) as

$$\int_0^\infty dt \, P(\{x_i\}, n|t) \, e^{-st} = c(s)^n \prod_{i=1}^{n} \tilde{p}_s(x_i) \, , \tag{33}$$

where $c(s)$ is defined as

$$c(s) = \int_0^\infty d\tau \int_{-\infty}^\infty dx \, p(x, \tau) \, e^{-s\tau} \tag{34}$$

and

$$\tilde{p}_s(x) = \frac{1}{c(s)} \int_0^\infty d\tau \, p(x, \tau) \, e^{-s\tau} \, . \tag{35}$$

Note that $\tilde{p}_s(x)$ can be interpreted as a probability density function. Indeed, it is clearly non-negative and normalized to unity. Moreover, since we assume $p(x, \tau)$ to be continuous and symmetric with respect to $x$, $\tilde{p}_s(x)$ will also be continuous and symmetric. The probability that the walker enters in the positive axis for the first time at time $t$ can be simply written as

$$\pi(t) = \sum_{n=1}^{\infty} \int_0^{\infty} dx_1 \ldots \int_0^{\infty} dx_n \, P(\{x_i\}, n|t) \, \Theta_n(\{x_i\}) \,, \tag{36}$$

with the notation

$$\Theta_n(\{x_i\}) = \theta(X_1)\, \theta(X_2) \, \ldots \theta(X_{n-1}) \theta(-X_n), \tag{37}$$

where $X_i$'s are the partial sums defined in Eq. (28) and $\theta(x)$ is the Heaviside step function: $\theta(x) = 1$ if $x > 0$ and $\theta(x) = 0$ otherwise. In other words, $\Theta_n(\{x_i\})$ enforces that the negative axis is reached for the first time at step $n$. Taking a Laplace transform of both sides of Eq. (36) and using Eq. (33), we obtain

$$\hat{\pi}(s) = \sum_{n=1}^{\infty} c(s)^n f_n \,, \tag{38}$$

where

$$f_n = \int_0^{\infty} dx_1 \ldots \int_0^{\infty} dx_n \prod_{i=1}^{n} \tilde{p}_s(x_i) \Theta_n(\{x_i\}) \,. \tag{39}$$

Notably, $f_n$ can be interpreted at the probability of first passage to the negative $x$-axis for a RW

$$X_k = X_{k-1} + \eta_k \qquad y_0 = 0 \,, \tag{40}$$

where $\eta_k$ is a random number extracted from the PDF $\tilde{p}_s(x_i)$. Then, since $\tilde{p}_s(x_i)$ is continuous and symmetric, according to the Sparre Andersen theorem $f_n$ is universal and its generating function can be computed as follows. Clearly, $f_n = q_{n-1} - q_n$ for $n \geq 1$, where $q_n$ is the probability that the random walker stays positive up to step $n$. Taking a generating function, we get

$$\sum_{n=1}^{\infty} f_n \, z^n = \sum_{n=1}^{\infty} \left[ q_{n-1} - q_n \right] \, z^n = 1 - (1-z) \sum_{n=0}^{\infty} q_n \, z^n \,, \tag{41}$$

where we used $q_0 = 1$. Since, $\tilde{p}_s(x)$ is a continuous and symmetric PDF, the Sparre Andersen theorem can be applied which states that $\sum_{n=0}^{\infty} q_n \, z^n = 1/\sqrt{1-z}$. Hence, from Eq. (41) one gets

$$\sum_{n=1}^{\infty} f_n \, z^n = 1 - \sqrt{1-z} \,. \tag{42}$$

Using this result (42) in Eq. (38) we obtain

$$\hat{\pi}(s) = 1 - \sqrt{1 - c(s)} \,. \tag{43}$$

where $c(s)$ is given in Eq. (34). This is indeed the result of Artuso et. al. [2] obtained originally using combinatorial method. Our derivation above is non-combinatorial and a bit simpler in our opinion.

From Eq. (43) one can compute the Laplace transform of the survival probability $S(t)$. Indeed, using Eq. (29) it is easy to show that

$$\tilde{S}(s) = \int_0^{\infty} dt \, S(t) \, e^{-st} = \frac{1 - \tilde{\pi}(s)}{s} \,. \tag{44}$$

Using Eq. (43) we obtain that

$$\tilde{S}(s) = \frac{\sqrt{1 - c(s)}}{s} \,, \tag{45}$$

where $c(s)$ is given in Eq. (34). To compare with the RTP model in $d$ dimensions, let us now choose

$$p(x, \tau) = p(x|\tau) p(\tau) = \frac{1}{v_0 \tau} f_d \left( \frac{x}{v_0 \tau} \right) \, p(\tau) \,, \tag{46}$$

where $f_d(z)$ is given in Eq. (26). Then we get from Eq. (34),

$$c(s) = \int_0^\infty d\tau \int_{-\infty}^{\infty} dx\, p(x,\tau)\, e^{-s\tau} = \int_0^\infty d\tau \int_{-\infty}^{\infty} dx\, \frac{1}{v_0\tau} f_d\left(\frac{x}{v_0\tau}\right) p(\tau)\, e^{-s\tau} \tag{47}$$

$$= \int_0^\infty d\tau\, e^{-s\tau} p(\tau) \int_{-\infty}^{\infty} dx\, \frac{1}{v_0\tau} f_d\left(\frac{x}{v_0\tau}\right) = \int_0^\infty d\tau\, e^{-s\tau} p(\tau) \int_{-\infty}^{\infty} dz\, f_d(z) \tag{48}$$

$$= \int_0^\infty d\tau\, e^{-s\tau} p(\tau) = \tilde{p}(s)\,. \tag{49}$$

where we have used the fact that $f_d(z)$ is normalized to unity in going from the second to the third line above. Note that $\tilde{p}(s)$ is simply defined as the Laplace transform of $p(\tau)$. Then, using Eq. (45), we obtain that

$$\tilde{S}(s) = \frac{\sqrt{1-\tilde{p}(s)}}{s}\,. \tag{50}$$

In the most relevant case of an exponential distribution $p(\tau) = \gamma\, e^{-\gamma\tau}$ one obtains that $c(s) = \gamma/(\gamma+s)$. Consequently, Eq. (50) gives $\tilde{S}(s) = 1/\sqrt{s(\gamma+s)}$. Inverting the Laplace transform explicitly, we then get the exact survival probability at all $t$ for this specific "wait-then-jump model" with exponential time distribution

$$S(t) = e^{-\gamma\, t/2}\, I_0(\gamma\, t/2)\,, \tag{51}$$

where $I_0(z)$ is again the modified Bessel function. The result in (51) is manifestly different from the RTP result in Eq. (18) (also in Eq. (1) of the main text). This clearly shows that the exact result in Eq. (45) for the "wait-then-jump model" can not be used to derive our main result for the RTP in Eq. (1) of the main text. Note however that for late times the result in Eq. (51) has the same asymptotic behavior as the RTP result, namely $S(t) \sim 1/\sqrt{\pi\gamma t}$.

Moreover, as explained in the main text, Eq. (50) can be useful to compute the late time behavior of $S(t)$ for the RTP model with a generic time distribution $p(\tau)$. Indeed, one expects that $S(t) \sim t^{-\theta}$ when $t \to \infty$ (and this is confirmed by our numerical simulations shown in Fig. 3 of the Letter). Moreover, for late times, it is natural to conjecture that the exponent $\theta$ is the same for the RTP model and for the "wait-then-jump model". Here, we compute the exponent $\theta$ for different time distributions $p(\tau)$ in the "wait-then-jump" setup. It is useful to distinguish two cases, depending on whether $p(\tau)$ has a well defined first moment or not.

*The case where $p(\tau)$ has a well defined first moment.* In this case, the Laplace transform $\tilde{p}(s)$ can be expanded, for small $s$, as

$$\tilde{p}(s) \simeq 1 - \langle\tau\rangle\, s + o(s)\,, \tag{52}$$

where $\langle\tau\rangle = \int_0^\infty d\tau\, \tau\, p(\tau)$ is the first moment of $\tau$. Using Eq. (50) we obtain that, for small $s$

$$\tilde{S}(s) \sim \sqrt{\frac{\langle\tau\rangle}{s}}\,. \tag{53}$$

Inverting the Laplace transform gives for late times that

$$S(t) \sim \sqrt{\frac{\langle\tau\rangle}{\pi\, t}}\,. \tag{54}$$

Hence, if $\langle\tau\rangle$ is finite we obtain that $\theta = 1/2$. Note that for the exponential jump distribution with rate $\gamma$, one has $\langle\tau\rangle = 1/\gamma$ and this formula (54) yields back $S(t) \sim 1/\sqrt{\pi\gamma t}$, as it should.

*The case where $p(\tau)$ has a diverging first moment.* If the average value of $\tau$ is diverging, i.e. if $p(\tau) \sim \tau^{-\mu-1}$ for $\tau \to \infty$ with $0 < \mu < 1$, then $\tilde{p}(s)$ can be expanded for small $s$ as

$$p(s) = 1 - (a\, s)^\mu + o(s^\mu)\,, \tag{55}$$

where $a$ denotes a microscopic time scale. Using Eq. (50) we obtain that, when $s \to 0$,

$$\tilde{S}(s) \sim s^{\mu/2-1}\,. \tag{56}$$

Inverting the Laplace transform we get that when $t \to \infty$

$$S(t) \sim t^{-\mu/2}\,, \tag{57}$$

and, hence, in this case $\theta = \mu/2$.

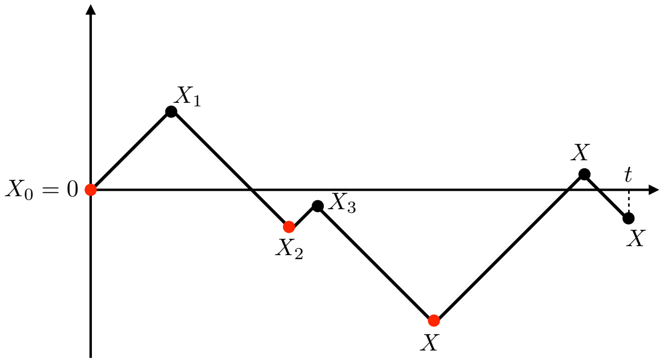

FIG. 2. Illustration of a trajectory of the RTP (black solid line) together with the positions of the associated random walk $X_0 = 0, X_1, \ldots X_n$ with $n = 6$, up to time $t$ (dots). The lower records are indicated in red, the first position $X_0$ being counted as a lower record. Note that the final position $X_n$ can in principle be also a record – although not in the above figure. The observable $S_N(t)$ is the probability that the random walk has exactly $N$ lower records up to time $t$. For $N = 1$, $S_1(t)$ coincides the survival probability up to time $t$.

## IV. UNIVERSAL RECORD STATISTICS FOR THE RTP

In this section we show that our results for the survival probability $S(t)$ for a $d$-dimensional RTP can be used to compute the statistics of records for the $x$-component of the RTP process. The universality of $S(t)$ for the RTP with an exponential distribution of the flight times (corresponding to a constant tumbling rate $\gamma$) also renders the statistics of the records for the $x$-component universal in this problem, i.e. independent of the dimension $d$ as well as the speed distribution $W(v)$. The statistics of records for a stochastic sequence has been extensively studied and has found many applications from climatology to finance [3]. In general, it is quite hard to obtain exact results for the record statistics for a correlated sequence. Below, we see that, using our method as detailed in the main text, we can compute the exact record statistics of the $x$-component of the RTP in $d$ dimensions and show that it is universal. This is one of the rare examples of an exact solution for the record statistics for a correlated sequence.

Let us start by defining a record. We consider a trajectory in $d$ dimensions of the RTP of duration $t$ starting at the origin. Let $n$ denote the number of runs in this trajectory, which itself is a random variable. We now look at the $x$-components of the $n$ successive runs and denote them by $x_1, x_2, \cdots, x_n$. The $x$-component of the positions of the RTP are denoted by $X_0 = 0, X_1 = x_1, X_2 = x_1 + x_2, X_3 = x_1 + x_2 + x_3, \ldots$ (see Fig. 2). The joint distribution of the $x_i$'s and $n$ has been computed in Eq. (8) of the main text and is given by

$$P\left(\{x_i\}, n|t\right) = \int \frac{ds}{2\pi\, i} e^{s\,t}\, \frac{1}{\gamma} \left(\frac{\gamma}{\gamma + s}\right)^n \prod_{i=1}^n \tilde{p}_s(x_i) \;, \tag{58}$$

where $\tilde{p}_s(x_i)$ is given in Eq. (14) of the main text for a general speed distribution $W(v)$ and general dimension $d$. Therefore, the $X_i$'s can be viewed as the position of a one-dimensional discrete-time random walker with correlated steps given in Eq. (58). A lower record happens at step $k$ iff the value $X_k$ is lower than all the previous values, i.e., $X_k < \min\{X_0 = 0, X_1, \cdots, X_{k-1}\}$ (see Fig. 2). By convention, $X_0 = 0$ is a lower record. Note that the final position $X_n$ can also be a record. A natural question is then: how many records occur in time $t$? We denote by $S_N(t)$ the probability that there are exactly $N$ lower records up to time $t$. Clearly, when $N = 1$ this corresponds to the event that the position has never gone below 0 up to time $t$. But this precisely the survival probability $S(t)$ that we have computed in the main text, thus $S_1(t) = S(t)$. We can then think of $S_N(t)$ as a natural generalization of the survival probability $S(t)$. One can similarly define upper records for the $x$-component of the RTP, whose statistics are exactly identical to the lower records, due to the $x \to -x$ symmetry of the RTP. An alternative physical picture of this record process is as follows: whenever the particle achieves a new lower record, one can imagine that the absorbing barrier gets pushed to this new record value. For example, before the second record happens the absorbing barrier is at $X_0 = 0$. If the second lower record happens at step $k$ with value $X_k < 0$ (for example in Fig. 2 the second record happens at $k = 2$), the absorbing barrier gets shifted to $X_k$, till the occurence of the next lower record (see Fig. 2).

Thanks to our mapping to the one-dimensional discrete-time random walk via Eq. (58), we can use the known results for the record statistics of an $n$-step discrete-time random walk, whose steps are i.i.d. variables, each drawn from $\tilde{p}_s(x_i)$ which is continuous and symmetric, and given in Eq. (14) in the main text. It is well known that the probability $q_N(n)$ that a $n$-step random walk has exactly $N$ lower records is universal, i.e. independent of the distribution $\tilde{p}_s(x_i)$ [4]. In particular, its generating function with respect to $n$ is given by [4]

$$\sum_{n=N-1}^{\infty} q_N(n) z^n = \frac{(1-\sqrt{1-z})^{N-1}}{\sqrt{1-z}} \ . \tag{59}$$

The result in Eq. (58) conveniently translates the results for any observable in the discrete-time $n$-step random walk problem to the RTP in continuous time $t$. The statistics of records is one such observable. Therefore, combining Eq. (58) gives (for $N \geq 2$)

$$S_N(t) = \int \frac{ds}{2\pi\, i} e^{s\,t}\, \frac{1}{\gamma} \sum_{n=N-1}^{\infty} \left(\frac{\gamma}{\gamma+s}\right)^n q_N(n) \tag{60}$$

where the integral is over the Bromwich contour (imaginary axis in this case). Recall that, for $N=1$, $S_1(t) = S(t)$ where $S(t)$ is given in Eq. (1) of the main text. Using (59) for $z = \gamma/(\gamma+s)$ in (60) one finds, for $N \geq 2$

$$S_N(t) = \int \frac{ds}{2\pi\, i} e^{s\,t}\, \frac{1}{\gamma} \sqrt{\frac{\gamma+s}{s}} \left(1 - \sqrt{\frac{s}{\gamma+s}}\right)^{N-1} \ . \tag{61}$$

The inverse Laplace transform on the right hand side of Eq. (61) can be performed explicitly for the first few values of $N$, yielding

$$S_1(t) = S(t) = \frac{1}{2} e^{-\gamma t/2} \left(I_0\left(\gamma t/2\right) + I_1\left(\gamma t/2\right)\right) \ , \tag{62}$$

$$S_2(t) = S(t) \ , \tag{63}$$

$$S_3(t) = e^{-\gamma t/2} I_1\left(\gamma t/2\right) \ . \tag{64}$$

The fact that $S_2(t) = S_1(t) = S(t)$ at all $t$ is quite remarkable and is far from obvious. These results for $N=2$ and $N=3$ are plotted in Fig. 4 and one sees that $S_3(t)$ exhibits a maximum at some characteristic time $t_3^*$ (actually for all $N \geq 3$, $S_N(t)$ exhibits a maximum at some characteristic time $t_N^*$ which can be shown to grow linearly with $N$ for large $N$). It seems hard to evaluate explicitly $S_N(t)$ for higher values of $N$. One can however compute the generating function $\tilde{S}(z,t)$ of $S_N(t)$, i.e.

$$\tilde{S}(z,t) = \sum_{N=1}^{\infty} z^N S_N(t) = \int \frac{ds}{2\pi\, i} e^{s\,\gamma t} \left[\frac{1+s}{s + \frac{1-z}{z}\sqrt{s(1+s)}} - z\right] \ , \tag{65}$$

where we have made the change of variable $s \to s/\gamma$. Clearly $S_N(t)$ is universal, i.e. independent of the dimension $d$ and the speed distribution $W(v)$. From this expression, we can compute the average number of records $\langle N(t) \rangle$ up to time $t$ and we get, for all $t$ (see also Fig. 3)

$$\langle N(t) \rangle = \frac{1}{2} e^{-\gamma t/2} \left((2\gamma t + 3) I_0\left(\frac{t}{2}\right) + (2\gamma t + 1) I_1\left(\frac{\gamma t}{2}\right)\right) \ . \tag{66}$$

For large $t$, it grows like $\langle N(t) \rangle \approx 2\sqrt{\gamma t}/\sqrt{\pi}$.

The Bromwich integral on the right hand side of Eq. (65) can be computed explicitly. Skipping details, we get

$$\tilde{S}(z,t) = \frac{z(1-z)}{1-2z} S(t) - \frac{z^3}{1-2z} e^{-\frac{(1-z)^2}{1-2z}\gamma t} - \frac{z^3(1-z)}{(1-2z)^2}\gamma \int_0^t e^{-\frac{(1-z)^2}{1-2z}\gamma(t-t')} S(t') dt' \ , \tag{67}$$

where $S(t)$ is given in Eq. (62). By setting $z=1$ in Eq. (67), we can check the normalization condition, i.e. $\sum_{N=1}^{\infty} S_N(t) = \tilde{S}(z=1,t) = 1$, for $t > 0$. We can also check, by expanding the generating function in (67) in powers of $z$ up to order $z^3$, that we recover the results for $S_N(t)$ for $N = 1,2,3$ in Eqs. (62-64). For generic $N$, we can check by expanding in powers of $z$ and performing the integral over $t'$ in Eq. (67) that, for all $N$, $S_N(t)$ has the following structure,

$$S_N(t) = e^{-\gamma t/2} \left(P_{0,N}(\gamma t) I_0(\gamma t/2) + P_{1,N}(\gamma t) I_1(\gamma t/2)\right) + e^{-\gamma t} Q_N(\gamma t) \ , \tag{68}$$

where $P_{0,N}(x), P_{1,N}(x)$ and $Q_N(x)$ are some polynomials.

One can also extract the asymptotic behaviors of $S_N(t)$ at small and large time $t$. At small time, from Eq. (60), one sees that the large $s$ behavior of the Laplace transform of $S_N(t)$ is $\sim \gamma^{N-2} q_{N-1}^N / s^{N-1}$, for $N \geq 2$. Using the known expression of $q_{N-1}^N = 2^{-N+1}$, from Ref. [4], one obtains

$$S_N(t) \sim \frac{(\gamma t)^{N-2}}{(N-2)!} q_{N-1}^N = \frac{1}{2^{N-1}(N-2)!} (\gamma t)^{N-2} \ . \tag{69}$$

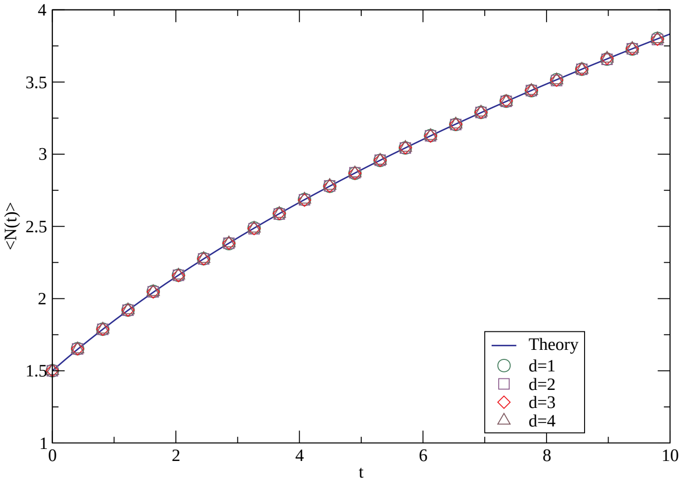

FIG. 3. Plot of the average number of records $\langle N(t)\rangle$ vs $t$. The solid line is given by the exact formula (66) while the symbols represent numerical simulations in $d = 1, 2, 3, 4$ with $\gamma = 1$ and $v_0 = 1$.

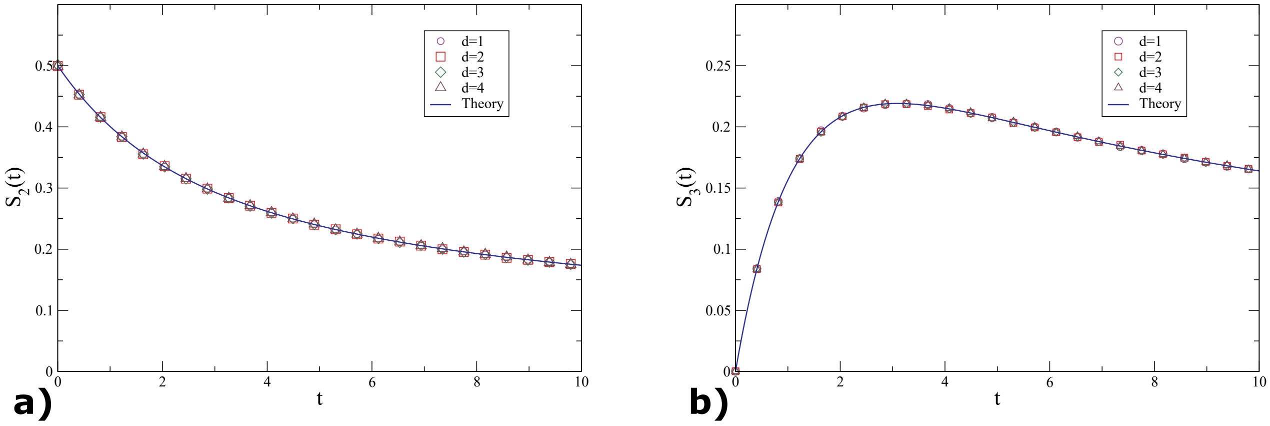

FIG. 4. Plot of $S_2(t)$ in (a) and $S_3(t)$ in (b) for different dimensions $d = 1, 2, 3$ and $d = 4$ (symbols correspond to numerical simulations) and an exponential distribution $p(\tau) = \gamma e^{-\gamma\tau}$ with $\gamma = 1$. The solid line corresponds to the exact results for $S_2(t) = S(t)$ in (63) and $S_3(t)$ in (64).

One sees explicitly that the small time behavior of $S_N(t)$ is dominated by trajectories where the RTP goes downwards at time $t$ and is breaks a record at time $t$.

The behavior of $S_N(t)$ for large time is easily obtained from the small $s$ of the Laplace transform in Eq. (61) and one finds, at leading order,

$$S_N(t) \sim \frac{1}{\sqrt{\pi\gamma t}} \ , \tag{70}$$

independently of $N$. This behavior indicates that $S_N(t)$ is dominated by the probability that, after breaking exactly $N$ lower records, the particle needs to stay above the value of the $N^{\rm th}$ record, which, for large $t$, coincides with the survival probability $S_1(t) \sim \frac{1}{\sqrt{\pi\gamma t}}$.

[1] E. Sparre Andersen, Math. Scand. **2**, 195 (1954).
[2] R. Artuso, G. Cristadoro, M. Degli Esposti and G. Knight, Phys. Rev. E **89**, 052111 (2014).

[3] C. Godrèche, S. N. Majumdar, and G. Schehr, J. Phys. A: Math. Theor. **50**, 333001 (2017).
[4] S. N. Majumdar, R. M. Ziff, Phys. Rev. Lett. **101**, 050601 (2008).

Cell Reports

Article

# Spatial consistency of cell growth direction during organ morphogenesis requires CELLULOSE SYNTHASE INTERACTIVE1

## Graphical abstract

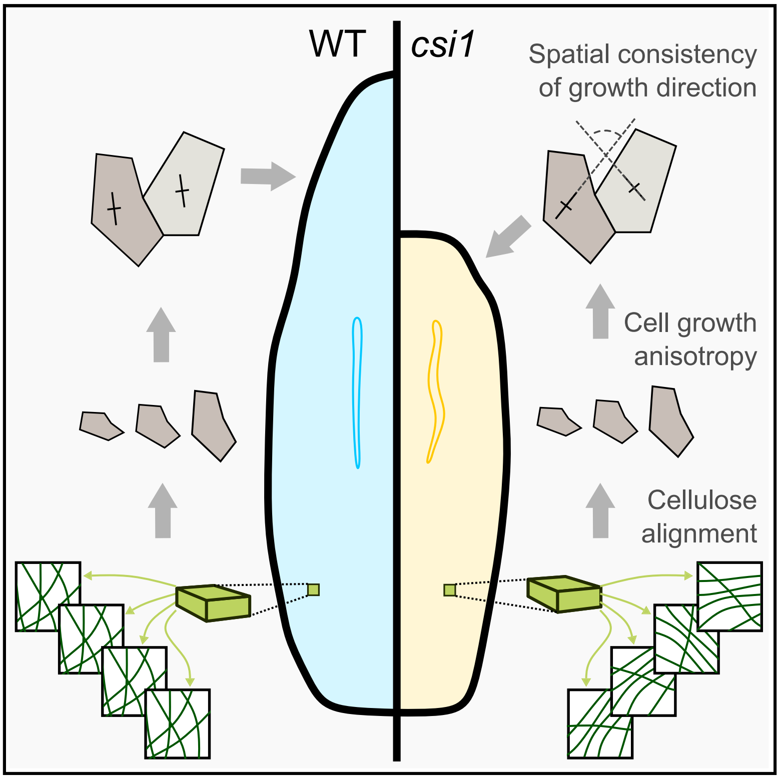

## Highlights

- *csi1* sepals are less elongated than WT, and their giant epidermal cells are snaky
- *csi1* sepals are mechanically less anisotropic than WT sepals
- Growth directions in *csi1* sepal cells are spatially less consistent than in WT
- CSI1 is required for spatial consistency of growth direction across the sepal

## Authors

Corentin Mollier, Joanna Skrzydeł,
Dorota Borowska-Wykręt, ...,
Françoise Monéger,
Dorota Kwiatkowska, Arezki Boudaoud

## Correspondence

dorota.kwiatkowska@us.edu.pl (D.K.),
arezki.boudaoud@polytechnique.edu
(A.B.)

## In brief

Mollier et al. show that elongation of *Arabidopsis* organs requires the maintenance of spatial consistency of growth direction across the organ, involving the guidance of cellulose synthesis into the plant extracellular matrix by CELLULOSE SYNTHASE INTERACTIVE1.

Mollier et al., 2023, Cell Reports *42*, 112689
July 25, 2023 © 2023 The Author(s).
https://doi.org/10.1016/j.celrep.2023.112689

CellPress

**Cell Reports**

CellPress OPEN ACCESS

Article

# Spatial consistency of cell growth direction during organ morphogenesis requires CELLULOSE SYNTHASE INTERACTIVE1

**Corentin Mollier,[1] Joanna Skrzydeł,[2] Dorota Borowska-Wykręt,[2] Mateusz Majda,[3,10] Vincent Bayle,[1] Virginie Battu,[1] Jean-Chrisologue Totozafy,[4] Mateusz Dulski,[5,6] Antoine Fruleux,[1,8] Roman Wrzalik,[5,7] Grégory Mouille,[4] Richard S. Smith,[3] Françoise Monéger,[1] Dorota Kwiatkowska,[2,*] and Arezki Boudaoud[1,9,11,*]**

[1]Reproduction et Développement des Plantes, Université de Lyon, ENS de Lyon, UCB Lyon 1, CNRS, INRAE, 69364 Lyon Cedex, France
[2]Faculty of Natural Sciences, Institute of Biology, Biotechnology and Environmental Protection, University of Silesia in Katowice, 40-032 Katowice, Poland
[3]John Innes Centre, Norwich Research Park, Colney Lane, Norwich NR4 7UH, UK
[4]Institut Jean-Pierre Bourgin, INRAE, AgroParisTech, Université Paris-Saclay, 78000 Versailles, France
[5]Silesian Center for Education and Interdisciplinary Research, University of Silesia in Katowice, 41-500 Chorzów, Poland
[6]Faculty of Science and Technology, Institute of Materials Engineering, University of Silesia in Katowice, 41-500 Chorzów, Poland
[7]August Chełkowski Institute of Physics, University of Silesia in Katowice, 41-500 Chorzów, Poland
[8]LPTMS, CNRS, Université Paris-Saclay, 91405 Orsay Cedex, France
[9]LadHyX, Ecole Polytechnique, CNRS, IP Paris, 91128 Palaiseau Cedex, France
[10]Present address: Department of Plant Molecular Biology, University of Lausanne, 1015 Lausanne, Switzerland
[11]Lead contact
*Correspondence: dorota.kwiatkowska@us.edu.pl (D.K.), arezki.boudaoud@polytechnique.edu (A.B.)
https://doi.org/10.1016/j.celrep.2023.112689

## SUMMARY

**Extracellular matrices contain fibril-like polymers often organized in parallel arrays. Although their role in morphogenesis has been long recognized, it remains unclear how the subcellular control of fibril synthesis translates into organ shape. We address this question using the *Arabidopsis* sepal as a model organ. In plants, cell growth is restrained by the cell wall (extracellular matrix). Cellulose microfibrils are the main load-bearing wall component, thought to channel growth perpendicularly to their main orientation. Given the key function of CELLULOSE SYNTHASE INTERACTIVE1 (CSI1) in guidance of cellulose synthesis, we investigate the role of CSI1 in sepal morphogenesis. We observe that sepals from *csi1* mutants are shorter, although their newest cellulose microfibrils are more aligned compared to wild-type. Surprisingly, cell growth anisotropy is similar in *csi1* and wild-type plants. We resolve this apparent paradox by showing that CSI1 is required for spatial consistency of growth direction across the sepal.**

## INTRODUCTION

Living organisms display an amazing variety of forms. Although a given form may be achieved through several morphogenetic trajectories, morphogenesis often involves elongation or anisotropic growth (i.e., increased growth along one axis of the organ). Elongated forms may result from coordinated cell rearrangements such as intercalation,[1,2] from patterned heterogeneity in the physical properties of cells,[3–6] or from guidance of growth by a matrix surrounding cells or tissues, usually a material reinforced by fibrils.[7–9] Here, we consider the link between fibril arrangement and elongation.

The nature of fibrils and the guidance of fibril synthesis largely vary between kingdoms. In several rod-shaped bacteria, the synthesis of peptidoglycans is guided by MreB, an actin homologue, following membrane curvature[10,11] and driving bacterial elongation. In *Drosophila* oocytes, microtubules guide the polar secretion of collagen in the surrounding epithelium.[8,9] Collagen deposition is associated with a global rotation of the oocyte inside the matrix, yielding a circumferential arrangement of fibrils and a mechanically anisotropic extracellular matrix, which is required for oocyte elongation.[7,12] Finally in plants, cells are surrounded by a cell wall composed of cellulose microfibrils embedded in a matrix of pectins, hemicelluloses, and structural proteins. Cellulose microfibrils may lead to mechanical anisotropy of the cell wall and channel growth.[13] Despite increasing knowledge about the link between cellulose microfibrils arrangement and cellular growth,[13–15] how this yields well-defined organ forms remains poorly understood.

Cellulose chains are polymerized at the plasma membrane by complexes of cellulose synthase (CESA) and bundle into microfibrils in the cell wall. CESA complexes are associated with other proteins, such as KORRIGAN, which is involved in targeting CESA to the membrane[16,17]; CELLULOSE COMPANION 1, which stabilizes the microtubules guiding the CESA[18]; and CELLULOSE SYNTHASE INTERACTIVE PROTEIN 1 (CSI1), which binds

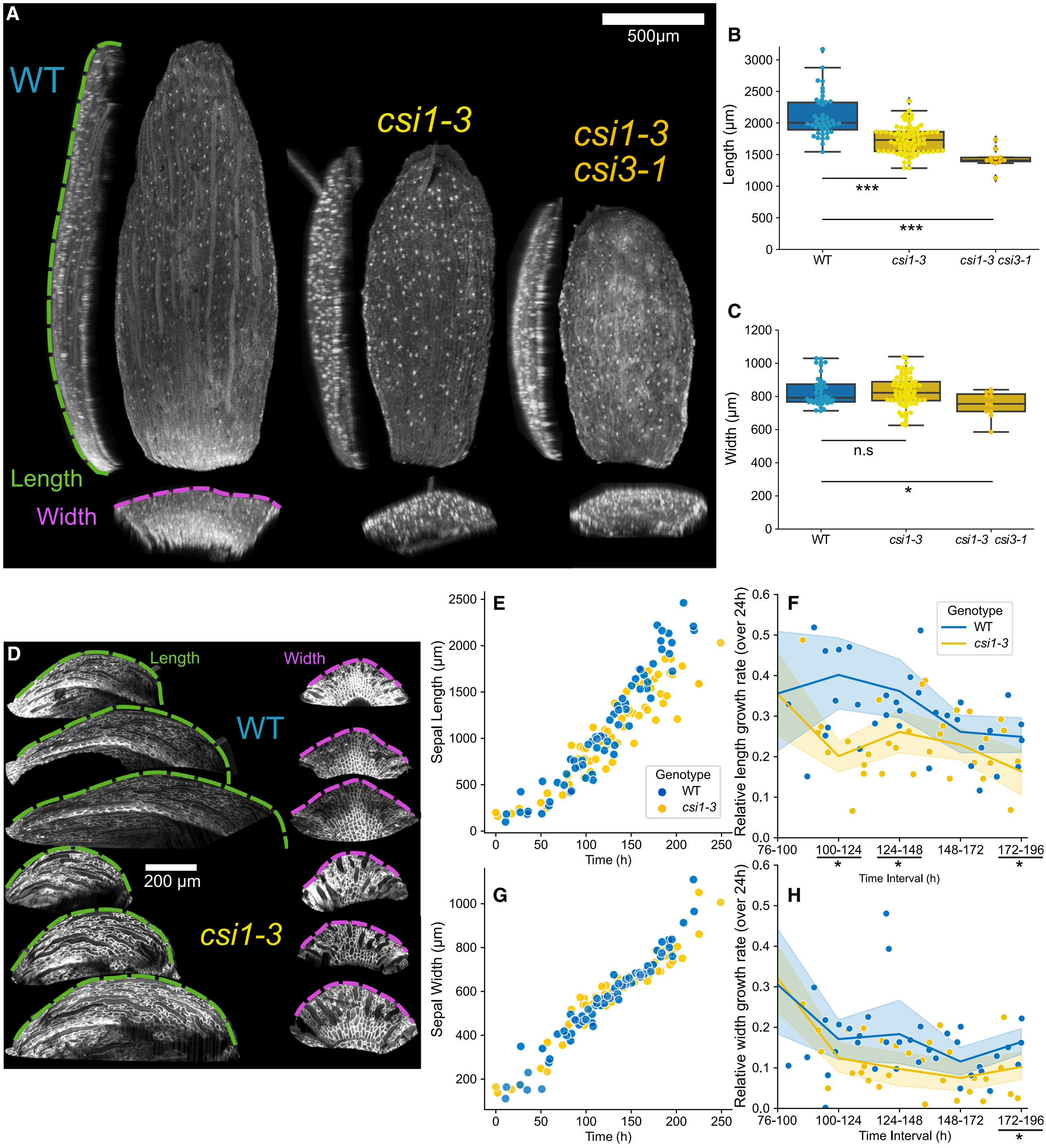

**Figure 1. *csi1* sepals are shorter because of reduced elongation rates**

(A) Representative front, top, and side views of WT, *csi1-3*, and *csi1-3 csi3-1* double mutant fully grown sepals (stage 12 of flower development), obtained from projections of confocal images. Cell walls were stained using propidium iodide. The dotted lines show sepal maximal width and length as measured along the outer (abaxial) surface of the sepal.

(B and C) Comparison of length and width among WT, *csi1-3*, and *csi1-3 csi3-1* double mutant sepals, measured as in (D) (n = 39, 67, and 11 sepals, respectively). t test p values between WT and *csi1-3* = $2 \times 10^{-11}$ and 0.93 for length and width, respectively. t test p values between WT and *csi1-3 csi3-1* double mutant = $3 \times 10^{-8}$ and 0.01 for length and width, respectively.

(D) Representative time series of sepal growth in WT (top) and *csi1-3* (bottom). Cell membranes are labeled using a *pATML1::RCI2A-mCitrine* construct. Colored dashed lines indicate measured sepal length and width. Time between acquisitions = 24 h.

*(legend continued on next page)*

microtubules and CESA complexes.[19–21] Two genes with functions related to *CSI1* have been identified: expression of *CSI2* is restricted to pollen, while mutations of *CSI3* alone yield no visible phenotype.[22] The function of CSI1 has been characterized in the cotyledon[23,24] (embryonic leaf) and in the hypocotyl (embryonic stem).[25] In the cotyledon of *csi1* mutants, the guidance of CESA complexes by microtubules is not lost[24] although detailed quantification of CESA complexes colocalization with cortical microtubules shows that the guidance is reduced in the mutant.[23] *csi1* mutants exhibit hyper aligned cellulose microfibrils in the hypocotyl,[25] probably because in the absence of microtubule guidance, CESA are mostly guided by previously deposited cellulose microfibrils.[26] Strangely, this hyperalignment of cellulose in *csi1* hypocotyls was not associated with longer hypocotyls, suggesting decreased cell/organ growth anisotropy[19,20] and calling into question the link between microfibrils alignment and anisotropic growth. In this work we addressed this link, from cellular to tissue scale.

Although the hypocotyl is an excellent system for plant cell biology, growth of etiolated hypocotyls is stereotyped[5] and mostly uniaxial, making it difficult to conclude about the relation between cellulose microfibrils deposition and growth direction in a morphogenetic context. We chose to investigate this relation in the *Arabidopsis* sepal, the green leaf-like organ that protects a flower before its opening. Sepal shape and size are robust,[27] despite variability in areal cell growth[28,29] and putatively in growth direction. We studied the links among cellulose organization, growth anisotropy, and main growth direction, from cell to organ scale, using *csi1* and other mutations to test our conclusions.

## RESULTS

### *csi1* sepals are shorter because of reduced elongation rates

Because *Arabidopsis* sepals are curved, we used three-dimensional (3D) confocal microscopy to quantify their shape parameters (Figure 1A). We found that *csi1-3* sepals were shorter compared with wild-type (WT) but had a similar width (Figures 1B and 1C). This phenotype was similar for the *csi1-6* allele and was rescued when complemented with *pCSI1::RFP-CSI1* (Figures S1A–S1C). We also compared mutant alleles between them and did not find any significant difference (see Table S1). The *csi3-1* mutant has been shown to present no phenotype, but the *csi3-1 csi1-3* double mutant is more affected than *csi1-3*, suggesting that CSI3 partially takes over the functions of CSI1 in *csi1-3*[22]. We therefore analyzed sepal shape in the *csi1-3 csi3-1* double mutant. We found sepals of *csi1-3 csi3-1* to be even shorter compared with *csi1-3* alone (Figure 1A). Altogether, these data show that sepal elongation involves *CSI1* and *CSI3* functions. Sepal contours (as seen from front, Figure 1A) also differed between genotypes, with for instance a narrower base for *csi1-3*. We quantified curvature and found that *csi1-3* sepals were significantly more curved compared with WT (Figures S1D and S1E). To understand the differences in final length between WT and *csi1-3* sepals, we considered sepal morphogenesis and performed live imaging of developing sepals (Figure 1D). As we used dissected inflorescences grown *in vitro*, we first checked whether our *in vitro* growth conditions produced similar organs compared with normally grown plants. We compared sepal length and width between inflorescences growing in the two conditions (Figure S1F). We found that sepal dimensions are similar throughout development showing that *in vitro* conditions do not affect sepal morphogenesis. In order to compare developmental trajectories between the two genotypes, WT and *csi1-3*, we developed a common temporal frame for all sepals. Because width is similar between WT and *csi1-3* sepals at a given developmental stage.[30] (stage 12 in Figure 1C; other stages in Figure S1G), we used width to shift the time of each live imaging sequence and put all sepals into the same time frame, further referred to as registered time (Figures S1H–S1K). The outcome is shown in Figures 1E and 1G, with a common initial time (0 h) that corresponds to stage 5 of flower development.

We found that sepal growth can be approximately decomposed in two different phases, see Figure S1F. In the first, overall sepal growth is isotropic, with length and width increasing similarly, up to a size of about 500 μm, corresponding to stage 7 of flower development (Figure S1G) and to a time of about 75 h in our registered time frame. Differences between WT and *csi1-3* are small in this isotropic growth phase. In the second phase, sepal growth is anisotropic and trajectories of WT and *csi1-3* appear to diverge (Figure S1F), which is most visible at stages 11 and 12 of flower development (Figures S1G and 1B). We quantified the rate of increase in dimensions of WT and *csi1-3* sepals during this second phase. We found no differences concerning width except for the last time interval (Figure 1H). Rate of increase in length is however smaller in *csi1-3* throughout development (Figure 1F) showing that sepals from *csi1-3* plants are shorter because they elongate less compared with the WT all along the second phase of sepal morphogenesis, and not because of an early arrest of growth.

### Giant cells in *csi1* sepals are snaky

When characterizing sepal morphology, we noticed altered cell shapes in *csi1*. More specifically, we observed that giant cells are approximately straight in WT whereas they are snaky in

---

(E and G) Sepal length (E) and width (G) as a function of time. Temporal sequences were registered with regard to time to define a common starting time using width, which can be mapped to developmental stages (see Figure S1).

(F and H) Relative growth rates in length (F) and width (H) as a function of registered time. Comparisons were made over a sliding 24 h window, which corresponds to the imaging interval. Asterisks at the bottom indicate significant differences (p value of Mann-Whitney test $< 0.05$, see exact p values and sample number in Table S1). WT is in blue and *csi1-3* in yellow. The lines correspond to median, the shading to the interquartile range, and the points to individual sepals. Here and elsewhere, the boxes extend from the first to the third quartiles of the distributions, the line inside the box indicates the median, the whiskers span the full range of the data (except when outliers are present, corresponding to points further than 1.5 × interquartile range from the corresponding quartile), and the points correspond to individual values. Statistical significance: n.s., non-significant; $^{*}p < 0.05$, $^{**}p < 0.005$, and $^{***}p < 0.0005$.
See also Figure S1.

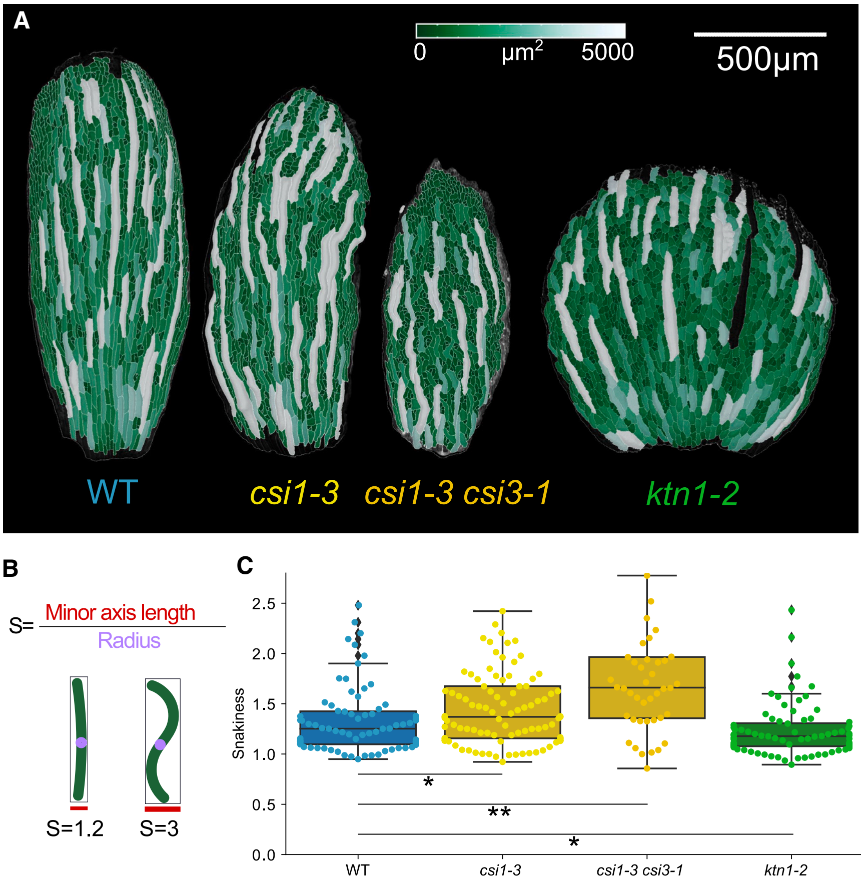

**Figure 2. *csi1* sepals have snaky giant cells**

(A) Representative confocal images of cells of WT, *csi1-3*, and *csi1-3 csi3-1* double mutant and *ktn1-2* mature sepals. Cell area is color coded.

(B) Illustration of the quantification of snakiness.

(C) Boxplot of the quantification of cell snakiness (n = 75 cells from 4 sepals for WT, 101 cells from 5 sepals for *csi1-3*, 44 cells from 3 sepals for *csi1-3 csi3-1* double mutant, 80 cells from 3 sepals for *ktn1-2*). p value of Mann-Whitney test = $8 \times 10^{-3}$, $6 \times 10^{-6}$, and $3 \times 10^{-2}$ for the comparison between WT and *csi1-3*, *csi1-3 csi3-1* double mutant and *ktn1-2*, respectively. Note that values for *ktn1-2* are smaller than for WT.

See also Figure S2.

*csi1-3* (Figure 2A). To quantify "snakiness" we computed the ratio between the small side of the rectangle that wraps the cell and the radius of the largest circle fitting inside the cell (Figure 2B). Cells that are straight will present similar values for these two parameters, while snaky cells will have the small side of the rectangle bigger than cell radius (Figure 2B). Following quantification, we observed that giant cells from *csi1-3* sepals are indeed more snaky than in WT (Figures 2A and 2C). This phenotype was similar for the *csi1-6* allele and rescued in the complementation of *csi1-6* with *pCSI1::RFP-CSI1* (Figures S2A and S2B). We compared mutant alleles between them and did not find any significant difference (see Table S1). We also analyzed cell shapes of the *csi1-3 csi3-1* double mutant which presented even higher levels of snakiness (Figures 2A and 2C). Because we wondered whether snakiness is associated with reduced sepal elongation, we considered the *katanin1-2* (*ktn1-2*) mutant, the sepals of which are even more rounded than in *csi1*.[31] We found that *ktn1-2* sepals do not present snaky cells, with lower levels of snakiness than in WT (Figures 2A and 2C). Accordingly, reduced elongation and cell snakiness are uncoupled. We also investigated changes in cell size between WT and *csi1-3* and found no significant differences during sepal morphogenesis (Figure S2C). Altogether, it appears that *CSI1* function is required to make giant cells straight. In order to understand the origin of snakiness, we then investigated cell growth in area and cell growth anisotropy.

## At cellular scale, neither areal growth nor growth anisotropy can explain differences in sepal length-to-width ratio

We sought to understand the cellular basis of the differences in sepal elongation rates. We first focused on the simplest aspect of growth: cell areal growth. We imaged sepals in dissected inflorescences with cellular resolution, segmented and tracked over time the surface of outer epidermal cells from the live imaging sequences of highest quality among those used for Figures 1E–1H (n = 4 for WT and for *csi1-3*). We quantified cell areal growth as the ratio of cell surface area between two consecutive time points (area at the second time point over the first time point, if a cell has divided, we fuse the daughter cells to compute this ratio). We found cell areal growth slightly higher in WT compared with *csi1-3* when looking at the whole sepal, which may explain the difference in final sepal area (Figures 3A and 3B). In order to test this, we built a geometric model to assess the effect of cell growth (see Data S1). Briefly, we described average sepal shape at each time point for WT and *csi1.* We gave the model the initial dimensions of WT and *csi1-3* sepals and grew the shapes on the basis of the measured average cellular growth. We thus predicted the final dimensions of sepals and compared these predictions to the final dimensions of sepals. In particular, the model predicted a value of 0.79 for the ratio of *csi1-3* final sepal area to WT final sepal area, in agreement with the estimation of 0.83 from observations of stage 12 sepals. Although these differences in areal growth explain the differences in area of mature sepals between *csi1* and WT, they are not informative about sepal shape.

We also examined whether a possible difference in base-to-tip growth gradient could explain the differences in sepal shape (Figures S3A and S3B). We found similar trends between WT and *csi1-3* growth gradients overall. We therefore examined other growth parameters.

Other parameters that could explain macroscopic differences are the main direction in which cells are growing (i.e., the direction of maximal growth), and the ratio of growth in this direction

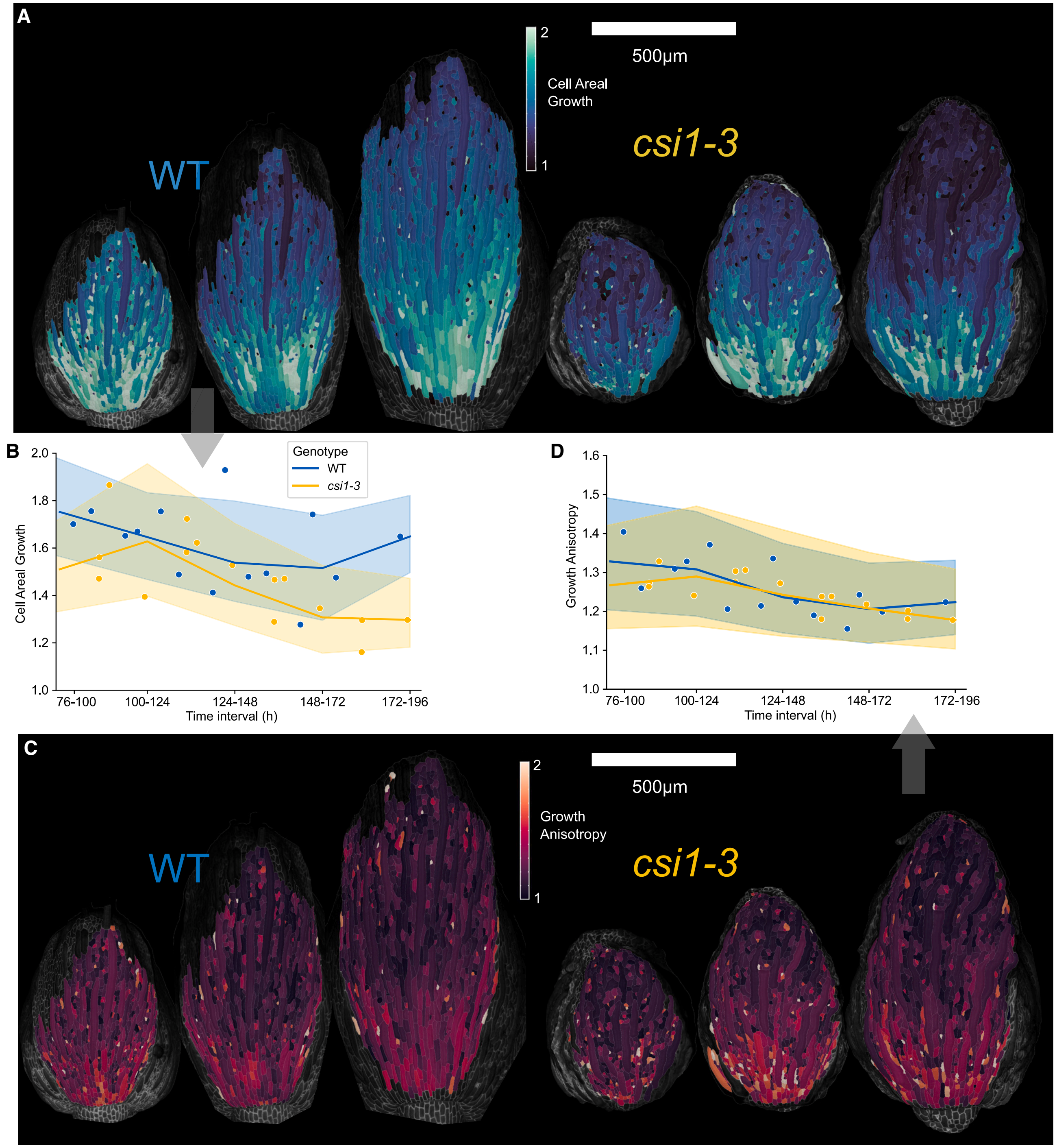

**Figure 3. Cell areal growth is slightly reduced in *csi1*, but cell growth anisotropy levels are similar**

(A) Top view of representative time series, with areal growth of cells color-coded. Growth was calculated as the ratio of cell surface area between consecutive time points. The first sepal images are at the beginning of the 100–124 h interval. Time between acquisitions = 24 h. The initial time point of each series was chosen so that sepals have similar width.

(B) Quantification of areal growth as a function of registered time, measured as shown in Figure 1F. The lines correspond to median, the shading to the interquartile range, and the points to average values for individual sepals (four series for each genotype). Time registration and symbols are the same as for panels Figures 1E–1H. n = 4 sepals for WT and *csi1-3*. p value of t test between sepal values = 0.1, 0.9, 0.5, and 0.2 for time intervals 76–100 h, 100–124 h, 124–148 h, and 148–172 h, respectively.

*(legend continued on next page)*

to growth in the perpendicular direction (i.e., the direction of minimal growth), which is known as cell growth anisotropy. Using the same live imaging data, we quantified cell growth anisotropy (Figures 3C and S3C). We found no strong differences between WT and *csi1-3* (Figure 3D). To assess this more quantitatively, we used our geometric model (Data S1), in which we grew sepals numerically using measured values of growth anisotropy and we predicted the final aspect ratio (length-to-width ratio) of sepals. The prediction of the change between WT and *csi1-3* final aspect ratio (reduction of 7%) was three times smaller than in observations (reduction of 19%), showing that cell growth anisotropy alone cannot account for differences in final sepal shape. We then reconsidered cell growth anisotropy and investigated its mechanistic basis by comparing cell wall structure between WT and *csi1-3*.

### Cellulose in *csi1* is more aligned in the most recently deposited layer compared to WT but is less aligned over the whole cell wall thickness

We compared cellulose microfibrils patterns between the cell walls of WT and *csi1-3* sepals. To expose the inner surface of the outer epidermal wall before imaging, we gently scratched inner sepal tissues and removed protoplasts using chemical treatment, until we had only the outer cell wall remaining. Because this method did not require grinding, this allowed us to ensure the observation of the external wall of the epidermis, as confirmed by optical microscopy (Figure S4A). We then used atomic force microscopy (AFM) to visualize recently deposited cellulose microfibrils in the outer wall of the abaxial epidermis of sepals[32]: a nanometer-sized probe was used to scan the protoplast-facing surface of the wall sample and measure the height of contact (Figures 4A, 4B, and S4B). Maps presented various orientations of microfibrils (Figures 4A and 4B). There was also a proportion of regions with only one apparent orientation (2 of 62 for WT, 12 of 100 for *csi1-3*), although the difference between these proportions was not significant (p value of normal $Z$ test = 0.08). Therefore, we developed an index to quantify to what extent the microfibrils are aligned (Figure 4C). Briefly, microfibrils orientation distribution was decomposed into Gaussians and the alignment index was computed as the normalized maximum angular distance between these Gaussians (Figure S7). For maps with only one obvious orientation this yields an index of 1, while maps with a less anisotropic orientation of microfibrils present indices closer to 0. We found that cellulose microfibrils were locally more aligned in *csi1-3* compared with WT. This weak but significant difference in cellulose alignment is consistent with the results on guidance of CESA by CSI1 in the hypocotyl.[19–21] Given the debate about CSI1 function in cotyledons,[23,24] we assessed whether CSI1 contributes to guidance of CESAs in the sepal. We used total internal reflection fluorescence (TIRF) microscopy to image simultaneously microtubules (*p35S::mCHERRY-TUA5*) and CESA (*pCESA3::GFP-CESA3*) localized close to the sepal surface, in WT or in the *csi1-1* mutant (Figure S4C). We found that the colocalization of CESA dots with cortical microtubules was not abolished in *csi1-1*, although significantly weaker than in WT (reduction of about 30%; Figure S4D). This suggests that, in sepals, CSI1 contributes to CESA guidance, while other mechanisms may partially compensate for the absence of CSI1, consistent with our results on recently synthesized cellulose microfibrils.

Higher anisotropy of microfibrils arrangement is usually associated with a higher cell growth anisotropy,[13–15] which would be expected to yield longer sepals. Surprisingly, higher anisotropy of microfibrils arrangement in *csi1-3* is associated with similar levels of cellular growth anisotropy. Because AFM only shows relatively small regions of the most recently deposited layer, we examined the cell wall in its entire thickness.

We first used cellulose staining with calcofluor white and confocal microscopy to examine cellulose at the scale of a few hundreds of nanometers (optical resolution). The staining was rather inhomogeneous and we could not detect any difference between *csi1-3* and WT sepals (Figure S4E). We then used Raman spectroscopy to study the wall at the scale of a micrometer (optical resolution for Raman microscopy). Polarized Raman microspectroscopy is an imaging mode that provides spatial information on the molecular structure of the cell wall, including crystallinity and, thanks to light polarization, main orientation of the functional groups of cell wall polymers.[33,34] Cellulose that forms microfibrils is an example of such polarization-sensitive polymer, as its chains can be strongly ordered (aligned) in the cell wall. This makes polarized Raman microspectroscopy well suited for the assessment of cellulose organization in the cell wall. We thus compared the Raman spectra of outer cell walls of *csi1-3* and WT sepal epidermis (Figures 4D, 4E, S4F, and S4G) with two reference samples composed of pure crystalline cellulose (Figure S4H) or pure amorphous cellulose (Figure S4I). We considered the integrated intensity ratio of two spectral bands: one centered at 1,096 $\mathrm{cm}^{-1}$ that is related to C-O-C linkages and the other centered at 2,898 $\mathrm{cm}^{-1}$, related to C-H and H-C-H linkages. If cellulose microfibrils are aligned, the signal intensity of these two bands is anticorrelated (one is maximal while the other is minimal, at the same polarizer angle).[35] We defined the 0° polarizer angle as that for which the signal of 1,096 $\mathrm{cm}^{-1}$ band attains the maximum value, and 90° as an angle of the minimal signal (Figures 4D, 4E, and S4F–S4I). First, we found that for the crystalline cellulose such computed signal intensity ratio changes dramatically when the polarizer angle changes, as expected for a highly organized material, depicting a strongly anisotropic cellulose arrangement (Figures 4F and S4H). Also as expected, amorphous cellulose

---

(C) Representative time series, with cellular growth anisotropy color coded. Growth anisotropy of a cell, computed as the ratio between growth in the maximal growth direction and growth in the minimal growth direction, was quantified on the basis of relative displacements of three-way wall junctions: a value of 1 means that growth is isotropic, and the highest values of anisotropy are above 2 (the color scale was capped at 2 to avoid saturation).

(D) Quantification of cellular growth anisotropy as a function of registered time, corresponding to all times series as in (C). WT is in blue and *csi1-3* in yellow. The lines correspond to median, the shading to the interquartile range, and the points to average values for individual sepals (four series for each genotype). n = 4 sepals for WT and *csi1-3*. p value of t test between sepal values: 0.2, 0.7, 0.9, 0.7 for time intervals 76–100 h, 100–124 h, 124–148 h, and 148–172 h, respectively. See also Figure S3.

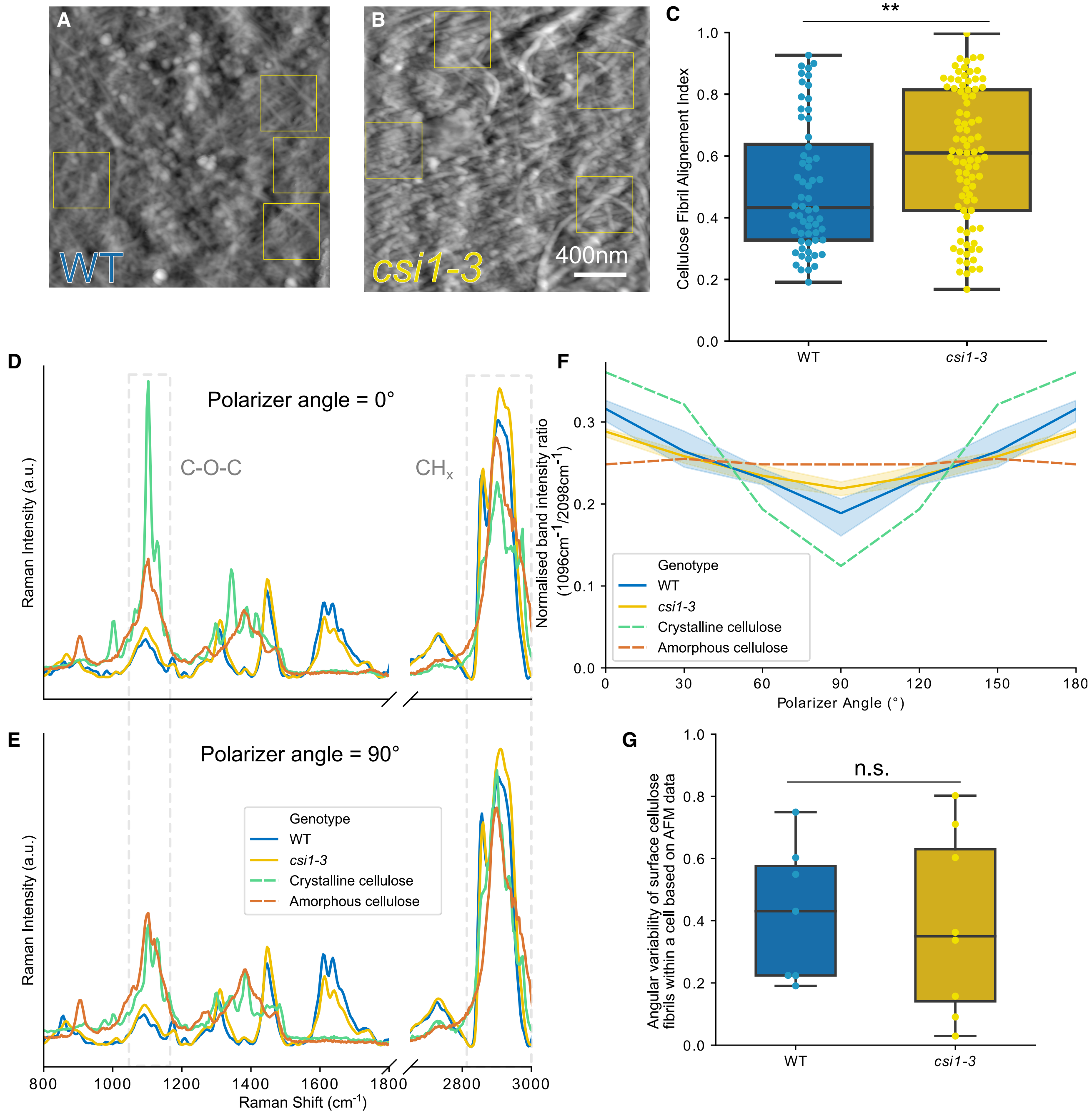

**Figure 4. Recently deposited cellulose microfibrils are more aligned in *csi1* than in wild-type (WT), whereas cellulose over the whole wall is less aligned in *csi1* than in WT**

(A and B) Representative height maps, obtained with atomic force microscopy (AFM), of WT and *csi1-3* outer epidermis cell wall imaged from the protoplast side after removing internal tissues and epidermis protoplasts of the sepal (maps corresponding to the median value of the alignment index for each genotype). Yellow squares outline regions used for the index assessment.

(C) Alignment index of cellulose microfibrils, with high values corresponding to more aligned microfibrils. Boxplots for WT and *csi1-3* (n = 5 and 6 stage 12 sepals and n = 60 and 89 regions of 400 × 400 nm from 9 and 14 cells, respectively; means = 0.5 and 0.59 for WT and *csi1-3*, respectively; p value of Mann-Whitney test = 0.005).

(D and E) Representative Raman spectra of cell walls from WT and *csi1-3* sepals and purified extract of crystalline and amorphous cellulose collected at different polarization angles (0° is shown in D and 90° in E). Spectrum fragments include two cellulose-specific bands: centered at 1,096 $cm^{-1}$ (related to C-O-C linkage), and at 2,898 $cm^{-1}$ ($CH_x$, x = 1,2 linkages).

*(legend continued on next page)*

presented no obvious maximum, but rather a constant signal intensity independent of the polarizer angle, indicating an isotropic material (Figures 4F and S4I). In both WT and *csi1-3*, changes in the signal intensity ratio lie between the reference samples indicating an intermediate anisotropy of cellulose microfibrils arrangement (Figure 4F). Furthermore, *csi1-3* cell wall is more similar to amorphous cellulose than WT cell wall (Figure 4F). This indicates that, at micrometric scale, the arrangement of cellulose is less anisotropic in *csi1-3* sepals.

We also investigated potential differences in cell wall composition that could affect growth, using high-performance anion-exchange chromatography coupled with pulsed amperometric detection (HPAEC-PAD). We did not observe any strong modification of the monosaccharide composition of the non-cellulosic compounds of the cell wall (with the exception of the fucose content, no difference was statistically significant) nor of the cellulose content in *csi1-3* when compared with the WT (Figure S4K).

### Temporal consistency of growth direction is weakly impaired in *csi1*

Considering that microfibrils arrangement in recently deposited wall layers in *csi1-3* is more anisotropic than in WT, we interpreted the Raman results as an indication that microfibrils orientation varies more either along the cell wall or across cell wall thickness in the mutant. To test this, we looked at variation along the surface of the cell wall in our AFM data. For cells that had several regions that were imaged with high cellulose microfibrils alignment, we measured the main microfibrils orientation on each map and quantified the circular variance associated with each cell (Figure 4G). We found no significant differences between WT and *csi1-3*, favoring the hypothesis that the differences observed between the AFM and the Raman results come from variations of cellulose microfibrils orientation across the thickness of the wall. If microfibrils orientation across the cell wall layer kept changing in *csi1*, we would expect cell growth to be less persistent over time (cells cannot maintain growth direction over a long period of time). Indeed, cell capacity to maintain a growth direction over extended periods of time likely depends on how long they are able to keep a consistent reinforcement of their cell walls (dependent on orientation of cellulose microfibrils).

As found above, neither variations in cell areal growth nor in cellular growth anisotropy explain differences in final organ shape between WT and *csi1-3*. We therefore tested whether temporal changes in growth direction may explain the macroscopic phenotype. To quantify temporal persistence of growth directions, we projected cell growth directions at consecutive time intervals (computed from 3 consecutive segmented images) on the image corresponding to the intermediate time point and quantified the angle between the two vectors corresponding to the maximal growth direction (Figures 5A–5C and S5A). We found temporal variations of growth direction to be higher in *csi1-3* cells compared with WT, with medians of 34° and 29°, respectively, however these differences were not significant when comparing sepals (see p values in the legend of Figure 5 and in Table S1). The microtubules that guide CESAs in WT are known to vary not only temporally but also spatially.[36,37] We thus decided to investigate how cells grow with respect to their neighbors as this may be affected in *csi1-3*.

### Spatial consistency of growth direction is lower in *csi1*

Given that *csi1* sepals present snaky giant cells, we hypothesized that there may be spatial changes in growth direction that explain the macroscopic phenotype. We assessed spatial consistency by measuring the angle between the directions of maximal growth of all pairs of neighboring cells (Figures 5D–5G). A small angle means that the two cells grow in a similar direction. In order to assess the meaning of these values, we computed a theoretical maximum for this angle. When we assigned random orientations to cell growth on a sepal mesh, we found a median of 45° for the angle between growth directions of two cells. In live imaging data, we found that the median angle between the main growth directions of cells in *csi1-3* is higher compared with WT, 30° and 25°, respectively (Figures 5G; Table S1). These values are smaller than 45°, which means that there is some level of spatial consistency in the two genotypes, with higher consistency for WT than for *csi1-3*. Because the definition of cell growth direction is not meaningful in the case of cells with nearly isotropic growth, we also computed the same metrics for cells with a growth anisotropy higher than a threshold of 1.4 and ended up with the same conclusion (Figure S5B). These results show that CSI1 plays a role in the spatial consistency of growth direction. Finally, we modified the geometric model to assess whether the differences in consistency of growth direction are sufficient to explain the differences in final sepal shape. We started from measured initial sepal dimensions; we used the values measured here for spatial variability in growth direction and implemented them as random variations in cell growth direction. Predicted final sepal dimensions are similar to the values measured experimentally (Data S1). In addition, this model predicted a reduction of 14% in length-to-width ratio, which better accounts for the observed reduction of 19% than without spatial variability of growth direction (prediction of 7%, see above). Additionally, weaker consistency of growth direction in *csi1-3*, compared with WT, may explain altered cell shape in *csi1-3*. Indeed, a group of cells on one side of a giant cell in

---

(F) Overall cellulose alignment in the outer epidermal cell walls assessed by ratio of integrated intensity changes from cellulose-specific bands accompanying polarizer angle changes in the 0°–180° range. Analysis of WT and *csi1-3* was compared with two reference samples: crystalline and amorphous cellulose. Each ratio value was normalized by the sum of all ratios for the sample to better illustrate the relative changes between samples. The values from 120° to 180° have been duplicated from the 0°–60° values to show periodicity. The lines correspond to median, the shading to the interquartile range for sepals. n = 4 sepals for WT and *csi1-3.* p values of Mann-Whitney test for each angle between WT and *csi1-3* = 0.02, 0.44, 0.33, and 0.02 for angles 0°, 30°, 60°, and 90°, respectively.

(G) Angular variability within a cell of the main cellulose microfibrils orientation on the wall surface facing the protoplast, computed on the basis of AFM maps obtained from individual cells. Angular variability is defined as the circular variance and is therefore bounded between 0 and 1. n = 7 and 8 sepals, for WT and *csi1-3*, respectively. p value of t test between values of angular variability in WT and *csi1-3* = 0.78.

See also Figure S4.

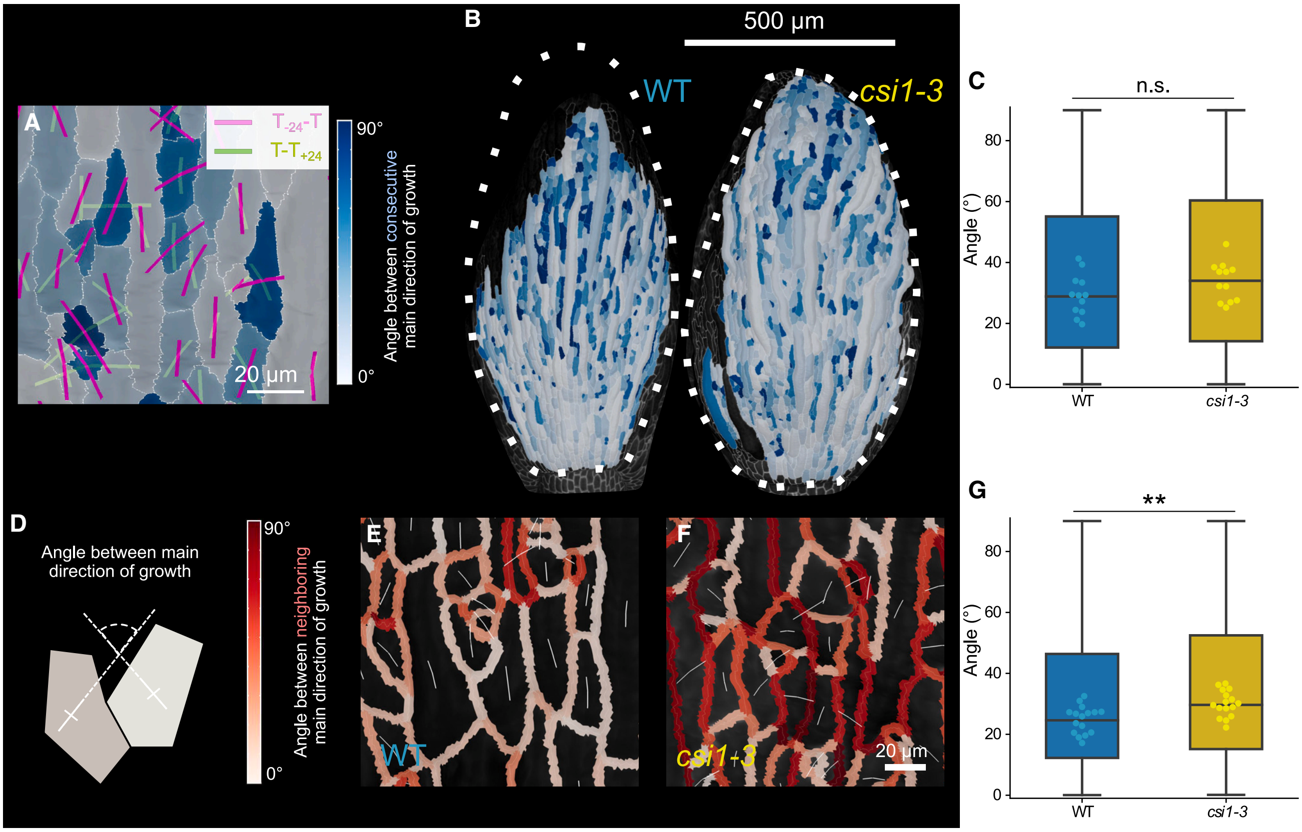

**Figure 5. Spatial consistency of growth direction is decreased in *csi1***

(A) Illustration of the quantification of temporal changes shown in (B and C). Maximal growth directions of the cells for the preceding time interval and for the following time interval are represented by magenta and green lines, respectively. Cells are colored depending on the angle between growth directions at consecutive time intervals. Color bar is the same as in (B).

(B) Representative maps with cell color coded depending on the angle between growth directions at consecutive time intervals. Sepals were partially segmented and their outer contours are indicated by the dashed white line.

(C) Angle between maximal growth directions at consecutive time intervals. Points represent the median angle for a given sepal. Boxplots were constructed using all cells. n = 4 sepals × 4 time points for each genotype. p value of t test between the values for sepals = 0.1.

(D) Schematic drawing explaining the quantification of spatial consistency of maximal growth direction shown in (E) and (F). The angle is measured between the 3D vectors corresponding to the maximal growth directions of each pair of neighboring cells.

(E and F) Representative images of maximal growth direction (white lines, with line length proportional to cell growth anisotropy) and of angle between growth directions of pairs of neighboring cells visualized by the color of their common anticlinal wall (the red color bar spans angles from 0° to 90°) in WT (E) and in *csi1-3* (F).

(G) Angle between maximal growth directions in neighboring cells. Boxplots were constructed using all pairs of neighboring cells. Points represent the median angles for individual sepals. n = 4 sepals × 4 time points for each genotype. p value of t test between the values for individual sepals = 0.002.

See also Figure S5.

*csi1* may grow nearly perpendicularly to the axis of the giant cell, while another group of cells, on the other side, could grow parallel to this axis, leading to the snaky phenotype. Snakiness is expected to be enhanced when the function of CSI1 is further impaired and this is indeed the case as shown for the *csi1-3 csi3-1* double mutant (Figure 2A).

We also examined spatial heterogeneity of cell areal growth. Differences in spatiotemporal correlations of areal growth between WT and *csi1* are expected to only affect variability of sepal contours and not average sepal aspect ratio.[27] However, they may play a role in the formation of snaky cells. Thus for each pair of neighboring cells we computed the ratio of the higher divided by the smaller areal growth of the two cells. We found no significant difference when comparing the ratio for WT and *csi1-3* sepals (Figure S5C).

## Sepal mechanical anisotropy is reduced in *csi1*

We next examined how the difference in sepal length-to-width ratio between WT and *csi1* could emerge from cell wall mechanics. *csi1-3* shows reduced anisotropy of cellulose arrangement across the outer abaxial cell wall and reduced spatial consistency in the abaxial epidermis. This would imply lower sepal mechanical anisotropy in *csi1-3* compared with WT, provided that observations on the abaxial epidermis extend to other cell layers or that the epidermis has a major role in sepal mechanics. We first examined sepal cross-sections with transmission

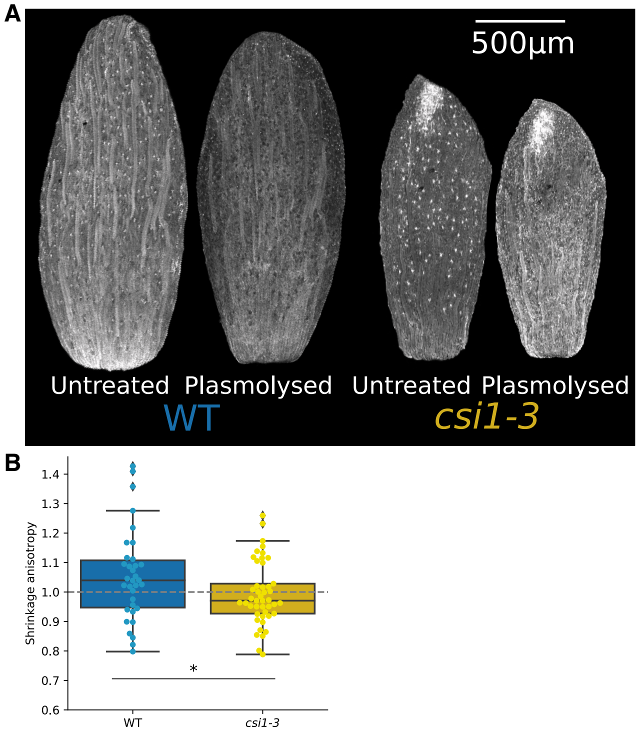

**Figure 6. *csi1* sepals are mechanically less anisotropic**

(A) Representative front view of sepals before and after plasmolysis in 0.4 M NaCl for 1 h.

(B) Boxplot of anisotropy of sepal shrinkage upon osmotic treatment. Points represent individual sepals (n = 33 sepals for WT, 43 for *csi1-3*, p value of t test = 0.04).

See also Figure S6.

electron microscopy and found that the external cell wall of the abaxial epidermis was much thicker than other walls, suggesting an important contribution of this wall to sepal mechanics. Interestingly, cell walls in *csi1-3* are thicker than in WT, which may explain reduced areal growth in the mutant (Figure S6A). Next, to assess differences in sepal mechanical anisotropy, we assessed shrinkage of the whole sepal upon osmotic treatment,[27] which integrates tissue mechanical properties across the width, length, and thickness of the sepal. We determined sepal shape parameters with our imaging pipeline (Figure 6A). We measured shrinkage in width (length) as the ratio of sepal width (length) after treatment to before treatment; we defined shrinkage anisotropy as the ratio of shrinkage in length to shrinkage in width (Figures 6B and S6B–S6D). We found significant differences between WT and *csi1-3* in the shrinkage in width (Figure S6D) but no differences in the shrinkage in length (Figure S6C). Consequently, *csi1-3* shrinks less anisotropically than WT (Figure 6B). We performed independent measurements of the mechanical properties in length via tensile testing[38] (Figure S6E). Sample mounting only allowed quantification of the properties along the long axis of the sepal. We measured the force required to deform sepals up to a controlled value of relative displacement (strain). At large strain values, *csi1-3* sepals appeared softer than WT sepals (Figure S6E). Nevertheless, the two genotypes appeared more similar at strain values in the range of osmotic treatments (Figure S6F). We therefore quantified the slope of the stress/strain curve in this lower range (Figure S6G) and we did not detect any difference in modulus between *csi1-3* and WT, consistent with shrinkage in length in osmotic treatments. Altogether, we conclude that sepal mechanical anisotropy is reduced in *csi1*.

## DISCUSSION

We investigated the link between the arrangement of cellulose microfibrils in the cell wall and sepal morphogenesis using the *csi1* mutant. We found that despite increased anisotropic arrangement of recently deposited cellulose microfibrils, sepals are less elongated in this mutant, similar to hypocotyls. This could not be ascribed to cell growth anisotropy alone which is comparable between *csi1* and WT. However, we found that growth directions in *csi1* cells are spatially less consistent and temporally slightly less persistent than in WT. This lack of consistency in *csi1* may explain shorter sepals and snaky cells and is likely associated with mechanically less anisotropic organs.

Although newly synthesized cellulose microfibrils in *csi1* hypocotyls appear highly aligned,[25] we observed that they were not as strongly aligned in *csi1* sepals. When guidance by cortical microtubules was impaired, previous studies showed that CESAs follow previous microfibrils, follow cortical microtubules, or move along a straight line.[26,39] In the *Arabidopsis* sepal, we found that the *csi1-1* mutation reduces colocalization of CESA with microtubules, suggesting less CESA moving along microtubules. The relative weight of these modes of CESA motion may depend on the organ, possibly because of different proteomes between the three types of organs,[40] potentially explaining differences in the *csi1* phenotype between hypocotyl, cotyledon, and sepal. In addition, other matrix polysaccharides are also likely involved in guidance of CESA.[41–43]

Here, we found that CSI1 does not influence the degree of cellular growth anisotropy but rather cell growth direction. Disruption of *CSI1* function increased spatial and temporal variations of growth direction. As proposed in,[26] synthesis along previous fibrils could provide memory of the wall state and help resisting perturbations by forming a template for CESA when cellulose synthesis starts again,[18,44,45] whereas guidance by microtubules provides the control needed for morphogenetic events[46] or to keep track of an organ-level direction of polarity. Similar ideas might extend to the extracellular matrix in animals, with regimes in which direction of matrix synthesis is steady,[47] and other regimes associated with morphogenetic events.[48,49]

How cells in a tissue all align in the same direction has been partly elucidated in animals. Cell polarity may be oriented by an instructive signal formed by a large-scale gradient or by polarity of neighboring cells via surface proteins.[50,51] Similar ideas have been proposed for plants,[50,52] in which the coupling between polarities of neighboring cells would involve a large set of actors.[53] Although CSI1 could have other functions than guidance, such as in delivery of CESA to the plasma membrane[54] and in regulation of microfibril length as observed for the secondary cell wall,[55] our work suggests that CSI1 contributes to growth coordination by translating cell polarity into growth direction, through CESA guidance by microtubules. Whereas we did not observe any twisting phenotype in sepal, *csi1* mutation leads to twisting of other organs such as the leaf,[55,56] hypocotyl or shoot.[57] Instead, *csi1* sepal featured snaky cells. Interestingly, *Drosophila* mutant oocytes with deficient polarity also show snaky cell files.[58] Organ twisting and cell snakiness could be interpreted as impaired orientation by large-scale instructive signals.

Plant hormones are good candidates for such organ-level signals. In particular, auxin presents gradients and its movement is polarly facilitated by PIN proteins,[59] notably in lateral organs such as the leaf.[60] PIN1 polarity is coupled with microtubule orientation,[61] supporting a potential role for auxin in orienting cell growth direction. Indeed, sepals with affected auxin polarity displayed reduced length,[62] although it is unclear whether this involves lack of consistency of growth direction. Mechanical stress is another potential organ-level instructive signal, and studies in animals suggest that it may orient cell polarity.[63,64] In plants, microtubules align with maximal stress direction,[37,65] which may explain the transverse orientations of microtubules seen in sepal.[36]

Here, we propose that during organ morphogenesis, the main role of guidance of CESA by microtubules is to enable growth direction to follow large-scale signals. Interestingly, chemical perturbation of the consistency of cortical microtubules orientation in the root reduces overall organ elongation.[66] We extend these results by describing consistency of cell growth direction and pinpoint the role of CSI1 in consistency. It would be worthwhile to examine whether similar ideas apply to elongation of animal organs. For instance, cell division is oriented during limb bud elongation in the mouse,[67] but the spatial consistency of division orientation has not been assessed.

Altogether, our work illustrates the potential of deciphering the basis of the robustness of morphogenesis by assessing spatial and temporal variability of growth and of its regulators, from subcellular to organ scale, and by combining experimental and theoretical approaches.

### Limitations of the study

The limitations of our study stem mainly from the cuticular ridges on the sepal surface and from the diffusion of light by the sepal. This makes it difficult to obtain information about internal cell walls or about internal cell layers using optical microscopy. Indeed we could not assess the degree of alignment of cellulose in internal walls nor cell growth in inner layers. Nevertheless, the sepal deflation assay integrates the effect of all cell layers. In addition, like in other studies, it is challenging to establish causal links between different spatial and temporal scales, because of difficulty to induce perturbations that are precisely controlled in space and time. We tried to address this issue by combining several experimental approaches and a geometrical model of sepal growth. This geometrical model accounts for average cell behavior but does not fully account for correlations between growth parameters of neighboring cells due to shared edges and vertices. We could conclude that consistency of cell growth direction is involved in overall organ elongation, but we could not fully assess the contribution of other growth parameters to the *csi1* phenotype.

## STAR★METHODS

Detailed methods are provided in the online version of this paper and include the following:

- KEY RESOURCES TABLE
- RESOURCE AVAILABILITY
    - ○ Lead contact
    - ○ Materials availability
    - ○ Data and code availability
- EXPERIMENTAL MODEL AND SUBJECT DETAILS
- METHOD DETAILS
    - ○ Confocal imaging and analysis
    - ○ Geometric model for sepal growth
    - ○ Atomic Force Microscopy (AFM)
    - ○ Raman spectroscopy
    - ○ Imaging of cellulose with confocal microscopy
    - ○ Assessment of cell wall thickness using electron microscopy
    - ○ Imaging of cellulose synthase complexes and cortical microtubules
    - ○ Cell wall monosaccharide composition
    - ○ Extensometry
- QUANTIFICATION AND STATISTICAL ANALYSIS
    - ○ Statistical analyses
    - ○ Cell and organ growth
    - ○ Quantification of cellulose microfibrils arrangement on protoplast-facing wall surface
    - ○ Analysis of colocalization of cellulose synthase complexes with cortical microtubules
    - ○ Spatial consistency of growth direction

## SUPPLEMENTAL INFORMATION

Supplemental information can be found online at https://doi.org/10.1016/j.celrep.2023.112689.

## ACKNOWLEDGMENTS

We acknowledge the contribution of SFR Biosciences (UAR3444/CNRS, US8/Inserm, ENS de Lyon, UCBL) imaging facility, PLATIM/Lymic. We acknowledge A. Lacroix, J. Berger, P. Bolland, H. Leyral, and I. Desbouchages for assistance with plant growth and logistics. We thank Mathilde Dumond and Justine Chabredier for the initial exploration of the *csi1* phenotype. We thank Olivier Hamant, Adrienne Roeder, and Christophe Tréhin for fruitful discussions and suggestions. We thank Yoshiharu Nishiyama for the generous gift of reference cellulose samples. We thank Ying Gu and Arun Sampathkumar for providing seeds of plant lines of interest. This work was funded by the French National Research Agency (ANR; grant ANR-17-CAPS-0002-01 V-Morph to A.B.), the National Science Centre, Poland (NCN; grant 2017/24/Z/NZ3/00548 to D.K.), and the German Research Foundation (DFG; grant 355722357 to R.S.S.) through a European ERA-NET Coordinating Action in Plant Sciences (ERA-CAPS) grant. This work was also directly funded by ANR (grants ANR-17-CE20-0023-02 WALLMIME and ANR-21-CE30-0039-01 GrowFlat to A.B.), by the National Science Centre, Poland (SHENG1 grant 2018/30/Q/NZ3/00189 to D.B.-W.), and by a BBSRC Institute Strategic Program Grant to the John Innes Center (BB/P013511/1). This work has benefited from a French State grant (Saclay Plant Sciences, reference ANR-17-EUR-0007, EUR SPS-GSR) managed by ANR under an Investments for the Future program integrated into France 2030 (reference ANR-11-IDEX-0003-02). This work has benefited from the support of IJPB's Plant Observatory technological platforms.

## AUTHOR CONTRIBUTIONS

Conceptualization, C.M., F.M., D.K., and A.B.; Methodology, C.M., J.S., D.B.-W., M.M., V. Bayle, M.D., A.F., R.W., G.M., D.K., and A.B.; Software, C.M., J.S., R.S.S., and D.K.; Modeling, A.B.; Validation, C.M., J.S., M.M., M.D., and G.M.; Formal Analysis, C.M., J.S., M.M., M.D., A.F., R.S.S., D.K., and A.B.; Investigation, C.M., J.S., D.B.-W., M.M., V. Battu, V. Bayle, J.C.-T., M.D., G.M., and D.K.; Data Curation, C.M., J.S., D.B.-W., M.M., M.D., G.M., and D.K.; Writing – Original Draft, C.M., F.M., and A.B.; Writing – Review & Editing, C.M., J.S., D.B.-W., V. Bayle, M.D., G.M., R.S.S., F.M., D.K., and A.B.; Visualization, C.M.; Supervision, G.M., R.S.S., F.M., D.K., and A.B.; Project Administration, R.S.S., D.K., and A.B.; Funding Acquisition, D.B.-W., R.S.S., D.K., and A.B.

## DECLARATION OF INTERESTS

The authors declare no competing interests.

Received: July 26, 2022
Revised: March 1, 2023
Accepted: June 9, 2023
Published: June 22, 2023

## REFERENCES

1. Rauzi, M., Verant, P., Lecuit, T., and Lenne, P.-F. (2008). Nature and anisotropy of cortical forces orienting Drosophila tissue morphogenesis. Nat. Cell Biol. *10*, 1401–1410. https://doi.org/10.1038/ncb1798.
2. Bertet, C., Sulak, L., and Lecuit, T. (2004). Myosin-dependent junction remodelling controls planar cell intercalation and axis elongation. Nature *429*, 667–671. https://doi.org/10.1038/nature02590.
3. Umeda, A., and Amako, K. (1983). Growth of the Surface of Corynebacterium diphtheriae. Microbiol. Immunol. *27*, 663–671. https://doi.org/10.1111/j.1348-0421.1983.tb00629.x.
4. Peaucelle, A., Wightman, R., and Höfte, H. (2015). The Control of Growth Symmetry Breaking in the Arabidopsis Hypocotyl. Curr. Biol. *25*, 1746–1752. https://doi.org/10.1016/j.cub.2015.05.022.
5. Bou Daher, F., Chen, Y., Bozorg, B., Clough, J., Jönsson, H., and Braybrook, S.A. (2018). Anisotropic growth is achieved through the additive mechanical effect of material anisotropy and elastic asymmetry. Elife *7*, e38161. https://doi.org/10.7554/eLife.38161.
6. Singh, A., Saha, T., Begemann, I., Ricker, A., Nüsse, H., Thorn-Seshold, O., Klingauf, J., Galic, M., and Matis, M. (2018). Polarized microtubule dynamics directs cell mechanics and coordinates forces during epithelial morphogenesis. Nat. Cell Biol. *20*, 1126–1133. https://doi.org/10.1038/s41556-018-0193-1.
7. Haigo, S.L., and Bilder, D. (2011). Global Tissue Revolutions in a Morphogenetic Movement Controlling Elongation. Science *331*, 1071–1074. https://doi.org/10.1126/science.1199424.
8. Isabella, A.J., and Horne-Badovinac, S. (2016). Rab10-Mediated Secretion Synergizes with Tissue Movement to Build a Polarized Basement Membrane Architecture for Organ Morphogenesis. Dev. Cell *38*, 47–60. https://doi.org/10.1016/j.devcel.2016.06.009.
9. Zajac, A.L., and Horne-Badovinac, S. (2022). Kinesin-directed secretion of basement membrane proteins to a subdomain of the basolateral surface in Drosophila epithelial cells. Curr. Biol. *32*, 735–748.e10. https://doi.org/10.1016/j.cub.2021.12.025.
10. White, C.L., and Gober, J.W. (2012). MreB: pilot or passenger of cell wall synthesis? Trends Microbiol. *20*, 74–79. https://doi.org/10.1016/j.tim.2011.11.004.
11. Shi, H., Bratton, B.P., Gitai, Z., and Huang, K.C. (2018). How to Build a Bacterial Cell: MreB as the Foreman of E. coli Construction. Cell *172*, 1294–1305. https://doi.org/10.1016/j.cell.2018.02.050.
12. Chlasta, J., Milani, P., Runel, G., Duteyrat, J.-L., Arias, L., Lamiré, L.A., Boudaoud, A., and Grammont, M. (2017). Variations in basement membrane mechanics are linked to epithelial morphogenesis. Development *144*, 4350–4362. https://doi.org/10.1242/dev.152652.
13. Green, P.B. (1962). Mechanism for Plant Cellular Morphogenesis. Science *138*, 1404–1405. https://doi.org/10.1126/science.138.3548.1404.
14. Suslov, D., and Verbelen, J.-P. (2006). Cellulose orientation determines mechanical anisotropy in onion epidermis cell walls. J. Exp. Bot. *57*, 2183–2192. https://doi.org/10.1093/jxb/erj177.
15. Baskin, T.I. (2005). Anisotropic expansion of the plant cell wall. Annu. Rev. Cell Dev. Biol. *21*, 203–222. https://doi.org/10.1146/annurev.cellbio.20.082503.103053.
16. Mansoori, N., Timmers, J., Desprez, T., Alvim-Kamei, C.L., Dees, D.C.T., Vincken, J.-P., Visser, R.G.F., Höfte, H., Vernhettes, S., and Trindade, L.M. (2014). KORRIGAN1 Interacts Specifically with Integral Components of the Cellulose Synthase Machinery. PLoS One *9*, e112387. https://doi.org/10.1371/journal.pone.0112387.
17. Robert, S., Bichet, A., Grandjean, O., Kierzkowski, D., Satiat-Jeunemaître, B., Pelletier, S., Hauser, M.-T., Höfte, H., and Vernhettes, S. (2005). An Arabidopsis Endo-1,4-β-d-Glucanase Involved in Cellulose Synthesis Undergoes Regulated Intracellular Cycling. Plant Cell *17*, 3378–3389. https://doi.org/10.1105/tpc.105.036228.
18. Endler, A., Kesten, C., Schneider, R., Zhang, Y., Ivakov, A., Froehlich, A., Funke, N., and Persson, S. (2015). A Mechanism for Sustained Cellulose Synthesis during Salt Stress. Cell *162*, 1353–1364. https://doi.org/10.1016/j.cell.2015.08.028.
19. Gu, Y., Kaplinsky, N., Bringmann, M., Cobb, A., Carroll, A., Sampathkumar, A., Baskin, T.I., Persson, S., and Somerville, C.R. (2010). Identification of a cellulose synthase-associated protein required for cellulose biosynthesis. Proc. Natl. Acad. Sci. USA *107*, 12866–12871. https://doi.org/10.1073/pnas.1007092107.
20. Bringmann, M., Li, E., Sampathkumar, A., Kocabek, T., Hauser, M.-T., and Persson, S. (2012). POM-POM2/CELLULOSE SYNTHASE INTERACTING1 Is Essential for the Functional Association of Cellulose Synthase and Microtubules in Arabidopsis. Plant Cell *24*, 163–177. https://doi.org/10.1105/tpc.111.093575.
21. Li, S., Lei, L., Somerville, C.R., and Gu, Y. (2012). Cellulose synthase interactive protein 1 (CSI1) links microtubules and cellulose synthase complexes. Proc. Natl. Acad. Sci. USA *109*, 185–190. https://doi.org/10.1073/pnas.1118560109.
22. Lei, L., Li, S., Du, J., Bashline, L., and Gu, Y. (2013). CELLULOSE SYNTHASE INTERACTIVE3 Regulates Cellulose Biosynthesis in Both a Microtubule-Dependent and Microtubule-Independent Manner in Arabidopsis. Plant Cell *25*, 4912–4923. https://doi.org/10.1105/tpc.113.116715.
23. Schneider, R., Ehrhardt, D.W., Meyerowitz, E.M., and Sampathkumar, A. (2022). Tethering of cellulose synthase to microtubules dampens mechano-induced cytoskeletal organization in Arabidopsis pavement cells. Nat. Plants *8*, 1064–1073. https://doi.org/10.1038/s41477-022-01218-7.
24. Belteton, S.A., Li, W., Yanagisawa, M., Hatam, F.A., Quinn, M.I., Szymanski, M.K., Marley, M.W., Turner, J.A., and Szymanski, D.B. (2021). Real-time conversion of tissue-scale mechanical forces into an interdigitated growth pattern. Nat. Plants *7*, 826–841. https://doi.org/10.1038/s41477-021-00931-z.
25. Xin, X., Lei, L., Zheng, Y., Zhang, T., Pingali, S.V., O'Neill, H., Cosgrove, D., Li, S., and Gu, Y. (2019). CELLULOSE SYNTHASE INTERACTIVE1- and Microtubule-Dependent Cell Wall Architecture Is Required for Acid Growth in Arabidopsis Hypocotyls. Preprint at bioRxiv. https://doi.org/10.1101/692202.
26. Chan, J., and Coen, E. (2020). Interaction between Autonomous and Microtubule Guidance Systems Controls Cellulose Synthase Trajectories. Curr. Biol. *30*, 941–947.e2. https://doi.org/10.1016/j.cub.2019.12.066.
27. Hong, L., Dumond, M., Tsugawa, S., Sapala, A., Routier-Kierzkowska, A.-L., Zhou, Y., Chen, C., Kiss, A., Zhu, M., Hamant, O., et al. (2016). Variable Cell Growth Yields Reproducible Organ Development through

Spatiotemporal Averaging. Dev. Cell *38*, 15–32. https://doi.org/10.1016/j.devcel.2016.06.016.

28. Meyer, H.M., Teles, J., Formosa-Jordan, P., Refahi, Y., San-Bento, R., Ingram, G., Jönsson, H., Locke, J.C.W., and Roeder, A.H.K. (2017). Fluctuations of the transcription factor ATML1 generate the pattern of giant cells in the Arabidopsis sepal. Elife *6*, e19131. https://doi.org/10.7554/eLife.19131.
29. Roeder, A.H.K., Chickarmane, V., Cunha, A., Obara, B., Manjunath, B.S., and Meyerowitz, E.M. (2010). Variability in the Control of Cell Division Underlies Sepal Epidermal Patterning in Arabidopsis thaliana. PLoS Biol. *8*, e1000367. https://doi.org/10.1371/journal.pbio.1000367.
30. Smyth, D.R., Bowman, J.L., and Meyerowitz, E.M. (1990). Early flower development in Arabidopsis. Plant Cell *2*, 755–767. https://doi.org/10.1105/tpc.2.8.755.
31. Hervieux, N., Tsugawa, S., Fruleux, A., Dumond, M., Routier-Kierzkowska, A.-L., Komatsuzaki, T., Boudaoud, A., Larkin, J.C., Smith, R.S., Li, C.-B., and Hamant, O. (2017). Mechanical Shielding of Rapidly Growing Cells Buffers Growth Heterogeneity and Contributes to Organ Shape Reproducibility. Curr. Biol. *27*, 3468–3479.e4. https://doi.org/10.1016/j.cub.2017.10.033.
32. Hanley, S., Giasson, J., Revol, J., and Gray, D. (1992). Atomic force microscopy of cellulose microfibrils: comparison with transmission electron microscopy. Polymer *33*, 4639–4642. https://doi.org/10.1016/0032-3861(92)90426-W.
33. Gierlinger, N., Luss, S., König, C., Konnerth, J., Eder, M., and Fratzl, P. (2010). Cellulose microfibril orientation of Picea abies and its variability at the micron-level determined by Raman imaging. J. Exp. Bot. *61*, 587–595. https://doi.org/10.1093/jxb/erp325.
34. Borowska-Wykręt, D., and Dulski, M. (2019). Raman Spectroscopy in Nonwoody Plants. In Plant Cell Morphogenesis: Methods and Protocols Methods in Molecular Biology, F. Cvrčková and V. Žárský, eds. (Springer), pp. 83–107. https://doi.org/10.1007/978-1-4939-9469-4_6.
35. Gierlinger, N., Reisecker, C., Hild, S., and Gamsjaeger, S. (2013). CHAPTER 7:Raman Microscopy: Insights into the Chemistry and Structure of Biological Materials. In Materials Design Inspired by Nature, pp. 151–179. https://doi.org/10.1039/9781849737555-00151.
36. Hervieux, N., Dumond, M., Sapala, A., Routier-Kierzkowska, A.-L., Kierzkowski, D., Roeder, A., Smith, R., Boudaoud, A., and Hamant, O. (2016). A Mechanical Feedback Restricts Sepal Growth and Shape in Arabidopsis. Curr. Biol. *26*, 1019–1028. https://doi.org/10.1016/j.cub.2016.03.004.
37. Burian, A., Ludynia, M., Uyttewaal, M., Traas, J., Boudaoud, A., Hamant, O., and Kwiatkowska, D. (2013). A correlative microscopy approach relates microtubule behaviour, local organ geometry, and cell growth at the Arabidopsis shoot apical meristem. J. Exp. Bot. *64*, 5753–5767. https://doi.org/10.1093/jxb/ert352.
38. Majda, M., Trozzi, N., Mosca, G., and Smith, R.S. (2022). How Cell Geometry and Cellular Patterning Influence Tissue Stiffness. Int. J. Mol. Sci. *23*, 5651. https://doi.org/10.3390/ijms23105651.
39. Duncombe, S.G., Chethan, S.G., and Anderson, C.T. (2022). Super-resolution imaging illuminates new dynamic behaviors of cellulose synthase. Plant Cell *34*, 273–286. https://doi.org/10.1093/plcell/koab227.
40. Mergner, J., Frejno, M., List, M., Papacek, M., Chen, X., Chaudhary, A., Samaras, P., Richter, S., Shikata, H., Messerer, M., et al. (2020). Mass-spectrometry-based draft of the Arabidopsis proteome. Nature *579*, 409–414. https://doi.org/10.1038/s41586-020-2094-2.
41. Yoneda, A., Higaki, T., Kutsuna, N., Kondo, Y., Osada, H., Hasezawa, S., and Matsui, M. (2007). Chemical Genetic Screening Identifies a Novel Inhibitor of Parallel Alignment of Cortical Microtubules and Cellulose Microfibrils. Plant Cell Physiol. *48*, 1393–1403. https://doi.org/10.1093/pcp/pcm120.
42. Yoneda, A., Ito, T., Higaki, T., Kutsuna, N., Saito, T., Ishimizu, T., Osada, H., Hasezawa, S., Matsui, M., and Demura, T. (2010). Cobtorin target analysis reveals that pectin functions in the deposition of cellulose microfibrils in parallel with cortical microtubules. Plant J. *64*, 657–667. https://doi.org/10.1111/j.1365-313X.2010.04356.x.
43. Xiao, C., Zhang, T., Zheng, Y., Cosgrove, D.J., and Anderson, C.T. (2016). Xyloglucan Deficiency Disrupts Microtubule Stability and Cellulose Biosynthesis in Arabidopsis, Altering Cell Growth and Morphogenesis. Plant Physiol. *170*, 234–249. https://doi.org/10.1104/pp.15.01395.
44. Himmelspach, R., Williamson, R.E., and Wasteneys, G.O. (2003). Cellulose microfibril alignment recovers from DCB-induced disruption despite microtubule disorganization. Plant J. *36*, 565–575. https://doi.org/10.1046/j.1365-313X.2003.01906.x.
45. Liu, Z., Schneider, R., Kesten, C., Zhang, Y., Somssich, M., Zhang, Y., Fernie, A.R., and Persson, S. (2016). Cellulose-Microtubule Uncoupling Proteins Prevent Lateral Displacement of Microtubules during Cellulose Synthesis in Arabidopsis. Dev. Cell *38*, 305–315. https://doi.org/10.1016/j.devcel.2016.06.032.
46. Sassi, M., Ali, O., Boudon, F., Cloarec, G., Abad, U., Cellier, C., Chen, X., Gilles, B., Milani, P., Friml, J., et al. (2014). An Auxin-Mediated Shift toward Growth Isotropy Promotes Organ Formation at the Shoot Meristem in Arabidopsis. Curr. Biol. *24*, 2335–2342. https://doi.org/10.1016/j.cub.2014.08.036.
47. Matsubayashi, Y., Sánchez-Sánchez, B.J., Marcotti, S., Serna-Morales, E., Dragu, A., Díaz-de-la-Loza, M.D.C., Vizcay-Barrena, G., Fleck, R.A., and Stramer, B.M. (2020). Rapid Homeostatic Turnover of Embryonic ECM during Tissue Morphogenesis. Dev. Cell *54*, 33–42.e9. https://doi.org/10.1016/j.devcel.2020.06.005.
48. Loganathan, R., Potetz, B.R., Rongish, B.J., and Little, C.D. (2012). Spatial Anisotropies and Temporal Fluctuations in Extracellular Matrix Network Texture during Early Embryogenesis. PLoS One *7*, e38266. https://doi.org/10.1371/journal.pone.0038266.
49. Proag, A., Monier, B., and Suzanne, M. (2019). Physical and functional cell-matrix uncoupling in a developing tissue under tension. Development *146*, dev172577. https://doi.org/10.1242/dev.172577.
50. Abley, K., De Reuille, P.B., Strutt, D., Bangham, A., Prusinkiewicz, P., Marée, A.F.M., Grieneisen, V.A., and Coen, E. (2013). An intracellular partitioning-based framework for tissue cell polarity in plants and animals. Development *140*, 2061–2074. https://doi.org/10.1242/dev.062984.
51. Nissen, S.B., Rønhild, S., Trusina, A., and Sneppen, K. (2018). Theoretical tool bridging cell polarities with development of robust morphologies. Elife *7*, e38407. https://doi.org/10.7554/eLife.38407.
52. Kuchen, E.E., Fox, S., de Reuille, P.B., Kennaway, R., Bensmihen, S., Avondo, J., Calder, G.M., Southam, P., Robinson, S., Bangham, A., and Coen, E. (2012). Generation of Leaf Shape Through Early Patterns of Growth and Tissue Polarity. Science *335*, 1092–1096. https://doi.org/10.1126/science.1214678.
53. Xu, T., Wen, M., Nagawa, S., Fu, Y., Chen, J.-G., Wu, M.-J., Perrot-Rechenmann, C., Friml, J., Jones, A.M., and Yang, Z. (2010). Cell Surface- and Rho GTPase-Based Auxin Signaling Controls Cellular Interdigitation in Arabidopsis. Cell *143*, 99–110. https://doi.org/10.1016/j.cell.2010.09.003.
54. Zhu, X., Li, S., Pan, S., Xin, X., and Gu, Y. (2018). CSI1, PATROL1, and exocyst complex cooperate in delivery of cellulose synthase complexes to the plasma membrane. Proc. Natl. Acad. Sci. USA *115*, E3578–E3587. https://doi.org/10.1073/pnas.1800182115.
55. Bünder, A., Sundman, O., Mahboubi, A., Persson, S., Mansfield, S.D., Rüggeberg, M., and Niittylä, T. (2020). CELLULOSE SYNTHASE INTERACTING 1 is required for wood mechanics and leaf morphology in aspen. Plant J. *103*, 1858–1868. https://doi.org/10.1111/tpj.14873.
56. Yang, Q., Wan, X., Wang, J., Zhang, Y., Zhang, J., Wang, T., Yang, C., and Ye, Z. (2020). The loss of function of HEL, which encodes a cellulose synthase interactive protein, causes helical and vine-like growth of tomato. Hortic. Res. *7*, 180. https://doi.org/10.1038/s41438-020-00402-0.
57. Landrein, B., Lathe, R., Bringmann, M., Vouillot, C., Ivakov, A., Boudaoud, A., Persson, S., and Hamant, O. (2013). Impaired Cellulose Synthase Guidance Leads to Stem Torsion and Twists Phyllotactic Patterns in Arabidopsis. Curr. Biol. *23*, 895–900. https://doi.org/10.1016/j.cub.2013.04.013.

58. Carvajal-Gonzalez, J.M., Balmer, S., Mendoza, M., Dussert, A., Collu, G., Roman, A.-C., Weber, U., Ciruna, B., and Mlodzik, M. (2015). The clathrin adaptor AP-1 complex and Arf1 regulate planar cell polarity in vivo. Nat. Commun. *6*, 6751–6766. https://doi.org/10.1038/ncomms7751.

59. Nemhauser, J.L., Feldman, L.J., and Zambryski, P.C. (2000). Auxin and ETTIN in Arabidopsis gynoecium morphogenesis. Development *127*, 3877–3888. https://doi.org/10.1242/dev.127.18.3877.

60. Mansfield, C., Newman, J.L., Olsson, T.S.G., Hartley, M., Chan, J., and Coen, E. (2018). Ectopic BASL Reveals Tissue Cell Polarity throughout Leaf Development in Arabidopsis thaliana. Curr. Biol. *28*, 2638–2646.e4. https://doi.org/10.1016/j.cub.2018.06.019.

61. Heisler, M.G., Hamant, O., Krupinski, P., Uyttewaal, M., Ohno, C., Jönsson, H., Traas, J., and Meyerowitz, E.M. (2010). Alignment between PIN1 Polarity and Microtubule Orientation in the Shoot Apical Meristem Reveals a Tight Coupling between Morphogenesis and Auxin Transport. PLoS Biol. *8*, e1000516. https://doi.org/10.1371/journal.pbio.1000516.

62. Yamaguchi, N., Wu, M.-F., Winter, C.M., and Wagner, D. (2014). LEAFY and Polar Auxin Transport Coordinately Regulate Arabidopsis Flower Development. Plants *3*, 251–265. https://doi.org/10.3390/plants3020251.

63. Dye, N.A., Popović, M., Iyer, K.V., Fuhrmann, J.F., Piscitello-Gómez, R., Eaton, S., and Jülicher, F. (2021). Self-organized patterning of cell morphology via mechanosensitive feedback. Elife *10*, e57964. https://doi.org/10.7554/eLife.57964.

64. Martin, E., Theis, S., Gay, G., Monier, B., Rouvière, C., and Suzanne, M. (2021). Arp2/3-dependent mechanical control of morphogenetic robustness in an inherently challenging environment. Dev. Cell *56*, 687–701.e7. https://doi.org/10.1016/j.devcel.2021.01.005.

65. Hamant, O., Heisler, M.G., Jönsson, H., Krupinski, P., Uyttewaal, M., Bokov, P., Corson, F., Sahlin, P., Boudaoud, A., Meyerowitz, E.M., et al. (2008). Developmental Patterning by Mechanical Signals in Arabidopsis. Science *322*, 1650–1655. https://doi.org/10.1126/science.1165594.

66. Baskin, T.I., Beemster, G.T.S., Judy-March, J.E., and Marga, F. (2004). Disorganization of Cortical Microtubules Stimulates Tangential Expansion and Reduces the Uniformity of Cellulose Microfibril Alignment among Cells in the Root of Arabidopsis. Plant Physiol. *135*, 2279–2290. https://doi.org/10.1104/pp.104.040493.

67. Boehm, B., Westerberg, H., Lesnicar-Pucko, G., Raja, S., Rautschka, M., Cotterell, J., Swoger, J., and Sharpe, J. (2010). The Role of Spatially Controlled Cell Proliferation in Limb Bud Morphogenesis. PLoS Biol. *8*, e1000420. https://doi.org/10.1371/journal.pbio.1000420.

68. Alonso, J.M., Stepanova, A.N., Leisse, T.J., Kim, C.J., Chen, H., Shinn, P., Stevenson, D.K., Zimmerman, J., Barajas, P., Cheuk, R., et al. (2003). Genome-wide insertional mutagenesis of Arabidopsis thaliana. Science *301*, 653–657. https://doi.org/10.1126/science.1086391.

69. McElver, J., Tzafrir, I., Aux, G., Rogers, R., Ashby, C., Smith, K., Thomas, C., Schetter, A., Zhou, Q., Cushman, M.A., et al. (2001). Insertional mutagenesis of genes required for seed development in Arabidopsis thaliana. Genetics *159*, 1751–1763.

70. Barbier de Reuille, P., Routier-Kierzkowska, A.-L., Kierzkowski, D., Bassel, G.W., Schüpbach, T., Tauriello, G., Bajpai, N., Strauss, S., Weber, A., Kiss, A., et al. (2015). MorphoGraphX: A platform for quantifying morphogenesis in 4D. Elife *4*, e05864. https://doi.org/10.7554/eLife.05864.

71. Ruel, K., Nishiyama, Y., and Joseleau, J.-P. (2012). Crystalline and amorphous cellulose in the secondary walls of Arabidopsis. Plant Sci. *193–194*, 48–61. https://doi.org/10.1016/j.plantsci.2012.05.008.

72. Hamant, O., Das, P., and Burian, A. (2019). Time-Lapse Imaging of Developing Shoot Meristems Using A Confocal Laser Scanning Microscope. In Plant Cell Morphogenesis: Methods and Protocols Methods in Molecular Biology, F. Cvrčková and V. Žárský, eds. (Springer), pp. 257–268. https://doi.org/10.1007/978-1-4939-9469-4_17.

73. Goodall, C.R., and Green, P.B. (1986). Quantitative Analysis of Surface Growth. Bot. Gaz. *147*, 1–15. https://doi.org/10.1086/337562.

74. Wuyts, N., Palauqui, J.-C., Conejero, G., Verdeil, J.-L., Granier, C., and Massonnet, C. (2010). High-contrast three-dimensional imaging of the Arabidopsis leaf enables the analysis of cell dimensions in the epidermis and mesophyll. Plant Methods *6*, 17. https://doi.org/10.1186/1746-4811-6-17.

75. Imoto, A., Yamada, M., Sakamoto, T., Okuyama, A., Ishida, T., Sawa, S., and Aida, M. (2021). A ClearSee-Based Clearing Protocol for 3D Visualization of Arabidopsis thaliana Embryos. Plants *10*, 190. https://doi.org/10.3390/plants10020190.

76. Lipowczan, M., Borowska-Wykręt, D., Natonik-Białoń, S., and Kwiatkowska, D. (2018). Growing cell walls show a gradient of elastic strain across their layers. J. Exp. Bot. *69*, 4349–4362. https://doi.org/10.1093/jxb/ery237.

77. Hong, L., Brown, J., Segerson, N.A., Rose, J.K.C., and Roeder, A.H.K. (2017). CUTIN SYNTHASE 2 Maintains Progressively Developing Cuticular Ridges in Arabidopsis Sepals. Mol. Plant *10*, 560–574. https://doi.org/10.1016/j.molp.2017.01.002.

78. Lebecq, A., Doumane, M., Fangain, A., Bayle, V., Leong, J.X., Rozier, F., Marques-Bueno, M.D., Armengot, L., Boisseau, R., Simon, M.L., et al. (2022). The Arabidopsis SAC9 enzyme is enriched in a cortical population of early endosomes and restricts PI(4,5)P2 at the plasma membrane. Elife *11*, e73837. https://doi.org/10.7554/eLife.73837.

79. Fang, L., Ishikawa, T., Rennie, E.A., Murawska, G.M., Lao, J., Yan, J., Tsai, A.Y.-L., Baidoo, E.E.K., Xu, J., Keasling, J.D., et al. (2016). Loss of Inositol Phosphorylceramide Sphingolipid Mannosylation Induces Plant Immune Responses and Reduces Cellulose Content in Arabidopsis. Plant Cell *28*, 2991–3004. https://doi.org/10.1105/tpc.16.00186.

80. Virtanen, P., Gommers, R., Oliphant, T.E., Haberland, M., Reddy, T., Cournapeau, D., Burovski, E., Peterson, P., Weckesser, W., Bright, J., et al. (2020). SciPy 1.0: fundamental algorithms for scientific computing in Python. Nat. Methods *17*, 261–272. https://doi.org/10.1038/s41592-019-0686-2.

81. Hartasánchez, D.A., Kiss, A., Battu, V., Dumond, M., Soraru, C., Delgado-Vaquera, A., Massinon, F., Brasó-Vives, M., Mollier, C., Dubrulle, N., et al. (2022). Robustness of organ morphology is associated with modules of co-expressed genes related to plant cell wall. Preprint at bioRxiv. https://doi.org/10.1101/2022.04.26.489498.

82. Robitaille, T.P., Tollerud, E.J., Greenfield, P., Droettboom, M., Bray, E., Aldcroft, T., Davis, M., Ginsburg, A., Price-Whelan, A.M., Kerzendorf, W.E., et al. (2013). Astropy: A community Python package for astronomy. Astron. Astrophys. *558*, A33. https://doi.org/10.1051/0004-6361/201322068.

83. The Astropy Collaboration; Price-Whelan, A.M., Sipőcz, B.M., Günther, H.M., Lim, P.L., Crawford, S.M., Conseil, S., Shupe, D.L., Craig, M.W., Dencheva, N., et al. (2018). The Astropy Project: Building an inclusive, open-science project and status of the v2.0 core package. Astron. J. *156*, 123. https://doi.org/10.3847/1538-3881/aabc4f.

84. Bolte, S., and Cordelières, F.P. (2006). A guided tour into subcellular colocalization analysis in light microscopy. J. Microsc. *224*, 213–232. https://doi.org/10.1111/j.1365-2818.2006.01706.x.

85. Dunn, K.W., Kamocka, M.M., and McDonald, J.H. (2011). A practical guide to evaluating colocalization in biological microscopy. Am. J. Physiol. Cell Physiol. *300*, C723–C742. https://doi.org/10.1152/ajpcell.00462.2010.

86. Manders, E.M.M., Verbeek, F.J., and Aten, J.A. (1993). Measurement of co-localization of objects in dual-colour confocal images. J. Microsc. *169*, 375–382. https://doi.org/10.1111/j.1365-2818.1993.tb03313.x.

87. Costes, S.V., Daelemans, D., Cho, E.H., Dobbin, Z., Pavlakis, G., and Lockett, S. (2004). Automatic and Quantitative Measurement of Protein-Protein Colocalization in Live Cells. Biophys. J. *86*, 3993–4003. https://doi.org/10.1529/biophysj.103.038422.

## STAR★METHODS

### KEY RESOURCES TABLE

| REAGENT or RESOURCE | SOURCE | IDENTIFIER |
|---|---|---|
| Chemicals, Peptides, and Recombinant Proteins | | |
| Apex culture medium (ACM, MS basal salt) | Duchefa Biochemie | M0221.0010 |
| Plant preservation mixture (PPM) | Plant Cell Technology | KY-PPM100 |
| Chloroform | Chempur | CAS 67-66-3 |
| Sodium dodecyl sulfate | Sigma | CAS 151-21-3 |
| α-amylase | Sigma-Aldrich | CAS 9014-01-1 |
| Chloral hydrate | Aldrich | CAS 302-17-0 |
| Pectinase from Aspergillus niger | Serva/Sigma | CAS 9032-75-1 |
| Fluorescent Brightener 28 (Calcofluor White) | Pol-Aura | CAS 4404-43-7 |
| ClearSee:<br>Urea<br>Sodium deoxycholate<br>Xylitol | Sigma-Aldrich<br>Sigma-Aldrich<br>Sigma-Aldrich | CAS 57-13-6<br>CAS 302-95-4<br>CAS 87-99-0 |
| Paraformaldehyde | Sigma-Aldrich | CAS 30525-89-4 |
| Glutaraldehyde | Sigma-Aldrich | CAS 111-30-8 |
| Uranyl Acetate | Polysciences | CAS 6159-44-0 |
| Osmium tetroxide | Polysciences | CAS 20816-12-0 |
| Epoxy Embedding Kit:<br>MNA<br>Epon 812<br>DDSA<br>DMP-30 | Sigma-Aldrich<br>Sigma-Aldrich<br>Sigma-Aldrich<br>Sigma-Aldrich | CAS 25134-21-8<br>CAS 25038-04-4<br>CAS 26544-38-7<br>CAS 90-72-2 |
| TFA | Pierce | CAS 76-05-01 |
| Experimental Models: Organisms/Strains | | |
| *Arabidopsis thaliana*, ecotype Col-0 | N/A | N/A |
| *Arabidopsis thaliana*, ecotype Col-0, pAR169 (*ATML1p::mCirtrine-RCI2A* line | Roeder et al.[29] | N/A |
| *Arabidopsis thaliana*, ecotype Col-0, *pCESA3::GFP-CESA3 p35S::mCHERRY-TUA5* | Schneider et al.[23] | N/A |
| *Arabidopsis thaliana*, ecotype Col-0, *pCESA3::GFP-CESA3 p35S::mCHERRY-TUA5* in *csi1-1/pom2-8* background | Schneider et al.[23] | N/A |
| *Arabidopsis thaliana*, ecotype Col-0, *csi1-3* | Alonso et al.[68] | SALK_138584 |
| *Arabidopsis thaliana*, ecotype Col-0, *csi1-6* | Alonso et al.[68] | SALK_115451 |
| *Arabidopsis thaliana*, ecotype Col-0, *ktn1-2* | McElver et al.[69] | SAIL_343_D12 |
| *Arabidopsis thaliana*, ecotype Col-0, *csi3-1* | Lei et al.[22] | GABI_308G07 |
| *Arabidopsis thaliana*, ecotype Col-0, *pCSI1::RFP-CSI1* in *csi1-6* | Gu et al.[19] | N/A |
| *Arabidopsis thaliana*, ecotype Col-0, *csi1-3 csi3-1* | This paper | N/A |
| Software and algorithms | | |
| MorphoGraphX | Barbier de Reuille et al.[70] | https://www.mpipz.mpg.de/MorphoGraphX |
| MorphoRobotX | N/A | https://www.MorphoRobotX.org |
| WITec Suite Five | Oxford Instruments | https://raman.oxinst.com |
| GRAMS/AI$^{TM}$ Spectroscopy Software | ThermoFisher | https://www.thermofisher.com/order/catalog/product/INF-15000 |
| OriginLab and OriginPro 2023 | OriginLab Corporation | https://www.OriginLab.com |
| Excel | Microsoft 365 | N/A |

(*Continued on next page*)

*Continued*

| REAGENT or RESOURCE | SOURCE | IDENTIFIER |
|---|---|---|
| ImageJ (Fiji) | | https://fiji.sc/ |
| JPK Data Processing | JPK Instruments AG | https://www.jpk.com |
| MATLAB | Mathworks, Nattick, MA, USA | https://www.mathworks.com/ |
| Geometric model for sepal growth | See Data S1 | N/A |
| Custom code in python | This paper | https://doi.org/10.5281/zenodo.7998638 |
| Custom code in MATLAB | This paper | https://doi.org/10.5281/zenodo.7998638 |
| Other | | |
| $CaF_2$ coverslips | LaserOptex | http://www.laseroptex.com/cs/cs.html CAMS 1602 |
| Crystalline cellulose | *Halocynthia roretzi* | Ruel et al.[71] |
| Amorphous cellulose | *Halocynthia roretzi* | Ruel et al.[71] |
| Carbon Film 200 Mesh, Cu, 50/bx | Electron Microscopy Sciences | CF200-Cu-50 |
| AFM rectangular Si cantilevers with resonant frequency of about 325 kHz, tip radius 8 nm | MikroMasch, Estonia | HQ:NSC15 |

## RESOURCE AVAILABILITY

### Lead contact

Requests should be sent to the lead contact, Arezki Boudaoud (arezki.boudaoud@polytechnique.edu).

### Materials availability

Seeds from the double mutant *csi1-3 csi3-1* are available upon request.

### Data and code availability

- All datasets and microscopy files reported in this paper have been deposited at Zenodo and are publicly available as of the date of publication at the https://doi.org/10.5281/zenodo.7998638.
- All original codes have been deposited at Zenodo and are publicly available as of the date of publication. DOIs are listed in the key resources table.
- Any additional information required to reanalyse the data reported in this paper is available from the lead contact upon request.

## EXPERIMENTAL MODEL AND SUBJECT DETAILS

*Arabidopsis thaliana* plant lines used for live imaging and analysis of mature sepal cell shape were pAR169 (*ATML1p::mCirtrine-RCI2A*,[29]) and *csi1-3* x pAR169. Plant lines used for CESA imaging harbored *pCESA3::GFP-CESA3 p35S::mCHERRY-TUA5* constructs in WT and in *csi1-1/pom2-8* backgrounds.[23] In all other cases the plants used were Col-0, *csi1-3* (SALK_138584,[68]), *csi1-6* (SALK_115451,[68]), *ktn1-2* (SAIL_343_D12,[69]), *csi3-1* (GABI_308G07,[22]), and *pCSI1::RFP-CSI1* in *csi1-6*.[19] All mutant lines are transfer DNA insertion lines. *csi1-1* has weak expression at the RNA level, whereas *csi1-3* and *csi1-6* are likely null mutants.[19] The double mutant was obtained by crossing *csi1-3* with *csi3-1*. All lines have a Col-0 background. Plants were grown on soil at 22°C in culture rooms with long day conditions (16 h light/8 h darkness). For *in vivo* imaging, inflorescences were cut off from the plants, dissected up to the desired bud (all buds used in this study were comprised between the 10th and 20th organ initiated along the inflorescence[27]) and grown into apex culture medium plates[72] supplemented by 0.1% V/V plant preservative mixture (PPM; Plant Cell Tech). Plates were then stored in growth cabinets with the same lighting/temperature conditions as in culture rooms.

## METHOD DETAILS

### Confocal imaging and analysis

Whole sepal images were collected using a LSM700 confocal microscope (Zeiss, Germany) equipped with a 5x air objective (NA = 0.25). Propidium iodide (PI) was excited using a 555 nm laser and the emitted light filtered through a 560–630 nm band-pass filter.

Live images were collected using an SP8 confocal microscope (Leica Microsystems, Germany) equipped with a 25× long-distance water objective (NA = 0.95). mCitrine was excited using a 514 nm laser and the emitted light filtered through a 520–550 nm band-pass filter.

Samples used for whole sepal measurements were stained in PI at 100μM final concentration in water for 15 min prior to imaging. Sepals used for osmotic treatments were then plasmolyzed for 1h in 0.4M NaCl solution supplemented with PI at 100μM.

## Geometric model for sepal growth

We built a parsimonious model for cell growth, starting from measurements, and we predicted differences in final size and aspect ratio between wild-type (WT) and *csi1-3* sepals. We used the geometric description of growth introduced by Goodall and Green.[73] The details are provided in Data S1.

## Atomic Force Microscopy (AFM)

Samples of recently formed cell wall surface (i.e., the protoplast-facing surface) were prepared for AFM measurements using a modified protocol of Wuyts et al.[74] Briefly, the sepals were plasmolyzed in 0.4 M NaCl for 10 min and fixed in 70% ethanol (first kept under vacuum for 1 h at room temperature, next fixed for at least 24 h at 4°C). Afterward they were treated with absolute chloroform for 10 min (to remove membranes and cuticle), rehydrated in decreasing ethanol series (70%, 50%, 30%) followed by deionized water (5 min in each medium), placed in protoplast lysis buffer of sodium dodecyl sulfate and sodium hydroxide (1% SDS in 0.2M NaOH) for 3 h, treated with 0.01% α-amylase (Sigma-Aldrich; from *Bacillus licheniformis*) in PBS (Phosphate Buffered Saline) (pH 7.0) in 37°C overnight (to remove residual starch), moved to over-saturated water solution of chloral hydrate (200 g/50 mL) for 4 h (to remove protoplast remnants), and rinsed in water (3 × 15 min). Superficial cell walls of the abaxial epidermis were then gently peeled off from the sepal and placed on the glass slide such that the protoplast facing wall surface was exposed. In order to better visualize the cellulose microfibrils in some samples, pectins were removed by treatment with 2% pectinase (Serva, Heidelberg, FRG; from *Aspergillus niger*) in sodium-phosphate buffer (pH 5.7) at room temperature for 30 min, or the buffer alone. The samples were then rinsed in water and dried at room temperature, during which the wall became attached to the glass slide by adhesion.

Atomic Force Microscopy (AFM) measurements were performed with a NanoWizard®3 BioScience (JPK Instruments, Berlin, Germany) operating in intermittent contact mode, using HQ:NSC15 rectangular Si cantilevers (MikroMasch, Estonia) with spring constant specified as 40 N/m, cantilever resonant frequency of about 325 kHz, and tip radius 8 nm. All scans were conducted in air in laboratory conditions (22°C, constant humidity of 45%). Images were obtained using the JPK Data Processing software (JPK Instruments). We examined both giant and non-giant epidermal cells of sepals (5 sepals in WT; 6 in *csi1-3*) from stage 12 flowers. In WT we obtained 16 AFM maps from 9 cells, in *csi1-3* - 32 maps from 14 cells.

## Raman spectroscopy

Sample preparation for Raman microspectroscopy followed the AFM protocol up to the treatment with chloral hydrate and rinsing in water.[74] Such prepared sepals were put on glass slides (1 mm thick), immersed in pure deionized water to preserve environmental conditions, and covered by $CaF_2$ 0.15–0.18 mm thick coverslips (CAMS1602, Laser Optex).

Raman data were collected using WITec confocal Raman microscope CRM alpha 300R, equipped with an air-cooled solid-state laser ($\lambda = 532$ nm), an thermoelectrically cooled CCD camera, and Zeiss C-Apochromat (100x/1.25 NA) water immersion objective. The excitation laser radiation was coupled to the microscope through a single-mode optical fiber (50 μm diameter). Raman scattered light was focused onto a multi-mode fiber (50 μm diameter) and monochromator with a 600 line $mm^{-1}$ grating. The spectrometer monochromator was calibrated using the emission of a Ne lamp, while the signal of a silicon plate (520.7 $cm^{-1}$) was used for checking beam alignment.

Surface Raman imaging was applied to differentiate the signal of the cuticular ridges and cell wall. Data were collected in a central fragment of the cell in a 10 μm × 10 μm area using 30 × 30 pixels (=900 spectra) and an integration time of 40 ms per spectrum. The precision of the horizontal movement of the sample during measurements was ±0.2 μm. The lateral resolution (LR) was estimated according to the Rayleigh criterion $LR = 0.61\lambda/NA$ as $LR = 427$ nm. All spectra obtained during Raman imaging were collected in the 120 - 4000 $cm^{-1}$ range with a resolution of 3 $cm^{-1}$ and at 30 mW on the sample.

The output data were processed by performing a baseline correction using an autopolynomial function of degree 3, submitted to an automatic cosmic rays removal procedure by comparing each pixel (i.e., each CCD count value at each wavenumber) to its adjacent pixels and finally smoothed by Savitzky–Golay filter. Chemical images were generated using cluster analysis (CA). *K*-means approach with the Manhattan distance for all Raman imaging maps was carried out to distinguish signal of cuticular ridges and cell wall. The clusters representing cuticular ridges were excluded from further analyses. Every spectrum obtained from the cell wall cluster was normalized by dividing by its total area using WITec Project Five Plus software. The procedure was repeated for ten non-giant pavement cells located in the basal half of different sepals.

Every time data were gathered for 13 consecutive orientations of the polarization plane (the angular range 0–180°), each rotated by 15°. From such obtained set of 13 averaged spectra after the *K*-means cluster analysis, the spectrum with maximal signal intensity of the C-O-C band (1096 $cm^{-1}$) was chosen to represent angular position 0°, while the other spectra represent angle-dependent integrated intensity alteration with minimum at 90°. Once positions of the two angular extrema were recognized, the 4 spectra (every 30° from 0° to 90°) were used for further analysis. For each spectrum the spectral parameters like band position, full width at half maximum, intensity and integrated intensity were determined by deconvolution of the spectra through the peak fitting procedure facilitated by GRAMS/AI 9.2 software. For each spectrum, the Voigt function with the minimum number of the components was used to reproduce the experimentally observed band arrangement. The applied procedure allows one to separate cellulose-specific bands, e.g. 1096 $cm^{-1}$ (C-O-C) and 2898 $cm^{-1}$ (CHx, x = 1,2) from non-cellulose bands originating from other polysaccharides present in the cell wall. Finally, the ratio of integrated intensity around the C-O-C and CHx bands was calculated to follow the angle-dependent character of the sample and estimate the extent of cellulose microfibrils ordering. The ratio of integrated intensity values estimated for those two regions was calculated for different polarizer angles (every 30° from 0° to 90°) and normalized by the sum of the four values.

Data from WT and *csi1-3* mutant were compared with purified reference samples of crystalline *(Halocynthia roretzi)* and amorphous (DMAc/LiCl) cellulose.[71]

## Imaging of cellulose with confocal microscopy

For visualization of cellulose fibrils in confocal microscopy isolated sepals (stage 10) were cleared using the modified ClearSee protocol.[75] In short, the samples were fixed in 4% paraformaaldehyde bufferd with 1x PBS (pH 7.4) for at least 1 h under vacuum, and subsequently for 3 h in room temperature. Next they were rinsed three times in PBS and put in a plastic container filled with ClearSee. The closed container with samples was placed in a rocking incubator for 3 weeks, the liquid was changed every day for 1 week, and every 2–3 days for the remaining 2 weeks. The samples were then stained with Calcofluor White for 1 h, washed in ClearSee by gentle shaking for 10 min, and analyzed using inverted confocal microscope Olympus FV-1000 equipped with 60x oil objective (UPLanSApo; NA = 1.35). Calcofluor White was excited using a 405 nm laser and the emitted light filtered through a 425–525 nm band-pass filter. Images were processed using ImageJ.

## Assessment of cell wall thickness using electron microscopy

Isolated sepals (stage 10–11) were fixed in solution of 2.5% glutaraldehyde buffered in 50 mM phosphate buffer (pH 7) in 4°C overnight, rinsed three times in 50 mM phosphate buffer, postfixed with 1% OsO4 for 2 h, rinsed in the di$H_2$O, dehydrated in ethanol and embedded in Epon resin.[76] Ultrathin cross sections (cut at half of sepal length, perpendicular to the long sepal axis), 90 nm thick, were examined in field emission scanning electron microscope UHR FE-SEM Hitachi SU 8010, operated in transmission mode (STEM) at accelerating voltage of 25 kV.

## Imaging of cellulose synthase complexes and cortical microtubules

To analyze the colocalization of Cellulose Synthesis complexes (CESA) with cortical microtubules (CMT), we dissected flower buds at stages 7–9, just before formation of cuticular ridges,[77] which would prevent visualization of CESA. Buds were placed between coverslip and microscope slide for imaging. Total Internal Reflection Fluorescence (TIRF) Microscopy was done using the inverted Zeiss microscope (AxioObserver Z1) equipped with azimuthal-TIRF iLas2 system (Roper Scientific), Prime 95B Camera (https://www.photometrics.com/) using a 100x Plan-Apochromat objective (numerical aperture 1.46, oil immersion) as previously described.[78] Time lapses were acquired during at least 10 min (one frame every 30s), acquisition time for GFP-CeSA3 (CESA channel) and mCH-TUA6 (CMT channel) were 500ms and 300ms respectively. Focal planes were adjusted manually.

## Cell wall monosaccharide composition

In order to have enough material for the quantification of monosaccharide composition, we dissected the 4 sepals (the two lateral and the adaxial sepals, in addition to the abaxial sepal, which is used elsewhere in this study) of about 100 stage 12 flowers from secondary inflorescences of WT and *csi1-3* plants, for each of 4 replicates. Freshly collected sepals were submerged into 96% ethanol incubated for 30 min at 70°C. The sepals were then washed once with 96% ethanol and twice with acetone at room temperature. The remaining pellet of AIR was dried in a fume hood overnight at room temperature. The monosaccharide composition of the noncellulosic fraction was determined by hydrolysis of 1–2 mg of AIR with 2 M TFA for 1 h at 120°C. The TFA-insoluble material was washed twice with 1 mL ethanol 70° and further hydrolyzed with 72% (v/v) sulfuric acid for 1h at 20°C. The sulfuric acid was then diluted to 1 M with water and the samples further incubated at 100°C for 3 h in order to hydrolyze the crystalline cellulose fraction.

The TFA and sulfuric acid hydrolysates were diluted 100 times and filtered using a 20 $\mu$m filter caps. The monosaccharides of these fractions were quantified by HPAEC PAD on a Dionex ICS-5000 instrument (Thermo Fisher Scientific) equipped with a CarboPac PA20 analytical anion exchange column (3 mm × 150 mm).[79] The following separation conditions were applied: an isocratic gradient of 4 mM NaOH from 0 to 6 min followed by a linear gradient of 4 mM NAOH to 1 mM NaOH from 6 to 19 min. At 19.1 min, the gradient was increased to 450 mM NaOH to elute the acidic sugars.

## Extensometry

The seeds of *Arabidopsis thaliana* WT and *csi1-3* mutant were sterilized using 70% EtOH with Tween 20 and 95% EtOH. Subsequently, the seeds were plated on vertical plates containing 1/2MS medium with 1% sucrose and 0.7% agar at pH 5.6. Afterward, the seeds were stratified at 4°C for 36 h and grown for 6 days with 16 h of light per day at 22°C. Following this, the seedlings were transferred to soil and grown for 3 weeks, with regular watering of the plants. At the stage 15b, the sepals were dissected and affixed to laboratory tags (Tough-Tags$^{TM}$, Sigma-Aldrich). Subsequently, they were immersed in a water bath to ensure a stable osmotic environment for the sample. Throughout the course of the experiment, the samples were maintained in a hydrated state by misting water onto their surfaces. The samples were fixed to the micro-extensometer (ME), which was equipped with a force sensor (10g Futek, LSB200, Miniature S-Beam Jr. Load Cell) and connected to a micro-robotic actuator (SmarAct GmbH, SLC-1780). The MorphoRobotX software (https://www.MorphoRobotX.org), a fully automated system, managed the ME. It regulated the positioner, documented the force variation during displacement, and aided in obtaining the stiffness data of the sample. The Cheese software was utilized to control a DigiMicro 2.0 digital microscope camera (dnt GmbH), which captured the images of the sample under the exerted force. To ensure adequate illumination, additional AmScope LED rings were situated within the camera's field of view. The stiffness of the sample was quantified as the ratio of force to width, with respect to the percentage of displacement.[38]

## QUANTIFICATION AND STATISTICAL ANALYSIS

### Statistical analyses

Analysis and statistical testing were performed with custom made python scripts. Statistical testing for differences between sample means was performed using the scipy.stats library.[80] When the samples were typical cellular properties of sepals, we chose to use median of the cell property over a sepal, and to test for differences between sepal medians because medians are more robust to outliers. Details of all statistical comparisons are provided in Table S1.

### Cell and organ growth

Whole sepal measurements were performed following.[81] Quantification of macroscopic growth rates was done by measuring manually sepal curved length and width using oriented images in ImageJ.

Live imaging data was analyzed using MorphoGraphX,[70] which included segmentation, lineage tracking and computation of the cell areas and principal directions of growth. Principal growth directions of each cell were computed based on the relative displacement of three-way cell junctions between consecutive imaging time points. Growth anisotropy was then calculated as the ratio between magnitudes associated with the maximum and minimum principal directions of growth.

### Quantification of cellulose microfibrils arrangement on protoplast-facing wall surface

Anisotropy of cellulose microfibrils arrangement was assessed for square regions (400 nm × 400 nm) with distinct microfibrils chosen from measured height images of 2 μm × 2 μm AFM scans (2–4 regions per scan). Histogram of microfibrils orientation was obtained for each region using Directionality tool (https://imagej.github.io/plugins/directionality) of Fiji (Fourier components method). In the Directionality tool, alignment is assessed for a single curve fitted to the highest peak while in most cell wall regions the distribution of microfibrils orientation was multimodal. Thus, we developed a bespoke protocol written in MATLAB (Mathworks, Nattick, MA, USA) to quantify microfibrils arrangement using the following steps (see Figure S7 for details): (i) smooth the histogram by a moving average; (ii) obtain a series of least square approximations of the histogram by a sum of an increasing number of Gaussian models (up to 8); (iii) choose the approximation with the lowest number of Gaussians with adjusted $R2>0.94$; (iv) exclude Gaussians with half-width bigger than 180°; (v) concatenate Gaussians with peaks separated by less than 10°; (vi) exclude Gaussians with height smaller than ¼ of the highest peak; (vii) compute the alignment index as the relative maximal angular distance between the remaining Gaussian peaks. The index values are between 0 and 1: the lower the value, the less aligned fibrils, index value equal to 1 means that there is only one Gaussian.

Angular variability was computed for cells on which at least three AFM regions with alignment index greater than 0.78° were obtained. Angles were periodised and circular variability was measured using the Python astropy package.[82,83]

### Analysis of colocalization of cellulose synthase complexes with cortical microtubules

In order to better visualize cellulose synthases (CESA) moving at the membrane (see below), we used projections of all frames of CESA channel (covering 10 min or more) and the first image from the cortical microtubule (CMT) channel. In order to determine the proportion of CESA particles in projections that co-localize with CMTs, we followed classical approaches in colocalization analysis.[84,85] We used Mander's overlap coefficient[86] for pixels with intensities above the thresholds automatically determined by the approach of Costes et al.,[87] as implemented in the plugin 'Coloc 2', which is included in the Fiji distribution of ImageJ. First, the background of each of the two channels was removed with 'Process>Subtract background … ' by using the Otsu threshold, a rolling ball radius of 10 μm, and disabling smoothing. Objects too big to be compatible with CESA particles[23,24] or corresponding to CESA particles moving inside cytoplasm were removed by creating a mask eliminating big regions as follows. After removing the background, we applied a local threshold to the CESA channel using 'Image>Adjust>Auto Local Threshold' with the Otsu method, a rolling ball radius of 10 μm, and white objects selected; the resulting binary image was then inverted ('Edit>Invert') and opened morphologically ('Process>Binary>Open'). The resulting mask was then combined with a polygonal region of interest selected based on the presence of CMT patterns in cells (due to the use of TIRF, CMT are more visible for cells that are in contact with the microscope cover). Last, colocalization was quantified for each region using 'Analyze>Colocalisation>Coloc 2' for the CESA channel vs. the CMT channel and the mask obtained as above, and the default parameters (in particular PSF value of 3). We recorded Mander's tM1 and used it as a colocalization score.

### Spatial consistency of growth direction

To obtain a default value of spatial consistency, we computed the median angle between neighboring cells in a sepal, ascribing a random orientation to each cell. Indeed, the maximal angle between two cells is 90°, but three neighboring cells cannot all be oriented at 90° to each other. Here, we used one example of segmented sepal mesh and we replaced growth direction with a random vector that is tangential to the surface of the epidermis because we are only considering growth of the sepal outer surface. In practice, the random vector was drawn on the plane best-fitting centroids of neighboring cells. We then applied the same pipeline used for the quantification of spatial consistency of growth direction.

# Generalized Lotka-Volterra equations with random, non-reciprocal interactions: the typical number of equilibria

Valentina Ros
*Université Paris-Saclay, CNRS, LPTMS, 91405, Orsay, France*

Felix Roy and Giulio Biroli
*Laboratoire de Physique de l'Ecole Normale Supérieure, ENS, Université PSL, CNRS, Sorbonne Université, Université de Paris, F-75005 Paris, France*

Guy Bunin and Ari M. Turner
*Department of Physics, Technion-Israel Institute of Technology, Haifa 32000, Israel*

We compute the typical number of equilibria of the Generalized Lotka-Volterra equations describing species-rich ecosystems with random, non-reciprocal interactions using the replicated Kac-Rice method. We characterize the multiple-equilibria phase by determining the average abundance and similarity between equilibria as a function of their diversity (i.e. of the number of coexisting species) and of the variability of the interactions. We show that linearly unstable equilibria are dominant, and that the typical number of equilibria differs with respect to the average number.

Systems of many degrees of freedom with heterogeneous and *non-reciprocal* (asymmetric) interactions emerge naturally when modelling neural networks [1–8], natural ecosystems [9–12], economic networks or agents playing games [13–16]. The dynamics of these systems are characterized by a large number of attractors such as equilibria, limit cycles and chaotic attractors. Systems admitting an energy landscape, as it is the case for symmetric interactions, only display equilibria, which are the stationary points of the landscape. A rugged landscape is central in the theory of glassy systems, since local minima are associated to metastable states; as a consequence, in-depth investigations and refined tools for counting and classifying local minima of highly non-convex landscapes have been developed extensively in the context of glassy physics [17–20]. Most of these studies focused on systems admitting an energy landscape, though. Recently, the interest in non-conservative systems (devoid of an energy landscape) has grown substantially and pioneering works have shown that such systems can also display many equilibria [21–25]. Developing a general theory in order to count them and to investigate their *stability* is a challenging goal, with potentially relevant implications for understanding the dynamics.

Here we address this problem for a prototypical non-conservative dynamical system, the random Generalized Lotka-Volterra model (rGLV), which describes the dynamics of population sizes of multiple species with pairwise interactions between them. The rGLV equations are used extensively in theoretical ecology to describe well-mixed ecosystems [26–31], and they are related to models used in evolutionary game theory and in economic theory [32–35]. They are known to admit a multiple equilibria phase when the variability of the random interactions is strong enough [27, 36–38], an interesting feature for theoretical ecology [39, 40]. Our main result is a full characterization of multiple equilibria in terms of average abundance, diversity and stability as summarized in the phase-portrait of Fig. 1. There is a general expectation that the vast majority (if not all) of the equilibria are linearly unstable when the interactions are asymmetric [24, 41]; our analysis confirms this surmise, which directly implies a complex dynamical behavior, as the system can never settle in a fixed point, even at long times. In order to properly count the *typical* number of equilibria, we combine random matrix theory with standard tools in the theory of glasses. We thus go beyond the previous analysis performed for systems with asymmetric interactions [21–24, 42], which focused on the *average* number of equilibria. The latter is in fact much larger than the former and not representative of the typical behavior of the rGLV model, as we shall show below (and as it happens in many other disordered and glassy systems).

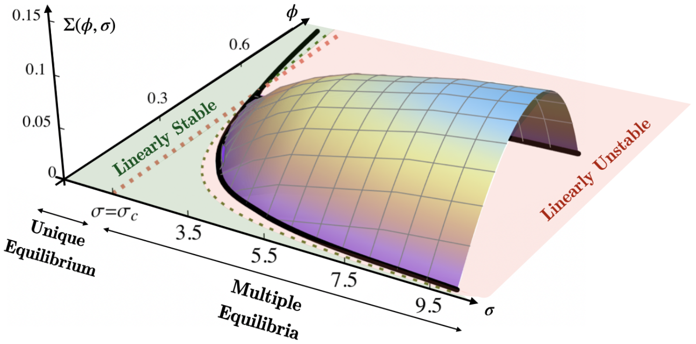

FIG. 1: Quenched complexity $\Sigma(\phi,\sigma)$ of uninvadable equilibria for uncorrelated interactions ($\gamma = 0$). Black lines correspond to vanishing complexity; the green dotted line to the diversity $\phi_{\rm May}(\sigma)$ above which equilibria are linearly unstable (red area); the orange dotted line to the transition between the unique ($\sigma < \sigma_c$) and the multiple ($\sigma > \sigma_c$) equilibria phases.

The rGLV equations determine the dynamics of a pool of $S \gg 1$ species. They read

$$\frac{dN_i(t)}{dt} = N_i(t) F_i(\vec{N}), \tag{1}$$

where $N_i(t) \geq 0$ is the abundance of species $i$ at time $t$. The vector $\vec{F}$ represents the growth rates or forces:

$$F_i(\vec{N}) = \kappa_i - N_i - \frac{\mu}{S} \sum_{j=1}^{S} N_j - \frac{\sigma}{\sqrt{S}} \sum_{j=1}^{S} a_{ij} N_j. \tag{2}$$

Here $\kappa_i$ are the carrying capacities, $\mu, \sigma$ are the average interaction strength and the variability, and $a_{ij}$ are components of a random matrix encoding the fluctuations in the interactions between the different species [77]. To describe interactions where $a_{ij}$ and $a_{ji}$ are correlated but not exactly the same, we take them as two variables with a joint Gaussian distribution defined by covariances:

$$\langle a_{ij} a_{kl} \rangle = \delta_{ik}\delta_{jl} + \gamma \, \delta_{il}\delta_{jk}, \quad |\gamma| \leq 1 \tag{3}$$

corresponding to $\langle a_{ij}^2 \rangle = \langle a_{ji}^2 \rangle = 1$ and $\langle a_{ij} a_{ji} \rangle = \gamma$. In the extreme case $\gamma = \pm 1$ one obtains perfect correlations $a_{ij} = \pm a_{ji}$, while for $\gamma = 0$ the interactions are uncorrelated. We focus on $\kappa_i = \kappa$, but the calculation can be easily generalized to heterogeneous $\kappa_i$.

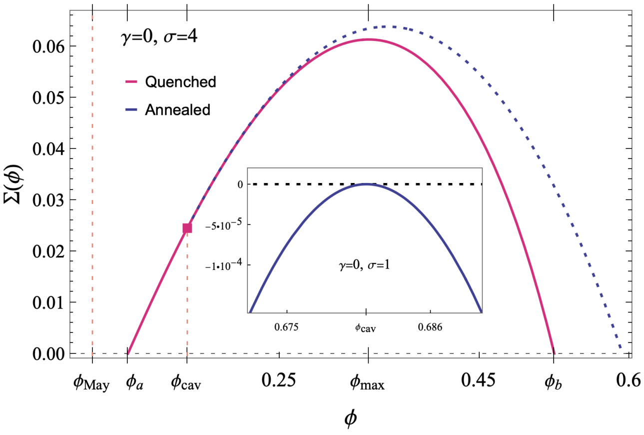

FIG. 2: Complexity of equilibria as a function of their diversity, for $\gamma = 0$. Main panel: Complexity in the multiple equilibria phase (at $\sigma = 4$). A difference between quenched (magenta) and annealed (blue) is apparent. All the equilibria are unstable ($\phi > \phi_{\rm May}$). Inset: Annealed complexity in the unique equilibrium phase (at $\sigma = 1$), negative except at the diversity predicted by the cavity formalism consistent with the existence of a unique equilibrium.

Equilibria are configurations $\vec{N}^*$ satisfying

$$\frac{dN_i^*}{dt} = N_i^* F_i(\vec{N}^*) = 0 \quad \forall\, i, \qquad N_i^* \geq 0. \tag{4}$$

Numerical simulations and analytical results [27, 30, 36, 41, 43, 44] reveal two distinct regimes for large $S$: a *unique equilibrium* regime in which any arbitrary initialization of the population vector converges to a fixed equilibrium $\vec{N}^*$ which is globally stable, and a *multiple equilibria* regime. The transition between the two regimes takes place at $\sigma_c = \sqrt{2}(1+\gamma)^{-1}$ [43]. Characterizing the *multiple equilibria* phase when $-1 < \gamma < 1$ is still an open challenge as mappings to physical systems work only for $\gamma = 1$ [27, 33, 36, 38, 45, 46] and $\gamma = -1$ [47]. In the former case the problem is conservative and the force is obtained as the derivative of an energy, $F_i(\vec{N}) = -\partial_i L(\vec{N})$ with $L(\vec{N}) = \sum_{i=1}^{S} N_i [\frac{N_i}{2} - \kappa_i + \frac{\mu}{2} \sum_{j=1}^{S} N_j + \frac{\sigma}{2\sqrt{S}} \sum_{j=1}^{S} a_{ij} N_j]$. Stable equilibria are identified with metastable states (local minima of the energy). Spin-glass techniques [36, 38] can be used to show that there exist exponentially many (in $S$) metastable states, the relevant ones being marginally stable, which makes the system critical [48] and hence very fragile to non-conservative perturbations [41, 49–51]. This formalism requires the existence of an energy landscape. When $-1 < \gamma < 1$, Dynamical Mean Field Theory [44] has provided information on the dynamics but not directly on the equilibria. Here we tackle this challenge by the Kac-Rice formalism [52–55]. To study the *typical* number of equilibria for $\gamma \neq 1$ we make use of the so called quenched Kac-Rice formalism introduced in [56].

There are many equilibria solving (4), that differ by which species are present. We classify their typical number as a function of their *diversity*: each equilibrium $\vec{N}^*$ has a certain number of absent species ($N_i^* = 0$), and a number $s(\vec{N}^*)$ of present species ($N_i^* > 0$). The diversity is defined as $\phi(\vec{N}^*) = s(\vec{N}^*)/S \in [0,1]$. This quantity is a central property in ecology, which also sets the stability of the equilibria [57], as we recall below. Our counting of equilibria at varying $\phi$ is also motivated by the fact that it is not known a priori which equilibria will affect the systems dynamics (and how), at variance with equilibrium frameworks where the relevant equilibria are marginally stable minima, usually the more numerous ones (see however [58]). Therefore, determining the *range* of diversities where equilibria are present is crucial. We focus on *uninvadable* equilibria, such that $F_i(\vec{N}^*) < 0$ for any $i$ such that $N_i^* = 0$ (notice that similar constraints appear naturally in constraint satisfaction problems, too [59]). These equilibria are relevant as they are stable with respect to small positive fluctuations in the abundance of the absent species. The total number $\mathcal{N}_S(\phi)$ of uninvadable equilibria with diversity $\phi$ scales exponentially with $S$ [60]. As known from glassy physics, $\mathcal{N}_S(\phi)$ is a random variable which in general does not concentrate around its average (it is not self-averaging). In this case the typical number is obtained by focusing on the large-$S$ limit of its logarithm, which does concentrate around a deterministic value $\Sigma(\phi)$:

$$\lim_{S\to\infty} \frac{\log[\mathcal{N}_S(\phi)]}{S} = \lim_{S\to\infty} \frac{\langle \log[\mathcal{N}_S(\phi)] \rangle}{S} \equiv \Sigma(\phi). \tag{5}$$

$\Sigma(\phi)$ governs the exponential scaling of the *typical* value of $\mathcal{N}_S(\phi)$: borrowing the terminology from glassy physics, we refer to it as the *quenched complexity*. The computation of the average of the logarithm is done via the replica trick:

$$\langle \log \mathcal{N}_S(\phi)\rangle = \lim_{n\to 0} \frac{\log \langle \mathcal{N}_S^n(\phi)\rangle}{n}. \tag{6}$$

When evaluated at $n = 1$ the right hand of side of eq. (6) gives the *annealed complexity* associated with the average number of equilibria [24, 61–63]: $\Sigma^{(A)}(\phi) \equiv \lim_{S\to\infty} \frac{1}{S} \log \langle \mathcal{N}_S(\phi)\rangle$. When $\mathcal{N}_S(\phi)$ is not self averaging, $\Sigma^{(A)} > \Sigma$: the average of $\mathcal{N}_S(\phi)$ is dominated by exponentially rare ecosystems displaying an unusually large number of equilibria. It is therefore much larger than the typical value, which captures the properties of the ecosystems occurring with probability that is not suppressed exponentially in $S$.

The main steps of the replicated Kac-Rice computation are explained in the SI. The value of $\langle \mathcal{N}_S^n(\phi)\rangle$ can be determined by introducing $n$ copies of the ecosystem and by finding the probability that any $n$ given vectors $\vec{N}^a$, $a = 1, \cdots, n$ satisfy Eq. (4) simultaneously, together with the uninvadability condition. This is a function of order parameters measuring properties of the equilibria, like the amount of correlation between them. The number of equilibria is dominated (according to a large deviation principle) by specific values of these order parameters. The order parameters are the first two empirical moments of the vectors $\vec{N}^a$ and $\vec{F}^a$, i.e. the $2n$ quantities:

$$m_a \equiv \lim_{S\to\infty} \frac{\sum_{i=1}^S N_i^a}{S}, \quad p_a \equiv \lim_{S\to\infty} \frac{\sum_{i=1}^S F_i^a}{S} \tag{7}$$

as well as the $n(n+1) + n(n-1)$ correlations (or *overlaps*):

$$\begin{gathered} q_{ab} \equiv \lim_{S\to\infty} \frac{\vec{N}_a \cdot \vec{N}_b}{S},\ \xi_{ab} \equiv \lim_{S\to\infty} \frac{\vec{F}_a \cdot \vec{F}_b}{S}, \\ z_{ab} \equiv \lim_{S\to\infty} \frac{\vec{N}_a \cdot \vec{F}_b}{S} \end{gathered} \tag{8}$$

where $z_{aa} = 0$ follows from (4). These order parameters encode the correlations in the location of the different fixed points in configuration space, which emerge because all the fixed points arise from the same interactions between the species. We consider a symmetric ansatz for the order parameters, i.e. $m_a = m, q_{ab} = \delta_{ab} q_1 + (1 - \delta_{ab}) q_0, p_a = p, \xi_{ab} = \delta_{ab}\xi_1 + (1 - \delta_{ab})\xi_0 z_{ab} = (1 - \delta_{ab}) z$, which is the simplest approximation that takes such correlations into account. Under this assumption, the moments can be written as an integral over all possible values of the order parameters:

$$\langle \mathcal{N}_S^n(\phi)\rangle = \int d\mathbf{x}\; e^{S\, n\, \bar{\mathcal{A}}(\mathbf{x};\phi) + o(nS)}, \tag{9}$$

with $\mathbf{x} = (m, p, q_1, q_0, \xi_1, \xi_0, z)$, see the SI for details of the calculation of $\bar{\mathcal{A}}$ and for its explicit expression. The large deviation principle then implies that asymptotically

$$\Sigma(\phi) = \bar{\mathcal{A}}(\mathbf{x}^\star;\phi), \tag{10}$$

where $\mathbf{x}^\star$ is the solution of the saddle-point equations $\left.\frac{\delta \bar{\mathcal{A}}(\mathbf{x};\phi)}{\delta \mathbf{x}}\right|_{\mathbf{x}^\star} = 0$. This results in self-consistent equations for the typical properties of equilibria at fixed $\phi$, such as their typical average abundance $m^*$ or the typical similarity between two equilibria $q_0^*$.

The Kac-Rice computation allows us to determine the linear stability of the equilibria at each given $\phi$ with respect to perturbations $N_i^* \to N_i^* + \delta N_i^*$ of the populations of coexisting species. This depends on the spectral properties of the matrix:

$$H_{ij}(\vec{N}^*) = \left( \frac{\partial F_i(\vec{N}^*)}{dN_j} \right)_{i,j: N_i^*, N_j^* > 0}. \tag{11}$$

For stable equilibria all the eigenvalues of (11) have negative real part. The asymmetry of the matrix $a_{ij}$ implies that (11) are themselves asymmetric random matrices [64]. The typical eigenvalue density (neglecting possible isolated eigenvalues) of $H_{ij}$ depends on $\vec{N}^*$ only through its diversity $\phi$. For

$$\phi < \phi_{\text{May}} = \frac{1}{\sigma^2 (1+\gamma)^2}. \tag{12}$$

the density has support on the negative real sector; therefore a typical equilibrium with $\phi < \phi_{\text{May}}$ (if it exists) is stable. At $\phi = \phi_{\text{May}}$, the support of the eigenvalue density touches zero and the corresponding equilibrium is marginally stable; for larger $\phi$ the equilibrium is unstable. The criterion (12) for linear stability is related to that identified by May in [57], and we henceforth refer to it as the *May stability bound*. More details on the Kac-Rice computation, with a thorough discussion of the structure of the equations and their resolution, are given in [65].

We now present our main results, focusing on the case of uncorrelated interactions $\gamma = 0$ and setting $\kappa = 1$. We find that although the saddle point values $\mathbf{x}^*$ depend explicitly on $\mu$, the complexity at fixed diversity does not, allowing us to discuss the behavior of $\Sigma(\phi)$ as a function of $\sigma$ only. As shown in Fig. 1, when $\sigma > \sigma_c$ there is a range of diversities $\phi \in [\phi_a(\sigma), \phi_b(\sigma)]$ for which $\Sigma(\phi) > 0$ (a negative annealed $\Sigma(\phi)$ signifies that no equilibria exist typically [55]). The rGLV equations thus admit an exponentially large number of uninvadable equilibria with a continuous distribution of diversities. All the equilibria are unstable, as their diversity exceeds the May stability bound, Eq. (12). In Fig. 2 we show a cut at fixed $\sigma$ of the plot of Fig. 1. In addition to the quenched complexity we show the annealed one for comparison. We find that the complexity and the diversity $\phi_{\max}$ associated to the typical, i.e. most numerous equilibria at the given $\sigma$ are overestimated by the annealed calculation. Annealed and quenched complexity only coincide for small $\phi$. The point $\phi_{\text{cav}}$ where they begin to deviate from one another turns out to coincide with the value of diversity predicted by the cavity method discussed in Refs. [27, 30, 41]. The cavity method assumes the existence of a unique stable equilibrium and allows one to characterizes its abundance $m$ and overlap $q_1$, by imposing consistency relations between the properties of the system with $S+1$ and $S$ species. The above result shows that despite being only approximate for $\sigma > \sigma_c$, this method still captures the properties of a given family of equilibria, even though they are exponentially rare with respect to the typical ones at $\phi_{\max}$.

We have studied how the properties of equilibria change as $\phi$ is increased. Fig. 3 shows that imposing a larger diversity leads to less populated (lower average abundance $m^*$) equilibria. Similarly, it leads to less correlated (lower overlap $q_0^*$) equilibria. Fig. 4 shows the $\sigma$-dependence of the special values of $\phi$ discussed above (it corresponds to Fig.1 seen from the top). The grey area is the support of the quenched complexity, which increases with $\sigma$. When $\sigma \to \sigma_c^+$ all the special values of $\phi$ merge together and reach $\phi_{\text{May}}$. Correspondingly the complexity vanishes.

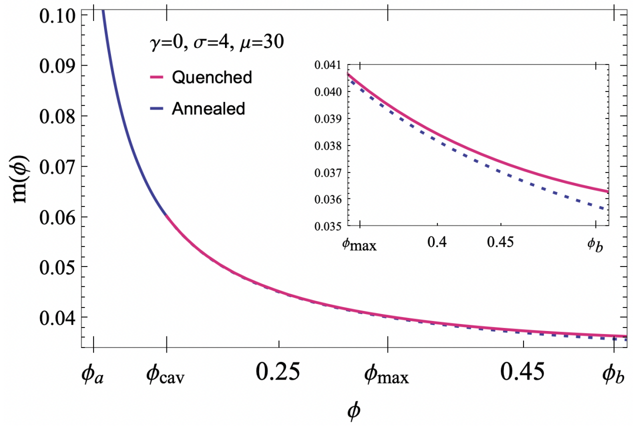

FIG. 3: Typical averaged population size as a function of diversity $\phi$ for $\sigma = 4$ and $\mu = 30$, in the annealed (blue) and quenched (magenta) calculation. More diverse equilibria have a smaller averaged population size $m$, which for $\phi > \phi_{\text{cav}}$ is underestimated by the annealed approximation. The inset is a zoomed plot.

Just above $\sigma_c$, where the complexity goes to zero, the quenched and annealed calculations have great discrepancies, see the inset of Fig. 4, probably due to the larger correlation between equilibria. In fact, the average number of equilibria (annealed calculation) is dominated by equilibria having a diversity $\phi_{\max}^{\text{ann}}$ for which *typically* there are no equilibria, i.e. the quenched complexity vanishes. This feature had already been identified in Ref. [35] for a slightly different model arising in the context of portfolio optimization (and describing, in its ecological interpretation, species competing for a single common resource).

For larger $\sigma$ the cavity approximation underestimates more strongly the diversity (and thus the instability) with respect to that of typical equilibria at $\phi_{\max}$. For $\sigma < \sigma_c$, the complexity (annealed and quenched) is non-negative only at $\phi = \phi_{\text{cav}}$, which now correctly describes the diversity of the system as there is a unique equilibrium [66]. The analysis of the multiple equilibria also allows us to characterize thoroughly the transition to an additional phase, the unbounded phase, where some abundances diverge as a function of time, see the SI.

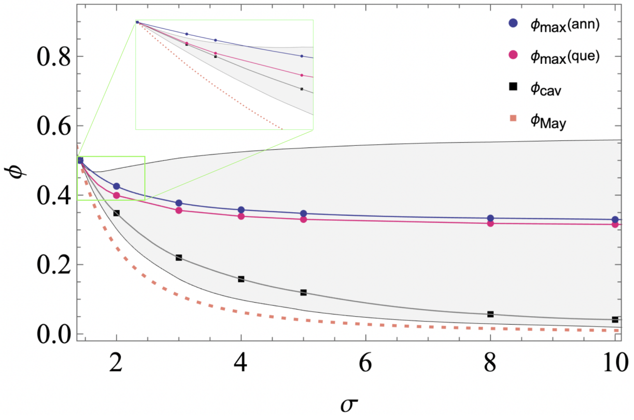

FIG. 4: Diversity vs. variability diagram. The range of possible diversities is indicated by the grey region. Curves of maximal complexity are shown in magenta (quenched) and blue (annealed). The black squares give $\phi_{\text{cav}}$. The orange dashed line corresponds to $\phi_{\text{May}}$ above which all equilibria are linearly unstable. *Inset.* Zoom in the vicinity of $\sigma_c = \sqrt{2}$.

Finally, let us focus on the properties of the transition to the unique equilibrium phase at $\sigma_c$. Following the terminology introduced in [23], this is *a trivialization transition* and corresponds to the point at which the total quenched complexity $\Sigma_{\text{tot}} = \Sigma(\phi_{\text{Max}})$ first vanishes. The way in which $\Sigma_{\text{tot}}$ vanishes for $\sigma \to \sigma_c$ has been the focus of several works. It has been studied in models with a quadratic single-species confinement potential within an annealed calculation [67, 68]. Importantly, it has also been conjectured to be connected to the emergence of chaos and of a finite Lyapunov exponent [62]. For the rGLV model at $\gamma = 0$ we find that the complexity grows quadratically with $\sigma$ when entering the multiple equilibria phase, $\Sigma_{\text{tot}} \sim (\sigma - \sigma_c)^2$ as in [67, 68]. As found in models of recurrent neural networks, the emergence of a non-zero complexity is concomitant with the emergence of a complex dynamical behavior, including chaos and aging [44]. We notice that the annealed approximation locates correctly the trivialization transition in this case, and also captures the quadratic increase but with a different prefactor. We do not expect this quadratic behavior to be general, unless the total complexity in the vicinity of $\sigma_c$ is captured by the annealed framework. If this is not the case, our calculation suggests that one should find a different power law for $\gamma \neq 0$ (see [65] and the SI for more details).

In summary, we have characterized the multiple-equilibria phase of the rGLV equations by computing explicitly the complexity of uninvadable equilibria. On a technical ground our approach, giving access to the quenched complexity, has allowed us to assess when and to what degree the annealed calculation is precise: we have found a transition at the value of diversity $\phi_{\rm cav}$, below which the annealed calculation is exact and above which the quenched calculation gives a quantitatively different result; the latter regime always includes the maximum of the complexity, which corresponds to the typical equilibria.

We performed the calculation assuming a symmetry of the order parameters with respect to permutations of replicas: we are thus restricting the region of parameter space where to look for solutions of the self-consistent equations obtained from the variation of (10). For $\gamma = 1$ it is know that the symmetric assumption is an approximation, as (10) is optimized by parameters that break the symmetry between the replicas. Verifying that Replica Symmetry Breaking (RSB) is not needed for generic $\gamma$ is a challenge that we leave for further studies.

Our calculations show that for non-reciprocal uncorrelated interactions all the uninvadable equilibria are linearly unstable. This marks a difference with respect to the symmetric case, where marginally stable equilibria are present and correspondingly the dynamics is glassy. With unstable equilibria, a chaotic dynamics is expected in presence of migration [6] and signatures of it emerge in theoretical models [69] and even in controlled experiments [70]. Similarly to the case of landscape studies which were instrumental to understand glassy dynamics in terms of local minima and metastable states, it would be very interesting to connect the properties of these unstable equilibria (more generally, of heteroclinic networks formed by them [71]) to the dynamical behavior. We envisage that *invadable* equilibria also play a role in the dynamics [72], and the calculation of their complexity is ongoing, as well as the generalization to inhomogeneous carrying capacities $\kappa_i$ [67, 73, 74].

## Acknowledgements

We thank D. Fisher for discussions on this topic. VR also thanks P. Urbani for hints on the calculation of the quenched complexity, and B. Lacroix-A-Chez-Toine, J. Berg, J. Krug and M. Mungan for suggestions of references. VR acknowledges funding by the "Investissements d'Avenir" LabEx PALM (ANR-10-LABX-0039-PALM).

---

[1] S.-I. Amari, "Characteristics of random nets of analog neuron-like elements," *IEEE Transactions on systems, man, and cybernetics*, no. 5, pp. 643–657, 1972.

[2] G. Parisi, "Asymmetric neural networks and the process of learning," *Journal of Physics A: Mathematical and General*, vol. 19, no. 11, p. L675, 1986.

[3] J. Hertz, G. Grinstein, and S. Solla, "Memory networks with asymmetric bonds," in *AIP Conference Proceedings*, vol. 151, pp. 212–218, American Institute of Physics, 1986.

[4] A. Crisanti and H. Sompolinsky, "Dynamics of spin systems with randomly asymmetric bonds: Langevin dynamics and a spherical model," *Phys. Rev. A*, vol. 36, pp. 4922–4939, Nov 1987.

[5] B. Derrida, E. Gardner, and A. Zippelius, "An exactly solvable asymmetric neural network model," *Europhysics Letters (EPL)*, vol. 4, pp. 167–173, jul 1987.

[6] B. Cessac, "Increase in complexity in random neural networks," *Journal de Physique I*, vol. 5, no. 3, pp. 409–432, 1995.

[7] F. Aguirre-López, M. Pastore, and S. Franz, "Satisfiability transition in asymmetric neural networks," *arXiv preprint arXiv:2204.03577*, 2022.

[8] J. Stubenrauch, C. Keup, A. C. Kurth, M. Helias, and A. van Meegen, "Phase space analysis of chaotic neural networks," *arXiv preprint arXiv:2210.07877*, 2022.

[9] J. Bascompte, P. Jordano, and J. M. Olesen, "Asymmetric coevolutionary networks facilitate biodiversity maintenance," *Science*, vol. 312, no. 5772, pp. 431–433, 2006.

[10] M. Loreau and C. De Mazancourt, "Biodiversity and ecosystem stability: a synthesis of underlying mechanisms," *Ecology letters*, vol. 16, pp. 106–115, 2013.

[11] S. Allesina and S. Tang, "Stability criteria for complex ecosystems," *Nature*, vol. 483, no. 7388, pp. 205–208, 2012.

[12] T. Galla, "Random replicators with asymmetric couplings," *Journal of Physics A: Mathematical and General*, vol. 39, no. 15, p. 3853, 2006.

[13] Y. Choi and R. Douady, "Financial crisis and contagion: A dynamical systems approach," *Handbook on systemic risk*, pp. 453–479, 2013.

[14] S. Alfarano, T. Lux, and F. Wagner, "Estimation of agent-based models: the case of an asymmetric herding model," *Computational Economics*, vol. 26, no. 1, pp. 19–49, 2005.

[15] A. McAvoy and C. Hauert, "Asymmetric evolutionary games," *PLoS computational biology*, vol. 11, no. 8, p. e1004349, 2015.

[16] P. Bayer, G. Kozics, and N. G. Szőke, "Best-response dynamics in directed network games," *arXiv preprint arXiv:2101.03863*, 2021.

[17] R. Monasson, "Structural glass transition and the entropy of the metastable states," *Physical review letters*, vol. 75, no. 15, p. 2847, 1995.

[18] S. Franz and G. Parisi, "Recipes for metastable states in spin glasses," *Journal de Physique I*, vol. 5, no. 11, pp. 1401–1415, 1995.

[19] A. Cavagna, I. Giardina, and G. Parisi, "Structure of metastable states in spin glasses by means of a three replica potential," *Journal of Physics A: Mathematical and General*, vol. 30, no. 13, p. 4449, 1997.

[20] G. Parisi, P. Urbani, and F. Zamponi, *Theory of simple glasses: exact solutions in infinite dimensions*. Cambridge University Press, 2020.

[21] J. Berg and M. Weigt, "Entropy and typical properties of nash equilibria in two-player games," *EPL (Europhysics*

*Letters)*, vol. 48, no. 2, p. 129, 1999.

[22] M. Schreckenberg, "Attractors in the fully asymmetric sk-model," *Zeitschrift für Physik B Condensed Matter*, vol. 86, no. 3, pp. 453–459, 1992.

[23] Y. V. Fyodorov, "Topology trivialization transition in random non-gradient autonomous odes on a sphere," *Journal of Statistical Mechanics: Theory and Experiment*, vol. 2016, no. 12, p. 124003, 2016.

[24] Y. V. Fyodorov and B. A. Khoruzhenko, "Nonlinear analogue of the may- wigner instability transition," *Proceedings of the National Academy of Sciences*, vol. 113, no. 25, pp. 6827–6832, 2016.

[25] S. B. Fedeli, Y. V. Fyodorov, and J. Ipsen, "Nonlinearity-generated resilience in large complex systems," *Physical Review E*, vol. 103, no. 2, p. 022201, 2021.

[26] N. S. Goel, S. C. Maitra, and E. W. Montroll, "On the volterra and other nonlinear models of interacting populations," *Reviews of modern physics*, vol. 43, no. 2, p. 231, 1971.

[27] G. Bunin, "Ecological communities with lotka-volterra dynamics," *Physical Review E*, vol. 95, no. 4, p. 042414, 2017.

[28] V. A. Jansen and G. D. Kokkoris, "Complexity and stability revisited," *Ecology letters*, vol. 6, no. 6, pp. 498–502, 2003.

[29] M. Barbier, J.-F. Arnoldi, G. Bunin, and M. Loreau, "Generic assembly patterns in complex ecological communities," *Proceedings of the National Academy of Sciences*, vol. 115, no. 9, pp. 2156–2161, 2018.

[30] T. Galla, "Dynamically evolved community size and stability of random lotka-volterra ecosystems," *EPL (Europhysics Letters)*, vol. 123, no. 4, p. 48004, 2018.

[31] J. Hu, D. R. Amor, M. Barbier, G. Bunin, and J. Gore, "Emergent phases of ecological diversity and dynamics mapped in microcosms," *Science*, vol. 378, no. 6615, pp. 85–89, 2022.

[32] J. Moran and J.-P. Bouchaud, "May's instability in large economies," *Physical Review E*, vol. 100, no. 3, p. 032307, 2019.

[33] S. Diederich and M. Opper, "Replicators with random interactions: A solvable model," *Physical Review A*, vol. 39, no. 8, p. 4333, 1989.

[34] T. Galla and J. D. Farmer, "Complex dynamics in learning complicated games," *Proceedings of the National Academy of Sciences*, vol. 110, no. 4, pp. 1232–1236, 2013.

[35] J. Garnier-Brun, M. Benzaquen, S. Ciliberti, and J.-P. Bouchaud, "A new spin on optimal portfolios and ecological equilibria," *Journal of Statistical Mechanics: Theory and Experiment*, vol. 2021, no. 9, p. 093408, 2021.

[36] G. Biroli, G. Bunin, and C. Cammarota, "Marginally stable equilibria in critical ecosystems," *New Journal of Physics*, vol. 20, no. 8, p. 083051, 2018.

[37] H. Lischke and T. J. Löffler, "Finding all multiple stable fixpoints of n-species lotka–volterra competition models," *Theoretical Population Biology*, vol. 115, pp. 24–34, 2017.

[38] A. Altieri, F. Roy, C. Cammarota, and G. Biroli, "Properties of equilibria and glassy phases of the random lotka-volterra model with demographic noise," *Physical Review Letters*, vol. 126, no. 25, p. 258301, 2021.

[39] M. Barbier, C. de Mazancourt, M. Loreau, and G. Bunin, "Fingerprints of high-dimensional coexistence in complex ecosystems," *Phys. Rev. X*, vol. 11, p. 011009, Jan 2021.

[40] P. Petraitis, *Multiple stable states in natural ecosystems.* OUP Oxford, 2013.

[41] M. Opper and S. Diederich, "Phase transition and 1/f noise in a game dynamical model," *Physical review letters*, vol. 69, no. 10, p. 1616, 1992.

[42] M. Opper and S. Diederich, "Replicator dynamics," *Computer Physics Communications*, vol. 121-122, pp. 141–144, 1999. Proceedings of the Europhysics Conference on Computational Physics CCP 1998.

[43] H. Rieger, "Solvable model of a complex ecosystem with randomly interacting species," *Journal of Physics A: Mathematical and General*, vol. 22, no. 17, p. 3447, 1989.

[44] F. Roy, G. Biroli, G. Bunin, and C. Cammarota, "Numerical implementation of dynamical mean field theory for disordered systems: Application to the lotka–volterra model of ecosystems," *Journal of Physics A: Mathematical and Theoretical*, vol. 52, no. 48, p. 484001, 2019.

[45] P. Biscari and G. Parisi, "Replica symmetry breaking in the random replicant model," *Journal of Physics A: Mathematical and General*, vol. 28, no. 17, p. 4697, 1995.

[46] S. Marcus, A. M. Turner, and G. Bunin, "Local and collective transitions in sparsely-interacting ecological communities," *PLoS computational biology*, vol. 18, no. 7, p. e1010274, 2022.

[47] M. T. Pearce, A. Agarwala, and D. S. Fisher, "Stabilization of extensive fine-scale diversity by ecologically driven spatiotemporal chaos," *Proceedings of the National Academy of Sciences*, vol. 117, no. 25, pp. 14572–14583, 2020.

[48] M. Müller and M. Wyart, "Marginal stability in structural, spin, and electron glasses," *Annu. Rev. Condens. Matter Phys.*, vol. 6, no. 1, pp. 177–200, 2015.

[49] P. Spitzner and W. Kinzel, "Freezing transition in asymmetric random neural networks with deterministic dynamics," *Zeitschrift für Physik B Condensed Matter*, vol. 77, no. 3, pp. 511–517, 1989.

[50] G. Iori and E. Marinari, "On the stability of the mean-field spin glass broken phase under non-hamiltonian perturbations," *Journal Of Physics A: Mathematical and General*, vol. 30, no. 13, p. 4489, 1997.

[51] L. F. Cugliandolo, J. Kurchan, P. Le Doussal, and L. Peliti, "Glassy behaviour in disordered systems with nonrelaxational dynamics," *Physical review letters*, vol. 78, no. 2, p. 350, 1997.

[52] Y. Fyodorov, "High-dimensional random fields and random matrix theory," *Markov Processes and Related Fields*, vol. 21, no. 3, pp. 483–518, 2015.

[53] Y. V. Fyodorov, "Counting stationary points of random landscapes as a random matrix problem," *arXiv preprint cond-mat/0507059*, 2005.

[54] Y. V. Fyodorov, "Complexity of random energy landscapes, glass transition, and absolute value of the spectral determinant of random matrices," *Physical review letters*, vol. 92, no. 24, p. 240601, 2004.

[55] A. Auffinger, G. B. Arous, and J. Černỳ, "Random matrices and complexity of spin glasses," *Communications on Pure and Applied Mathematics*, vol. 66, no. 2, pp. 165–201, 2013.

[56] V. Ros, G. B. Arous, G. Biroli, and C. Cammarota, "Complex energy landscapes in spiked-tensor and simple glassy models: Ruggedness, arrangements of local minima, and phase transitions," *Physical Review X*, vol. 9, no. 1, p. 011003, 2019.

[57] R. M. May, "Will a large complex system be stable?," *Nature*, vol. 238, no. 5364, pp. 413–414, 1972.

[58] G. Folena, S. Franz, and F. Ricci-Tersenghi, "Rethinking mean-field glassy dynamics and its relation with the energy landscape: The surprising case of the spherical mixed p-spin model," *Physical Review X*, vol. 10, no. 3, p. 031045, 2020.

[59] S. Franz and G. Parisi, "The simplest model of jamming," *Journal of Physics A: Mathematical and Theoretical*, vol. 49, no. 14, p. 145001, 2016.

[60] Y. Fried, N. M. Shnerb, and D. A. Kessler, "Alternative steady states in ecological networks," *Phys. Rev. E*, vol. 96, p. 012412, Jul 2017.

[61] T. Galla, "Two-population replicator dynamics and number of nash equilibria in matrix games," *EPL (Europhysics Letters)*, vol. 78, no. 2, p. 20005, 2007.

[62] G. Wainrib and J. Touboul, "Topological and dynamical complexity of random neural networks," *Phys. Rev. Lett.*, vol. 110, p. 118101, Mar 2013.

[63] G. B. Arous, Y. V. Fyodorov, and B. A. Khoruzhenko, "Counting equilibria of large complex systems by instability index," *Proceedings of the National Academy of Sciences*, vol. 118, no. 34, 2021.

[64] H. J. Sommers, A. Crisanti, H. Sompolinsky, and Y. Stein, "Spectrum of large random asymmetric matrices," *Phys. Rev. Lett.*, vol. 60, pp. 1895–1898, May 1988.

[65] V. Ros, F. Roy, G. Biroli, and G. Bunin, "Quenched complexity of equilibria for asymmetric generalized lotka-volterra equations," *Journal of Physics A: Mathematical and Theoretical*, 2023.

[66] M. Clenet, F. Massol, and J. Najim, "Equilibrium and surviving species in a large lotka-volterra system of differential equations," *arXiv preprint arXiv:2205.00735*, 2022.

[67] G. B. Arous, P. Bourgade, and B. McKenna, "Landscape complexity beyond invariance and the elastic manifold," *arXiv preprint arXiv:2105.05051*, 2021.

[68] B. Lacroix-A-Chez-Toine and Y. V. Fyodorov, "Counting equilibria in a random non-gradient dynamics with heterogeneous relaxation rates," *Journal of Physics A: Mathematical and Theoretical*, vol. 55, no. 14, p. 144001, 2022.

[69] D. A. Kessler and N. M. Shnerb, "Generalized model of island biodiversity," *Phys. Rev. E*, vol. 91, p. 042705, Apr 2015.

[70] E. Benincà, J. Huisman, R. Heerkloss, K. D. Jöhnk, P. Branco, E. H. Van Nes, M. Scheffer, and S. P. Ellner, "Chaos in a long-term experiment with a plankton community," *Nature*, vol. 451, no. 7180, pp. 822–825, 2008.

[71] J. D. O'Sullivan, J. C. D. Terry, and A. G. Rossberg, "Intrinsic ecological dynamics drive biodiversity turnover in model metacommunities," *Nature Communications*, vol. 12, no. 1, pp. 1–11, 2021.

[72] T. A. de Pirey and G. Bunin, "Aging by near-extinctions in many-variable interacting populations," *Physical Review Letters*, vol. 130, no. 9, p. 098401, 2023.

[73] E. Bouchbinder, E. Lerner, C. Rainone, P. Urbani, and F. Zamponi, "Low-frequency vibrational spectrum of mean-field disordered systems," *Physical Review B*, vol. 103, no. 17, p. 174202, 2021.

[74] P. Mergny and S. N. Majumdar, "Stability of large complex systems with heterogeneous relaxation dynamics," *Journal of Statistical Mechanics: Theory and Experiment*, vol. 2021, no. 12, p. 123301, 2021.

[75] V. Ros and Y. V. Fyodorov, "The high-d landscapes paradigm: spin-glasses, and beyond," *arXiv preprint arXiv:2209.07975*, 2022.

[76] J. W. Baron, T. J. Jewell, C. Ryder, and T. Galla, "Non-gaussian random matrices determine the stability of lotka-volterra communities," *arXiv preprint arXiv:2202.09140*, 2022.

[77] The self-interactions are often absorbed in the carrying capacities ($a_{ii} = 0$). In order for the calculations with random matrices to work easily, we consider $a_{ii} \neq 0$ with the same statistics as for the off-diagonal $a_{ij}$. This choice does not affect any large-$S$ result discussed in the work.

# Supplemental Material

We report in the following the main steps to obtain the quantity $\bar{\mathcal{A}}(\mathbf{x}; \phi)$ appearing in Eq. (9) in the main text. Moreover, we discuss additional results on the unbounded phase and on the vanishing of the total complexity, which are mentioned in the main text. For a more detailed exposition of the formalism underlying this calculation, we refer the reader to Ref. [65].

**The Kac-Rice formula for the moments.** The Kac-Rice formalism is a framework that allows one to characterize the number of solutions of dynamical equations containing randomness: in particular, given that the number of solutions is itself a random variable, the formalism gives a recipe to determine the moments of this random variable. For an introduction to the formalism and to its application to the high-dimensional setting, see [52, 75] and references therein. This formalism provides us with an expression for the moments of the number of equilibria at fixed diversity, denoted with $\mathcal{N}_S(\phi)$ in the main text. To compute the $n$-th moment of this random variable, we need to introduce $n$ different configurations $\vec{N}^a$ of the ecosystem (with $a = 1, \cdots n$), which we refer to as *replicas*. Each $\vec{N}^a$ represents a realization of the ecosystem at fixed values of the rand interaction terms $a_{ij}$. We let $\mathbf{N} = (\vec{N}^1, \cdots, \vec{N}^n)$ denote the concatenation of configurations of all replicas. In each configuration $\vec{N}^a$, some species will be present ($N_i^a > 0$) while some others will be absent ($N_i^a = 0$). We let $I_a = I(\vec{N}^a)$ be the index set collecting the indices of the species that are present in the configuration $\vec{N}^a$. Since we are interested in counting the equilibria having fixed diversity $\phi$, we enforce that $|I_a| = S\phi$ for all $a$. We introduce the vectors of growth rates or forces $\vec{F}^a = \vec{F}(\vec{N}^a)$ and $\mathbf{F}(\mathbf{N}) = (\vec{F}^1, \cdots, \vec{F}^n)$. Let $\mathbf{f}$ denote the value taken by this random vector, and $\mathscr{P}_{\mathbf{N}}(\mathbf{f})$ the joint distribution of the $S$-dimensional vectors $\vec{F}^a$ evaluated at $\vec{f}^a$,

$$\mathscr{P}^{(n)}_{\mathbf{N}}(\mathbf{f}) = \int \prod_{i,j=1}^{S} da_{ij} \mathbb{P}(\{a_{ij}\}_{ij})\, \delta\left(\mathbf{F}(\mathbf{N}) - \mathbf{f}\right). \tag{13}$$

We also introduce the following conditional expectation value:

$$\mathscr{D}^{(n)}_{\mathbf{N}}(\mathbf{f}) = \left\langle \left( \prod_{a=1}^{n} \left| \det \left( \frac{\delta F_i^a}{dN_j^a} \right)_{i,j \in I_a} \right| \right) \;\middle|\; \mathbf{F}(\mathbf{N}) = \mathbf{f} \right\rangle. \tag{14}$$

The latter is the expectation of the product of the absolute values of $n$ determinants of the $S\phi \times S\phi$ matrices of derivatives of the components of $\mathbf{F}$, conditioned to $\mathbf{F}$ itself taking value $\mathbf{f}$. The Kac-Rice formula for the $n$-th moment of the number $\mathcal{N}_S(\phi)$ of uninvadable equilibria reads:

$$\langle \mathcal{N}^n(\phi) \rangle = \sum_{\substack{I_1 \\ |I_1| = S\phi}} \cdots \sum_{\substack{I_n \\ |I_n| = S\phi}} \prod_{a=1}^{n} \int d\vec{N}^a\, d\vec{f}^a \prod_{i \in I_a} \theta(N_i^a)\, \delta(f_i^a) \prod_{i \notin I_a} \delta(N_i^a) \theta(-f_i^a) \mathscr{D}^{(n)}_{\mathbf{N}}(\mathbf{f})\, \mathscr{P}^{(n)}_{\mathbf{N}}(\mathbf{f}). \tag{15}$$

We now briefly summarize how to determine the behaviour of the moments (15) for generic values of $n$ to leading exponential order in $S$, and how to extract the quenched (and annealed) complexity from it.

**The order parameters and the complexity.** By performing the averages over the random interactions $a_{ij}$, one sees that the quantities $\mathscr{D}^{(n)}_{\mathbf{N}}(\mathbf{f})$ and $\mathscr{P}^{(n)}_{\mathbf{N}}(\mathbf{f})$ in (15) depend on the vectors $\vec{N}^a$ and $\vec{f}^a$ only through their scalar products. For $a, b = 1, \cdots, n$ we can therefore introduce a set of *order parameters* defined as follows:

$$S q_{ab} = \vec{N}^a \cdot \vec{N}^b, \quad S\xi_{ab} = \vec{f}^a \cdot \vec{f}^b, \quad S z_{ab} = \vec{N}^a \cdot \vec{f}^b, \quad S m_a = \vec{N}^a \cdot \vec{1}, \quad S p_a = \vec{f}^a \cdot \vec{1}, \tag{16}$$

where $\vec{1} = (1, \cdots, 1)^T$ is an $S$-dimensional vector with all entries equal to one. It follows that the integration over $\vec{N}^a, \vec{f}^a$ in (15) can be replaced by an integration over the order parameters, with the appropriate change of variables. The calculation proceeds in a few steps that we briefly summarize. First, the order parameters are introduced in (15) by means of the identities:

$$1 = \int dq_{ab}\, \delta\left( \frac{\vec{N}^a \cdot \vec{N}^b}{S} - q_{ab} \right) = S \int dq_{ab} \int \frac{d\hat{q}_{ab}}{2\pi} e^{i\hat{q}_{ab}\left(\vec{N}^a \cdot \vec{N}^b - S q_{ab}\right)}, \tag{17}$$

where the auxiliary variables $\hat{q}_{ab}$ are *conjugate parameters* (and similarly for the other order parameters in (16)). Then, we make use of the assumption that the order parameters are symmetric with respect to permutations of the replicas, which implies that:

$$q_{ab} = \delta_{ab} q_1 + (1 - \delta_{ab}) q_0, \quad \xi_{ab} = \delta_{ab}\xi_1 + (1 - \delta_{ab})\xi_0, \quad z_{ab} = (1 - \delta_{ab}) z, \quad m^a = m, \quad p^a = p, \tag{18}$$

and similarly for the conjugate ones. Let then $\mathbf{x} = (m, p, q_1, q_0, \xi_1, \xi_0)$ denote the collection of all of these order parameters, and $\hat{\mathbf{x}} = (\hat{m}, \hat{p}, \hat{q}_1, \hat{q}_0, \hat{\xi}_1, \hat{\xi}_0)$ the collection of the conjugate ones. Performing the integration over $\vec{N}^a, \vec{f}^a$ at fixed values of $\mathbf{x}, \hat{\mathbf{x}}$ and performing an expansion of the resulting expressions for large $S$, one then obtains the following integral representation for the moments:

$$\langle \mathcal{N}^n(\phi) \rangle = \int d\mathbf{x}\, i d\hat{\mathbf{x}}\, e^{S \mathcal{A}_n(\mathbf{x}, \hat{\mathbf{x}}, \phi) + o(S)}, \tag{19}$$

where the function $\mathcal{A}_n(\mathbf{x}, \hat{\mathbf{x}}, \phi)$ depends only on the order parameters and on the conjugate parameters, as well as on the number $n$ of replicas. Given that $S$ is large, the leading order contribution to the moments can be determined by means of a saddle point approximation, by evaluating $\mathcal{A}_n(\mathbf{x}, \hat{\mathbf{x}}, \phi)$ at the stationary point $\mathbf{x}^*, \hat{\mathbf{x}}^*$ which maximizes it. This can be done in principle for arbitrary values of $n$. We recall that the *annealed* complexity is obtained taking the logarithm of (19) with $n = 1$, while the *quenched* complexity is obtained taking the limit $n \to 0$ according to Eq. (6). By choosing $n = 1$, we obtain:

$$\mathscr{A}_1(\mathbf{x}, \hat{\mathbf{x}}, \phi) = \mathscr{p}_1(\mathbf{x}) + \mathscr{I}(\phi) + \left(\hat{q}_1 q_1 + \hat{\xi}_1 \xi_1 + \hat{m} m + \hat{p} p + \hat{\phi}\phi\right) + \mathscr{G}_1(\hat{\mathbf{x}}), \tag{20}$$

with

$$\mathscr{p}_1(\mathbf{x}) = -\frac{1}{2\sigma^2 q_1^2}\left[(\kappa - \mu m)^2\left(q_1 - \frac{\gamma\, m^2}{1+\gamma}\right) - 2(\kappa - \mu m) q_1 \left(p + \frac{m}{1+\gamma}\right) + \xi_1 q_1\right] - \frac{1}{2}\log(2\pi\sigma^2\, q_1) - \frac{1}{2\sigma^2(1+\gamma)}, \tag{21}$$

$$\mathscr{G}_1(\hat{\mathbf{x}}) = \log\left[\frac{1}{2}\sqrt{\frac{\pi}{\hat{\xi}_1}}\, e^{\frac{\hat{p}^2}{4\hat{\xi}_1}}\,\mathrm{Erfc}\left(-\frac{\hat{p}}{2\sqrt{\hat{\xi}_1}}\right) + \frac{e^{-\hat{\phi}}}{2}\sqrt{\frac{\pi}{\hat{q}_1}}\, e^{\frac{\hat{m}^2}{4\hat{q}_1}}\,\mathrm{Erfc}\left(\frac{\hat{m}}{2\sqrt{\hat{q}_1}}\right)\right], \tag{22}$$

and

$$\mathscr{I}(\phi) = \frac{\phi}{\pi}\int_{-1}^{1} dx \int_0^{\sqrt{1-x^2}} dy \log\left\{\left[\sigma\sqrt{\phi}(1+\gamma)x + 1\right]^2 + \sigma^2\phi(1-\gamma)^2 y^2\right\}. \tag{23}$$

This double integral can be evaluated explicitly, and one finds:

$$\mathscr{I}(\phi) = \begin{cases} \frac{1}{4\gamma\sigma^2}\left(1 - \sqrt{1 - 4\gamma\sigma^2\phi}\right) + \phi\log\left(1 + \sqrt{1 - 4\gamma\sigma^2\phi}\right) - \phi\left(\frac{1}{2} + \log 2\right) & \phi \le \phi_{\mathrm{May}} = \frac{1}{\sigma^2(1+\gamma)^2} \\ \frac{1}{2\sigma^2}\frac{1}{1+\gamma} - \frac{\phi}{2} + \frac{\phi}{2}\log(\sigma^2\phi) & \phi > \phi_{\mathrm{May}} = \frac{1}{\sigma^2(1+\gamma)^2}. \end{cases} \tag{24}$$

As expected, the functional (20) does not depend on $q_0, \xi_0, z$ and on the associated conjugate parameters, that have a meaning only whenever more than one replica is present ($n > 1$). We consider now the case $n \to 0$, relevant to determine the quenched complexity. It can be shown that $\mathscr{A}_n(\mathbf{x}, \hat{\mathbf{x}}, \phi)$ admits the expansion:

$$\mathscr{A}_n(\mathbf{x}, \hat{\mathbf{x}}, \phi) = n\,\bar{\mathscr{A}}(\mathbf{x}, \hat{\mathbf{x}}, \phi) + o(n). \tag{25}$$

Explicitly, for general $\gamma$ we find:

$$\bar{\mathscr{A}}(\mathbf{x}, \hat{\mathbf{x}}, \phi) = \bar{\mathscr{p}}(\mathbf{x}) + \mathscr{I}(\phi) + \hat{q}_1 q_1 + \hat{\xi}_1\xi_1 + \hat{m} m + \hat{p} p + \hat{\phi}\phi - \frac{1}{2}\left(\hat{q}_0 q_0 + \hat{\xi}_0\xi_0\right) - \hat{z} z + \bar{\mathscr{G}}(\hat{\mathbf{x}}), \tag{26}$$

where $\mathscr{I}(\phi)$ is as above, while

$$\begin{aligned} \bar{\mathscr{p}}(\mathbf{x}) = {} & \frac{(\kappa - \mu m)}{\sigma^2(1+\gamma)}\frac{m(q_1 - q_0 + z\gamma)}{(q_1 - q_0)^2} + \frac{(\kappa - \mu m)}{\sigma^2}\frac{p}{(q_1 - q_0)} - \frac{\gamma}{2\sigma^2(1+\gamma)}\frac{z^2(q_1 + q_0)}{(q_1 - q_0)^3} - \frac{\xi_1}{2\sigma^2(q_1 - q_0)} \\ & - \frac{q_0(\xi_0 - \xi_1)}{2\sigma^2(q_1 - q_0)^2} - \frac{1}{2\sigma^2(1+\gamma)}\left[1 + \frac{2q_0 z}{(q_1 - q_0)^2}\right] - \frac{1}{2\sigma^2}\frac{(\kappa - \mu m)^2}{q_1 - q_0} - \frac{\log[2\pi\sigma^2(q_1 - q_0)]}{2} - \frac{q_0}{2[q_1 - q_0]}, \end{aligned} \tag{27}$$

and where $\bar{\mathscr{G}}(\hat{\mathbf{x}})$ admits the following integral representation:

$$\begin{aligned} \bar{\mathscr{G}}(\hat{\mathbf{x}}) = {} & \int \frac{du_1 du_2}{2\pi\sqrt{\hat{q}_0\hat{\xi}_0 - \hat{z}^2}} \exp\left[\frac{\hat{\xi}_0 u_1^2 + \hat{q}_0 u_2^2 - 2\hat{z} u_1 u_2}{2(\hat{q}_0\hat{\xi}_0 - \hat{z}^2)}\right] \times \\ & \times \log\left[e^{-\hat{\phi}}\sqrt{\frac{\pi}{2}}\frac{1}{\sqrt{2\hat{q}_1 - \hat{q}_0}}\, e^{\frac{(u_1 - \hat{m})^2}{2(2\hat{q}_1 - \hat{q}_0)}}\,\mathrm{Erfc}\left(\frac{\hat{m} - u_1}{\sqrt{2(2\hat{q}_1 - \hat{q}_0)}}\right) + \sqrt{\frac{\pi}{2}}\frac{1}{\sqrt{2\hat{\xi}_1 - \hat{\xi}_0}}\, e^{\frac{(u_2 - \hat{p})^2}{2(2\hat{\xi}_1 - \hat{\xi}_0)}}\,\mathrm{Erfc}\left(\frac{-[\hat{p} - u_2]}{\sqrt{2(2\hat{\xi}_1 - \hat{\xi}_0)}}\right)\right], \end{aligned} \tag{28}$$

derived under the assumptions:

$$2\hat{q}_1 - \hat{q}_0 > 0, \quad 2\hat{\xi}_1 - \hat{\xi}_0 > 0, \quad \hat{q}_0 < 0 \quad \hat{\xi}_0 < 0, \quad \hat{q}_0\hat{\xi}_0 - \hat{z}^2 > 0. \tag{29}$$

The saddle point equations fixing the values of the order and conjugate parameters can be obtained taking the derivatives of these expressions, as we recall below. Once the saddle point values are determined by solving the appropriate system of equations, plugging the resulting values into $\mathcal{A}_1$ and $\bar{\mathcal{A}}$ one obtaines the expression for the annealed and quenched complexity, respectively.

**The variational problem and the self-consistent equations.** Given the explicit form of the functionals $\mathcal{A}_1$ and $\bar{\mathcal{A}}$, the last step to obtain the complexity is to determine the values $\mathbf{x}_\star, \hat{\mathbf{x}}_\star$ of the order and conjugate parameters that solve the stationarity conditions

$$\frac{\delta \bar{\mathcal{A}}(\mathbf{x},\hat{\mathbf{x}},\phi)}{\delta \mathbf{x}}\Big|_{\mathbf{x}_\star,\hat{\mathbf{x}}_\star} = 0 = \frac{\delta \bar{\mathcal{A}}(\mathbf{x},\hat{\mathbf{x}},\phi)}{\delta \hat{\mathbf{x}}}\Big|_{\mathbf{x}_\star,\hat{\mathbf{x}}_\star}, \tag{30}$$

as well as the values $\mathbf{x}_\star^{(1)}, \hat{\mathbf{x}}_\star^{(1)}$ that optimize $\mathcal{A}_1$. In the quenched case, taking the variation of $\bar{\mathcal{A}}(\mathbf{x},\hat{\mathbf{x}},\phi)$ with respect to the 15 order and conjugate parameters we obtain two sets of equations of the form $\mathbf{x} = F_1[\hat{\mathbf{x}}]$ and $\hat{\mathbf{x}} = F_2[\mathbf{x}]$, respectively. These equations couple the 7 order parameters $\mathbf{x}$ with the 8 conjugate parameters $\hat{\mathbf{x}}$: inverting one of these sets, one can express the order parameters as a function of the conjugate parameters, $\mathbf{x} = f_3[\hat{\mathbf{x}}]$. The latter can then be fixed by solving the set of coupled self-consistent equations $\hat{\mathbf{x}} = F_2[f_3[\hat{\mathbf{x}}]]$: once the self-consistent values of the conjugate parameters $\hat{\mathbf{x}}$ are found, the order parameters can be determined and the quenched complexity can be obtained computing the action $\bar{\mathcal{A}}$ at the corresponding values of parameters. The annealed calculation is formally analogous. This scheme can be implemented for generic values of $\gamma$. A detailed discussion of the structure of the self-consistent equations and of the strategy to solve them can be found in [65].

**On the unbounded phase.** While the quenched complexity $\Sigma(\phi)$ is independent of $\mu$, the typical properties of the equilibria (given by the saddle-point values of the parameters $m, q_1, q_0$) change with $\mu$; in particular, decreasing $\mu$ at fixed $\sigma, \phi$ one finds that the solutions to the self-consistent equations $m^*, q_1^*, q_0^*$ all increase and the system is driven towards the unbounded phase, signalled by a divergence of these parameters [27, 30, 41, 76]. Given that we have access to the distribution of equilibria as a function of diversity, for each $\sigma$ we can define a $\mu_c(\phi)$ such that for $\mu < \mu_c$ the system is in the unbounded phase. This curves is monotonically decreasing with $\phi$, see Fig. 5. This suggests to define the boundary of the bounded phase in the $\sigma, \mu$ diagram thorough $\mu^* = \max_{\phi:\Sigma(\phi)\geq 0} \mu_c(\phi) = \mu_c(\phi_{\rm a})$, to ensure that *none* of the equilibria is in the unbounded phase, no matter their diversity. We remark that the unbounded phase defined in this way has a larger extension with respect to that estimated via the cavity approximation, since $\mu^* > \mu_c(\phi_{\rm cav})$. On the other hand, for $\mu = \mu^*$ the most numerous equilibria having $\phi = \phi_{\rm Max}$ are still in the bounded phase, so the phase boundary obtained using typical equilibria is yet different.

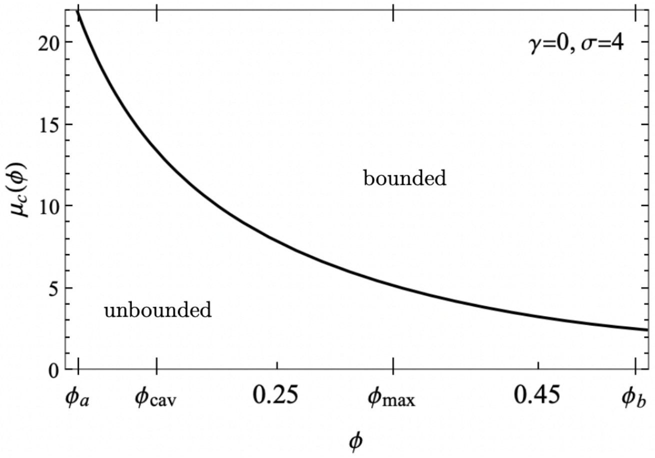

FIG. 5: Curve separating the unbounded ($\mu < \mu_c$) from the bounded ($\mu > \mu_c$) phase as a function of the diversity $\phi$.

**On the vanishing of the total complexity.** We claimed in the main text that the total complexity $\Sigma_{\rm tot} = \Sigma(\phi_{\max})$ vanishes as $\Sigma_{\rm tot} \sim (\sigma - \sigma_c)^2$ as $\sigma \to \sigma_c^+$ for $\gamma = 0$, and that we expect this behavior to extend to $\gamma \neq 0$ *provided that* the maximum of $\Sigma(\phi)$ in the vicinity of $\sigma_c$ lies in a region of $\phi$ in which the annealed calculation is correct. On the other hand, if at the maximum of $\Sigma(\phi)$ the quenched formalism has to be employed, we have indications of the fact that the exponent controlling the vanishing of the complexity is a different one. We motivate these claims in this subsection, and refer to Ref. [65] for the details. The total variation of $\Sigma_{\rm tot}$ with respect to $\sigma$ is given by:

$$\frac{d\Sigma_{\rm tot}}{d\sigma} = \partial_\sigma \bar{\mathcal{A}}(\mathbf{x},\hat{\mathbf{x}},\phi)\Big|_{\mathbf{x}^*,\hat{\mathbf{x}}^*,\phi_{\max}} = \partial_\sigma \bar{p}(\mathbf{x})\Big|_{\mathbf{x}^*,\hat{\mathbf{x}}^*,\phi_{\max}} + \partial_\sigma \mathscr{I}(\phi)\Big|_{\mathbf{x}^*,\hat{\mathbf{x}}^*,\phi_{\max}}, \tag{31}$$

where we used the fact that $(\mathbf{x}^*, \hat{\mathbf{x}}^*, \phi_{\max})$ are a stationary point of $\bar{\mathscr{A}}(\mathbf{x}, \hat{\mathbf{x}}, \phi)$. For $\sigma < \sigma_c = \sqrt{2}(1+\gamma)^{-1}$, the system is in the unique equilibrium phase and a single, stable equilibrium exists. Its properties (described by the order parameters $m, q_1$) can be derived using the cavity method. For general $\gamma$ and $\kappa = 1$, one finds [65] that at $\sigma_c$ the equilibrium satisfies $m = \mu^{-1} = -(1+\gamma)p$, $q_1 = (1+\gamma)^2\xi_1$ and $\phi = \phi_{\max} = \phi_{\text{May}} = [\sigma(1+\gamma)]^{-2}$. This implies:

$$\partial_\sigma \mathscr{I}(\phi)\Big|_{\sigma_c, \phi_{\max}} = -\frac{\gamma(1+\gamma)}{2\sqrt{2}}. \tag{32}$$

In order for the complexity to vanish quadratically at $\sigma_c$, this term should be compensated by the one obtained deriving the distribution of the forces $\bar{p}(\mathbf{x})$. If for $\sigma > \sigma_c$ and $\phi = \phi_{\max}$ the annealed calculation is exact, than one can replace $\bar{p}(\mathbf{x}) \to p_1(\mathbf{x})$, and use that for the values of parameters predicted by the cavity approximation it holds:

$$\partial_\sigma p_1\Big|_{\sigma_c, \phi_{\max}} = \frac{\gamma(1+\gamma)}{2\sqrt{2}}, \tag{33}$$

which cancels exactly (32). Therefore, if $\Sigma_{\text{tot}}$ is analytic at $\sigma_c$, it has to vanish quadratically (one can check that the second derivative is not vanishing at the critical point). On the other hand, for $\gamma = 0$ we know that at $\phi_{\max}$ the annealed calculation is never correct, for any $\sigma > \sigma_c$. Assuming that this is still true for $\gamma = 0$, imposing that (31) vanishes and using the conditions given by the cavity approximation (in addition to $q_0 = (1+\gamma)^2\xi_0$ by symmetry) we obtain the following conditions for the order parameters:

$$\frac{z}{(1+\gamma)(q_1 - q_0)^2}\left(\frac{\gamma z(q_1 + q_0)}{2(q_1 - q_0)} + q_0\right) = 0, \tag{34}$$

which implies either $z = 0$, or $z = 2q_0(q_1 - q_0)/[\gamma(q_1 + q_0)]$. Both these solutions however can be shown to be incompatible with the quenched self-consistent equations for this order parameter [65] except for the case $\gamma = 0$, when in fact it holds $z = 0$ at the transition point. Therefore, if for $\gamma \neq 0$ the total complexity at $\sigma \sim \sigma_c^+$ is quenched, one should expect a different power law since the linear contribution is not vanishing. We remark that the symmetric case $\gamma = 1$ is special, since the total complexity should vanish in a non-analytic way at the transition, due to the square root term in (24) whose argument vanishes when $\phi = \phi_{\text{May}}, \sigma = \sigma_c$.